



T.C.

NIGDE UNIVERSITY

THE GRADUATE SCHOOL OF NATURAL AND APPLIED SCIENCES

MECHANICAL ENGINEERING DEPARTMENT

DEVELOPMENT OF REDOX TOLERANT SOLID OXIDE FUEL CELLS

PhD THESIS

THE GRADUATE SCHOOL OF NATURAL AND
APPLIED SCIENCES OF NIGDE UNIVERSITY

BORA TIMURKUTLUK

SEPTEMBER 2013

T.C.
NIGDE UNIVERSITY
THE GRADUATE SCHOOL OF NATURAL AND APPLIED SCIENCES
MECHANICAL ENGINEERING DEPARTMENT

REDOX TOLERANT SOLID OXIDE FUEL CELLS

BORA TIMURKUTLUK

PhD Thesis


Supervisor

Prof. Dr. Mahmut D. MAT

September 2013

Bora TİMURKUTLUK tarafından **Prof. Dr. Mahmut D. MAT** danışmanlığında hazırlanan “**Development of Redox Tolerant Solid Oxide Fuel Cells**” adlı bu çalışma jürimiz tarafından Niğde Üniversitesi Fen Bilimleri Enstitüsü **Makine Mühendisliği** Anabilim Dalında Doktora tezi olarak kabul edilmiştir.

Başkan : Prof. Dr. Sadık KAKAÇ, TOBB Üniversitesi



Üye : Prof. Dr. Mahmut D. MAT, Melikşah Üniversitesi



Üye : Prof. Dr. Mustafa İLBAŞ, Gazi Üniversitesi



Üye : Doç. Dr. İlker TARI, Ortadoğu Teknik Üniversitesi



Üye : Yrd. Doç. Dr. Fatih AY, Niğde Üniversitesi



ONAY:

Bu tez, Fen Bilimleri Enstitüsü Yönetim Kurulunca belirlenmiş olan yukarıdaki jüri üyeleri tarafından/...../20.... tarihinde uygun görülmüş ve Enstitü Yönetim Kurulu'nun/...../20.... tarih ve sayılı kararıyla kabul edilmiştir.

...../...../20...

Doç. Dr. Osman SİVRİKAYA
MÜDÜR

I hereby declare that all information in this document has been obtained and presented in accordance with academic rules and ethical conduct. I also declare that, as required by these rules and conduct, I have fully cited and referenced all material and results that are not original to this work.

Bora Timurkutluk

SUMMARY

DEVELOPMENT OF REDOX TOLERANT SOLID OXIDE FUEL CELLS

TIMURKUTLUK, Bora

Nigde University

The Graduate School of Natural and Applied Sciences

Department of Mechanical Engineering

Supervisor : Professor Dr. Mahmut D. MAT

September 2013, 187 pages

Anode supported solid oxide fuel cells (SOFCs) having various properties are developed and the effects of fabrication parameters on the cell performance and redox behavior of the cell are investigated experimentally and theoretically. In the experimental program, an yttria stabilized zirconia based anode supported membrane electrode group (MEG) is developed with the tape casting, co-sintering and screen printing methodology. For comparison, various anode supported cells with different electrolyte thickness and anode support porosities are also fabricated. An experimental setup is devised for the performance measurement of the cells before and after redox cycling. The effects of anode fabrication parameters on the cell performances and the redox stability of the cells are investigated. The mechanical performance of the cell before and after redox cycling is also measured via three point bending tests. Experimental results reveal that the porosity of the anode support and the thickness of the electrolyte should be carefully decided by considering not only the cell performances but also the redox stability.

In theoretical study a mathematical model is developed to represent the fluid flow, the heat transfer, the species transport and the electrochemical reaction in solid oxide fuel cells. In addition, a redox model representing the mechanical damage in the

electrochemical reaction zones due to redox cycling is developed by defining a damage function as a function of strains and a damage coefficient. The differential equations are solved numerically with a commercial code which employs a finite element based approach. The effects of anode porosity and the electrolyte thickness on the cell performance and redox stability of the cells are numerically investigated.

The experimental and numerical results are compared to validate the mathematical model. The mathematical model is found to agree reasonable with experimental data.

Keywords: Solid oxide fuel cell, anode supported, performance measurement, three point bending, mathematical modeling, redox modeling, damage function

ÖZET

REDOKS TÖLERANSLI KATI OKSİT YAKIT PİLİ GELİŞTİRİLMESİ

TIMURKUTLUK, Bora

Niğde Üniversitesi

Fen Bilimleri Enstitüsü

Makina Mühendisliği Ana Bilim Dalı

Danışman : Prof. Dr. Mahmut D. MAT

Eylül 2013, 187 sayfa

Farklı özelliklere sahip anot destekli katı oksit yakıt pilleri (KOYP) geliştirilmiş ve anot destek üretim parametrelerinin hücre performansına ve redoks dayanımına olan etkisi deneysel ve teorik olarak incelenmiştir. Deneysel programda itriyum oksit ile stabilize edilmiş zirkonyum oksit (YSZ) temelli anot destekli membran elektrot grupları (MEG) şerit döküm, birlikte sinterleme ve ipek baskı teknikleri kullanılarak geliştirilmiştir. Karşılaştırma amaçlı, farklı anot gözenekliliğine ve elektrolit kalınlığına sahip anot destekli hücreler de imal edilmiştir. Hücrelerin redoks öncesi ve sonrasındaki performanslarının ve redoks dayanımlarının belirlenmesi için bir deneysel düzenek hazırlanmıştır. Deneysel sonuçlar anot destek gözenekliliği ve elektrolit kalınlığının hem hücre performansı hem de redoks dayanımını göz önüne alarak belirlenmesi gerektiğini ortaya koymuştur.

Teorik programda KOYP içerisinde akış, ısı transferi, madde transferi, elektrokimyasal reaksiyonları ifade eden matematiksel bir model geliştirilmiştir. Ayrıca, elektrokimyasal reaksiyon bölgelerinde redoks kaynaklı mekanik hasarları ifade eden bir redoks modeli de geliştirilmiştir. Modelde tanımlanan hasar fonksiyonu gerinme bağımlı olarak ifade edilmiştir. Diferansiyel denklemler ticari bir sonlu elemanlar programı yardımı ile

sayısal olarak çözülmüştür. Anot destek gözenekliliği ve elektrolit kalınlığının hücre performans ve redoks dayanımı üzerindeki etkileri sayısal olarak incelenmiştir.

Deneysel ve sayısal sonuçlar, matematiksel modeli doğrulamak için karşılaştırılmıştır. Matematiksel modelin deneysel datalarla uyumlu olduğu belirlenmiştir.

Anahtar Sözcükler: Katı oksit yakıt pili, anot destek, performans ölçümleri, üç nokta bükme, matematiksel modelleme, redoks modeli, hasar fonksiyonu

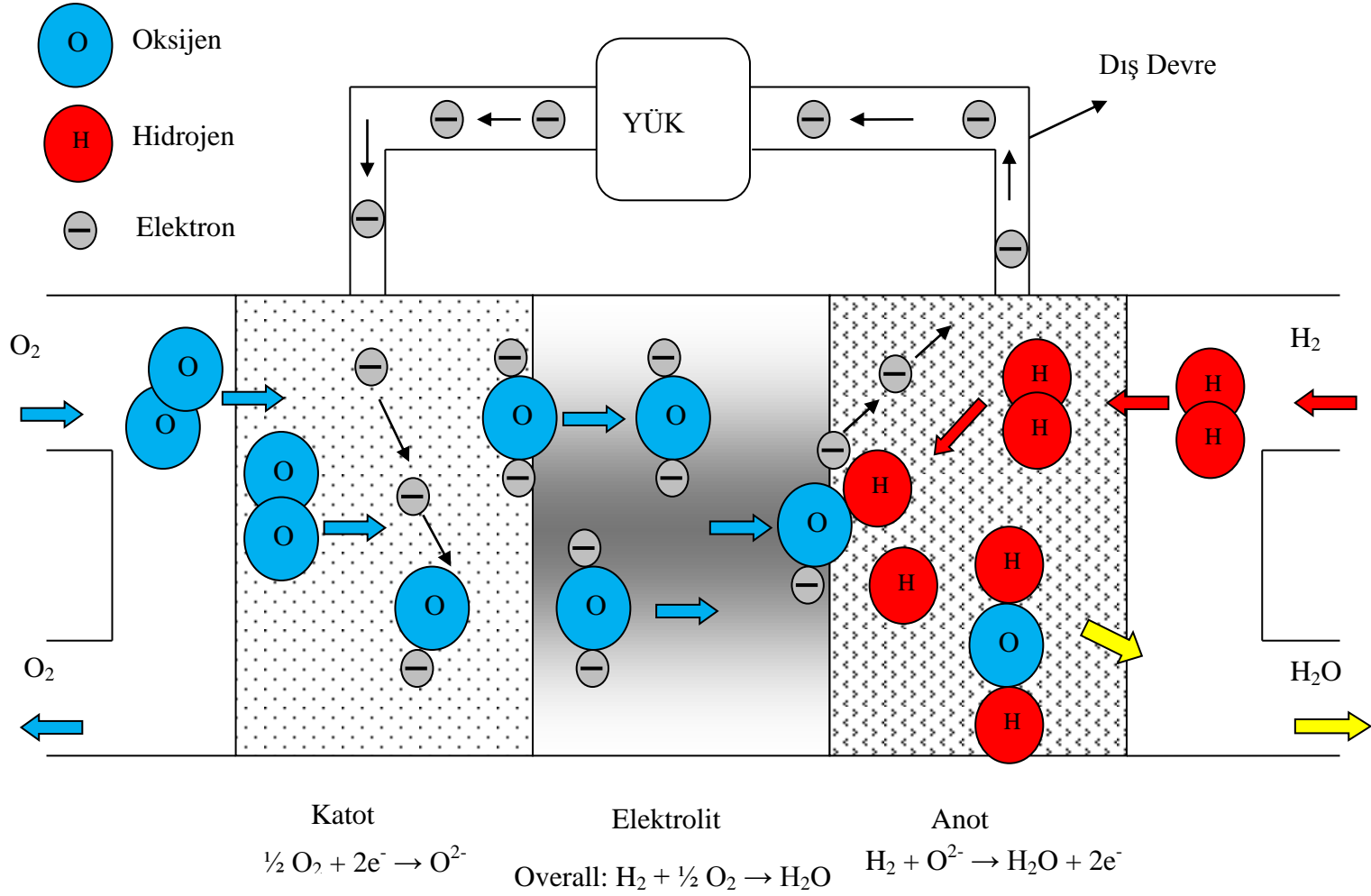
GENİŞLETİLMİŞ ÖZET

1. GİRİŞ

Katı oksit yakıt pilleri (KOYP), yakıt kimyasal enerjisini doğrudan elektrik ve önemli miktarda ısı enerjisine dönüştüren yeni nesil çevre dostu elektrokimyasal cihazlardır. Bu dönüşüm herhangi bir ara basamak içermediği için KOYP elektrik verimleri, benzer olgun teknolojilerden olan içten yanmalı motorlar veya jeneratörlere oranla daha yüksek olmaktadır. KOYP yüksek sıcaklıklarda (600-1000°C) çalışmakta olup çalışma sıcaklığı kullanılan elektrolit malzemesine göre değişmektedir. Yüksek çalışma sıcaklığının bir sonucu olarak artan elektrokimyasal reaksiyon kinetiği, KOYP elektrik verimini daha da yükseltmekte ve bu durum KOYP'yi yakıt pilleri arasında en verimli yakıt pili haline getirmektedir. Ayrıca diğer yakıt pillerinde kullanılması zorunlu olan saf hidrojenin yanı sıra hidrokarbon yakıtlar da doğrudan veya bir reformlama işlemi sonrasında KOYP'de yakıt olarak kullanılabilir. Bu açıdan KOYP aynı zamanda yakıt esnekliğini de beraberinde sunmaktadır.

Anot, elektrolit ve katot tabakalarından oluşan membran elektrot grubu (MEG), KOYP sisteminin kilit elemanıdır. Anot; yakıt oksidasyonu görevini üstlenirken, katot elektrokimyasal reaksiyonu sonucunda ortaya çıkan oksijen iyonları elektrolit tabakasından anot tabakasından transfer edilmektedir. KOYP çalışma prensibi Şekil 1.1'de verilmiştir. Elektrik akımı bir dış devre ile toplanırken elektrokimyasal reaksiyonlar üçlü faz bölgesi olarak adlandırılan (ÜFB) ve iyon iletken, elektronik iletken/katalizör ve reaktant fazlarının bulunduğu alanlarda meydana gelmektedir.

İttriyum oksit ile stabilize edilmiş zirkonyum oksit (YSZ) en yaygın KOYP elektrolit malzemesi olarak dikkat çekmektedir. Fakat, YSZ elektrolit destekli bir KOYP'den istenilen performansın elde edilmesi için 1000°C gibi yüksek bir çalışma sıcaklığı gerekmektedir. YSZ'nin kabul edilebilir bir iyonik iletkenlik göstermesi için gerekli olan bu denli yüksek çalışma sıcaklıklarında ise hücre elamanlarından iyi bir stabilite beklemek oldukça zor görünmektedir. Ayrıca, yüksek sıcaklığa dayanıklı interkonnektör ve sızdırmazlık malzemelerinin sınırlı ve pahalı olması sistem maliyetini arttırmaktadır.



Şekil 1.1. KOYP çalışma prensibi

1.1 İlgilenilen Fiziksel Problem

KOYP çalışma sıcaklığının düşürülmesi, KOYP sistem maliyetinin azaltılması, servis süresinin iyileştirilmesi ve ticarileşebilme açısından çok büyük önem taşımaktadır. KOYP çalışma sıcaklığını azaltmanın bir yolu YSZ elektrolit kalınlığının, hücre tasarımını elektrolit destekli anot destekliye değiştirerek azaltılması şeklinde olmaktadır. Şerit döküm ve ipek baskı gibi gelişen ince film teknolojilerini (Wang vd., 2011; Le vd., 2010; Park vd., 2010; Ana vd., 2010) veya buhar kaplama (Meng vd., 2008; Jung vd., 2006; Meng vd., 2004, Sasaki vd., 2008; Kuo vd., 2009), lazer kaplama (Yang vd., 2007; Rodrigo vd., 2007; Pryds vd., 2006) ve elektroforez (Hosomi vd., 2007; Majhi vd., 2011; Matsuda vd., 2007) gibi yüzey kaplama tekniklerini kullanarak 1-10 µm kalınlıkta elektrolit tabakasına sahip olan anot destekli KOYP hücreleri üretmek mümkün olmaktadır. Anot destekli tasarım her ne kadar standart YSZ elektrolit destekli tasarıma göre 200-300°C daha düşük sıcaklıklarda yüksek performans sergilese de, en yaygın KOYP anot malzemesi olan nikel tabanlı anotların döngüsel indirgenme ($NiO \rightarrow Ni$) ve yükseltgenme ($Ni \rightarrow NiO$) sırasındaki hacimsel değişiklikler pil servis süresi açısından ciddi bir problem oluşturmaktadır. Redoks olarak adlandırılan bu sürekli faz değişimi KOYP servis süresi boyunca kaçınılmaz olarak tekrarlanmaktadır. Bu faz dönüşümleri sırasında ortaya çıkan hacimsel değişiklikler hücreye mekanik olarak zarar vermekte ve KOYP sistem ömrünü sınırlamaktadır. Bu yüzden nikel tabanlı KOYP anotların redoks dayanımlarının detaylı bir şekilde incelenmesi ve sorunsuz uzun süreli bir pil ömrü için iyileştirilmesi gerekmektedir.

1.1.1 KOYP Anot

KOYP anodunun sistem içerisindeki en önemli rolü, yakıt oksidasyon reaksiyonu için elektrokimyasal reaksiyon alanları oluşturmaktır. Anot elektrokimyasal reaksiyonunda üretilen elektronlar da anot aracılığı ile interkonnektörlere taşınarak kullanılabilir elektrik enerjisine dönüştürülmektedir. Bu kapsamda, KOYP anodunun aşağıdaki özellikleri taşıması gerekmektedir:

- Yüksek iyonik ve elektronik iletkenlik
- Kimyasal kararlılık ve uyum

- Uygun bir ısıl genleşme katsayısı
- Yakıtı karşı yüksek katalitik aktivite
- Akışa ve reaksiyonların gerçekleşmesine izin veren gözenekli bir yapı
- Karbonlaşma ve kükürt dayanımı
- Yakıt esnekliği
- Kolay ve ucuz imalat

Fakat yukarıdaki özelliklerin tamamını ortaya koyan tek bir anot malzemesi henüz geliştirilememiştir. Bu yüzden kompozit malzemeler en uygun anot malzemesi olarak dikkat çekmektedir. Tipik bir KOYP anodu, metalik ve oksit olmak üzere iki kısımdan oluşmaktadır. Metalik malzeme katalitik görevinin yanı sıra gerekli elektronik iletkenliği de sağlamaktadır. Her ne kadar metalik malzemeleri tek başlarına KOYP anodu olarak kullanmak mümkün olsa da, bu durum anot elektrokimyasal reaksiyon bölgesinin sadece anot/elektrolit ara yüzeyi ile sınırlanmasına ve anot ile elektrolit ısıl genleşme uyumsuzluğuna yol açmaktadır. Bu yüzden gerek yüksek performans gerekse de yapısal kararlılık için ikinci bir malzeme eklenmesi gerekmektedir. Bu durum metalik kısma eklenen bir miktar elektrolit malzemesi ile sağlanmaktadır. Eklenen elektrolit malzemesi sayesinde anot ile elektrolit arasındaki termal genleşme uyumunun sağlanmasının yanı sıra artan elektrokimyasal reaksiyon bölgeleri sayesinde pil performansı da iyileşmektedir.

Nikel oksit (NiO)/itriyum oksit ile stabilize edilmiş zirkonyum oksit (YSZ) en yaygın anot malzemesi olarak dikkat çekmektedir. Ucuz maliyetinin yanı sıra (Huang vd., 2003; Horita vd., 2006; Lee vd., 2006), NiO çok iyi bir akım toplayıcı olarak değerlendirilmektedir (Radovic ve Curzio, 2004; Mori vd., 2003). Ayrıca NiO/YSZ hidrojen yakıtlı KOYP çalışma koşullarında yüksek bir katalitik aktivite (Skarmoutsos vd., 2000; Finnerty vd., 1998; Lu vd., 2004) ve iyi bir kimyasal kararlılık göstermektedir (Jiang vd., 2006; Kendall vd., 2002; Yin vd., 2006). Bu denli iyi avantajlara sahip olan NiO/YSZ anot, hidrokarbon yakıt kullanılması durumunda iki kritik problemi de beraberinde getirmektedir. İlk problem karbonlaşma olarak adlandırılmaktadır. Nikel, katı karbonlaşma reaksiyonu için de çok iyi bir katalizör olarak bilinmektedir. Fakat hidrokarbon yakıt kullanıldığında biriken bu katı karbonlar anot aktif yüzeylerini kaplayarak nikel katalizörünü deaktive etmektedir. Bu yüzden pil

performansında ciddi kayıplar meydana gelmektedir (Haldane ve Etsell, 2005; Xie vd., 2006; Wang vd., 2004). Bu durumun önüne geçmek için Cu (McIntosh vd., 2002; Gunji vd., 2004; Pudmich vd., 2000) ve CeO₂ (Gunji vd., 2004; Zhu vd., 2006; Sauvet ve Fouletier, 2001) başta olmak üzere anoda belli oranlarda Ru (Koh vd., 2002), Mo (Zhu ve Deevi, 2003; Sauvet ve Irvine, 2004) ve Au (Zhu ve Deevi, 2003) eklenmesi önerilmektedir. İkinci büyük problem ise yakıt içerisindeki kirliliklerden kaynaklanmaktadır. Özellikle neredeyse bütün hidrokarbonlarda bulunan kükürt bileşikleri nikel ile reaksiyona girerek nikel sülfat oluşturmaktadır. Kükürt zehirlenmesi olarak adlandırılan bu durum sonrasında anot, katalitik özelliğini kaybetmekte ve pil performansı ciddi boyutlarda düşmektedir (Cheng vd., 2005; Fu vd., 2006; He vd., 2004). Bu yüzden hidrokarbon yakıtlarla çalışan KOYP sistemine bir sülfür giderici ünite eklenmesi kaçınılmaz görünmektedir.

1.1.2 Redoksun tanımı ve etkileri

Yukarıda ifade edilen problemlerin yanı sıra, KOYP çalışması sırasında nikel temelli anotta meydana gelen döngüsel indirgenme ve yükseltgenmeler (redoks) nikel tabanlı KOYP anodunun en ciddi problemi olarak dikkat çekmektedir. Karbonlaşma ve sülfür zehirlenmesinin aksine, literatürde redoksun tamamen önüne geçecek bir çözüm bulunamamıştır. Her ne kadar yüksek redoks toleranslı alternatif anot malzemeleri geliştirilmiş olsa da bu malzemelerin hiçbiri nikel performansına ulaşamadığı için tercih edilmemektedir.

KOYP üretimi sırasında anotta bulunan nikel başlangıçta oksit formatında (NiO) bulunmaktadır. Sistemin çalıştırılması ile beslenen hidrojen neticesinde nikel oksit, aşağıda verilen reaksiyon sonucunda metalik nikel dönüşmektedir:



Bu indirgenme sonrasında meydana gelen hacimsel değişiklik Çizelge 1.1'de verilen değerler kullanılarak aşağıdaki gibi hesaplanabilir:

$$\Delta V_{indirgenme} = \frac{V_{Ni} - V_{NiO}}{V_{NiO}} = -41.7 \% \quad (1.2)$$

Çizelge 1.1. Nikel ve nikel oksit özellikleri

	NiO	Ni
Mol ağırlığı (g/mol)	74.71	58.71
Yoğunluk (g/cm ³)	6.60	8.90
Hacim (cm ³ /mol)	11.32	6.60

İndirgenme sonrasında oluşan metalik nikelin, nikel oksite göre % 42 daha az hacim kapladığı görülmektedir. Başka bir ifade ile, nikel oksit-nikel dönüşümü sırasında hacimce % 42'lik bir küçülme meydana gelmektedir.

İndirgenen anottaki nikel, sisteme hidrojen beslendiği sürece metalik formunu korumaktadır. Fakat, KOYP çalışması sırasında meydana gelebilecek olası sızdırmazlık problemi, yakıt besleme problemi, yüksek yakıt tüketimi ve hatta acil kapama durumlarındaki anodun oksijen ile temas etmesi metalik nikeli tekrar oksit formuna dönüştürmektedir. Bu yüzden sistem çalışma ömrü göz önüne alındığında, KOYP anodunun defalarca bu döngülere maruz kalması kaçınılmaz görünmektedir.

Oksidasyon reaksiyonu aşağıda verilmiştir:



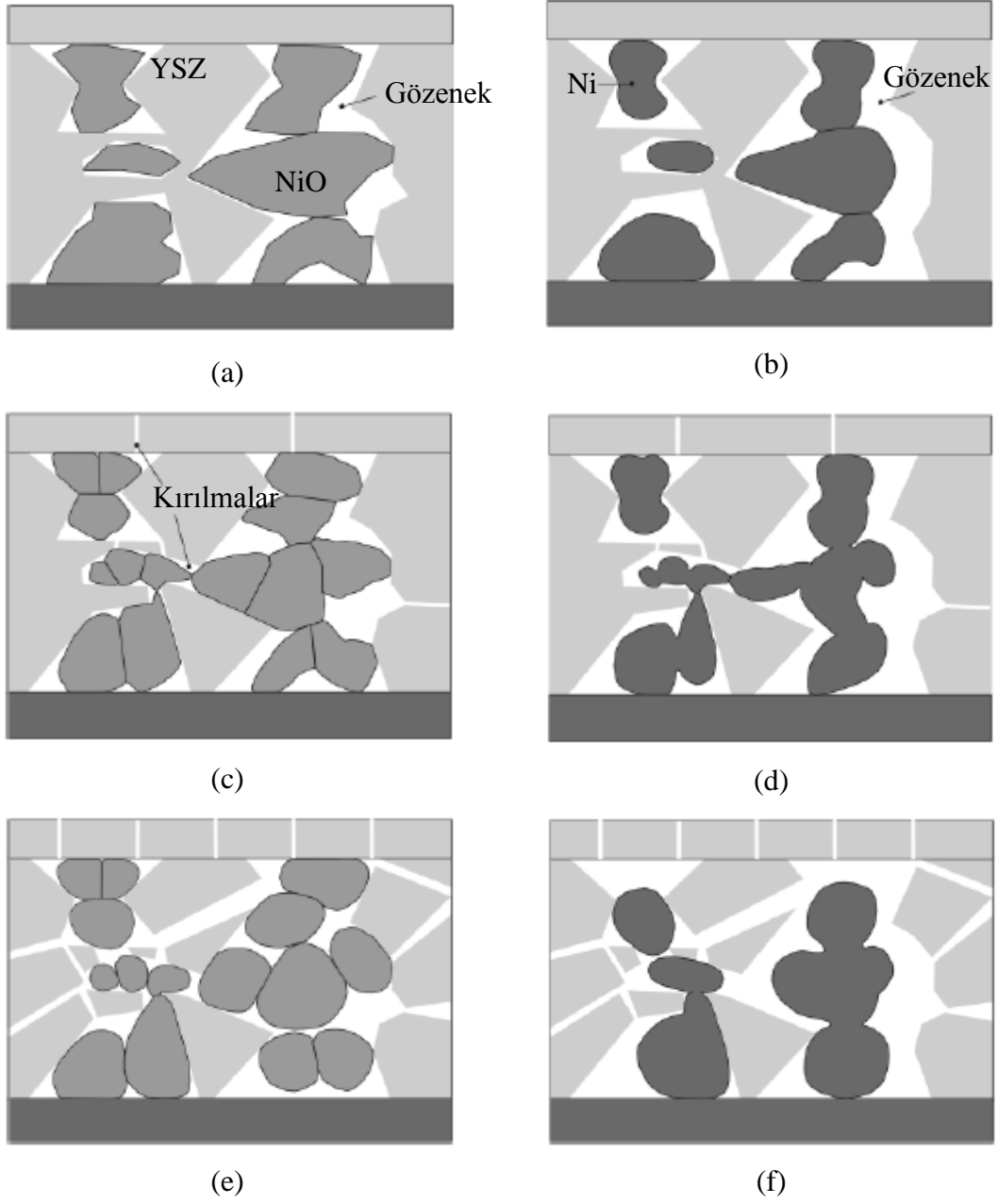
Benzer şekilde oksidasyon sonrasında meydana gelen hacim değişikliği

$$\Delta V_{oksidasyon} = \frac{V_{NiO} - V_{Ni}}{V_{Ni}} = 71.2 \% \quad (1.4)$$

olarak hesaplanabilir.

Redoks döngüleri sırasında meydana gelen bu denli büyük hacim değişiklikleri NiO/YSZ bağlarına ciddi zararlar vererek mikro kırılmalara yol açmaktadır. Artan

redoks döngüleri ile bu zararlar katlanarak artmakta ve pil performansında ciddi kayıplar ve hatta pilde kırılmalar meydana gelmektedir.



Şekil 1.2. Redoksün anot mikroyapısına olan etkisi

Bu durum Klemensø and Mogensen (2007) çalışmasında çizgisel gösterim ile gözler önüne serilmiştir (Şekil 1.2). Sinterleme sonrasındaki anot mikroyapısı Şekil 1.2(a)'da verilirken ilk indirgenme sonrasındaki mikroyapısal değişim Şekil 1.2(b)'de gösterilmiştir. İndirgenme sonrasında meydana gelen hacimsel azalmadan dolayı nikel

fazının yeniden organize olduğu, daha dairesel bir yapı kazandığı ve sinterlendiği görülmektedir. İlk oksidasyon ve ikinci indirgenme sonrasındaki mikroyapının aldığı haller sırası ile Şekil 1.2(c) ve Şekil 1.2(d)'de verilmiştir. İlk oksidasyon sonrasındaki mikroyapının sinterleme sonrasındaki yapıdan çok farklı olduğu görülmektedir. Oksidasyon kinetiğinin çok hızlı olması durumunda Ni/NiO taneciklerinin şekilde görüldüğü gibi birkaç küçük parçaya bölünerek boşluklara doğru yayılacağı ifade edilmiştir. Ayrıca oksidasyon sırasında meydana gelen hacimsel genişlemenin ortaya çıkaracağı gerilmelerin yapısal olarak tölere edilememesi durumunda ise NiO/YSZ bağlarında şekilde de verilen kırılmaların olabileceği belirtilmiştir. Redoks döngülerinin devam etmesi durumlarında ise oksidasyon ve indirgenme sonrasındaki son durumlar sırası ile Şekil 1.2(e) ve Şekil 1.2(f)'de verilmiştir. İleriki oksidasyon aşamalarında YSZ ağında ve hatta elektrolitte de kırılmaların meydana gelebileceği ifade edilmiştir. İndirgemenin sonra ise nikelin birleştiği ve hemen hemen hiç reaksiyon bölgesinin kalmadığı görülmektedir (Şekil 1.2(f)).

1.2 Tezin Amacı

Anot destekli tasarım 1-10 µm kalınlığa kadar inceltmiş elektrolit tabakası sayesinde hem düşük çalışma sıcaklıkları hem de yüksek performansı bir arada sunmaktadır. Fakat geleneksel nikel içerikli anodun kaçınılmaz döngüsel indirgenme ve yükseltgenmeleri sırasında meydana gelen hacimsel değişiklikler sonucunda ortaya çıkan mekanik hasarlar, KOYP performansını ve dolayısı ile ömrünü ciddi şekilde düşürmektedir. Bu yüzden gerek KOYP sistemlerinin ticarileşebilmesini sağlamak gerekse de çalışma süresini uzatmak için KOYP anot redoks dayanımının iyileştirilmesi gerekmektedir. KOYP'nin deneysel olarak incelenmesi veya KOYP çalışmasının hücre ve stak boyutlarında sayısal olarak modellenmesi ve KOYP anot redoks davranışının deneysel olarak incelenmesi üzerine literatürde birçok çalışma bulunmasına rağmen, redoks modellemesini deneysel çalışmalar ile birleştiren çalışmaların oldukça sınırlı olduğu görülmektedir.

Bu yüzden bu tez ile:

1. Farklı elektrolit kalınlığı ve anot gözenekliliğine sahip anot destekli hücre geliştirilmesi,
2. Yüksek sıcaklık redoks test prosedürü geliştirilmesi,
3. Performans ve redoks davranışının incelenmesi için deneysel düzenek kurulması,
4. Hücre performansının yanı sıra hücre içerisindeki sıcaklık, akım ve madde dağılımlarını ortaya koyan bir matematiksel model geliştirilmesi,
5. Tekrar oksitlenme sonrasında ortaya çıkan mekanik hasarın tahmini için bir redoks modelinin geliştirilmesi,
6. Bu iki modelin birleştirilmesi ve çözümü,
7. Deneysel çalışmalarla matematiksel modelin doğrulanması ve iyileştirilmesi,
8. Önemli üretime parametrelerinin hücre performansı ve redoks dayanımı açısından incelenmesi ve
9. Yüksek redoks dayanımlı anot özelliklerinin belirlenmesi veya tahmin edilmesi

amaçlanmaktadır.

2. LİTERATÜR ÖZETİ

2.1 Redoksun Etkileri

Yaygın olarak kullanılan KOYP anot malzemesinin NiO/YSZ olması ve anot destekli hücrelerin redoks döngülerine elektrolitin oldukça ince olması sebebi ile daha az dayanıklı olması nedeni ile araştırmacılar daha çok NiO/YSZ anot destekli hücrelerin redoks davranışı üzerinde yoğunlaşmıştır. Redoks döngüsünün hücre yapısı, fiziksel/mekanik/elektriksel özelliklere ve anot/hücre performansına olan etkileri dilatometre, elektron mikroskobu, termo gravimetrik ve empedans analizleri gibi yöntemlerle incelenmiştir.

Young ve Birss (2011) NiO/YSZ anot destekli hücrelerde 700 °C ve üzeri sıcaklıklarda meydana gelen tam oksidasyonun daha düşük sıcaklıklardakine göre elektrolitte daha fazla ve daha büyük kırılmalara sebep olduğunu göstermiştir. 700 °C, 800 °C ve 900 °C sıcaklıklarda gerçekleştirilen sadece iki tam oksidasyon sonrasında YSZ elektrolitte kırılmalar olduğu rapor edilmiştir. Bu durum termo gravimetrik analiz ile doğrulanan difüzyon kontrollü oksitlenme kaynaklı homojen olmayan oksidasyon ve anot tabakası içerisindeki Ni/NiO ve oksijen gradyanı ile açıklanmıştır. Elektron mikroskobu da özellikle yüksek sıcaklıklardaki veya düşük oksijen kısmi basınçlarındaki nikel oksidasyonunun homojen olmadığını göstermiştir. Bu durumda anodun dış kısmındaki nikelin tamamen oksitlendiği fakat iç kısımlardakilerin metalik fazını koruduğu ifade edilmiştir. Nikelin oksitlenmesine devam edilmesi durumunda ise nikel oksit dönüşümü sırasındaki ortaya çıkan hacimsel genişlemenin elektrolite doğru olacağı ve bu durumun hücrenin bükülmesi ve nihayetinde elektrolitin kırılması ile sonuçlanacağı rapor edilmiştir.

Klemensø ve Mogensen (2007) NiO/YSZ anodun redoks davranışını elektriksel karakterizasyon ile incelemiştir. Redoks döngüleri sonrasında iletkenliğin azaldığı belirlenmiştir. Elektriksel iletkenlikte bu düşüş redoksa bağlı olarak meydana gelen nikel taneciklerinin büyümesi ve kümeleşmesine bağlanmıştır. Redoks sırasında meydana gelen Ni-NiO dönüşümlerinden kaynaklanan mikroyapısal değişimin YSZ ağına zarar verdiği belirlenmiştir. Meydana gelen mekanik hasarın anot içeriği ve

gözenekliliği ile ilişkili olduğu tespit edilmiştir. Fakat sinterleme sonrasındaki anot gözenekliliğinin % 8'den küçük olması durumunda gözenekliliğin önemli olmadığı görülmüştür.

Walbillig vd. (2005) ise NiO/YSZ anodun redoks davranışını elektrokimyasal ve mikroyapısal olarak ele almıştır. Redoks döngü süresinin etkisi, çalışmada ayrıca incelenmiştir. Elektrokimyasal testler, her redoks döngüsü sonrasında hücre performansında azalmalar olduğunu ve özellikle 1 saatten daha fazla redoks sürelerinde bu düşüşlerin önemli boyutlara ulaştığını ortaya koymuştur. Benzer davranış açık devre potansiyellerinde de görülmüştür. Özellikle uzun redoks sürelerinde azalan açık devre voltajı elektrolitte kırılmalar oluştuğunu göstermiştir. Mikroyapısal incelemeler redoks döngüleri sonrasında anot yapısının önemli ölçüde değiştiğini ve bu yüzden elektrolitte kırılmalar oluştuğunu doğrulamıştır.

Zhang vd. (2005) oksidasyon sıcaklığının anot mikroyapısı üzerinde önemli bir etkiye sahip olduğunu rapor etmiştir. 800 °C sıcaklıkta 80 mm x 8 mm x 0,8 mm boyutuna sahip örnekler üzerinde yapılan oksidasyon testleri nikel parçacıklarının değişken boyutlarda olduğunu ve NiO taneciklerinin sürekli büyüdüğünü göstermiştir. Öte yandan 600 °C sıcaklıktaki testlerde ise tane boyutu değişimi gözlemlenmezken Ni-NiO dönüşümünün de yavaşladığı tespit edilmiştir.

Sarantaridis vd. (2008) ise NiO/YSZ anodun 900 °C sıcaklıktaki redoks döngülerindeki fiziksel ve mekanik özelliklerindeki değişimi araştırmıştır. Nikel oksidin nikel indirgenmesi sırasında anodun elastisite modülüs değişiminin tersinir olduğu ve bu yüzden anot YSZ ağının zarar görmediği görülmüştür. Fakat oksidasyon sırasında meydana gelen hacimsel genişlemelerinin tersinmez olduğu tespit edilmiştir. Mikroyapısal incelemeler oksidasyon sırasındaki tersinmez genişlemelerin, nikel kısmi sinterlenmesi ve özgün oksidasyon özelliklerinden kaynaklı kapalı gözeneklilik oluşmasından kaynaklandığını göstermiştir. Benzer bir çalışmada Klemensø vd. (2006) NiO/3YSZ anodun 850 °C sıcaklıktaki redoks döngüleri sırasındaki anlık mikroyapısal değişimini incelemiştir. Nikel oksit indirgenmesi sırasında nikel taneciklerinin yuvarlaklaşmasının yanı sıra gözeneklilikte artma ve hacimsel küçülmeler tespit edilmiştir. Oksitlenme sırasında ise NiO fazının yapı içerisine indirgenme konumuna

göre yeniden yerleştiği görülmüştür. Nikel oksit taneciklerinin tersinmez olan bu morfolojik değişiminin sıcaklıkla ilişkili olduğu belirlenmiş ve bu yüzden doğrudan oksidasyon kinetiğine bağlı olduğu ifade edilmiştir. Hızlı oksitlenmelerde nikel oksit taneciklerinin 2-4 parçaya bölüdüğü, yavaş oksitlenmelerde ise sadece oksit tabakası oluştuğu dile getirilmiştir. Jeangros vd. (2010), Klemensø vd. (2006) çalışmasını teorik hesaplamalar ekleyerek geliştirmiştir. NiO/3YSZ/YSZ (kütlesel % 55:22.5:22.5) anot destekli hücrelerin anlık redoks stabilitesinin incelendiği çalışmada hidrojen tutulma bölgelerinin oluştuğu, indirgenmenin ise oksijenin, nikel oksitten YSZ'ye olan transferi ile mümkün olduğu ve bu transferin indirgenmedeki itki kuvveti olduğu bulunmuştur. Redoks döngülerinden kaynaklanan oksidasyon genişlemesi ve buna bağlı olarak YSZ fazı üzerindeki streslerin mikroyapıda tersinmez değişikliklere sebep olduğu belirlenmiştir.

Sumi vd. (2010) NiO/YSZ anodun redoks döngüleri sonrasındaki mikroyapısal ve elektrokimyasal karakterizasyonunu ortaya koymuştur. Hücre performansının sadece bir redoks döngüsü sonrasında düştüğü görülmüştür. Bu durum redoks döngüsü sırasında meydana gelen mikroyapısal değişim sonrasında azalan reaksiyon bölgelerinin bir sonucu olarak artan anot polarizasyon direnci ile açıklanmıştır. 10 redoks döngüsü sonrasında yapılan mikroyapısal incelemeler anot yapısı içerisinde bir çok mikro çatlakların varlığını gözler önüne sermiştir. Bu durum anot içerisindeki nikel ve YSZ bağlarına zarar verdiği için polarizasyon direncinin yanı sıra anot ohmik direncinin de arttığı belirlenmiştir. Benzer sonuçlar 48 cm^2 aktif alana sahip NiO/YSZ anot destekli hücrelerin incelendiği Faes vd. (2011) çalışmasında da rapor edilmiştir. Çalışmada gerçekleştirilen toplam 40 redoks döngüsü sırasında açık devre voltajının her bir redoks sonrasında ortalama % 0.1 azaldığı görülmüştür. Empedans ölçümleri hücre performansındaki bu azalmaların ohmik ve polarizasyon direncindeki artışlardan kaynaklandığını ortaya çıkarmıştır. Nikel fazının büyümesinin bir sonucu olan bu durumun, elektriksel iletkenlik ve reaksiyon bölgelerinde azalmalara sebep olduğu ifade edilmiştir. Benzer şekilde Mosch vd. (2007) da $850 \text{ }^\circ\text{C}$ sıcaklıkta NiO/YSZ anot üzerinde gerçekleştirdikleri redoks çalışmasında anot ohmik ve polarizasyon direncindeki artışların hücre performans kaybının ana nedeni olduğunu ortaya koymuştur. 6 redoks döngüsü sonrasında yapılan mikroyapı incelemeleri, anodun redoks döngüleri sonrasında eski yapısını geri kazanamadığını göstermiştir.

Sonuç olarak literatürde yer alan redoks çalışmaları göz önüne alındığında nikelin tekrar oksitlenmesinin anot mikroyapısına geri dönüşü olmayan hasarlar verdiği görülmektedir. Redoks döngülerine devam edilmesi durumunda ise özellikle anot destekli hücrelerde bu durumun elektrolit kırılması ile sonuçlandığı rapor edilmiştir. Bu kapsamda redoks, KOYP'nin ticarileşmesi ve yaygınlaşmasının önündeki en büyük engel olarak durmaktadır.

2.3 Redoks Çözüm Önerileri

Literatürde yer alan redoks çözüm önerileri, malzeme/bileşen veya sistem çözümleri ana başlıkları altında sınıflandırılabilir (Wood vd., 2006). Malzeme veya bileşen çözümleri genelde anot malzemesinin tipi ve mikroyapısı ile ilişkili iken sistem çözümleri tasviye gazı veya buhar tasviyesi gibi genel sistem ile ilgili olmaktadır. Fakat sistem çözüm önerileri, yeni bir sistem elemanının montajı ve kurulumu veya ekstra elektrik enerjisi gerektirdiğinden sistem maliyetini ve karmaşıklığını arttırmaktadır. Bu kapsamda nikel tabanlı KOYP anot redoks problemini tam olarak ortadan kaldıracak kolay, uygulanabilir ve az maliyetli bir çözüm henüz bulunamamıştır.

Waldbillig vd. (2005) nikelin tekrar oksitlenmesi sırasında meydana gelen hacimsel genişlemelerin anot içeriğindeki nikel miktarının azaltılması veya oksidasyon sıcaklığının düşürülmesi ile azaldığını göstermiştir. Başka bir çalışmada (Waldbillig vd., 2007) ise NiO/YSZ anot redoks dayanımının mikroyapısal değişikliklerle iyileştirilebileceğini bulmuşlardır. Bu kapsamda, anot işlevsel tabakanın farklı nikel içeren katmanlardan oluşturulması ve anodun en alt bölgesine bir oksidasyon tabakası uygulanması olmak üzere iki hücre modifikasyonu gerçekleştirilmiştir. Termal mekanik analizler anottaki nikel içeriğinin azaltılması durumunda meydana gelen tekrar oksitlenme genişlemesinin, standart anoda kıyasla azaldığını göstermiştir. Anot işlevsel tabakadaki değişikliğin ise anot redoks dayanımını %28 oranında arttırdığı rapor edilmiştir. Kütlece %57 NiO ve %43 YSZ içeren oksidasyon tabakası uygulandığında ise bu artışın % 37 olduğu belirlenmiştir.

Busawon vd. (2008) ise nikel infiltre edilmesini KOYP anot redoks probleminin bir çözümü olarak ortaya atmıştır. Bu kapsamda etanol içerisinde çözülmüş $Ni(Ni_3)_2 \cdot 6H_2O$,

gözenekli YSZ içerisine infiltre edilmiştir. Kütlece %12-16 arasında nikel emdirilmiş örneklerde bir redoks döngüsü sonrasında herhangi bir hacimsel değişiklik gözlemlenmemiştir. Bu durum infiltre edilen nikel katalizörün indirgenme ve yükseltgenmesi sırasında rahat hareket edebileceği bir mikroyapının elde edilmesi ile açıklanmıştır. Fakat elektriksel iletkenlik ölçümleri redoks sonrasında iletkenlikte %20'lik bir düşüş olduğunu göstermiştir. Yapılan mikroyapısal incelemeler bu düşüşün infiltre edilen nikellerin kendileri arasında sürekli bir bağ yapmaması ve nikellerin kümeleşmesinden kaynaklandığını göstermiştir.

Literatürdeki malzeme/bileşen çözümlerinden bir diğeri ise nikel temelli anotlara alternatif olacak yüksek redoks dayanımlı yeni anot malzemelerin geliştirilmesidir. Fakat bu malzemelerin katalitik performansının, nikel temelli anoda göre oldukça düşük olduğu dikkat çekmektedir. Bu kapsamda en sık tercih edilen alternatif anot malzesinin dop edilmiş SrTiO_3 olduğu görülmektedir. Ma vd. (2010) Y dop edilmiş SrTiO_3 anot malzemesi geliştirmiş ve bu malzemenin redoks stabilitesini incelemiştir. 25 cm^2 aktif alana sahip hücreler üzerinde $750 \text{ }^\circ\text{C}$ sıcaklıkta gerçekleştirilen redoks testleri, Y dop edilmiş SrTiO_3 anodun yüksek redoks dayanımına sahip olduğunu ortaya koymuştur. 200 redoks döngüsü sonrasında açık devre voltajı %1,3 oranında düşmüştür. Fakat performans ölçümleri hücre çıkış gücündeki düşüşün çok daha fazla olduğunu göstermiştir. Yavaş redoks kinetiğine rağmen hücre performansı 500 mW/cm^2 'den %35'lik bir düşüş ile 325 mW/cm^2 'a gerilemiştir.

Smith vd. (2011) ise Ta dop edilmiş SrTiO_3 'ü KOYP anot malzemesi olarak incelemiştir. Bu kapsamda $x=0,01;0,05$ ve $0,1$ olacak şekilde üç farklı $\text{SrTa}_x\text{Ti}_{1-x}\text{O}_3$ üretilmiştir. Redoks döngüsü $1400 \text{ }^\circ\text{C}$ sıcaklıkta indirgeme ve farklı sıcaklıklarda tekrar oksitleme şeklinde uygulanmıştır. Yapılan iletkenlik ölçümleri redoks dayanımının dop oranı ile azaldığını göstermiştir. %1 Ta dop edilmiş örnek $0,9 \text{ S/cm}$ iletkenlik değerini göz önüne alınan bütün sıcaklıklarda korumuştur.

Blennow vd. (2008), Blennow vd. (2009) ve Gross vd. (2009) ise Nb dop edilmesi üzerine yoğunlaşmıştır. Geliştirilen $\text{Sr}_{0,94}\text{Ti}_{0,9}\text{Nb}_{0,1}\text{O}_3$ anodun redoks dayanımı umut verici olsa da hidrojen oksidasyonu için yeterli katalitik aktiviteye sahip olmadığı tespit edilmiş ve bu görevi yapabilecek başka bir katalizörün anot içeriğine eklenmesi

gerektiđi sonucuna varılmıřtır (Blenneow vd., 2009). Gross vd. (2009) ise dop miktarının etkisi üzerine incelemeler yapmıřlardır. Artan Nb miktarına paralel olarak elektrik iletkenlik deđerlerinde de artıř saptanmıřtır. Fakat 0,05 molden daha fazla oranlarda Nb dop edilmesi redoks dayanımı aısından uygun bulunmamıřtır.

2.4 KOYP Mekanik Modelleme

Katı oksit yakıt pili alıřması sırasında anot ve katotta meydana gelen heterojen elektrokimyasal reaksiyonlar, sınır řartları ve ısıl dngler pil ii sıcaklık gradyantına sebep olmaktadır. Bu sıcaklık gradyantı, stak elemanlarının farklı olan ısıl genleřme katsayıları ile birleřince ortaya ısıl gerilmeler ıkmakta ve bu durum pil mr ve performansını tehdit etmektedir. KOYP alıřma sıcaklıđı yksek olduđu iin pil alıřması sırasında ortaya ıkan sıcaklık ve gerilme dađılımlarının deneysel belirlemesi olduka zor olmaktadır. Bu yzden literatrde sıcaklık ve gerilme dađılımının belirlenmesi zerine olan alıřmaların ok byk bir blm geliřtirilen matematiksel modellerin sayısal zm ile elde edilen sayısal tahminlerden oluřmaktadır. Mevcut matematiksel modeller genellikle deneysel olarak elde edilmiř bir performans eđrisi ile dođrulandıktan sonra parametrik sayısal analizlere geilmiřtir. Sayısal analizler tek hcreli ve ok hcreli KOYP staklardaki sıcaklık ve ısıl gerilme dađılımının akıř tipi ve alıřma řartlarından olduka etkilendiđini ortaya ıkarmıřtır.

Hcre ve stakta daha ciddi gerilmelere sebep olan redoks zerine ise ok sınırlı sayıda matematiksel modelleme ve sayısal analiz alıřmalarının olduđu dikkat ekmektedir. Var olan alıřmalarda ise tek bir redoks dngsnn gz nne alındıđı, pil alıřması sırasındaki sıcaklık dađılımının ihmal edildiđi ve zellikle redokstan kaynaklanan gerilmelerin sebep olduđu mikro-bozuklukların pil performansı zerindeki nasıl bir etkisi olduđunun incelenmediđi grlmektedir.

2.4.1 Isıl gerilme modelleri

Her ne kadar literatrde hcre alıřması sırasında oluřan sıcaklık dađılımını gz nne almadan sadece belirli bir sıcaklık iin sayısal gerilme analizlerine rastlansa da (Seluk vd., 2001; Montross vd., 2002; Yakabe vd., 2004a, Yakabe vd., 2004b; Fischer vd.,

2005), gerilme hesaplamalarındaki genel yaklaşımın sonlu hacim tekniği ile termo-akış modelinden belirlenen sıcaklık dağılımının bir sonlu elemanlar programına aktarılması ile gerilme dağılımının belirlenmesi şeklinde olduğu görülmektedir. Bu çalışmalar arasında Yakabe vd. (2001) tek hücreli bir KOYP için üç boyutlu bir matematiksel model geliştirmiştir. Model geometrisi 0,1 mm kalınlığında anot ve elektrolit ile 0.15 mm kalınlığında katot içeren KOYP hücresi ve interkonnektörlerden oluşmaktadır. Fakat sayısal çözüm bütün geometri yerine tek bir anot ve katot akış kanalı için yapılmıştır. Akış konfigürasyonunun, sıcaklık dağılımı dolayısı ile ısıl gerilmeler üzerindeki etkisi daimi rejimde incelenmiştir. Paralel akış daha düşük sıcaklık gradyanı ortaya koyduğu için ısıl gerilmeleri azalttığı sonucuna varılmıştır. Benzer yaklaşımı kullanan Selimovic vd. (2005), Yakabe vd. (2001) modelini geçici rejimi de ekleyerek geliştirmiştir. Çalışmada ayrıca interkonnektör malzemesi (metalik ve seramik), akış konfigürasyonları (paralel, karşı ve çapraz akış) ve çalışma voltajının sıcaklık ve gerilme üzerindeki etkileri de incelenmiştir. Fakat gerilme analizleri sadece hücre için gerçekleştirilmiştir. İnterkonnektörler sadece sıcaklık dağılımının belirlenmesinde göz önüne alınmıştır. Daimi rejimde elde edilen sayısal sonuçlar metalik interkonnektörün yüksek olan ısıl iletim katsayısı sayesinde daha düşük sıcaklık gradyanı ve dolayısı ile daha düşük gerilmeye sebep olduğunu göstermiştir. Karşı akış, incelenen diğer akış tiplerine göre daha yüksek bir pil performansı ortaya koysa da, paralel akış tipinin daha düşük gerilmeler gösterdiği belirlenmiştir. Düşük çalışma voltajları ise yüksek lokal akımlardan kaynaklanan yüksek sıcaklık gradyanı ve gerilmelere sebep olmuştur. Geçici rejim sayısal analizlerinde ise ısıtma, başlangıç ve soğutma göz önüne alınmıştır. Fakat geçici rejim terimi sadece enerji denklemine dahil edilmiştir. Yapılan sayısal incelemeler, göz önüne alınan bütün durumlarda hücre elemanlarının malzeme sınırlarını aşan bir gerilmeye maruz kalmadığını göstermiştir.

Chiang vd. (2008) de aynı yaklaşımı tek hücreli anot destekli KOYP'ye uygulamıştır. Yakabe vd. (2001) ve Selimovic vd. (2005) tarafından elde edilen sonuçlara paralel olarak düşük çalışma voltajlarında daha yüksek gerilmeler olduğu rapor edilmiştir. Önceki çalışmalardan farklı olarak giriş sıcaklıklarının etkilerinin göz önüne alındığı bu çalışmada, giriş gazlarının ön ısıtmadan geçmesinin sıcaklık gradyanını ve dolayısı ile ısıl gerilmeleri azalttığı sonucuna varılmıştır. Aynı grubun takip eden çalışmasında (Chiang vd., 2010) üst interkonnektöre konulan ağırlığın (0,5-5kg) ve anot

gözenekliliğin (0,2-0,5) gerilme üzerindeki etkileri incelenmiştir. Hücrede oluşan maksimum gerilmenin artan yükte çok az oranda değiştiği görülmüş ve bu yüzden bu durum gerilmelerin daha çok sıcaklık gradyantına bağlı olması ile açıklanmıştır. Hücre performansının anot gözenekliliği ile arttığı bu yüzden düşük anot gözenekliliğinde daha yüksek gerilmeler olduğu belirlenmiştir.

Lin vd. (2007) üç hücreli bir stak için ısıl gerilme analizlerini içeren bir çalışma sunmuştur. Önceki çalışmalarda olduğu gibi, daha önce geliştirilen termo-akış modelinin (Chyou vd., 2005) daimi ve geçici rejimde sayısal olarak çözümü ile elde edilen sıcaklık dağılımı sonlu elemanlar programına aktararak gerilme analizleri gerçekleştirilmiştir. Selimovic vd. (2005) çalışmasında olduğu gibi daimi rejimin yanı sıra geçici rejimde sistemin kapanması ve çalıştırılması durumları göz önüne alınmıştır. Analizler staktaki en kritik elemanın cam seramik sızdırmazlık olduğunu ortaya koymuştur. Ayrıca, sistemin kapatılması sırasında ve daimi rejimde interkonnektörler üzerinde lokal plastik deformasyonlar da tespit edilmiştir. Aynı grup daha sonraki çalışmalarında (Lin vd., 2009) üst interkonnektöre kontağı iyileştirmek amaçlı yerleştirilen ağırlığın ve sızdırmazlık tasarımının etkilerini incelemiştir. 0,06 MPa ile 0,6 MPa arasındaki yüklerin hücrenin bükülme deformasyonlarını ortadan kaldırdığı görülmüştür. Fakat ağırlığın daha fazla arttırılmasının gerek mika gerekse de cam tabanlı sızdırmazlıklar açısından uygun olmadığı belirlenmiştir. Çalışmada, mika sızdırmazlık malzemelerinin oda sıcaklığında cam seramik malzemelerin ise çalışma sıcaklıklarında daha düşük gerilmeler ortaya koyduğu sonucunda varılmıştır.

2.4.2 Redoks modellemesi

Çok daha ciddi gerilmelere sebep olan bir diğer mekanizma ise redoks olarak bilinen ve anottaki nikelin sürekli olarak maruz kaldığı indirgenme ve yükseltgenme döngüsüdür. Fakat bu konu üzerine literatürde çok az modelleme çalışması bulunmaktadır. Örnek olarak Clague vd. (2012) sadece NiO indirgenmesini göz önüne almıştır. Geliştirilen sonlu elemanlar modeli sinterleme aşamasından soğuma, çalışma sıcaklığına ulaşma, çalışma ve oda sıcaklığına soğuma durumlarında anot destekli hücredeki oluşan gerilmelerinin sayısal olarak belirlenmesinde kullanılmıştır. Nikel oksidin nikel indirgenmesi ise sadece malzeme özelliklerindeki değişim olarak modele yansıtılmıştır.

Bu durum gözenekliliğe bağlı olan malzeme özelliklerinin tanımlanması ile sağlanmıştır. Sayısal sonuçlar indirgenme sonrasına bütün hücre elemanlarının gerilme değerlerinde azalma olduğunu göstermiştir. En yüksek azalmanın ise %15'lik oranla katot bölgesinde gerçekleştiği belirlenmiştir. Benzer sonuçlar, standart NiO/YSZ-YSZ-LSM malzemelerinden oluşan anot ve elektrolit desteli KOYP'de meydana gelen mekanik hasarlara sebep olan uzama aralığını sayısal olarak inceleyen Laurencin vd. (2008) tarafından da rapor edilmiştir. Bu çalışmada bir tam redoks döngüsü modellenmiştir. Nikel oksit indirgenmesi, anot elastik özelliklerinde azalma ile ifade edilirken nikelin yeniden oksitlenmesi sanal bir ısıl genleşme katsayısı olarak modele entegre edilmiştir. Anot destekli hücre için yapılan sayısal analizler katodun mekanik bütünlüğünü koruyabilmesi için anot gerinmesinin % 0,05 ile % 0,09 arasında olması gerektiğini ve elektrolit hasarının % 0,12 ile % 0,15 anot gerinmesinde gerçekleştiğini göstermiştir. Elektrolit destekli hücrede ise anot gerinmesinin % 0,30 ile % 0,35'ten yüksek olması durumunda nikelin tekrar oksitlenmesinin anot ve elektrolit ara yüzeyine zarar verdiği belirlenmiştir.

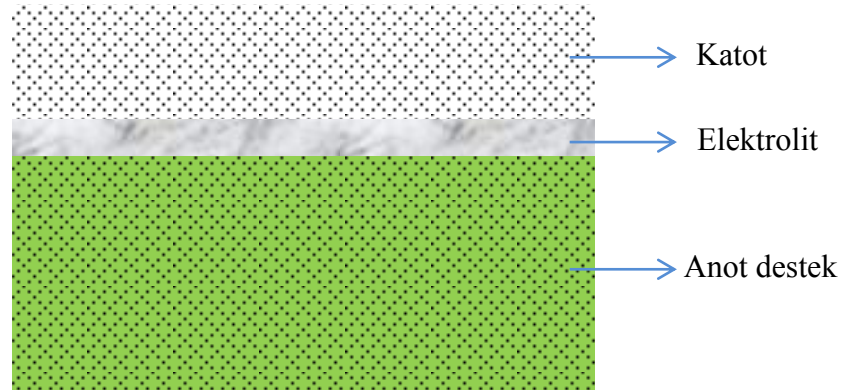
Laurencin vd. (2012) diğer bir çalışmalarında nikelin nikel okside dönüşme oranını ve bu dönüşümün gerçekleştiği sıcaklığın gerilme üzerindeki etkisini sayısal olarak incelemiştir. Deneysel çalışmada elde edilen anot hacimsel değişimi, oksidasyon hızı ve anot mekanik özellikleri doğrudan modele aktarılmıştır. Örneğin, 800 °C oksidasyon sıcaklığında tam oksidasyon durumunda anot gerinmesi % 0,97 olarak belirlenmiştir. Yapılan sayısal analizler elektrolitte hasarın 600 °C oksidasyon sıcaklığı için %59 dönüşüm oranından sonra, 800 °C oksidasyon sıcaklığında ise % 66 dönüşüm oranından sonra oluştuğunu ortaya koymuştur. Fakat kritik tekrar oksitlenme süreleri bunun tam tersi bir eğilim göstermiştir. Bu durum yüksek sıcaklıklarda iyileşen reaksiyon kinetiğinden dolayı daha hızlı bir oksidasyonun olması ile açılanmıştır. Fakat bu çalışmada da yine KOYP çalışması sırasında meydana gelen sıcaklık gradyanının gerilme üzerindeki etkisi göz önüne alınmamıştır.

Pihlatie vd. (2010) ise deneysel olarak inceledikleri 7 farklı tek redoks döngüsü için bir modelleme çalışması ortaya koymuştur. Model anot kimyasal gerinmesini, YSZ elektrolitin anelastik genişlemesini ve sıcaklıktan kaynaklı sünmesini göz önüne almıştır. Aynı zamanda nikel kümeleşmesi, NiO partikül büyümesi ve Ni/NiO tanecik

büyümleri modele yarı-ampirik eşitlikler yardımı ile eklenmiştir. Fakat pil çalışması sırasında oluşan sıcaklık gradyantının gerilmeler üzerindeki etkisi yine ihmal edilmiş sıcaklık sabit olarak alınmıştır. Laurencin vd. (2008) çalışmasından farklı olarak, malzemelerin mekanik özellikleri sıcaklığın bir fonksiyonu olarak tanımlanmış ve indirgenme/yükseltgenme gerinmesi ise nikelden nikel oksite dönüşüm oranının 0,16 katı olarak modellenmiştir. İndirgenme durumunda oran sıfır olduğu için herhangi gerinme oluşmazken tam oksidasyonda bu gerinme 0,16 olmaktadır. Çalışmada yüksek indirgenme sıcaklığının redoks stabilitesini olumsuz yönde etkilediği ve tekrar oksitlenme gerinmesinin sıcaklıkla arttığı sonuçlarına varılmıştır.

3. DENEYSEL ÇALIŞMA

Deneysel çalışmanın temel amacı geliştirilen termo-akış ve redoks modellerinin, değişim akım yoğunluğu (j_o), anot ve katot şarj transfer sabitleri ($\alpha_{a,c}$) ve hasar katsayısı (B) gibi parametrelerinin optimizasyonu ile doğrulanmasıdır. Bu kapsamda modelde kullanılan geometriye sahip olan farklı özelliklerde anot destekli hücreler şerit döküm, birlikte sinterleme ve ipek baskı teknikleri kullanılarak imal edilmiştir. Modelleri doğrulamada kullanılan 10 μm elektrolit kalınlığı ve % 40 anot gözenekliliğine sahip olan anot destekli hücre, baz hücre olarak adlandırılmıştır. Hücrelerin redoks öncesindeki ve sonrasındaki elektrokimyasal ve mekanik özellikleri sırası ile yakıt pili test istasyonu ve üç nokta bükme cihazı ile gerçekleştirilmiştir. Ayrıca elektrolit kalınlığı ve anot gözenekliliğinin hücrenin mekanik ve elektrokimyasal özelliklerine olan etkisini incelemek için farklı elektrolit kalınlığı ve anot gözenekliliğine sahip anot destekli hücreler de imal edilmiştir. Deneysel çalışmanın detayları takip eden bölümlerde verilmiştir.



Şekil 3.1. Anot destekli hücre yapısı

3.1 Baz Hücre İmalatı

İmal edilen anot destekli baz hücrenin tabakaları Şekil 3.1’de verilmiştir. Hücre NiO/YSZ anot destek, YSZ elektrolit ve LSM/YSZ katottan oluşmaktadır. Anot destek ve elektrolit imalatında şerit döküm ve birlikte sinterleme teknikleri kullanılırken, katot ipek baskı tekniği ile elektrolitin diğer yüzeyine kaplanmıştır. Bu kapsamda performans ölçümlerindeki deneysel hataları minimize etmek adına üçerli gruplar halinde farklı

özelliklere ve 1cm^2 aktif alana sahip toplamda 15 eş hücre ve mekanik ölçümlerdeki deneysel hataları minimize etmek adına 16cm^2 aktif alana sahip 10 eş hücre imatları gerçekleştirilmiştir.

3.1.1 Baz hücre elektrolit ve anot destek üretimi

Yüksek saflıkta satın alınan YSZ tozları (Nextech Materials, Ohio, ABD) uygun miktarlarda ayırıcı ve çözücü kullanılarak 24 saat boyunca bilyeli değirmende karıştırılmıştır. Daha sonra karışıma uygun oranlarda organik bağlayıcı ve plastikleştirici eklenerek ikinci bir 24 saatlik bilyeli değirmen karıştırması uygulanmıştır. Mylar şerit üzerine $45\ \mu\text{m}$ doktor blade boşluğunda dökülen elektrolit şeritleri atmosferik hava ortamında 30 dakikalık bir beklemeden sonra uygun boyutlarda kesilmiştir. Elektrolit şerit kalınlığı kuruma sonrasında $14\ \mu\text{m}$ olarak ölçülmüştür.

Anot destek imalatı için, satın alınan nikel oksit tozlarına (Novamet, New Jersey, ABD) kütlece eşit oranda YSZ eklenmiştir. Belli miktarlarda ayırıcı ve çözücünün de eklenmesinin ardından 24 saat süre ile bilyeli değirmende karıştırılan çamura daha sonra belli oranlarda bağlayıcı, plastikleştirici ve gözenek yapıcı malzemeler eklenerek ikinci bir 24 saat boyunca karıştırılmıştır. Benzer şekilde mylar şerit üzerine $210\ \mu\text{m}$ doktor blade aralığında dökülen anot destek tabakasının atmosferik ortamda 30 dakikalık kurutma sonrasındaki kalınlığı $55\ \mu\text{m}$ olarak ölçülmüştür.

Daha sonra 10 adet anot destek ve 1 adet elektrolit şeridi üst üste konularak $20\ \text{MPa}$ basınç altında 2 dakika bekletilmiştir. Bu ön laminasyonun ardından son laminasyon işlemi, 70°C sıcaklık ve $40\ \text{MPa}$ basınçta altında 10 dakika sürede izostatik pres yardımı ile sağlanmıştır. Lazer kesici yardımı ile $20\ \text{mm} \times 20\ \text{mm}$ boyutlarında kesilen anot destekli elektrolit yapısının sinterlenmesi $1350\ ^\circ\text{C}$ sıcaklıkta 5 saatlik bir bekletmeyle gerçekleştirilmiştir. Sinterleme sonrasındaki son boyutlar $15\ \text{mm} \times 15\ \text{mm}$ olarak ölçülmüştür.

3.1.2 Baz hücre için katot imalatı

Satın alınan LSM tozlarına ((La_{0,80}Sr_{0,20})_{0,95}MnO_{3-x}, Nextech Materials) kütlece eşit oranda YSZ eklenmiştir. İpek baskı için gerekli olan çamurun hazırlanması için tozlar belli miktarlarda etil selüloz bağlayıcı ve terpineol çözücü (Sigma-Aldrich, Münih, Almanya) ile karıştırılmıştır. 12 saat boyunca bilyeli değirmende karıştırılan solüsyonun homojenizasyonunda üç milli değirmen kullanılmıştır. Daha sonra elektrolitin diğer yüzeyine 1cm² (10mmx 10 mm) aktif alana sahip olacak şekilde kaplanan LSM/YSZ katot 1000°C sıcaklıkta 2.5 saat süreyle sinterlenmiştir. Katot sinterlenmesinden sonra hazır hale gelen 1cm² aktif alana sahip hücrenin fotoğrafı Fotoğraf 3.1’de verilmiştir.



Fotoğraf 3.1. 1cm² aktif alana sahip anot destekli hücre fotoğrafı

3.1.3 Farklı özelliklerdeki hücrelerin imalatı

Elektrokimyasal ve mekanik özellikleri belirleyen en önemli iki parametre anot gözenekliliği ve elektrolit kalınlığı olduğu için, farklı anot gözenekliliği ve elektrolit kalınlığına sahip anot destekli hücreler imal edilmiştir. Anot gözenekliliği, anot şerit döküm çamuruna eklenen gözenek yapıcı miktarı ile ayarlanırken, farklı elektrolit kalınlıkları doktor blade aralığı değiştirilerek elde edilmiştir. Bu kapsamda, baz hücre ile aynı elektrolit kalınlığına fakat 0.3 ve 0.5 anot gözenekliliğine sahip anot destekli hücreler benzer şekilde imal edilmiştir. Bu hücreler sırası ile Hücre 1 ve Hücre 2 olarak adlandırılmıştır. Gözeneklilik ölçümleri için öncelikle sadece anot destek tabakaları imal edilerek gözeneklilikleri Arşimet tekniği ile belirlenmiştir. Benzer şekilde baz hücre ile aynı anot porozitesine fakat 4 µm ve 6 µm elektrolit kalınlıklarına sahip 1cm²

aktif alana sahip hücreler de imal edilmiştir. Bu hücreler sırası ile Hücre 3 ve Hücre 4 olarak adlandırılmıştır. Elektrolit kalınlıkları taramalı elektron mikroskobu ile belirlenmiştir. Deneysel ölçümlerdeki hataları minimize etmek için her hücreden üçer adet olmak üzere toplamda 15 adet hücre üretilmiştir. Mekanik ölçümler için ise baz hücre ile aynı özelliklere fakat 16cm^2 aktif alana sahip 10 eş hücre benzer teknikler kullanılarak imal edilmiştir.

3.2 Hücre Karakterizasyonu

Redoksün hücre mekanik özelliklerine ve elektrokimyasal performansına olan etkisinin belirlenmesi için iki farklı redoks deneyi gerçekleştirilmiştir. Bunların ilkinde stak; iki interkonnektör, akım toplayıcı elektrolitler ve pastalar, cam seramik sızdırmazlık ve MEG'den oluşmaktadır. Hücrenin bir redoks döngüsü öncesindeki ve sonrasındaki elektrokimyasal performansı, performans ölçümleri ile belirlenmiştir. Bu testler aynı özelliklere sahip 3 hücre için tekrarlanmıştır. Etkin akım toplama için kullanılan pastaların sinterlenmesi ve sızdırmazlık amaçlı kullanılan cam seramik malzemelerin interkonnektör ve MEG ile kimyasal bağ yapması, mekanik ölçümler için hücrenin kırılmadan staktan ayrılmasını imkansız kılmaktadır. Bu kapsamda ikinci redoks testlerinde pasta kullanılmamış olup cam seramik yerine kimyasal tutunma sağlamayan mika temelli sızdırmazlık malzemeleri kullanılmıştır. Hücrelerin redoks öncesi ve sonrasındaki mekanik özellikleri üç nokta bükme ölçümleri ile belirlenmiştir. Bu testlerin güvenilirliğini artırmak için her durum için 5 hücre test edilmiştir.

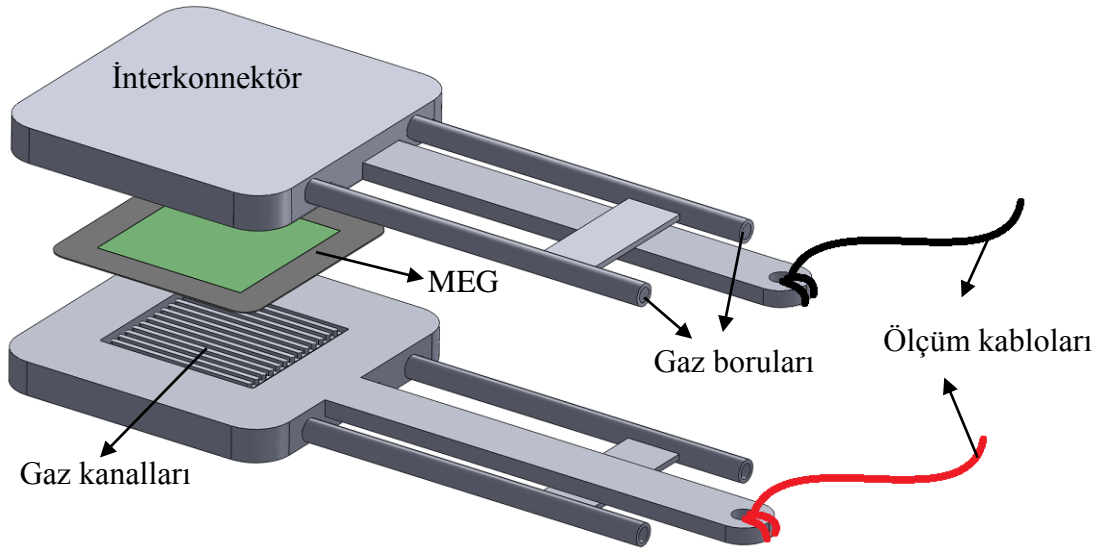
Elektrokimyasal performans ölçümleri için hazırlanan deneysel düzenek Fotoğraf 3.2'de stak tasarımı ise Şekil 3.2'de verilmiştir. Redoks deneylerinde uygulanan redoks prosedürünün aşamaları ise aşağıda sıralanmıştır:

1. Stağın $800\text{ }^\circ\text{C}$ çalışma sıcaklığına ısıtılması
2. Anodun 2 saat boyunca hidrojen ile indirgenmesi
3. Performans ölçümlerinin gerçekleştirilmesi
4. Anodun 2 saat boyunca hava ile oksitlenmesi
5. Anodun 2 saat boyunca hidrojen ile yeniden indirgenmesi
6. Performans ölçümlerinin gerçekleştirilmesi

Dört, beş ve altıncı aşamalar, baz hücre için 1-3 kez tekrarlanarak farklı redoks döngülerinin hücre performansı üzerindeki etkisi ayrıca incelenmiştir.

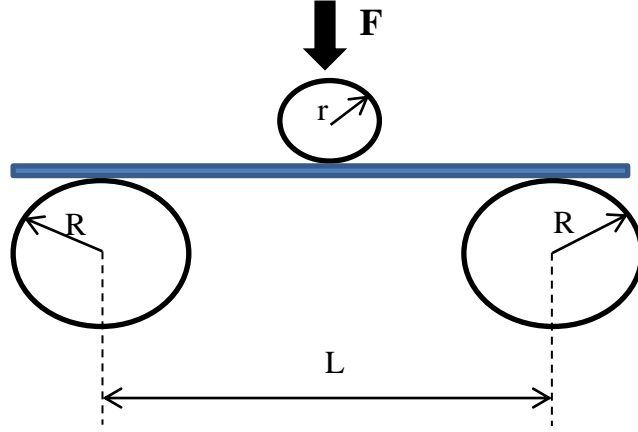


Fotoğraf 3.2. The experimental setup



Şekil 3.2. Stak tasarımı

Mekanik ölçümler Şekil 3.3'te verilen test aparatı ile gerçekleştirilmiştir. Destek silindir yarıçapları $R=15$ mm iken yük silindiri $r=5$ mm yarı çapındadır. Desteki silindirleri arasında mesafe $L=50$ mm olarak ayarlanmış olup bükme hızı 1 mm/dakika olarak seçilmiştir. Testlerde, örnekler kırılana kadar meydana gelen yük ve deformasyon dataları elde edilmiştir. Test sonuçlarının doğruluğunu arttırmak adına redoks öncesi ve sonrasındaki ölçümler her örnek için beşer kez tekrarlanmıştır.



Şekil 3.3. Üç nokta bükme test aparatı

4. MATEMATİKSEL MODELLEME

Matematiksel modellemede incelenen 1 cm² aktif alana sahip KOYP stak geometrisi Şekil 4.1(a)'da verilmiştir. Geometrinin detayları ise Şekil 1(b)'de gösterilmiştir. Üç boyutlu geometri temel olarak anot destek üzerine işlenmiş olan yoğun elektrolit ve gözenekli katottan, akış kanallarını üzerinde bulunduran anot ve katot interkonnektörlerinden ve sızdırmazlıktan oluşmaktadır. Anot ve katot akış kanallarının derinlik ve genişliği 2 mm olup baz hücre için modeldeki anot, elektrolit ve katot kalınlıkları ise sırası ile 400, 10 ve 40 µm'dir. Akış kanalları serpentin olarak tasarlanmış olsa da akış tipi olarak paralel akış seçilmiştir.

4.1 Termo-akış Modeli

KOYP çalışması sırasında meydana gelen olayları karakterize eden kütle ve madde dengesi, momentum, şarj ve enerji korunumu ile elektrokimyasal denklemler aşağıda verilmiştir.

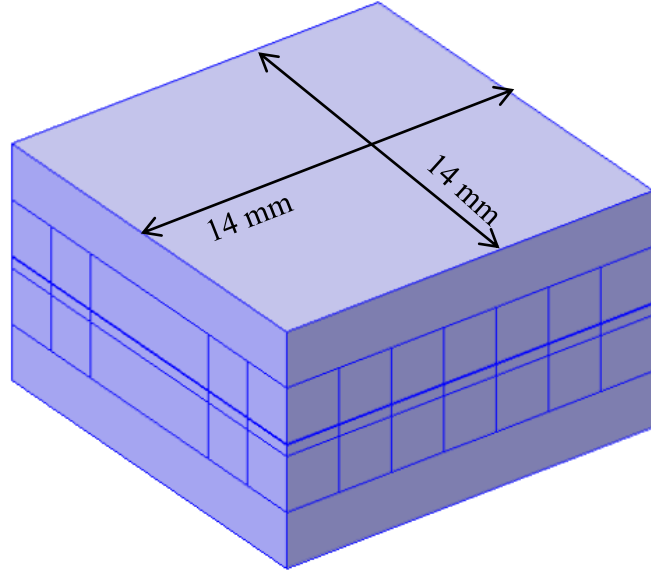
Süreklilik denklemi

$$\frac{\partial(\epsilon\rho)}{\partial t} + \nabla \cdot (\rho\epsilon\vec{V}) = S_{i,m} \quad (4.1)$$

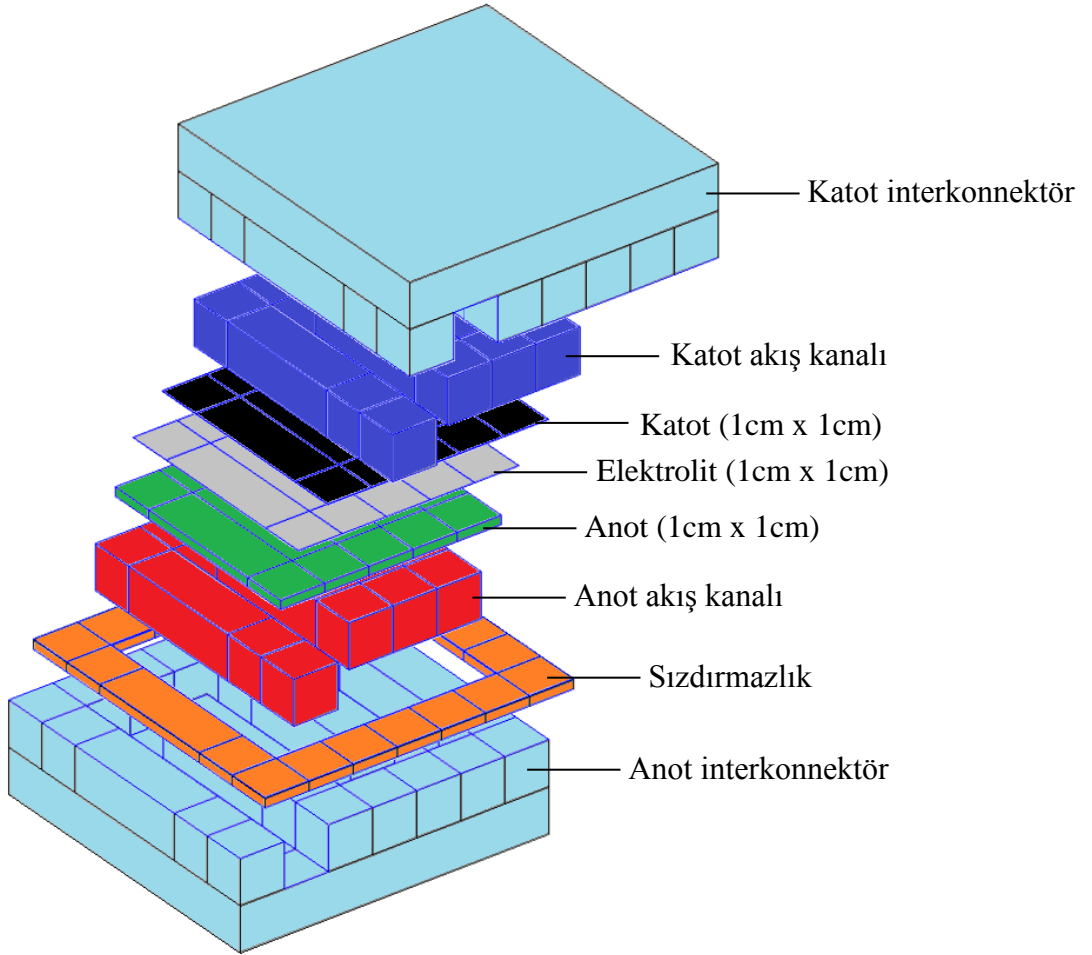
Burada ϵ gözenekliliği gösterirken ρ yoğunluğu ifade etmektedir. Eşitliğin sağ tarafındaki $S_{i,m}$ ise kaynak terimi göstermektedir. Katot bölgesinde oksijen tüketilirken anot bölgesinde hidrojen tüketilmekte ve açığa su buharı çıkmaktadır. Oluşan veya tüketilen maddeler aşağıdaki eşitlikten hesaplanmaktadır:

$$S_{i,m} = \frac{v_{i,m}i_v}{n_m F} \quad (4.2)$$

Eşitlik 3'te $v_{i,m}$, n_m ve i_v sırası ile i maddesinin stokiyometrik katsayısını, 1 mol i maddesinin üretimi için elektrokimyasal reaksiyona girmesi gereken elektron sayısını ve değişim akım yoğunluğunu ifade etmektedir. F ise Faraday sabitini simgelemektedir.



(a)



(b)

Şekil 4.1. Göz önüne alınan KOYP geometrisi

Madde dengesi

$$\frac{\partial(\rho \epsilon w_i)}{\partial t} + \nabla \cdot (\rho \epsilon \vec{V} w_i) = -\nabla \cdot \epsilon \vec{J}_i + S_{i,m} \quad (4.3)$$

Yukarıdaki eşitlikte sağdan ilk terim olan difüzyon terimi, \vec{J}_i , maddelerin sıcaklığı da göz önüne alarak aralarındaki etkileşimi ortaya koyan Maxwell-Stefan modeli ile aşağıdaki gibi verilmektedir:

$$\vec{J}_i = -\left(D_i^T \frac{\nabla T}{T} + \rho w_i \sum_k D_{ik} d_k\right) \quad (4.4)$$

Eşitliğin sağdan ilk terimi Soret etkisi olarak da bilinen sıcaklık gradyanı ile difüzyon üzerindeki etkisini ifade etmektedir. Fakat bu terim çok küçük olduğu için hesaplamalara dahil edilmemiştir. Difüzyon itki kuvveti olan d_k ise,

$$d_k = \nabla x_k + \frac{\nabla p_A}{p_A} [x_k - w_k] \quad (4.5)$$

eşitliğinden hesaplanmaktadır.

Eşitliklerdeki i indisi anot tarafında hidrojen ve suyu, katot tarafında ise oksijen ve azotu simgilemekte olup, anot bölgesinde su katot bölgesinde ise azot alt madde olarak modellenmiştir. Diğer maddelerin kütle oranları ise aşağıdaki gibi hesaplanmaktadır:

$$\sum_{i=1}^n w_i = 1 \quad (4.6)$$

Eşitlik (4.5)'teki eşitliğin sol tarafındaki ilk terim olan x_k aşağıdaki gibi hesaplanmaktadır:

$$x_k = \frac{w_i}{M_k} M_n \quad (4.7)$$

Eşitliğin sağ tarafındaki çarpan olan M_n ise,

$$M_n = \left(\sum_i \frac{w_i}{M_i} \right)^{-1} \quad (4.8)$$

eşitliğinden bulunmaktadır.

Denklem (4.4)'teki D_{ik} terimleri Maxwell-Stefan difüzyon katsayıları olup binary difüzyon katsayılarından hesaplanmaktadır:

$$D_{ik} = \frac{k_d T^{1.75}}{p M_{ik}^{1/2} (V_i^{1/3} + V_k^{1/3})^2} \quad (4.9)$$

Yukarıdaki denklemde p bar cinsinden basıncı, V_i kinetik hacmi (Çizelge 4.1) ve k_d referans difüzyon katsayısını simgelemekte olup 3.16×10^{-8} m²/s olarak kabul edilmiştir. M_{ik} ise birleşik molekül ağırlığını ifade etmekte olup aşağıdaki eşitlikten hesaplanmaktadır:

$$M_{ik} = 2 \left(\frac{1}{M_i} + \frac{1}{M_k} \right)^{-1} \quad (4.10)$$

Çizelge 4.1. Kinetik hacimler

Madde	Kinetik hacim
O ₂	16.6x10 ⁻⁶
N ₂	17.9x10 ⁻⁶
H ₂	6x10 ⁻⁶
H ₂ O	12.7x10 ⁻⁶

Özellikle gözenekli olan anot ve katot bölgeleri için binary difüzyon katsayılarının ortamın gözenekliliği (ϵ) ile düzeltilmesi gerekmektedir. Bu ortamlar için düzeltilmiş binary difüzyon katsayıları aşağıdaki gibi hesaplanmaktadır:

$$D_{ik}^{eff} = D_{ik} \epsilon^{1.5} \quad (4.11)$$

Momentum denklemi

$$\frac{\partial(\rho u)}{\partial t} + \rho u \cdot \nabla u = \nabla \cdot \left(-pI + \mu(\nabla u + (\nabla u)^T) - \frac{2}{3}(\nabla \cdot u)I \right) + \rho g \quad (4.12)$$

Yukarıdaki eşitlikteki ve diğer denklemlerdeki yoğunluklar (ρ) ideal gaz kanunu ile hesaplanmaktadır:

$$\rho = \frac{P}{RT} \sum_i x_i M_i \quad (4.13)$$

Burada x_i Maxwell-Stefan denkleminden hesaplanan mol oranı iken M_i moleküler ağırlığı göstermektedir.

Anot ve katot elektrotlarında ise denklem gözenekli ortamdaki transportu ifade eden Brinkman denklemine dönüştürülmüştür:

$$\frac{\partial}{\partial t} \left(\frac{\rho u}{\epsilon} \right) + \rho u \cdot \nabla u = \nabla \cdot \left(-pI + \frac{\mu}{\epsilon}(\nabla u + (\nabla u)^T) - \frac{2}{3\epsilon}(\nabla \cdot u)I \right) + \rho g - \frac{\mu}{K} u \quad (4.14)$$

Eşitliğin sağ tarafındaki sondan ikinci terimde yer alan K elektrotların geçirgenliği ifade etmektedir.

Enerji korunumu

Enerji korunum denklemi k ısı iletim katsayısını ve T sıcaklığı göstermek üzere aşağıdaki gibi ifade edilebilir:

$$\frac{\partial(\rho c_p T)}{\partial t} + \rho c_p u \cdot \nabla T = \nabla \cdot (k \nabla T) + Q \quad (4.15)$$

Akış olan anot ve katot katalizör ve akış kanallarında karışımın özgül ısısını ifade eden c_p aşağıdaki gibi hesaplanmaktadır:

$$c_p = \sum_i w_i c_{p,i} \quad (4.16)$$

Isıl iletkenlik katsayısı (k) ve momentum denkleminde yer alan viskozite (μ) de özgül ısılarla benzer şekilde hesaplanmıştır. Her bir maddenin özgül ısı, viskozite ve ısı iletim katsayıları ise sıcaklığın fonksiyonu olarak tanımlanmıştır (Çizelge 4.2).

Çizelge 4.2. Sıcaklık bağımlı akış parametreleri

Madde	Özgül ısı (J/(kgK))	Dinamik viskozite ($\times 10^7$ Pa.s)	Isıl iletim katsayısı (W/(m.K))
H ₂	12986+5.421*T-0.0045*T ²	46.96+0.156*T	0.0784+3.73*10 ⁻⁴ *T
H ₂ O	1672+0.477*T+0.00019*T ²	-9.88+0.361*T	0.0784+8.37*10 ⁻⁵ *T
O ₂	896+0.0115*T+0.00026*T ²	101.93+0.306*T	0.00850+6.3*10 ⁻⁵ *T
N ₂	1070-0.198*T+ 0.00034*T ²	114.5+0.371*T	0.0116+5.39*10 ⁻⁴ *T

Eşitlik (4.15)'teki son terim olan Q ısı üretimini ifade etmekte olup, asıl elektrokimyasal reaksiyonun gerçekleştiği anot bölgesinde lokal akımın bir fonksiyonu olarak aşağıdaki gibi tanımlanmıştır:

$$Q = (E_{max} - V_{hücre})i_{lokal} \quad (4.17)$$

E_{max} ise su oluşum entalpisine bağlı olarak aşağıdaki gibi hesaplanmaktadır:

$$E_{max} = \frac{h_{f,H_2O}}{2F} \quad (4.18)$$

Şarj dengesi

$$\frac{\partial \rho_e}{\partial t} + \nabla \cdot \vec{j} = S_c \quad (4.19)$$

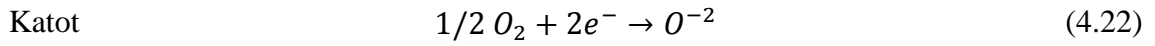
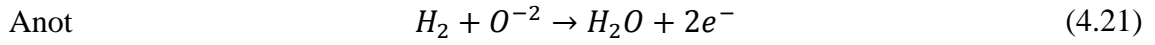
Bu denklemde ρ_e iyonik veya elektronik şarj yoğunluğunu ifade ederken, iletkenlik σ

ve elektriksel potansiyelin (ϕ) bir fonksiyonu olan \vec{j} iyonik veya elektronik akım yoğunluğunu göstermektedir. Ohm yasası olarak bilinen bu ilişki aşağıda verilmiştir.

$$\vec{j} = \sigma \nabla \phi \quad (4.20)$$

Elektrokimyasal reaksiyonlar

Hidrojen yakıtlı bir KOYP anot ve katodunda meydana gelen elektrokimyasal aşağıda verilmiştir.



Elektrokimyasal model

KOYP çalışması sırasında üretilen akım konsantrasyonlara bağlı reaksiyon kinetiği yaklaşımı ile aşağıdaki gibi hesaplanabilir:

$$i = A_v j_o \left[C_R \exp\left(\alpha_a \frac{nF\eta_{act}}{RT}\right) - C_O \exp\left(-\alpha_c \frac{nF\eta_{act}}{RT}\right) \right] \quad (4.23)$$

Burada η_{act} , j_o , α ve n sırası ile aktivasyon polarizasyonunu, değişim akım yoğunluğunu, anodik/katodik şarj transfer sabitini ve reaksiyona giren elektron sayısını simgelemektedir. A_v elektrokimyasal reaksiyonların meydana geldiği üçlü faz bölgelerini karakterize eden özgül alan olup katalizör yüzey alanının toplam hacmine olan oranını ifade etmektedir:

$$A_v = \frac{S}{V} \quad (4.24)$$

C_R ve C_O ise sırası ile indirgenen ve yükseltgenen maddelerin referans konsantrasyonlara bölümü ile elde edilen konsantrasyon oranlarını göstermektedir. Anot bölgesi için bu eşitlikler örnek olarak aşağıda verilmiştir:

$$C_R = \frac{C_{H_2}}{C_{H_2,ref}} \quad (4.25)$$

$$C_O = \frac{C_{H_2O}}{C_{H_2O,ref}} \quad (4.26)$$

Katı mekaniği

KOYP çalışması sırasında homojen olmayan elektrokimyasal reaksiyonlardan kaynaklanan farklı lokal akımlar pil içi sıcaklık gradyantına sebep olmaktadır. Oluşan bu sıcaklıklar pil elemanlarının ısı genleşmesine sebep olmaktadır. Pil elemanlarının farklı olan ısı genleşme katsayıları her bir elemanın farklı oranlarda ısıl distorsiyona uğramasına sebep olmaktadır. Sıcaklıktan kaynaklanan gerinme değerleri normal gerinme değerlerine eklenerek izotropik lineer elastik malzeme kabulü ile aşağıdaki gibi üç boyutlu olarak aşağıdaki gibi hesaplanmaktadır.

$$\varepsilon_{xx} = \frac{1}{E} (\sigma_{xx} - \nu\sigma_{yy} - \nu\sigma_{zz}) + \alpha\Delta T \quad (4.27)$$

$$\varepsilon_{yy} = \frac{1}{E} (-\nu\sigma_{xx} + \sigma_{yy} - \nu\sigma_{zz}) + \alpha\Delta T \quad (4.28)$$

$$\varepsilon_{zz} = \frac{1}{E} (-\nu\sigma_{xx} - \nu\sigma_{yy} + \sigma_{zz}) + \alpha\Delta T \quad (4.29)$$

Burada E malzemelerin elastisite modülünü, ν Poisson oranını ve α ısı genleşme katsayısını göstermektedir. Lineer elastik izotropik malzeler için sıcaklık sadece normal gerilmeler oluşturmaktadır. Bu gerilmeler matris formatında aşağıdaki gibi hesaplanabilir:

$$\begin{bmatrix} \sigma_{xx} \\ \sigma_{yy} \\ \sigma_{zz} \end{bmatrix} = \begin{bmatrix} \hat{E}(1-\nu) & \hat{E}\nu & \hat{E}\nu \\ \hat{E}\nu & \hat{E}(1-\nu) & \hat{E}\nu \\ \hat{E}\nu & \hat{E}\nu & \hat{E}(1-\nu) \end{bmatrix} \begin{bmatrix} \varepsilon_{xx} \\ \varepsilon_{yy} \\ \varepsilon_{zz} \end{bmatrix} - \frac{E\alpha\Delta T}{1-2\nu} \begin{bmatrix} 1 \\ 1 \\ 1 \end{bmatrix} \quad (4.30)$$

Burada \hat{E} efektif modül olup aşağıdaki gibi hesaplanmaktadır:

$$\hat{E} = \frac{E}{(1+\nu)(1-2\nu)} \quad (4.31)$$

4.2 Redoks Modeli

Nikel taneciklerinin yeniden oksitlenmesinden kaynaklanan ve performans kayıplarına neden olan mekanik hasarlar aşağıda verilen bir hasar fonksiyonu ile ifade edilmiştir:

$$D = B(\nabla\varepsilon) \quad (4.32)$$

Yukarıdaki denklemde, D hasar fonksiyonunu ve ε gerinmeyi ifade etmektedir. B ise hasar katsayısı olup redoks sonrasındaki performans değişiminden hesaplanmaktadır. KOYP çalışması sırasındaki toplam gerinme aşağıdaki gibi ifade edilebilir:

$$\varepsilon_{toplam} = \varepsilon_{termal} + \varepsilon_{redoks} \quad (4.33)$$

Burada $\varepsilon_{thermal}$ hücre içinde meydana gelen heterojen reaksiyonlardan ve sınır şartlarından kaynaklanan sıcaklık dağılımından dolayı oluşan ısıl gerinmeyi göstermektedir. ε_{redoks} ise nikel taneciklerinin yeniden oksitlenmesinden dolayı oluşan hacimsel büyümeyi ifade etmekte olup aşağıda gibi hesaplanmaktadır (Laurencin vd. 2012):

$$\varepsilon_{redoks} = 0.0097DoO \quad (4.34)$$

Yukarıdaki eşitlikte DoO , oksitlenme derecesi olup oksitlenen nikel miktarının toplama olan oranını göstermektedir. Meydana gelen mekanik bozulmalar üçlü faz bölgelerini etkilediği için hücrenin elektrokimyasal performansında da azalmalara sebep olmaktadır. Performansta meydana gelen bu kayıplar lokal akım yoğunluğu üzerinde aşağıdaki gibi yansıtılmıştır:

$$i = (1 - D)A_vj_o \left[C_R \exp\left(\alpha_a \frac{nF\eta_{act}}{RT}\right) - C_O \exp\left(-\alpha_c \frac{nF\eta_{act}}{RT}\right) \right] \quad (4.35)$$

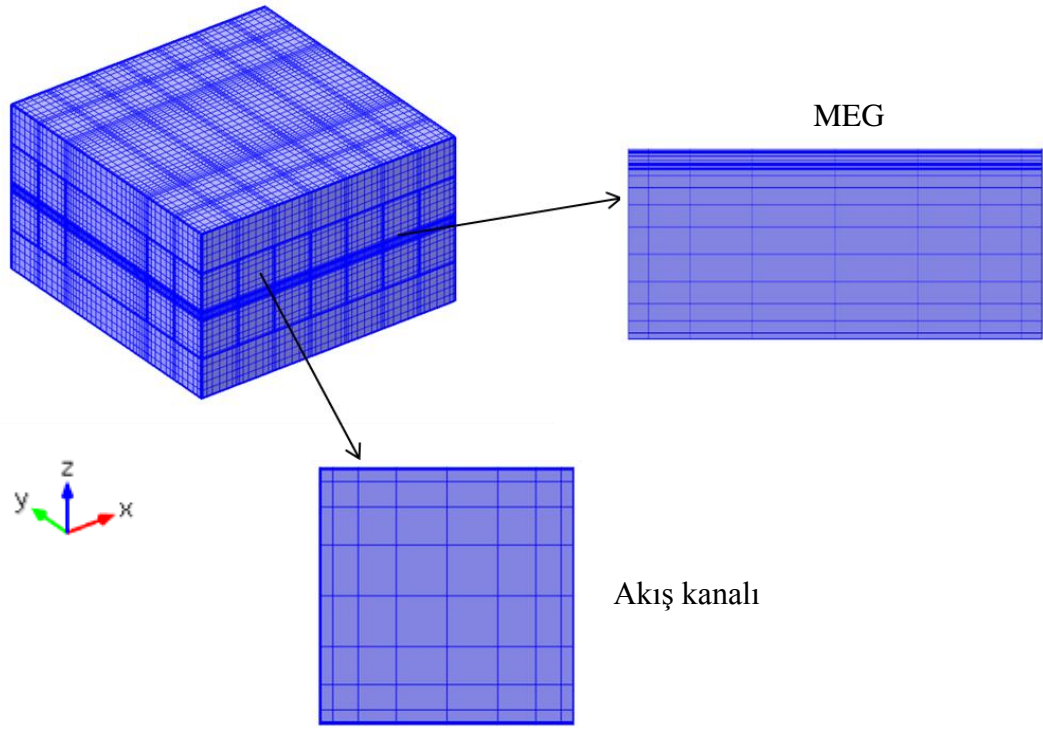
Deneysel olarak elde edilen redoks öncesi ve sonrasındaki performans değerleri kullanılarak hasar katsayısı (B) belirlenmiş ve bu katsayıya göre hasar fonksiyonu (D) normalize edilmiştir.

Sınır şartları ve kabüller

Maxwell-Stefan denklemlerinde anot ve katot girişlerinde kütle oranları sabitlenmiştir. Momentum denklemlerinde ise çıkışlar atmosferik olup anot ve katot giriş basıncı verilmiştir. Anot ve katot giriş sıcaklıkları 800 °C olarak kabul edilirken, tüm yan duvarlar yalıtılmıştır. Ayrıca akışta bütün duvarlar no-slip olarak kabul edilmiştir. Katı mekaniği modelinde, üst taraftaki katot interkonnektörünün üst yüzeyine 5 kg ağırlığa denk gelecek düzgün bir sıkıştırma kuvveti tanımlanırken, bu yüzeyin x ve y yönlerindeki hareketi sınırlandırılmıştır. Alt taraftaki anot interkonnektörünün en alt yüzeyi ise her yönde haraketsiz kabul edilmiştir.

4.3 Bölünmüş Geometri

Şekil 4.1’de verilen geometriye uygulanan mesh dağılımı Şekil 4.2’de gösterilmiştir. Göz önüne alınan geometriye yapısal elemanlı mesh uygulanması için geometriyi oluşturan elamanlar küçük hacimlere bölünmüştür. Anot ve katot akış kanalları ve bu kanalları üzerinde bulunduran interkonnektör parçalarının $2 \times 2 \times 2 \text{ mm}^3$ hacimleri her üç yönde de 8 parçaya bölünmüştür. Parçalar, element oranı 4 olan simetrik bir dağılıma sahip olup bu sayede sınırlara yakın bölgelerde küçük uzak bölgelerde ise büyük elamanlardan oluşan bir mesh dağılımı sağlanmıştır. Anot, katot ve elektrolit tabakalarının x ve y yönündeki meshleri bir önceki ile aynı iken kalınlık doğrultusunda anot destek, katot ve elektrolit sırası ile yine simetrik olarak 10, 5 ve 3 elamandan oluşturulmuştur. Bu tabakalara denk gelen sızdırmazlık kısımları da benzer elemanlara bölünmüştür. Anot ve katot interkonnektörlerinin üst kısımlarında ise yine x ve y doğrultusundaki meshler aynen uygulanmış olup söz konusu sadece elektriksel iletkenlik olduğu için mesh sayısı 8 yerine 5 olarak seçilmiştir. Sonuç olarak 14 mm x 14 mm x 14 mm hacmindeki KOYP birim hücresi toplamda 137984 elemandan oluşmaktadır.



Şekil 4.2. Bölünmüş stak geometrisi

4.4 Sayısal Çözüm Metodu

Geliştirilen matematiksel model ticari bir sonlu elemanlar çözüm programı olan COMSOL® ile çözülmüştür. Çözümlerde akım, konsantrasyon, akış, ısı transferi ve katı mekanik modülleri kullanılmıştır. Akım modülü sadece MEG elemanları için tanımlanmış olup verilen voltaj değerine göre hücre içi akım dağılımını ve hücre performansının çözülmesinde kullanılmıştır. Konsantrasyon modeli gerek elektrotlar gerekse de akış kanalları içerisindeki maddelerin dağılımlarını belirlemede kullanılmıştır. Akış modülü de benzer şekilde elektrot ve akış kanallarında tanımlanmış olup hız ve basınç çözümlesinde kullanılmıştır. Pil çalışması sırasındaki hücre içi sıcaklık dağılımı ise ısı transferi modülü ile sayısal olarak belirlenmiştir. Bu dört modül daimi rejimde eş zamanlı olarak çözüldükten sonra redoks modeli eklenmiş katı mekaniği modülü çözülmüştür. Çözümler, Dell T7500 iş istasyonunda yaklaşık üç günlük bir zaman almıştır. Baz hücre ve diğer hücrelerin termo-akış modeli 0,1-0,9 V arasında değişen voltaj değerleri için çözülmüştür. Baz hücre hariç diğer hücrelerin mekanik model çözümleri ise sadece 0,6 V çalışma voltajı için karşılaştırılmıştır.

Termo-akış ve katı mekaniği modellerinde kullanılan parametreler sırası ile Çizelge 4.3 ve Çizelge 4.4'te verilmiştir.

Çizelge 4.3. Termo-akış model parametreleri

Parametre	Değer
Çalışma sıcaklığı (°C)	800
Anot geçirgenliği (m ²)	10 ⁻¹⁰
Anot gözenekliliği	0.3-0.5
Anot giriş basıncı (Pa)	P _{atm} +10
Anot çıkış basıncı (Pa)	P _{atm}
Anot gazı giriş içeriği (kütlece %)	40 H ₂ /60 H ₂ O
Anot elektronik iletkenlik (S/m)	1000
Anot iyonik iletkenlik (S/m)	1
Katot geçirgenliği (m ²)	10 ⁻¹⁰
Katot gözenekliliği	0.4
Katot giriş basıncı (Pa)	P _{atm} +30
Katot çıkış basıncı (Pa)	P _{atm}
Katot gazı giriş içeriği (kütlece %)	21 O ₂ / 79 N ₂
Katot elektronik iletkenlik (S/m)	1000
Katot iyonik iletkenlik (S/m)	1
Elektrolit iyonik iletkenlik (S/m)	5
İnterkonnektör iletkenlik (S/m)	5000
Elektrolit kalınlığı (µm)	4-10
Anot destek kalınlığı (µm)	400
Katot kalınlığı (µm)	30
DoO (%)	10-100
Operation voltage (V)	0.05-0.9

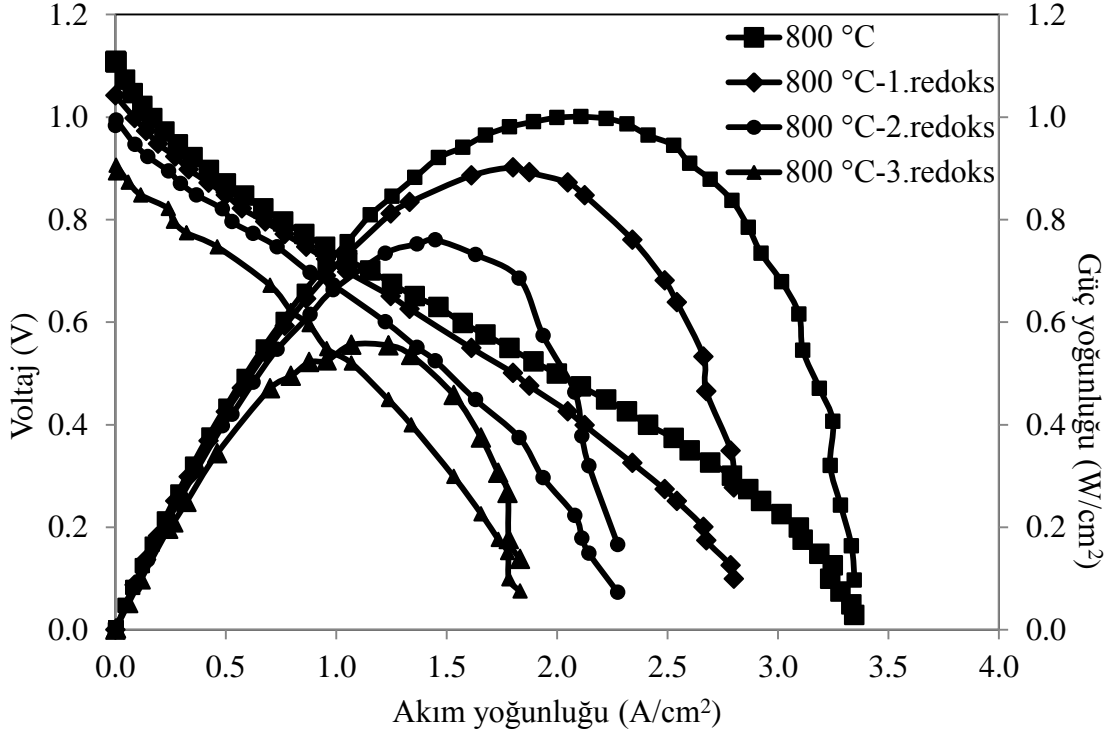
Anot elastisite modülündeki gözeneklilikle olan değişim Biswas vd. (2009) deneysel çalışmasına göre belirlenmiştir. Anot gözenekliliği ve elektrolit kalınlığının hasar fonksiyonu üzerindeki etkisi tipik bir KOYP çalışma voltajı olan 0,6 V için gerçekleştirilmiştir.

Çizelge 4.4. Katı mekanik model parametreleri

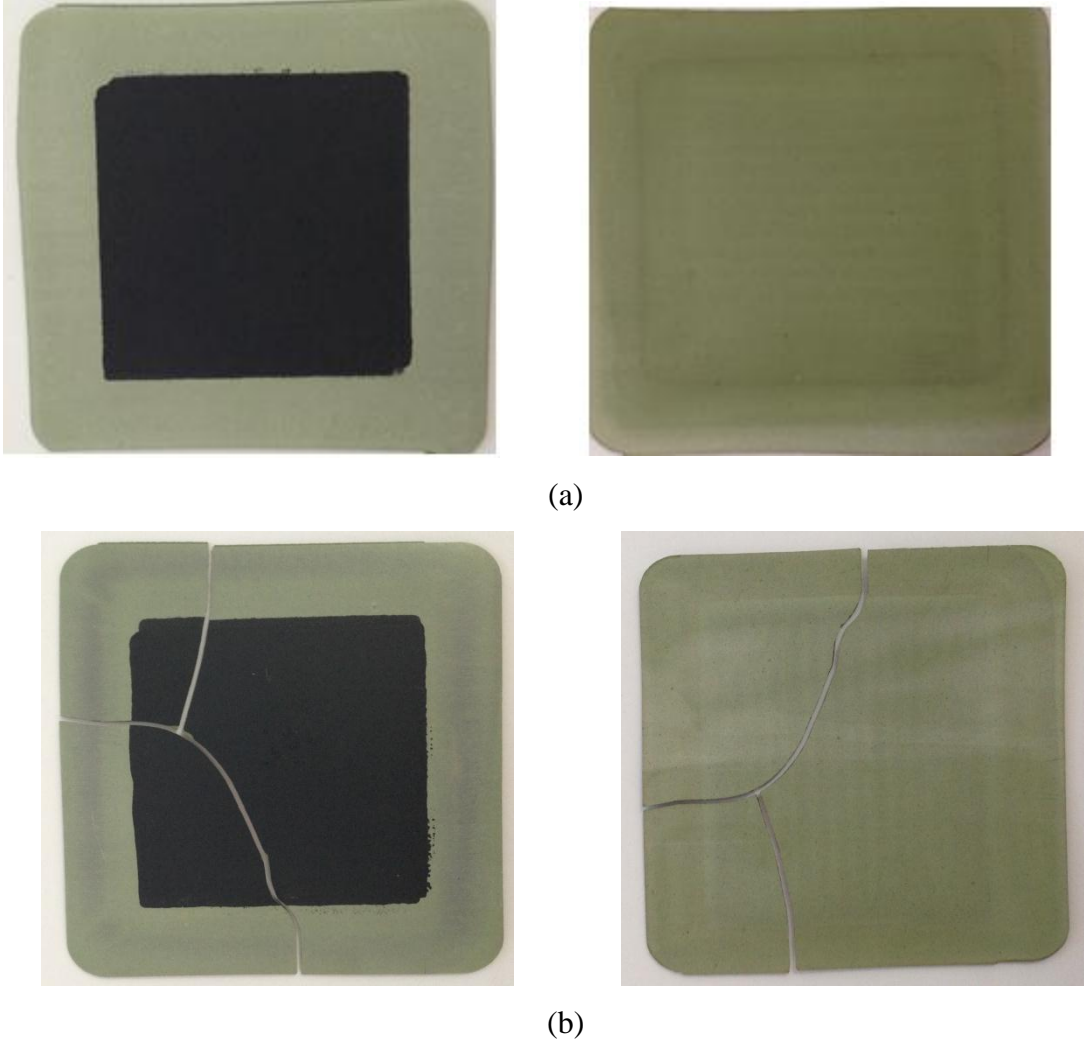
Parameter	Value
DoO (%)	10-100
Çalışma voltajı (V)	0.6
Elektrolit elastisite modülü (GPa)	190
Elektrolit Poisson oranı	0.308
Katot elastisite modülü (GPa)	35
Katot Poisson oranı	0.36
Anot elastisite modülü (GPa) 0.3 gözeneklilik	86
Anot elastisite modülü (GPa) 0.4 gözeneklilik	70
Anot elastisite modülü (GPa) 0.5 gözeneklilik	47
Anot Poisson oranı	0.3
Sızdırmazlık elastisite modülü (GPa)	67
Sızdırmazlık Poisson oranı	0.3
İnterkonnektör elastisite modülü (GPa)	160
İnterkonnektör Poisson oranı	0.3
Elektrolit ısı genleşme katsayısı (1/K)	10.8e-6
Katot ısı genleşme katsayısı (1/K)	11.7e-6
Anot ısı genleşme katsayısı (1/K)	12.5e-6
Sızdırmazlık ısı genleşme katsayısı (1/K)	12.6e-6
İnterkonnektör ısı genleşme katsayısı (1/K)	12.6e-6

5. DENEYSEL SONUÇLAR VE TARTIŞMA

Baz hücrenin farklı redoks döngüleri öncesi ve sonrasındaki performansı ise Şekil 5.1’de verilmiştir. İlk redoks döngüsü sonrasındaki maksimum güç yoğunluğu $0,9 \text{ W/cm}^2$ iken üçüncü döngü sonrasında performans 0.55 W/cm^2 ’ye düşmüştür. Ayrıca her bir redoks döngüsü sonrasındaki performans kaybının giderek arttığı dikkat çekmektedir. Açık devre potansiyelindeki azalmalar ise elektrolit tabakasında meydana gelen kırılmaları işaret etmektedir. Birinci ve üçüncü redoks döngüleri sonrasındaki hücre resimleri Fotoğraf 5.1’de verilmiştir. Özellikle üçüncü redoks döngüsü sonrasındaki kırılmalar açık devredeki kayıpları açıklamaktadır. Ayrıca artan redoks sayısına paralel olarak meydana gelen hasarların da giderek arttığı görülmektedir.

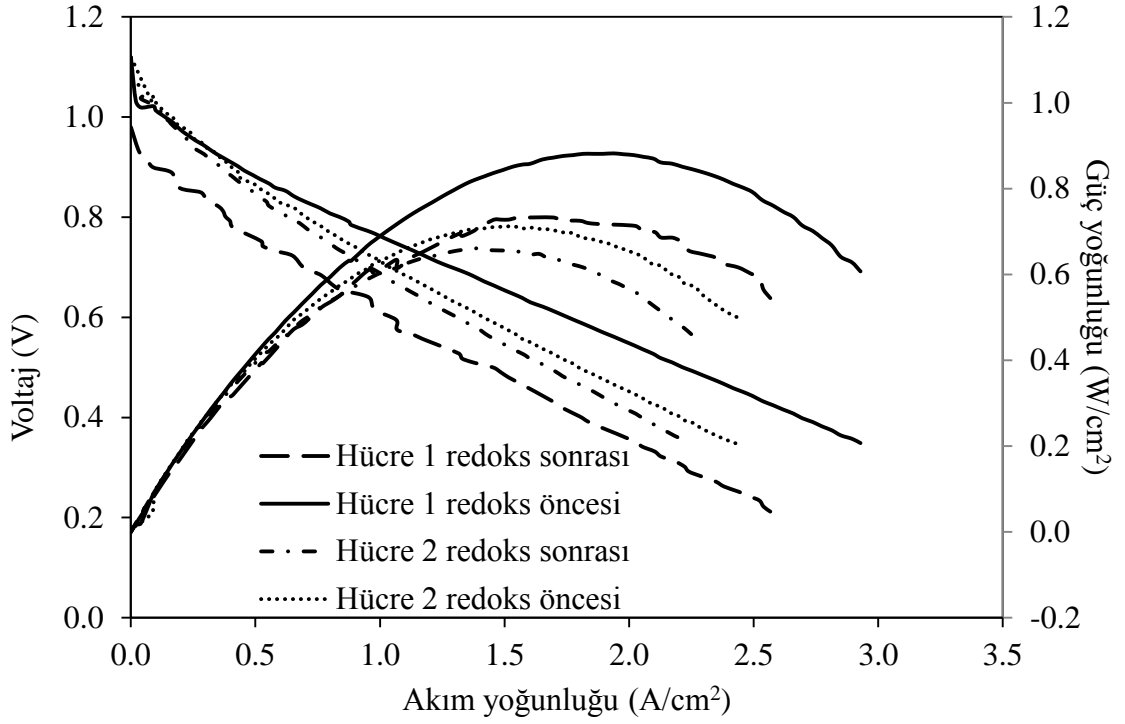


Şekil 5.1. Redoks döngülerinin baz hücre performansına etkisi 800 °C

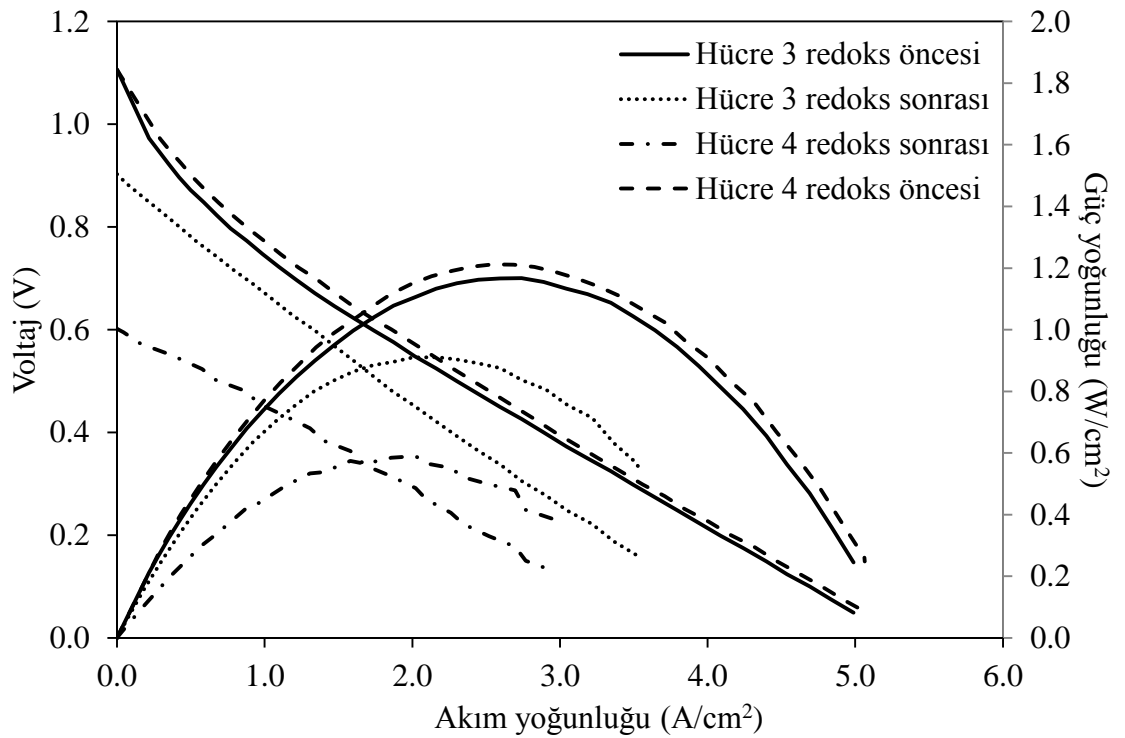


Fotoğraf 5.1. Brinci (a) ve üçüncü (b) redoks döngüsü sonrasındaki hücre fotoğrafları

Farklı anot porozitesinin hücre redoks davranışına olan etkisi Şekil 5.2’de verilmiştir. Redoks döngüleri sırasında meydana gelen hacimsel değişiklikler eğer hücre mikroyapısı tarafından tolere edilemezde kırılmalar meydana gelmektedir. Bu kapsamda nikel taneciklerinin yeniden oksitlenme sırasındaki hacimsel büyümesine izin vermek için anot yapısının gözenekliliğinin yüksek olması gerekmektedir. Bu yüzden en yüksek anot gözenekliliğine sahip olan Hücre 2 en iyi redoks dayanımını göstermiştir. Benzer şekilde en düşük anot gözenekliliğine sahip olan Hücre 1’in anot mikroyapısı bu hacimsel büyümelere izin vermediği için mekanik olarak zarar görmüş ve performans kaybı daha büyük olmuştur. Bu yüzden anot gözenekliliğinin gerek gaz akışı gerekse de redoks dayanımı açısından dikkatli bir şekilde belirlenmesi gerekmektedir.



Şekil 5.2. Hücre 1 ve Hücre 2'nin 800°C redoks öncesi ve sonrası performansları



Şekil 5.3. Hücre 3 ve Hücre 4'ün 800°C redoks öncesi ve sonrasındaki performansları

Farklı elektrolit kalınlığına sahip hücrelerin bir redoks döngüsü öncesi ve sonrasındaki performans eğrileri Şekil 5.3'te verilmiştir. Azalan elektrolit kalınlığına paralel olarak pil performansındaki kayıpların arttığı görülmektedir. Özellikle açık devre potansiyelindeki azalmalar her iki hücrenin de elektrolit tabakasında kırılmalar olduğunu göstermektedir. Elektrolit tabakası en ince olan Hücre 3'ün bu anlamda en ciddi mekanik zarara uğradığı tespit edilmiştir.

Baz hücrenin üç nokta bükme testleri ile redoks öncesi ve sonrasında ölçülen kuvvet-yer değiştirme eğrileri Şekil 5.4.'te verilmiştir. Redoks döngüsü sonrasında hücre mekanik dayanımında ciddi bir azalma olduğu görülmektedir. Hücrenin kırılma anındaki kuvvetinde redoks sonrasında %47 azalma olduğu belirlenmiştir. Hücre performansındaki azalmanın sadece yaklaşık %10 olduğu göz önüne alındığında (Şekil 5.1), redoksun hücre mekanik ve elektrokimyasal performansına olan etkisinin farklı olduğu sonucuna varılmıştır.

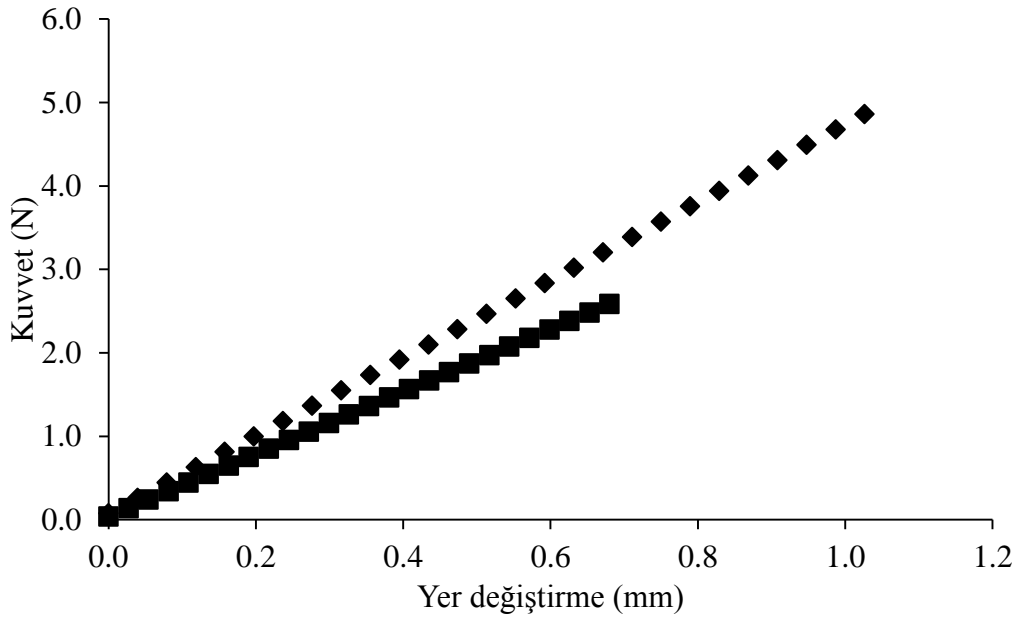
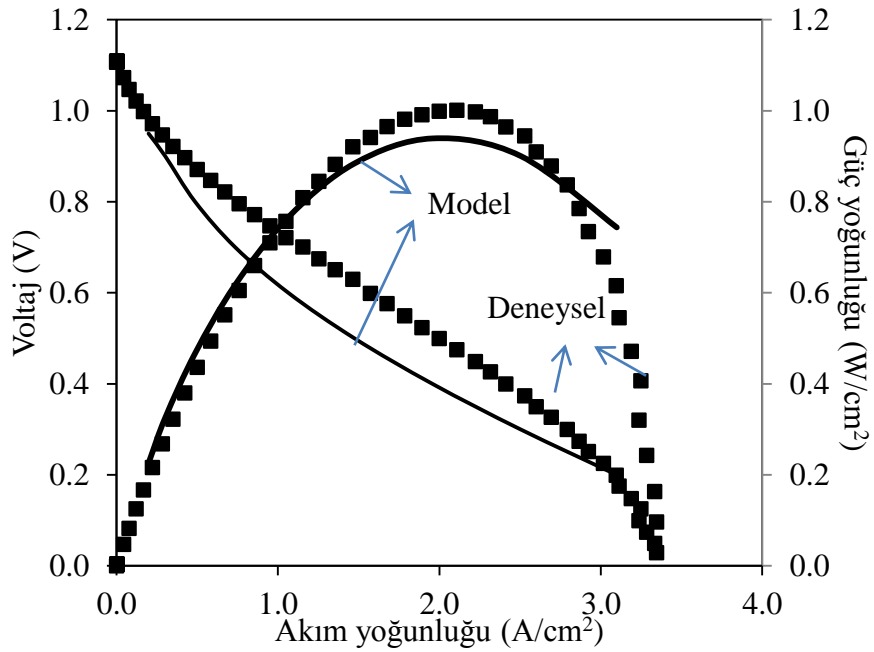


Figure 5.5. Baz hücrenin redoks öncesi ve sonrasındaki mekanik performansı

6. SAYISAL SONUÇLAR VE TARTIŞMA

6.1 Matematiksel Modelin Doğrulanması

Baz hücrenin deneysel ve sayısal performans eğrileri Şekil 6.1’de karşılaştırılmıştır. Kullanılan model parametreleri Çizelge 6.1’de verilmiştir. Deneysel ve sayısal sonuçların birbirine çok yakın olduğu görülmektedir. En yüksek hata oranı % 6,1 olarak hesaplanmıştır.



Şekil 6.1. Baz hücre için deneysel ve sayısal performans eğrilerinin karşılaştırması

Çizelge 6.1 Optimize edilmiş model parametreleri

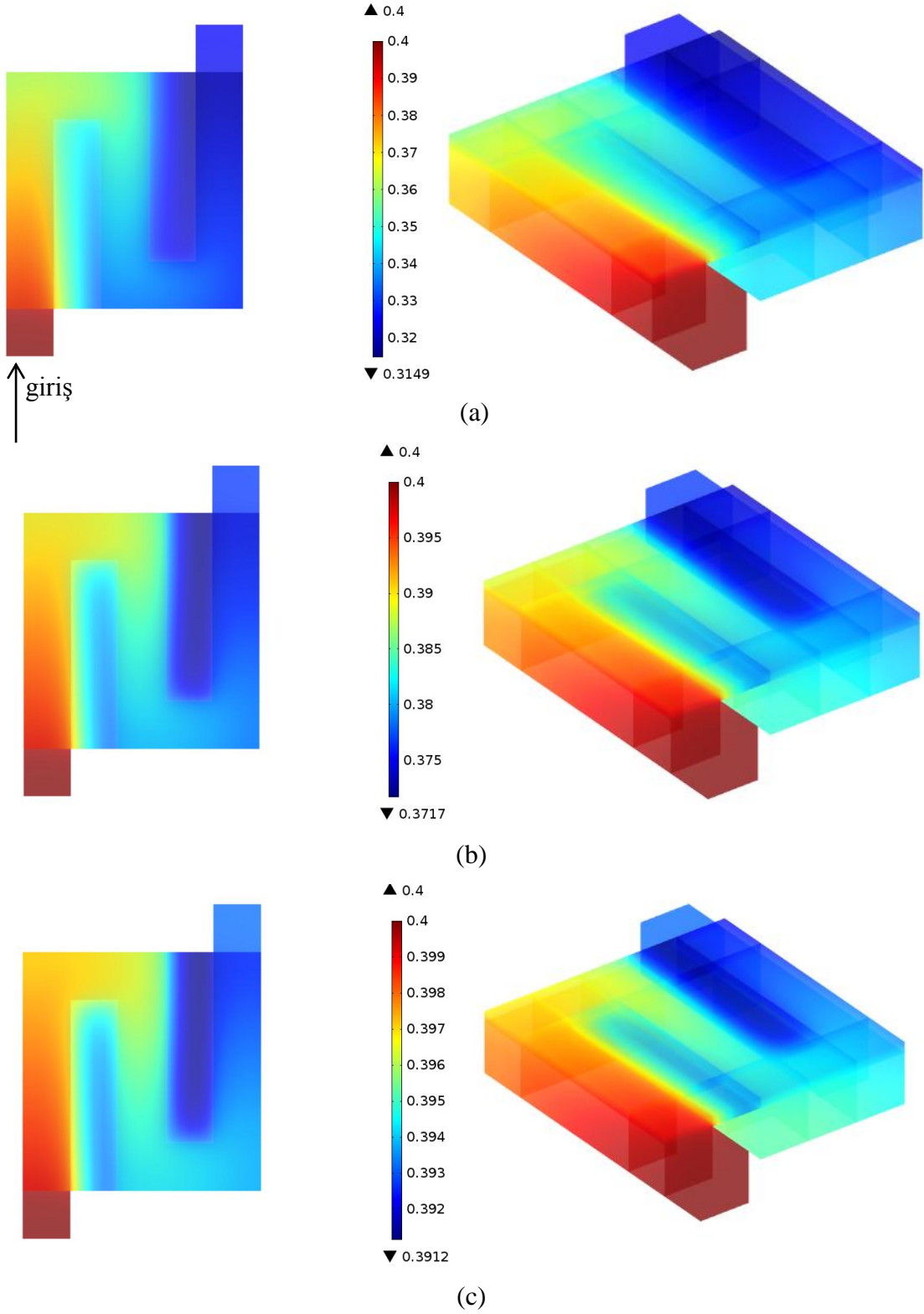
Parametre	Değer
$j_{o,anot}$ (A/m ²)	0.1
$\alpha_{a,anot}$	0.5
$\alpha_{c,anot}$	1.5
$j_{o,katot}$ (A/m ²)	0.01
$\alpha_{a,katot}$	3.5
$\alpha_{c,katot}$	0.5

6.2 Termo-Akış Modeli

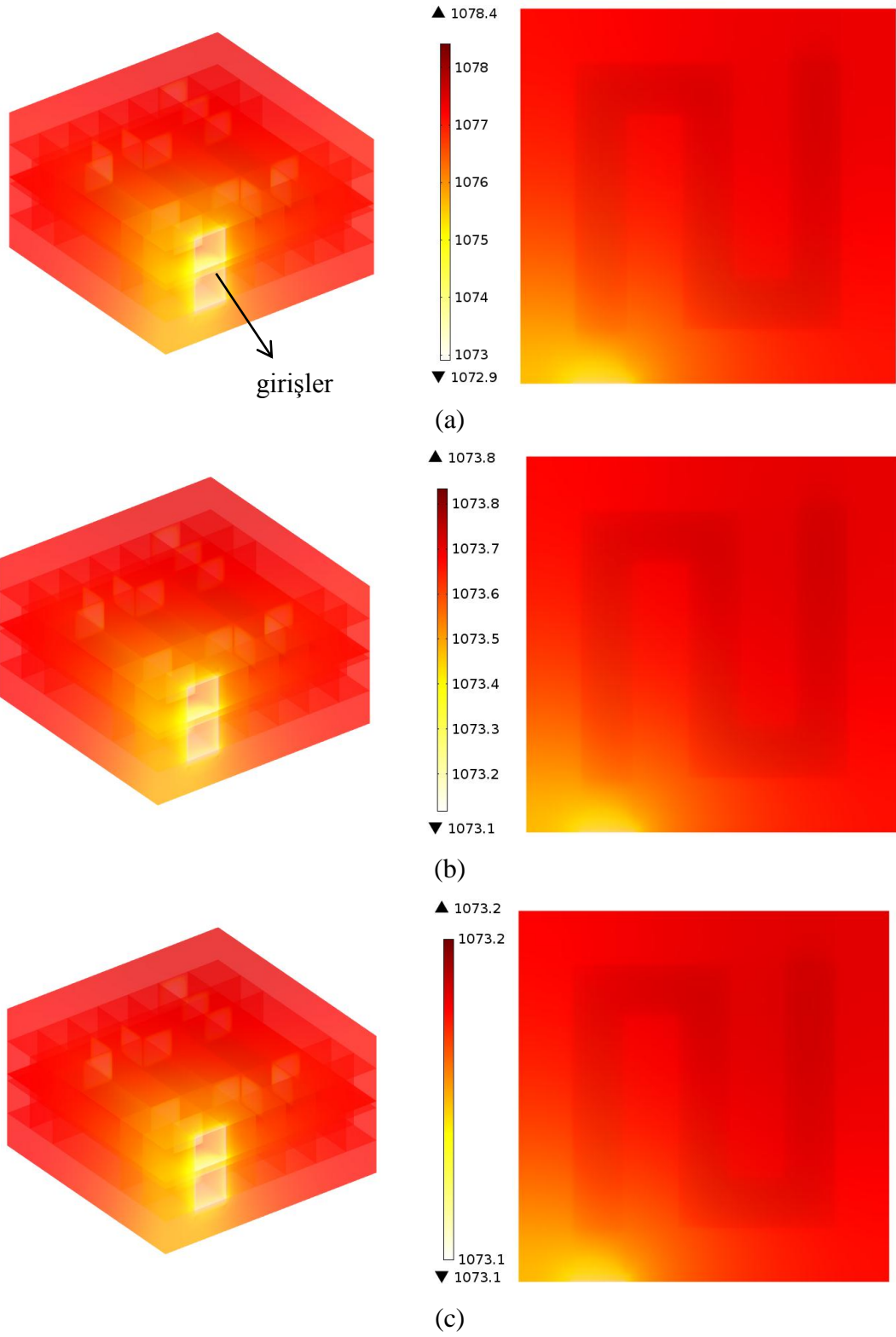
Baz hücreden farklı çalışma voltajlarında sayısal olarak elde edilen anot akış kanalı hidrojen konsantrasyonları Şekil 6.2’de verilmiştir. Azalan çalışma voltajına paralel olarak hidrojen tüketiminin arttığı görülmektedir. Bu durum düşük voltajlarda yüksek olan akım yoğunluğunun üretimi için gerekli olan elektrokimyasal reaksiyon sayısındaki artış ile açıklanmıştır. Ayrıca beklenildiği gibi hidrojen konsantrasyonunun çıkışa doğru giderek azaldığı belirlenmiştir.

Benzer durum Şekil 6.3’te verilen sıcaklık dağılımında da görülmektedir. Yüksek akım yoğunluklarında elektrokimyasal reaksiyonlar sırasında üretilen ısı miktarı daha yüksek olduğu için hücre sıcaklıkları da daha yüksek olmaktadır. Bu kapsamda 0,1 V çalışma voltajında pil içi sıcaklık artışı 6°C civarında iken voltaj 0,9 V’a çıkarıldığında hücre içinde önemli bir sıcaklık farklılığının oluşmadığı görülmektedir. Bu durum hücre aktif alanın oldukça küçük (1cm²) olmasına bağlanmıştır.

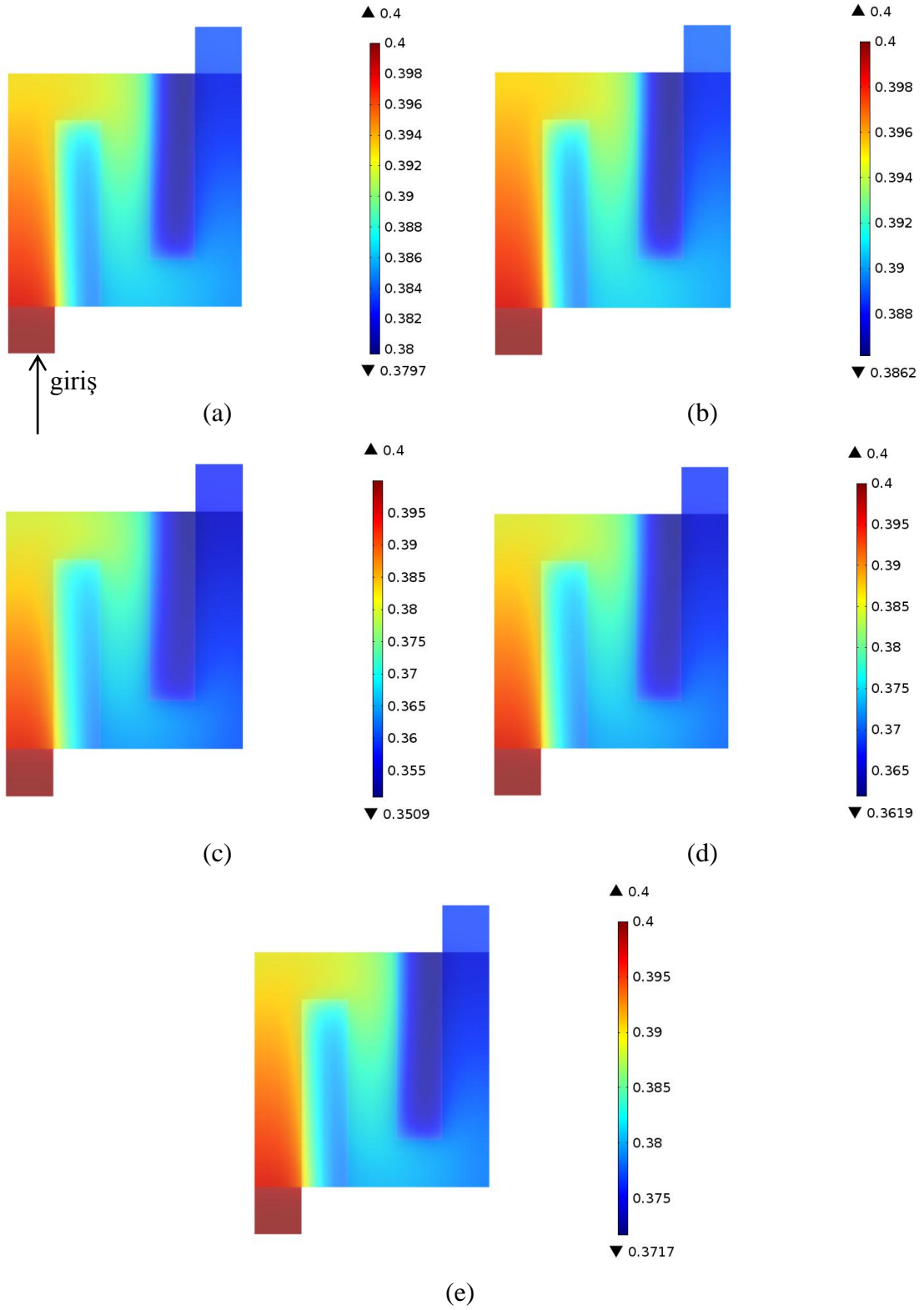
Hücre 1-4 ve baz hücrenin hidrojen tüketim miktarları ise Şekil 6.4’te karşılaştırılmıştır. Hidrojen tüketim miktarının deneysel olarak elde edilen performanslarla uyumlu olduğu görülmektedir. Deneysel ölçümlerde en yüksek performansı ortaya koyan Hücre 3’ün bu yüzden hidrojen tüketim miktarı da en yüksek olmuştur. Benzer şekilde deneysel sonuçlarda en düşük performansı sergileyen Hücre 2’nin hidrojen tüketim miktarı da bu yüzden en düşük olarak belirlenmiştir. İncelenen bütün durumlarda hidrojen konsantrasyonunun anot kanalı girişinden çıkışına doğru azaldığı görülmektedir. Bu durum pil içerisinde sürekli olarak meydana gelen elektrokimyasal reaksiyonların bir sonucudur. Ayrıca, özellikle anot destek bölgesi içerisindeki hidrojen konsantrasyonunun anot kanalına göre daha düşük olduğu görülmektedir. Bu durum gözenekli anot tabakasının oluşturduğu difüzyon direnci ile açıklanmıştır.



Şekil 6.2. Baz hücrenin anot akış kanalındaki 0.1 V (a), 0.6 V (b) ve 0.9 V (c) çalışma voltajlarındaki hidrojen kütle oranı değişimi



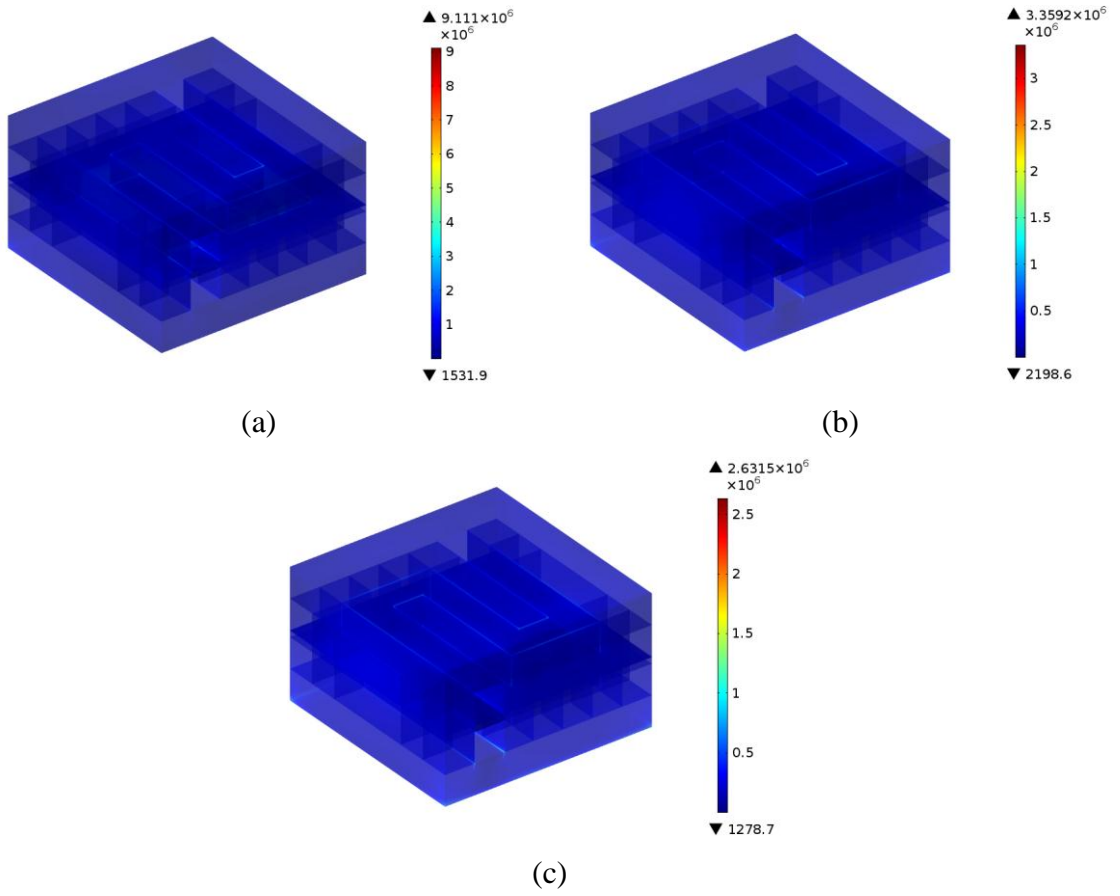
Şekil 6.3. Baz hücre içi sıcaklık dağılımı (a) 0.1 V, (b) 0.6 V ve (c) 0.9 V çalışma voltajı (K)



Şekil 6.4. 0,6 V çalışma voltajında Hücre 1-4 (a-d) ve baz hücre hidrojen tüketiminin karşılaştırması (kütle oranı)

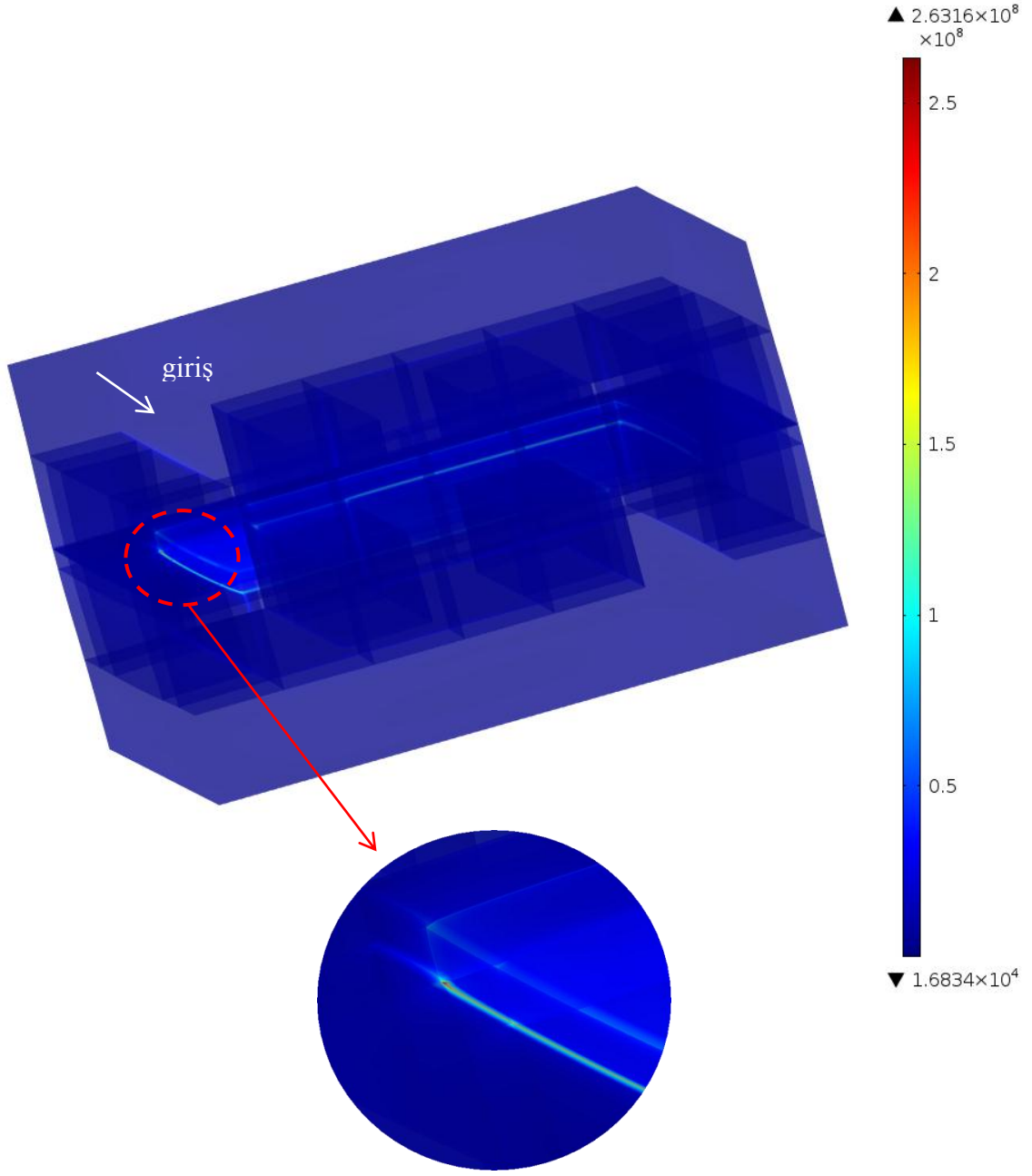
6.3 Katı Mekanik Modeli

Baz hücrenin 800 °C çalışma sonrasında ortaya çıkan sıcaklık farklılıkları ve hücre elamanlarının farklı olan ısıl genişleme katsayılarından kaynaklanan ısıl gerilmeler ve uygulanan sıkıştırma kuvveti sonrasındaki gerilme dağılımı Şekil 6.5'te verilmiştir. Beklenildiği gibi çalışma voltajı azaldıkça gerilme değerlerinin arttığı görülmektedir. Bu durum düşük voltajlarda yüksek olan sıcaklık farklılıkları ile açıklanmıştır. Fakat gerilme değerlerinin oldukça düşük olduğu belirlenmiştir.



Şekil 6.5. Baz hücrenin 0,1 V (a), 0,6 V (b) ve 0,9 V (c) çalışma voltajlarındaki gerilme dağılımı (Pa)

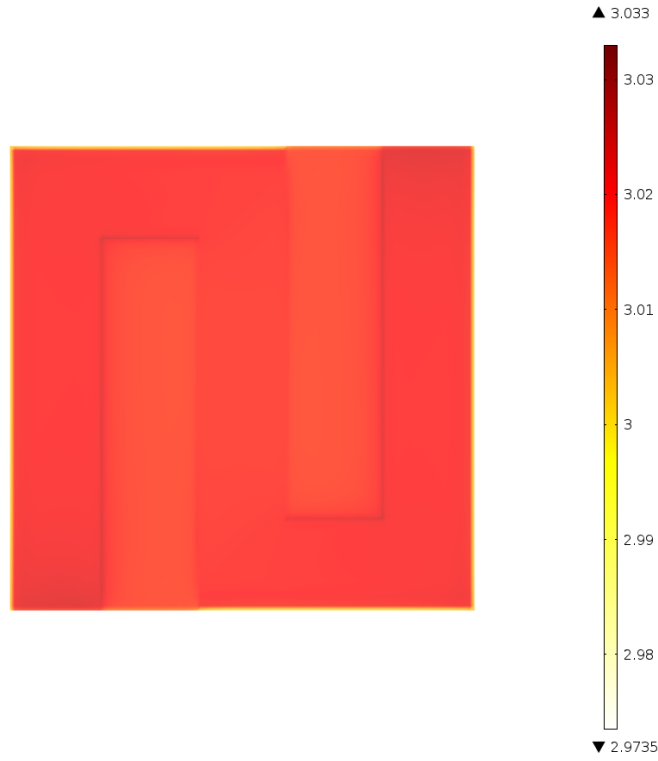
Anot oksidasyonu sonrasındaki gerilme dağılımı ise Şekil 6.6'da verilmiştir. Gerilme değerlerinde ciddi miktarlarda artış olduğu görülmektedir. Maksimum gerilmelerin özellikle MEG ile interkonnektör temas noktalarında olduğu ve bu yüzden kırılmaların bu noktalarda başlayabileceği belirlenmiştir.



Şekil 6.6. Redoks sonrası baz hücre içi gerilme (Pa) dağılımı (0,6 V)

Baz hücredeki hasar fonksiyonunun dağılımı ise Şekil 6.7’de verilmiştir. Hasar dağılımının 2.9735 ile 3,033 arasında değiştiği görülmektedir. Neredeyse homojen olan bu dağılım homojen olan sıcaklık dağılımı ve izotropik olarak tanımlanmış oksidasyon gerinmesi ile açıklanmıştır. Öte yandan anot tabakasının kanallara bakan kısımlarındaki hasarın daha büyük olduğu görülmektedir. Hasar fonksiyonu gerinmelere bağlı olarak

tanımlandığı ve bu bölgelerin hareket alanı interkonnektör tarafından sınırlanmadığı için, hasar bu bölgelerde daha yüksek olarak hesaplanmıştır.

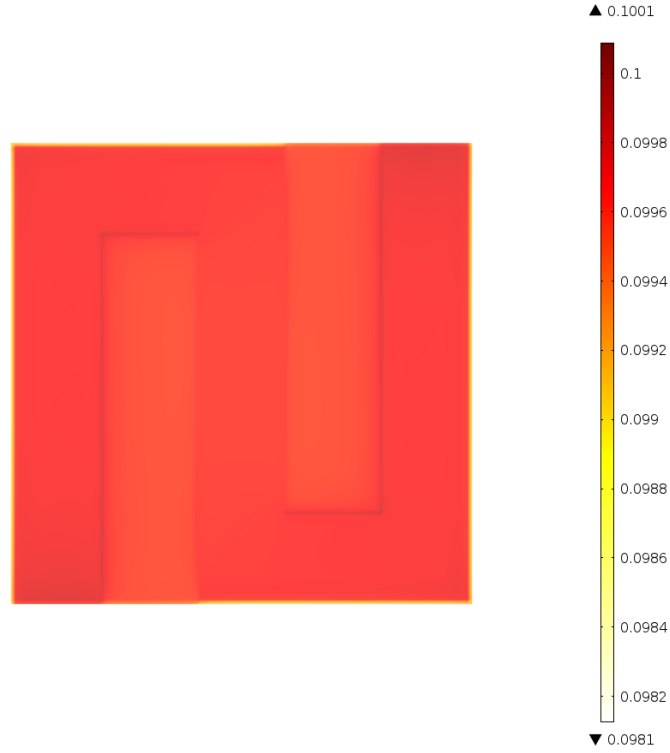


Şekil 6.7. Baz hücre içerisinde hasar dağılımı

Hasar fonksiyonun belirlenmesinden sonra başlangıçta 1 olan hasar katsayısının düzeltilmesine geçilmiştir. Düzeltilmiş hasar katsayısı redoks sonrasındaki performans kaybının anot içerisinde sayısal olarak hesaplanan ortalama hasara bölünmesi ile hesaplanmıştır:

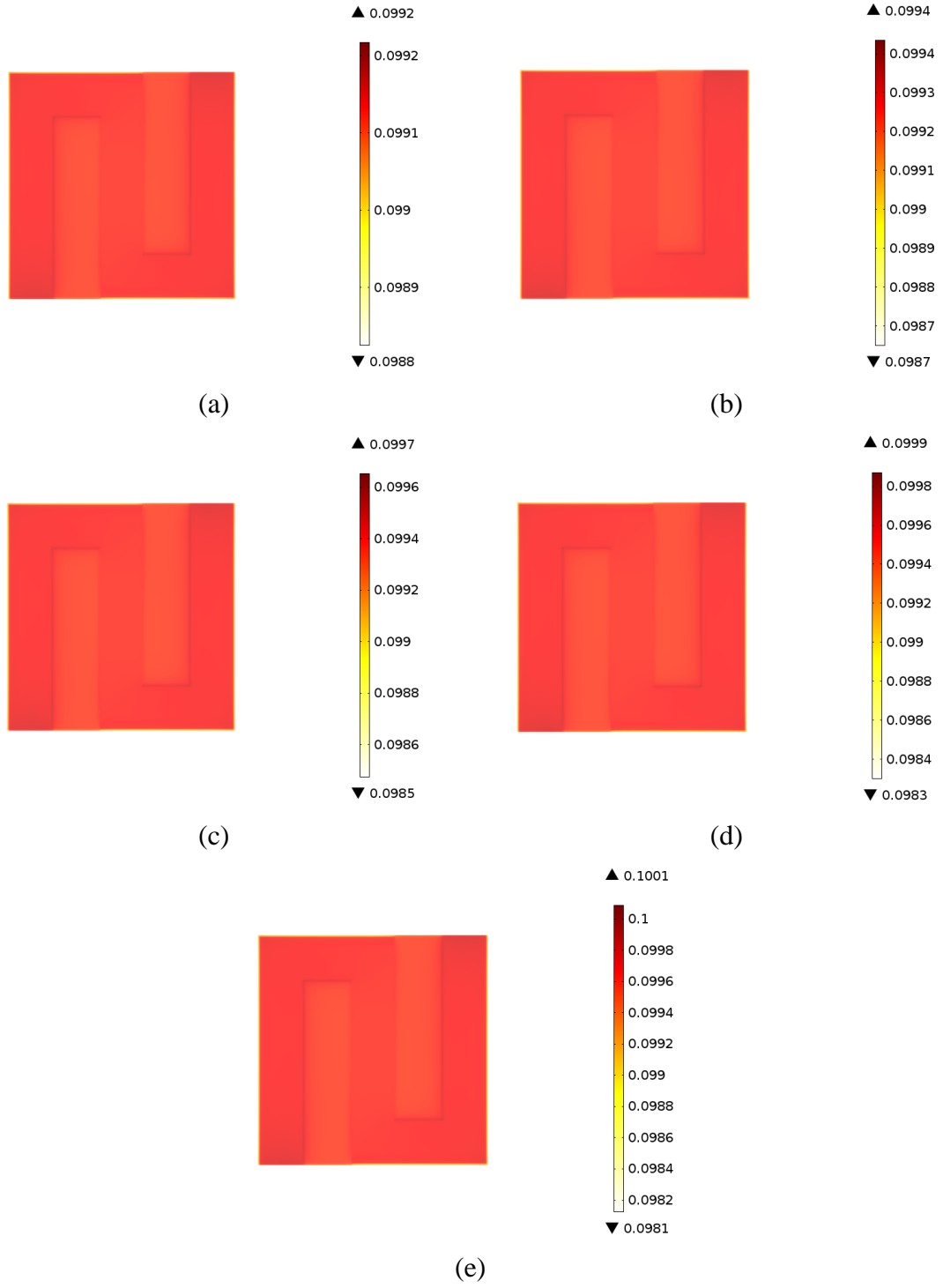
$$B_{dzt} = \left(\frac{PP_{redox\ \text{öncesi}} - PP_{redox\ \text{sonrası}}}{PP_{redox\ \text{öncesi}}} \right) / D_{av} \quad (6.1)$$

burada PP redoks öncesi ve sonrasındaki deneysel maksimum gücü D_{av} ise hasar katsayısının 1 olması durumunda sayısal olarak hesaplanmış anot ortalama hasarı ifade etmektedir. Düzeltilmiş hasar katsayısı kullanılarak elde edilmiş düzeltilmiş hasar dağılımı Şekil 6.8’de verilmiştir.

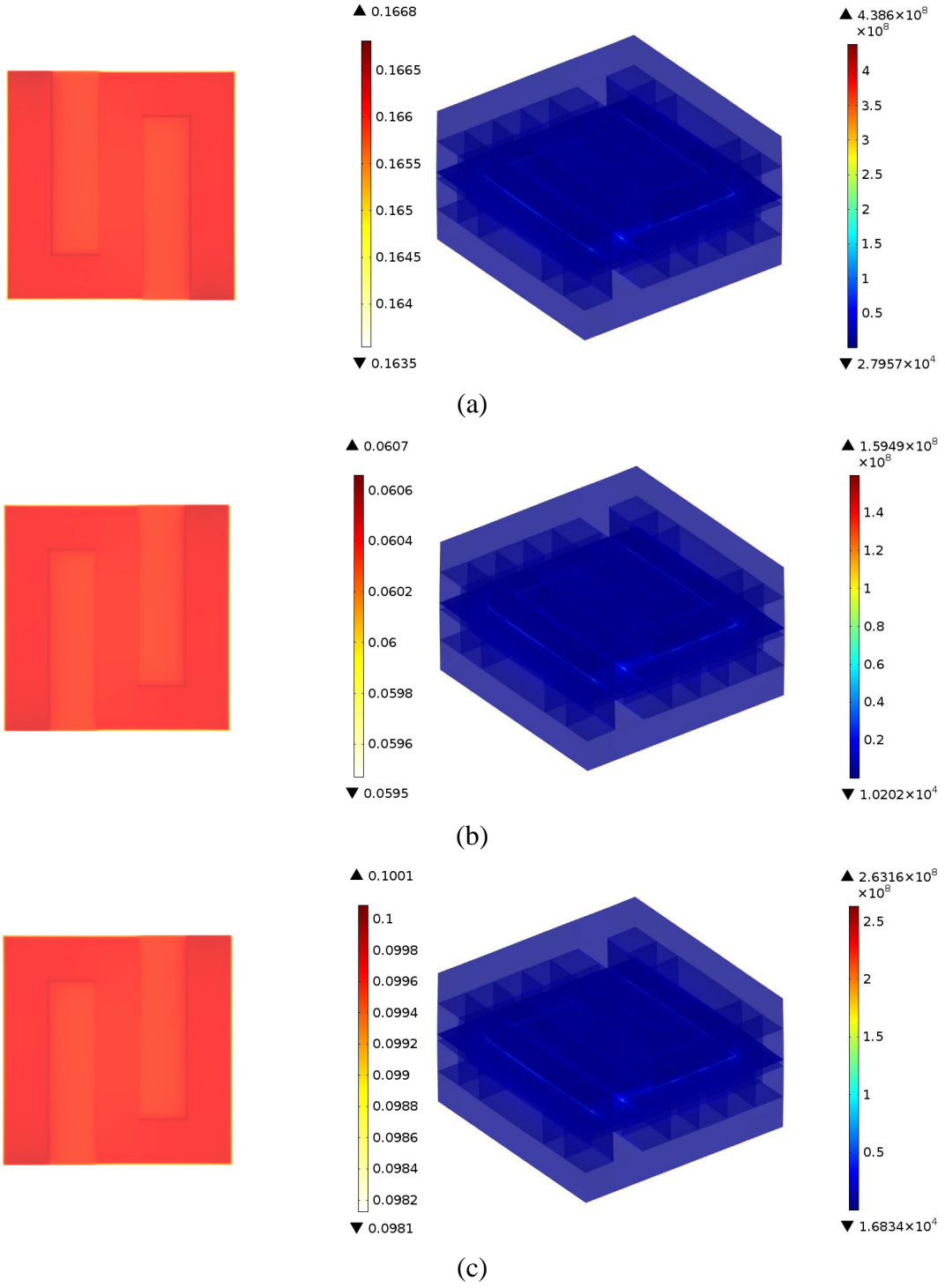


Şekil 6.8. Baz hücre içi düzeltilmiş hasar dağılımı

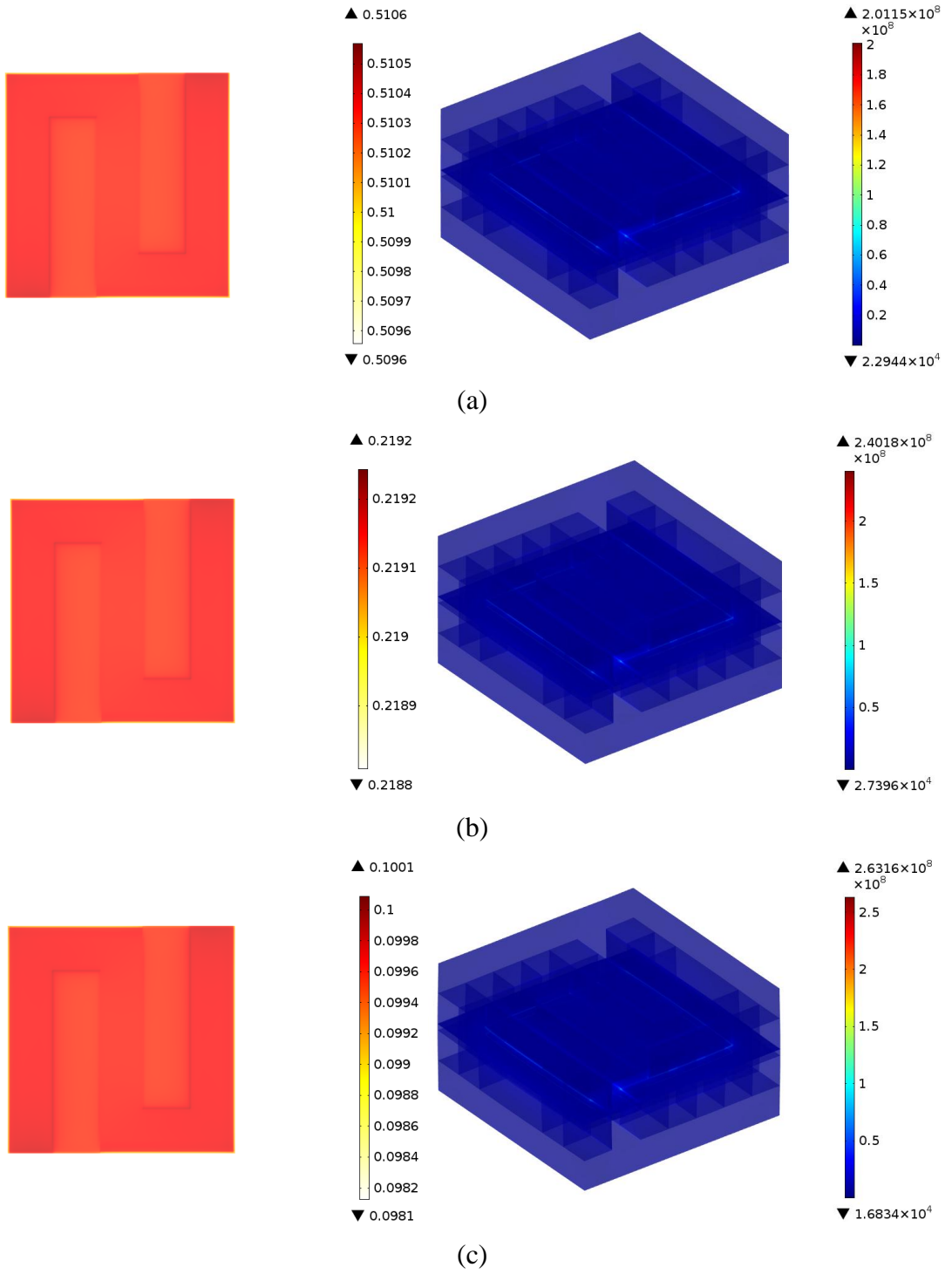
Baz hücre içi hasar dağılımının DoO ile değişimi Şekil 6.9’da verilmiştir. Beklenildiği gibi artan oksitlenme oranı ile üçlü faz bölgelerindeki hasarın da arttığı görülmektedir. Benzer hesaplamalar Hücre 1-4 için de gerçekleştirilmiş olup bu hücrelerin içerisinde meydana gelen hasar dağılımları Şekil 6.10 ve 6.11’de karşılaştırılmıştır. Şekil 6.10’da anot gözenekliliğinin hasar dağılımı üzerindeki etkisi verilmiştir. Beklenildiği gibi azalan gözenekliliğine paralel olarak redoks kaynaklı hasarların ve gerilmelerin arttığı görülmektedir. Gerilme değerlerindeki artışın bir başka nedeni ise azalan gözeneklilik değeri ile artan elastisite modülü değerleridir. Elektrolit kalınlığının hasar fonksiyonu üzerindeki etkisi ise Şekil 6.11’de verilmiştir. Deneysel sonuçlara paralel olarak elektrolit tabakası inceldikçe hasarın büyüdüğü görülmektedir.



Şekil 6.9. Baz hücre hasar dağılımının oksitlenme oranı ile değişimi (a) 0,2 (b) 0,4 (c) 0,6 (d) 0,8 ve (e) 1,0 DoO



Şekil 6.10. Hücre 1 (a), Hücre 2 (b) ve baz hücre (c) içerisindeki hasar (sol) ve gerilme (sağ) dağılımları (0,6 V)



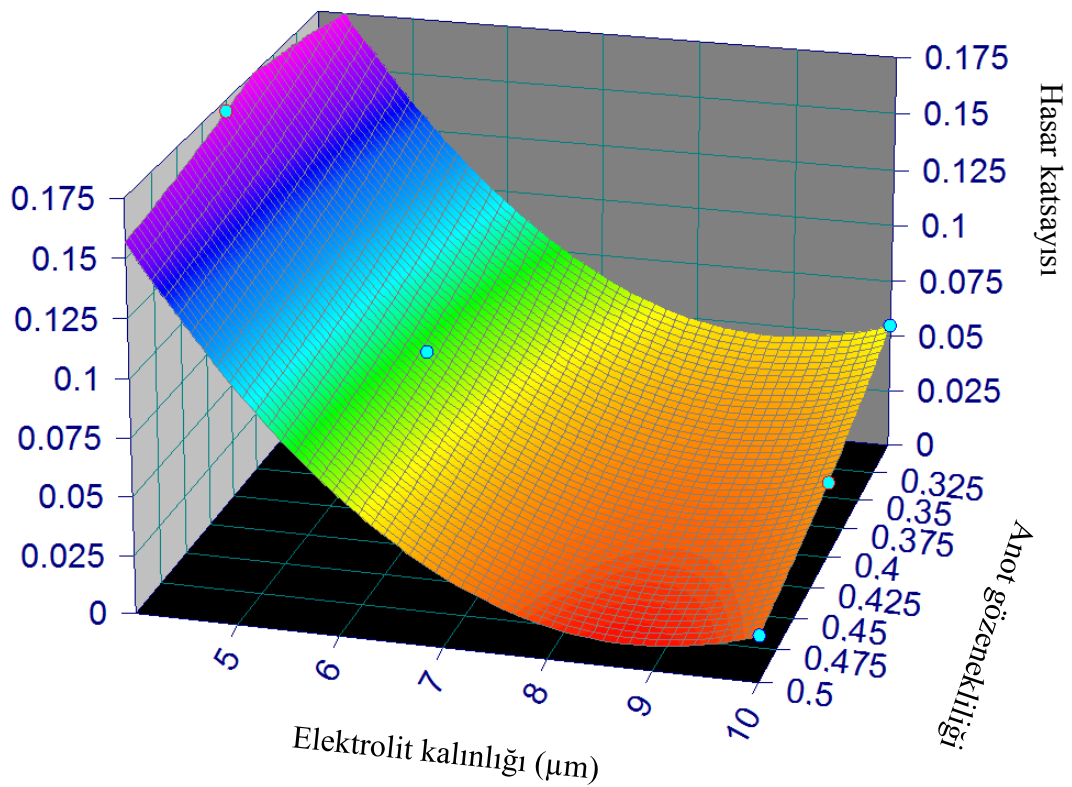
Şekil 6.11. Hücre 3 (a), Hücre 4 (b) ve baz hücre (c) içerisindeki hasar (sol) ve gerilme (sağ) dağılımları (0,6 V)

6.4 Hasar Katsayısının Modellenmesi

Gerçekleştirilen deneysel ve sayısal analizler neticesinde belirlenen hasar katsayısı (B), incelenen anot destek gözenekliliği ve elektrolit kalınlığına bağlı olarak 3D yüzey yaklaşımı ile modellenmiştir. Elde edilen model sonuçları Şekil 6.12’de verilmiştir. Elde edilen yüzeyin deneysel ve sayısal çalışmalar ile elde edilen data'lara uygun olduğu görülmektedir. Oluşturulan yüzeyde kullanılan denklem Eşitlik (6.2)’de verilmiştir. Kullanılan sabitler ise Çizelge 6.2’de listelenmiştir.

$$B = a + b/p + c.t + d.t^2 \quad (6.2)$$

Yukarıdaki denklemde p anot destek gözenekliliğini ve t elektrolit kalınlığını ifade etmektedir.

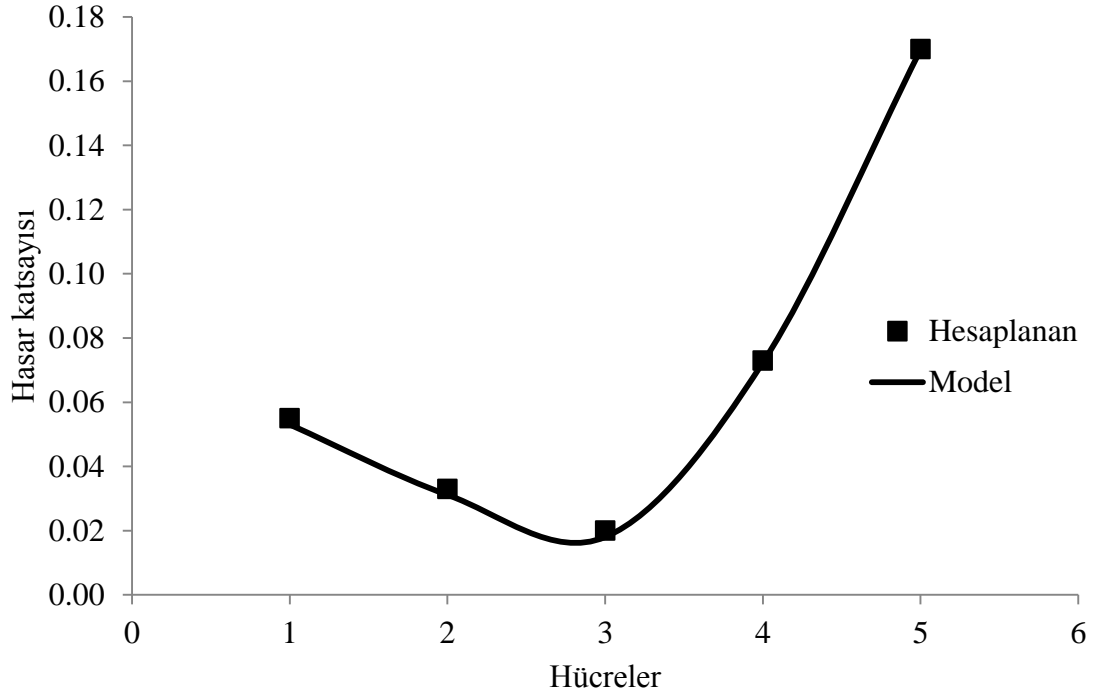


Şekil 6.12. Hasar katsayısı 3D model sonuçları

Çizelge 6.2. Yüzey oluşturma sabitleri

Parametre	Değer
<i>a</i>	0.4524
<i>b</i>	0.02626
<i>c</i>	-0.11270
<i>d</i>	0.0064

Modelin, deneysel ve sayısal olarak hesaplanan hasar katsayısı ile karşılaştırması Şekil 6.13'te verilmiştir. R^2 0.9999 olarak hesaplanmıştır.



Şekil 6.13. Modelin doğrulanması

7. SONUÇ

Bu çalışmada anot üretim parametrelerinin anot destekli hücre performansına ve redoks dayanımına olan etkisi deneysel ve sayısal olarak incelenmiştir. Deneysel çalışmada farklı anot gözenekliliği ve elektrolit kalınlığına sahip anot destekli hücreler imal ve test edilmiştir. Teorik çalışmada ise KOYP çalışmasını karakterize eden matematiksel bir model geliştirilmiş ve modele redoks kaynaklı performans kayıplarını ifade eden bir redoks modeli eklenmiştir. Deneysel ve sayısal çalışmalar sonrasında aşağıdaki sonuçlara varılmıştır:

- Anot destek gözenekliliğinin hücre performansı üzerinde önemli bir etkisi olduğu görülmüştür. Düşük gözenekliliklerde gaz transport problemlerinden yüksek gözenekliliklerde ise azalan elektrokimyasal reaksiyon bölgelerinden dolayı pil performansında kayıplar yaşanmaktadır. Anot destek porozitesinin 0,4 olduğu hücre bu kapsamda en iyi sonucu sergilemiştir.
- Hücre performansının azalan elektrolit kalınlığı ile iyileştiği görülmüştür. Bu kapsamda 4 µm kalınlıkta elektrolit tabakasına sahip olan hücre en yüksek performansı ortaya koymuştur.
- Anot destekli hücrelerin redoks dayanımının anot destek gözeneklilik ve elektrolit kalınlığı arttıkça iyileştiği tespit edilmiştir.
- Matematiksel modelin deneysel datalarla uyum içinde olduğu görülmüştür.
- Sayısal sonuçlar anot destekli hücre redoks dayanımının artan anot gözenekliliği ve elektrolit kalınlığı ile iyileştiği belirlenmiştir.
- Mekanik açıdan stak içerisindeki en kritik bölgenin interkonnektörlerin MEG ile temas ettiği kısımlar olduğu görülmüştür.

ACKNOWLEDGEMENTS

This work would not be possible without the support, advice and assistance of my family, friends and colleagues. Although this cannot be adequate to express my thought exactly, below I would like to acknowledge individuals who have made specific contribution to this thesis.

I would like to thank to my advisor Prof. Dr. Mahmut D. Mat for his guidance and support throughout the duration of my work.

I would like to give my deep gratitude again to my advisor to Prof. Dr. Mahmut D. Mat and Assoc. Prof. Dr. Yuksel Kaplan. Besides their truly advice and assistance, they provided a great research environment at Fuel Cell Laboratory at Nigde University and gave me freedom to explore.

I appreciate my friends and colleagues, especially Serkan Toros, Selahattin Celik and Abdullah Mat for their always readiness to help.

I wish to give my special thanks to my wife Cigdem Timurkutluk and two sons for their constant support and encouragement.

I also extend my thanks to VESTEL Savunma A.Ş. for equipment and materials support.

TABLE OF CONTENTS

SUMMARY	iv
ÖZET	vi
GENİŞLETİLMİŞ ÖZET	viii
ACKNOWLEDGEMENTS	lxv
TABLE OF CONTENTS.....	lxvi
LIST OF TABLES	lxviii
LIST OF FIGURES	lxix
LIST OF PHOTOS	lxxi
LIST OF SYMBOLS AND ABBREVIATIONS	lxxii
CHAPTER I INTRODUCTION.....	1
1.1 Physical Problem of Interest	3
1.1.1 Solid oxide fuel cell anode.....	3
1.1.2 Description of redox for Ni-based SOFC anodes	5
1.2 Thesis Objectives	8
1.3 Thesis Outline	9
CHAPTER II LITERATURE SURVEY	10
2.1 Redox Kinetics.....	10
2.1.1 Reduction of nickel oxide	10
2.1.2 Re-oxidation of nickel	12
2.2 Effects of Redox Cycling: Experimental Observations	14
2.3 Solutions to Redox Problem	22
2.4 SOFC Mechanical Modeling: Thermal Stress and Redox.....	26
2.5 SOFC Thermo-Fluid Modeling	31
2.5.1 Micro-modeling of SOFC	32
2.5.2 Macro-modeling of SOFC	33
CHAPTER III EXPERIMENTAL STUDIES	37
3.1 Base Cell Fabrication.....	37
3.1.1 Fabrication of the electrolyte and the anode support for the base cell.....	39
3.1.2 Fabrication of the cathode electrode for the base cell.....	40
3.1.3 Cases considered for the cell fabrication	40
3.2 Cell characterization	41
3.2.1 Electrochemical measurements.....	41

3.2.2 Samples for mechanical tests	43
3.2.3 Mechanical tests	44
CHAPTER IV MATHEMATICAL MODELING	45
4.1 Model Description	45
4.2 Governing Equations	45
4.2.1 Continuity equation.....	45
4.2.2 Species balance	48
4.2.3 Momentum equation	49
4.2.3 Energy conservation	50
4.2.4 Charge balance.....	51
4.1.4 Electrochemical reactions	51
4.2.5 Electrochemical model.....	52
4.2.5 Solid mechanics	52
4.2.6 Redox model	53
4.2.7 Boundary conditions and assumptions	54
4.3 Meshing	55
4.4 Numerical Solution Method.....	56
CHAPTER V EXPERIMENTAL RESULTS AND DISCUSSION	59
5.1 Base Cell	59
5.2 Effect of Anode Support Porosity on the Cell Performance and Redox Behavior...	62
5.3 Effect of Electrolyte Thickness on the Cell Performance and Redox Behavior.....	65
5.4 Three Point Bending	68
CHAPTER VI NUMERICAL RESULTS AND DISCUSSION.....	70
6.1 Validation of the Mathematical Model.....	70
6.2 Thermo-Fluid Model.....	72
6.3 Solid Mechanics Model	81
6.3.1 Base cell.....	81
6.3.2 Effect of anode porosity on the damage function	87
6.3.3 Effect of the electrolyte thickness on the damage function	87
6.4 Modeling of the Damage Coefficient	90
CHAPTER VII CONCLUSION	93
REFERENCES	94
CURRICULUM VITAE.....	111

LIST OF TABLES

Table 2.1. Nickel and nickel oxide molar mass, specific mass and molar volume	6
(Faes et al., 2009).....	6
Table 4.1. Kinetics volumes of the considered species	49
Table 4.2. Temperature dependent parameters of each species.....	50
Table 4.3. Thermo-fluid parameters used in the numerical analyses	57
Table 4.4. Solid mechanics parameters used in the numerical analyses.....	58
Table 5.1. Calculated porosities via Archimedes' technique.....	62
Table 6.1 Fitting parameters	71
Table 6.2. Maximum damages in the base cell for various DoO.....	87
Table 6.3. Surface fitting parameters	91

LIST OF FIGURES

Figure 1.1. Schematic of SOFC working principle	2
Figure 1.2. Cartoon illustrating the microstructural changes of NiO/YSZ anode upon successive redox steps (adopted from Klemensø and Mogensen, 2007).....	7
Figure 3.1. The structure of the anode supported cell (not to scale).....	38
Figure 3.2. The flowchart of the cell fabrication	38
Figure 3.3. Short stack configuration.....	43
Figure 3.4. The schematic of three point bending test bench	44
Figure 4.1. The SOFC short stack geometry of interest	46
Figure 4.2. Meshed structure of the geometry of interest.....	55
Figure 5.1. The performance curves obtained from the base cell at 700, 750 and 800°C	59
Figure 5.2. Effect of redox cycles on the cell performance at 800 °C.....	60
Figure 5.3. Dry (a), soaked (b) and suspended bodies (c)	62
Figure 5.4. Effect of anode support porosity on the cell performance at 800 °C	63
Figure 5.5. Performance curves of Cell 1 and Cell 2 before and after redox at 800 °C .	64
Figure 5.6. The microstructural images captured from the base cell (a),	66
Cell 3 (b) and Cell 4 (c)	66
Figure 5.7. Effect of electrolyte thickness on the cell performance at 800 °C.....	67
Figure 5.8. The performances of Cell 3 and Cell 4 before and after anode re-oxidation	68
Figure 5.9. Force-displacement curves of cells before and after redox	69
Figure 6.1. Comparison of experimental and numerical performance of the base cell ..	70
Figure 6.2. Comparison of experimental and numerical performance of Cell 1-4.....	71
Figure 6.3. Velocity contours (in m/s) at the anode (a) and at the cathode channel (b) of the base cell.....	72
Figure 6.4. Hydrogen distribution (weight fraction) in the anode and in the anode flow channel of the base cell at 0.1 V (a), 0.6 V (b) and 0.9 V (c).....	73
Figure 6.5. Hydrogen consumption in the base cell along with the anode flow channel at various operational voltages	74
Figure 6.6. The estimated temperature profile (in K) in the base cell	75
at 0.1 V (a), 0.6 V (b) and 0.9 V (c).....	75
Figure 6.7. Comparison of the maximum temperatures in the base cell	76

at various operation voltage	76
Figure 6.8. Hydrogen consumption (weight fraction) in Cell 1-4 (a-d) and.....	78
the base cell (e) at 0.6 V	78
Figure 6.9. Hydrogen consumption along with the anode flow channel	79
Figure 6.10. The temperature profiles (in K) in Cell 1-4 (a-d) and the base cell (e).....	80
Figure 6.11. The maximum temperatures in Cell 1-4 and the base cell	81
Figure 6.12. Estimated stresses (in Pa) at 0.1 V (a), 0.6 V (b) and 0.9 V (c)	82
in the base cell.....	82
Figure 6.13. The calculated stress distribution (in Pa) in the base cell after one redox cycle.....	83
Figure 6.14. The distribution of the damage function in the anode support layer of the base cell after full oxidation.....	84
Figure 6.15. The corrected damage distribution in the anode layer of the base cell after full oxidation.....	85
Figure 6.16. The effect of degree of oxidation after operation at 0.6 V: (a) DoO=0.2, (b) DoO=0.4, (c) DoO=0.6, (d) DoO=0.8 and (e) DoO=1.0	86
Figure 6.17. Damage (left) and stress (right) distribution in Cell 1 (a), Cell 2 (b) and the base cell (c)	88
Figure 6.18. Damage (left) and stress (right) distribution in Cell 3 (a), Cell 4 (b) and the base cell (c)	89
Figure 6.19. Comparison of the maximum damage for Cell 1-4 and the based cell	90
Figure 6.20. 3D surface modeling result of the damage coefficient.....	91
Figure 6.21. Model validation for the damage coefficient	92

LIST OF PHOTOS

Photo 3.1. The photo of the final anode supported cell with 1 cm ² active area.....	40
Photo 3.2. The experimental setup.....	42
Photo 5.1. Photos of the cell after the first (a) and after third redox cycle (b)	61
Photo 5.2. Fracture surfaces of the cell before (a) and after (b) redox cycle.....	69

LIST OF SYMBOLS AND ABBREVIATIONS

Symbols	Description
A_v	Specific area
B_{cor}	Corrected damage coefficient
C_O	Concentration ratio of oxidized species
C_R	Concentration ratio of reduced species
D_{jk}	Maxwell-Stefan diffusivities
\hat{E}	Effective modulus
E_{max}	Maximum voltage
h_f	Enthalpy of formation
M_{jk}	Combined molecular weight
V_{cell}	Cell voltage
c_p	Specific heat
d_k	Diffusion driving force
i_{exc}	Exchange current density
i_{local}	Local current density
\vec{j}	Ionic or electronic current density
j_o	Exchange current density
k_d	Reference diffusivity
k_{log}	Logarithmic rate constant
t_0	Time correction for the induction period
$\alpha_{a,c}$	Anode/cathode charge transfer coefficient
ε_{redox}	Re-oxidation strain
$\varepsilon_{thermal}$	Thermal strain
ε_{total}	Total strain
η_{act}	Activation polarization
ρ_e	Ionic or electronic charge density

ΔV	Volume change
e^-	Electron
m	Reduction exponent
B	Damage coefficient
D	Damage function
E	Young's modulus
F	Faraday's constant
G	Shear modulus
K	Permeability
MW	Molecular weight
P	Pressure
PP	Peak power
R	Specific gas constant
S	Source term
T	Temperature
V	Volume
c	Concentration
k	Overall reduction rate constant
n	Number of electrons involved in electrochemical reaction
t	Time
u	Velocity vector
ν	Poisson's ratio
w	Weight fraction
x	Fractional conversion
α	Coefficient of thermal expansion
γ	Shear strain
ε	Porosity and strain
μ	Dynamic viscosity

ρ	Density
σ	Ionic/electronic conductivity and normal stress
τ	Shear stress
ϕ	Ionic/electronic electrical potential

Abbreviations	Description
EDB	Erbium Doped Bismuth Oxide
ESEM	Environmental Scanning Electron Microscope
GDC	Gadolinium Doped Ceria
LSCF	Lanthanum Strontium Cobalt Iron Oxide
LSCM	Lanthanum Strontium Cobalt Manganese Oxide
LSM	Lanthanum Strontium Manganite
MEA	Membrane Electrode Assembly
OCV	Open Circuit Potential
ScSZ	Scandia Stabilized Zirconia
SDC	Samarium Doped Ceria
SEM	Scanning Electron Microscope
SIS-SOFC	Segmented-in-Series Solid Oxide Fuel Cell
SNT	Niobium Doped SrTiO ₃
SOFC	Solid Oxide Fuel Cell
TEM	Transmission Electron Microscopy
TGA	Thermal Gravimetric Analysis
TMA	Thermo-Mechanical Analysis
TPB	Triple Phase Boundary
YSZ	Yttria Stabilized Zirconia
DoO	Degree of Oxidation

CHAPTER I

INTRODUCTION

Solid oxide fuel cells (SOFC) are new generation environmentally friendly electrochemical devices which convert the chemical energy of a fuel into directly electricity with some amount of valuable heat energy. Since the conversion does not have any intermediate step, the electrical efficiency of SOFCs is relatively higher than the similar mature technologies such as internal combustion engines or generators. SOFCs operate at high temperature (600-1000°C) depending on the electrolyte material. Therefore, they have a higher tolerance to fuel impurities than then the low temperature fuel cell types. The enhanced reaction kinetics as a result of the high operation temperature further improve the electric efficiency of SOFC hence SOFC can be considered as one of the most efficient fuel cells. In addition to pure hydrogen, hydrocarbon fuels can be used as a fuel in SOFC directly or after a reforming process.

Ceramic membrane electrode assembly (MEA) composed of an anode, an electrolyte and a cathode is the key element of the SOFC system. While the anode is responsible for the fuel oxidation, the oxygen ions generated at the cathode as a result of the cathode electrochemical reaction are transferred through electrolyte to the anode layer. The operation principle of hydrogen fueled SOFC with the electrochemical reactions is shown in Figure 1.1. The generation of the electrical current is achieved via the external circuit during the transfer of electrons produced at the anode site to the cathode site while electrochemical reactions take place at triple phase boundaries (TPBs) where an ion conductor, an electronic conductor or catalyst and reactant phases meet.

Yttria stabilized zirconia (YSZ) is widely used electrolyte material for SOFCs. However, the operation temperature of around 1000°C is required to obtain an acceptable performance from the YSZ electrolyte supported cell. At such a high temperature that is required for the YSZ electrolyte to provide adequate ionic conductivity, it is difficult to expect a good long-term stability as well. In addition, high temperature-resistant materials are limited and this is the chief obstacle for interconnect and sealing elements.

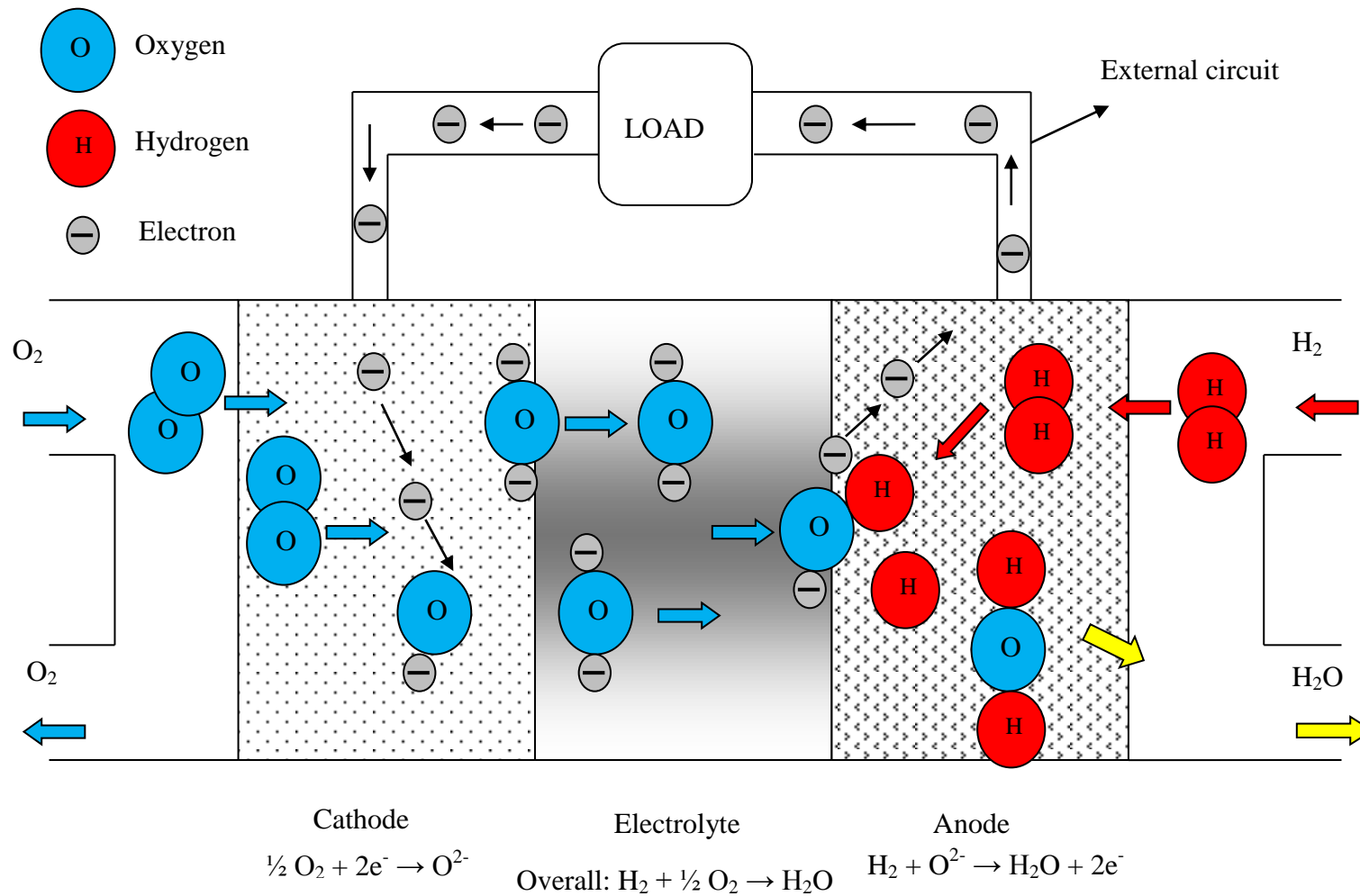


Figure 1.1. Schematic of SOFC working principle

1.1 Physical Problem of Interest

The lowering of SOFC operation temperature is one of the major issues in the aspect of cost reduction, long service life and commercialization of the SOFC systems. One way to reduce the SOFC operation temperature is to lower the YSZ electrolyte thickness by switching the cell design to anode supported from the electrolyte supported structure. With the development of thin film technologies, it is possible to fabricate 5-10 μm thin electrolytes on the anode support in order to reduce the operation temperature by employing tape casting and co-sintering (Wang et al., 2011; Le et al., 2010; Park et al., 2010 and Ana et al., 2010) or deposited by surface coating methods such as vapor deposition (Meng et al., 2008; Jung et al., 2006; Meng et al., 2004, Sasaki et al., 2008 and Kuo et al., 2009), laser deposition (Yang et al., 2007; Rodrigo et al., 2007 and Pryds et al., 2006) and electrophoretic deposition (Hosomi et al., 2007; Majhi et al., 2011 and Matsuda et al., 2007). Although the anode supported design offer high performance at an operation temperature of 200-300 $^{\circ}\text{C}$ lower than that of the standard YSZ electrolyte supported one, then another significant problem arises that Ni-based anodes, which is the most common SOFC anode material, suffer from the cyclic *reduction* ($\text{NiO} \rightarrow \text{Ni}$) and *oxidation* ($\text{Ni} \rightarrow \text{NiO}$). This continuous phase change is known as *redox* cycling and is likely to occur during the lifetime of the SOFC system. The volumetric changes during these conversions cause mechanical damage to the cell and thus limit the service life of the SOFC system. Therefore, the redox stability of Ni-based anodes should be investigated intensely and needs to be improved for a long term operation without degradation.

1.1.1 Solid oxide fuel cell anode

The most significant role of the solid oxide fuel cell anode is to provide electrochemical reactions zones for the fuel oxidation. Thus it should provide high catalytic activity. In addition, electrons produced via the anode electrochemical reaction are transferred to the interconnector by the anode in order to obtain useful electrical energy. Therefore, it should also provide high electronic conductivity. The significant features that an SOFC anode should serve are summarized below:

- High ionic and electronic conductivity
- Chemical compatibility and stability
- Compatible coefficient of thermal expansion
- High catalytic activity towards reactant fuels
- Porous structure allowing to continuous fluid flow and improved reaction zones
- Resistance to carbon deposition and sulfur poisoning
- Fuel flexibility
- Easy and low-cost fabrication
- High mechanical strength in case of anode supported cell design

On the other hand, a single anode material providing all of these above requirements has not been developed yet. Thus, composite materials have been considered as the most suitable materials as the SOFC anode. A typical SOFC anode includes two main elements namely metallic and oxide parts. In addition to providing electron transfer, the metallic component is the catalyst part of the anode. Although the single metallic material can be used as SOFC anode, the anodic electrochemical reaction zone is then limited to the interface between the anode and the electrolyte. In addition to this, thermal mismatch can possibly occur due to thermal expansion differences between the anode and the electrolyte. Therefore, the addition of second component is required for both improved performance and structural stability. This can be achieved by the addition of some amount of electrolyte material to the anode. In this way, not only the thermal expansion coefficient compatibility between the anode and the electrolyte is improved but more importantly an extended region of TPBs is also created.

In state of the art SOFCs, porous NiO/YSZ is the most common anode material. In addition to its low cost (Huang et al., 2003; Horita et al., 2006 and Lee et al., 2006), Ni is reported as a very good current collector (Radovic and Curzio, 2004 and Mori et al., 2003). Moreover, NiO/YSZ provides excellent catalytic activity (Skarmoutsos et al., 2000; Finnerty et al., 1998 and Lu et al., 2004) and good chemical stability (Jiang et al., 2006; Kendall et al., 2002 and Yin et al., 2006) under hydrogen fuelled SOFC operation conditions. In spite of having excellent features as an SOFC anode, Ni-based anode suffers from two major drawbacks when hydrocarbons are used as a fuel. The first problem is the carbon deposition. Since Ni is also known to be an excellent catalyst for

carbon deposition reactions, the deposited carbon covers the active sites of the anode and can deactivate the Ni catalyst (Haldane and Etsell, 2005; Xie et al., 2006 and Wang et al., 2004). Thus, rapid cell degradation can be possibly seen. In the literature, the addition of Ru (Koh et al., 2002), Mo (Zhu and Deevi, 2003 and Sauvet and Irvine, 2004), Au (Zhu and Deevi, 2003) and especially Cu (McIntosh et al., 2002; Gunji et al., 2004 and Pudmich et al., 2000) and CeO₂ (Gunji et al., 2004; Zhu et al., 2006 and Sauvet and Fouletier, 2001) has been suggested to reduce or to avoid the carbon deposition. The second major problem is impurity poisoning. Especially, the small amount of sulfur compounds normally found in many fuels even the odorant level like in the natural gas reacts with nickel to form nickel sulfate. This situation is known as sulfur poisoning and results in the loss of cell performance by blocking the active sites of anode like in the case of carbon deposition (Cheng et al., 2005; Fu et al., 2006 and He et al., 2004). Therefore, the addition of sulfur removing unit to a Ni-based anode-SOFC system driven by hydrocarbon fuels is necessary to avoid sulfur poisoning.

Besides, Ni-based anodes are susceptible to the cyclic reduction and oxidation (redox) typically occurring during SOFC operation independent of the fuel type. Unlike to carbon deposition or impurity poisoning, there has been still no certain solution suggested in the literature to eliminate the redox problem entirely.

1.1.2 Description of redox for Ni-based SOFC anodes

During the course of manufacturing SOFCs, the nickel in the anode primarily stays in the oxide form as NiO. After the system is started and hydrogen is supplied, it is reduced to metallic nickel via the following chemical reaction:



The decrease in volume during the reduction can be calculated using the properties given in Table 2.1 as follows:

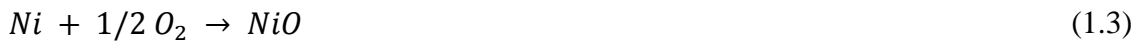
$$\Delta V_{reduction} = \frac{V_{Ni} - V_{NiO}}{V_{NiO}} = -41.7 \% \quad (1.2)$$

Table 2.1. Nickel and nickel oxide molar mass, specific mass and molar volume
(Faes et al., 2009)

	NiO	Ni
Molar mass (g/mole)	74.71	58.71
Density (g/cm ³)	6.60	8.90
Volume (cm ³ /mole)	11.32	6.60

Therefore, the volume occupied by the metallic Ni is ca. 41% less than the volume occupied by the corresponding NiO. As long as fuel is supplied, the nickel in the anode remains in the reduced state as metallic nickel. However, the presence of oxygen on the anode side due to a few of almost inevitable situations during the operation of SOFCs such as seal leakage, fuel supply failure, high fuel utilization or even system shutdown can possibly re-oxidize the metallic Ni. Therefore, the SOFC anode can be certainly expected to experience a number of redox cycles during the lifetime of the system.

The re-oxidation reaction is given below:



The increase in the volume due to re-oxidation can be calculated similarly as follows:

$$\Delta V_{oxidation} = \frac{V_{NiO} - V_{Ni}}{V_{Ni}} = 71.2 \% \quad (1.4)$$

During redox cycles, such volumetric changes because of the formation of Ni-NiO-Ni cause damaged or broken NiO/YSZ network (micro-cracks). The damage accumulates as the redox cycles increases leading to significant performance loss even cell failure. Anode-supported SOFC is especially more susceptible to an anode volume change because its electrolyte is much thinner than the anode support. Therefore it is essential to understand and improve the redox tolerance of the Ni based SOFC anodes in the view point of long term operation without degradation as well as commercialization of the SOFC systems.

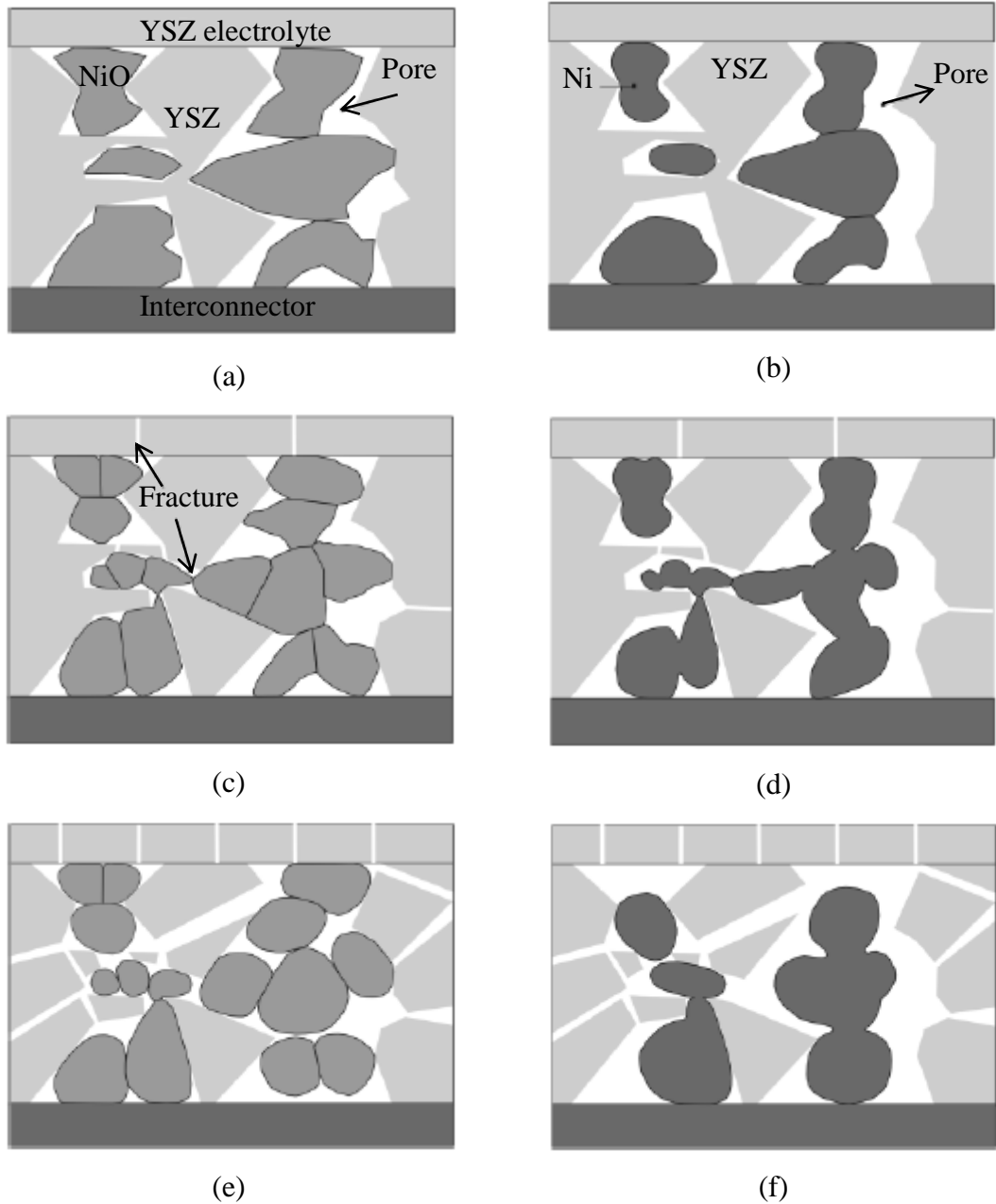


Figure 1.2. Cartoon illustrating the microstructural changes of NiO/YSZ anode upon successive redox steps (adopted from Klemensø and Mogensen, 2007)

The effect of redox cycling on the microstructure of anode supported cell is illustrated Figure 2.1 (Klemensø and Mogensen, 2007). The as-sintered structure is given in Figure 1.2a which has pores and NiO-YSZ networks. After the first reduction the nickel phases alter because of the volumetric reduction and become rounded with particle sintering (Figure 1.2b). Upon the first re-oxidation step, the microstructure does not return to the as-sintered state due to the nickel redistribution that occurred in the reduced state and

the oxide growth as shown in Figure 2.1c. The oxide growth is directly related to the oxidation kinetics and the local pore morphology. When the oxidation kinetics is fast, the Ni/NiO particles divide into two to four particles that grow into the surrounding voids (Klemensø and Mogensen, 2007). If the local porosity is not adequate to accommodate the oxidation expansion, cracks in the YSZ network and YSZ electrolyte can possibly occur. The microstructure of the anode after the second reduced state is illustrated in Figure 1.2d. An improved percolating nickel network is formed due to the redistribution of NiO during the previous oxidation step. These steps defined in Figure 1.2c and Figure 1.2d are repeated upon successive redox cycling. The microstructure after N^{th} re-oxidized and N^{th} reduced state is shown in Figure 1.2e and Figure 1.2f, respectively. The irreversible damage accumulates as the redox cycles increases leading to cell failure due to the fractures in YSZ matrix in the anode, bulk expansion of the anode and cracks in the YSZ electrolyte.

1.2 Thesis Objectives

The anode supported cell design provides both a significant reduction in the operation temperature and an increase in the performance of SOFCs by decreasing the electrolyte resistance due to employing a thin electrolyte of 1-10 μm . However, the cycling reduction and oxidation behavior of the conventional NiO containing anode, which is almost inevitable, limits the operational life and decreases significantly the performance of the SOFC system due to the mechanical damages of the cell during these redox cycles as a result of the volumetric change. Therefore, the redox behavior of the SOFC anode needs to be improved in order to increase the service life of the cell as well as commercialize the SOFC system. There exist numerous studies on the modeling of SOFC at cell and stack levels and the experimental studies on the redox behavior of NiO based SOFC anode, there is very little done for redox modeling of SOFCs together with the experimental investigation. Therefore the objectives of this study can be summarized as;

1. Develop solid oxide fuel cells with various anode porosities and electrolyte thicknesses.
2. Develop a high temperature redox test schedule.

3. Devise an experimental set up in order to determine the performance and the redox behavior of the cells fabricated.
4. Develop a mathematical model to estimate the temperature, current and species distribution in the cell as well as the performance of the cell.
5. Implement a redox model in order to estimate the mechanical damage due to re-oxidation.
6. Combine and solve both models numerically.
7. Compare and validate numerical results with experimental data and improve the mathematical model.
8. Investigate the significant cell fabrication parameters on both the cell performance and the redox behavior of the anode.
9. Develop high redox tolerant SOFC anode.

1.3 Thesis Outline

In the following chapter, literature survey is given covering the redox kinetics, effect of redox cycling and suggested solutions, SOFC thermo-fluid and mechanical modeling. The details of the experimental study and the mathematical modeling are provided in Chapters 3 and 4, respectively. The experimental results are discussed in Chapter 5. The validation of the cell model and the simulation results are presented in Chapter 6. Chapter 7 concludes the present study with a summary of findings and recommendations for further work.

CHAPTER II

LITERATURE SURVEY

2.1 Redox Kinetics

The kinetics of chemical reactions occurring during the reduction of nickel oxide and re-oxidation of nickel are significant in terms of understanding of causes and effects of the redox as well as taking the possible precautions, since they are the origin of the redox. There have been numerous experimental studies in the literature on the redox kinetics of nickel. The main objective of these studies is generally to determine reaction steps and the rate equation through fitting the experimental results to linear, parabolic or exponential kinetic equation.

2.1.1 Reduction of nickel oxide

The reduction of the nickel oxide was addressed as a way to determine the atomic weight of nickel by Baxter and Parsons (1921). However, the first methodical experimental study on the reduction of bulk nickel oxide by hydrogen was reported by Benton and Emmet (1924). The nickel oxide was obtained by the calcination of nickel nitrate and the reduction reaction was expressed in the amount of water produced. The effect of the reduction temperature was also investigated in the study and found to improve the reduction rate. It was concluded that the reduction reaction takes place at the interface between NiO and previously reduced Ni. It was found that reduction needs an induction period during which the nucleation of metallic clusters takes place. The dilution of the reduction hydrogen gas with steam was found to reduce the reduction whereas the induction period was increased with the addition of steam. The similar conclusions have been made by Taylor and Starkweather (1930) although they expressed the reduction in terms of the hydrogen volume consumed during the reduction instead of measuring the water formed.

According to Parravano (1952), the reduction of nickel oxide starts with the adsorption of the hydrogen on the surface, continues with the reaction between the nickel oxide and

adsorbed hydrogen forming water and metallic nickel and ends with the evaporation of the water. The reaction between the nickel oxide and adsorbed hydrogen and the growth of the nickel metallic nuclei formed was found to be driven by the migration of nickel ions and electrons. The rate of the reduction reaction was found to have a linear dependence with the partial pressure of hydrogen. Fouquet et al. (2003) confirmed that the process of NiO reduction starts with the chemisorption of hydrogen at NiO surfaces followed by an induction period until the process of covering of Ni on NiO surfaces begins. Thermogravimetry experiments on bulk NiO powders showed that after the formation of Ni all over the NiO surfaces, the reaction continued at a constant rate. The reduction kinetics was found to be hardly affected by the particle sizes and the sintering temperature of the starting powders.

Avrami (1939, 1940 and 1941) developed a relationship between the fractional conversion of nickel oxide (x_{NiO}) and the overall reduction rate constant (k) at time t with an exponent m as follows:

$$x_{NiO} = 1 - \exp(-kt^m) \quad (2.1)$$

Bandrowski et al. (1962) measured water produced during the reduction and found similar sigmoidal curves. The reduction was explained with a two-step kinetic model. The early stage of the reduction was dominated by the reaction between NiO and hydrogen adsorbed on NiO whereas the final part of the reduction was controlled by the reaction between NiO and hydrogen adsorbed by metallic nickel which was formed from previously reduced NiO. It was found that the first step is proportional to the square root of the hydrogen pressure while the second step was found to be independent of the hydrogen pressure.

Similar sigmoidal curves were found by Utigard et al. (2005). The reduction rate was given by the following equation:

$$\frac{dx_{NiO}}{dt} = k(1 - x_{NiO})^{2/3} \quad (2.2)$$

The rate of the reduction was found to increase with increasing the temperature up to 600 °C with the activation energy of 90 ± 10 kJ/mole. The rate also increased with increasing the hydrogen content and decreasing the particle size. Above 600 °C, the reduction rate was found to decrease up to 900 °C. The decrease in the reduction rate was attributed to grain growth of the nickel formed during reduction and the metallic nickel shell which covers the unreacted NiO limiting the hydrogen penetration. The optical micrograph of a NiO particle partially reduced at 1000 °C confirmed the outer metallic shell but in addition localized metallic bands within the particle was also detected. Rapid agglomeration and sintering of nickel was also observed above 950 °C.

Richardson et al. (2003) studied the hydrogen reduction of porous bulk NiO particles with X-ray diffraction at temperatures between 175-300 °C. They identified and tested fifteen different reduction rate equations previously reported and concluded that only Avrami model (Equation 2.5) and first-order model were consistent with the experiments. They offer the following first order reduction equation where t_0 is the time correction for induction period:

$$x_{NiO} = 1 - \exp[-k(t - t_0)] \quad (2.3)$$

The rate of the reduction was found to increase with the increasing temperature and the activation energy was found to be 85 ± 10 kJ/mole.

2.1.2 Re-oxidation of nickel

Stathis et al. (2002) showed the oxidation of Ni/YSZ cermet anode in air to be logarithmic at temperatures between 550 °C and 650 °C via the following formula:

$$y = k_{log} \log(t) + A \quad (2.4)$$

In the above equation, y stands for the percentage of nickel metal oxidized, t is the duration, k_{log} denotes the logarithmic rate constant and A is a constant. It was found that k_{log} increases with the increasing oxidation temperature. Similar experiments were carried out for humidified argon as an oxidant. However, the bending of the samples,

which was believed to cause possible damage to fuel cell, was reported due to the nonuniform oxidation in case of the humidified argon atmosphere.

Fouquet et al. (2003), on the other hand, compared the oxidation behaviors of Ni powder and die pressed NiO/YSZ anode bulk ceramic after reduction and found that the oxidation of the bulk ceramic is significantly faster than that of Ni powder. The effects of different particle sizes of NiO and YSZ and the sintering temperature of the anode on the re-oxidation were also considered in the study. It was observed that the sintering temperature adversely affect the re-oxidation expansion. The samples sintered at lower temperatures were considered to compensate for the volume change of nickel better since they were less rigid. The anode composed of fine graded NiO and YSZ was found to provide relatively lower oxidation expansion. Similarly, Waldbillig et al. (2005) investigated the oxidation kinetics of tape cast NiO/YSZ at temperatures between 400 °C and 850 °C. Two samples with fine microstructure mirroring the anode functional layer and coarse microstructure mirroring the anode substrate were considered in the study. Both samples experienced no volume change upon reduction. While the coarse structured anode shows no volume change, the volume of the fine structured sample increased by 0.9-2.5 % after re-oxidation different from the conclusion of Fouquet et al. (2003). The fine structured samples were also significantly damaged after oxidation. The oxidation kinetic was found to be parabolic at temperatures lower than 700 °C and the activation energy of the re-oxidation was determined to be 87 kJmol⁻¹. However, at temperatures higher than 700 °C, a divergence from parabolic kinetics was reported for NiO/YSZ. Similar deviations from parabolic kinetics at high temperatures were previously concluded for pure nickel also in several reports (Karmhag et al., 1999; Peraldi et al., 2002 and Ettler et al., 2010).

Tikekar et al. (2006), on the other hand, showed that the re-oxidation kinetic was independent of temperature and parabolic indicating a diffusion controlled mechanism. They studied the oxidation kinetics of fully reduced NiO/YSZ (wt. % 60:40) rectangular bars which was fully dense before the reduction. The re-oxidation studies were carried out in air over a temperature range between 650 °C and 800 °C. The square of the re-oxidized layer thickness was found to have a linear relation with the re-oxidation time.

This behavior was attributed to slow gas diffusion as a result of the decreasing porosity that remains when nickel re-oxidizes.

2.2 Effects of Redox Cycling: Experimental Observations

Since NiO/YSZ is the common SOFC anode material and the anode supported structure is more susceptible to redox cycling, researchers have mostly studied the redox behavior of NiO/YSZ anode supported cells. Effects of redox cycling on the structure, physical/mechanical/electrical properties and the performance of the anode/cell were investigated through various analyses including dilatometry, electron microscopy, thermal gravity and impedance. Redox cycling was found to result in damaged anode network (Hatae et al., 2009; Iwanschitz et al., 2010 and Dikwal et al., 2008), nickel agglomeration (Mosch et al., 2007; Pihlatie et al., 2009 and Laurencin et al., 2010), warped structure (Ettler et al., 2007; Sarantaridis et al., 2008 and Young and Birss, 2011) and cracks (Hagen et al., 2006; Waldbillig et al., 2007 and Smith et al., 2011).

Sumi et al. (2010) studied the microstructural and electrochemical characteristics of NiO/YSZ anode during redox cycles. The cell performance was found to deteriorate just after the first redox cycle as a result of the increase in the polarization resistance of the anode. SEM investigations showed that nickel particles became finer and more complicated in shape. In spite of this structural change, the length of TPB was found to decrease from 2.49 to 2.11 $\mu\text{m}/\mu\text{m}^3$ after four redox cycles at 800 °C. Thus, the increase in the anode polarization resistance was believed due to decrease in the length of TPB. After the 10th redox cycle, many large micro-cracks were observed in the anode structure leading to breakage of Ni and YSZ network. As a result of this, the ohmic loss of the anode was also found to increase. Similar results were concluded by Faes et al. (2011) who investigated the redox behavior of large size (48 cm² active cathode area) NiO/YSZ anode supported cells. It was found that OCV decreased by 0.1 % per redox cycle over a total of 40 cycles. Impedance measurements showed that the degradation in the cell performance was due to the increase in both ohmic and polarization resistance caused by nickel phase coarsening which lead to decrease both the number of three phase boundaries and electrical conductivity.

Mosch et al. (2007) investigated the redox stability of NiO/YSZ anodes for ScSZ electrolyte supported SOFCs with an LSM/YSZ cathode. Morphology and electrochemical performance of the cell after 6 redox cycle were determined under 0.7 V operating voltage at 850 °C. The increase in both ohmic and anode polarization resistance were detected and considered as main reasons for the cell degradation. SEM images confirmed that the anode did not recover the initial morphology after redox cycling at 850 °C causing performance degradation. Klemensø and Mogensen (2007) investigated the redox behavior of NiO/YSZ by electrical characterization. The degradation of the conductivity was reported after redox cycling. The decrease in the conductivity was believed to reflect Ni coarsening and agglomeration which reduces the number of electrical pathways. The microstructural changes of Ni/NiO during redox cycles were found to weaken the YSZ network. The degradation was observed to depend on the composition and porosity of the sample. However, when the as-sintered porosity was below 8 % porosity dependency was not observed.

Sarantaridis et al. (2008) studied changes in physical and mechanical properties of Ni-YSZ composites caused by redox cycling at 900 °C. It was shown that reduction results in reversible changes in elastic modulus thus no significant damage in YSZ network is observed. However, the expansion on oxidation was detected and found to be irreversible. Microstructural investigations reveal that the main reason of the expansion on oxidation is the formation of the closed porosity which is caused by both partial sintering of Ni and intrinsic oxidation properties. In a similar study by Klemensø et al. (2006), in situ microstructural changes in NiO/3YSZ anode during redox cycling at 850 °C was observed by ESEM. The reduction of NiO resulted in increased porosity and shrinkage as well as rounding of nickel particle. Re-oxidation, on the other hand, caused redistribution of the NiO phase. The irreversible morphology of oxide particles was found to be temperature dependent indicating that it is directly related to the oxidation kinetics. NiO particles were divided into 2-4 particles during rapid oxidation whereas an external oxide layer was observed around the individual particle for slower oxidation. Jeangros et al. (2010) improved the study of Klemensø et al. (2006) by adding theoretical calculations. They studied the redox stability of NiO/3YSZ/YSZ (wt. % 55-22.5-22.5) anode supported half cells with YSZ electrolyte in situ by TEM in combination with density functional theory calculations. It was found that the transfer of

oxygen from NiO to YSZ is the driving force for the reduction reaction by the creation of hydrogen adsorption sites. The microstructural change due to the redox cycling was found to be irreversible resulted from the expansion of nickel and the creation of stress in the YSZ phase. Imbalanced mass transport between outward Ni diffusion and inward oxygen diffusion in oxidizing Ni grains accounted for the redox instability of the anode. It was suggested that it is possible to improve the redox stability of the anode by microstructural modifications such that dispersed porosity after sintering accommodates redox expansion. If the Ni grains can expand into the porosity, the formation of cracks in the electrolyte can be delayed or avoided due to reduced stress on the YSZ electrolyte.

Young and Birss (2011) showed that the full oxidation of Ni/YSZ anode supported cells at high temperatures ($>700\text{ }^{\circ}\text{C}$) leads to larger quantity and wider cracks in the electrolyte than those at lower temperatures. After only 2 full redox cycles at 700, 800 and 900 $^{\circ}\text{C}$, the cracks in the YSZ electrolytes were detected. This was attributed to non-homogenous Ni oxidation in the anode correlated by TGA analysis which indicated that Ni oxidation is controlled by diffusion and there exist both Ni/NiO and O_2 gradients in the anode layer. SEM investigations confirmed that Ni oxidation is non-homogenous when performed at high temperature or low O_2 partial pressures. Both cases led to outer regions of the anode become fully oxidized whereas the inner regions remain metallic form. It was concluded that as Ni continues to be oxidized, the continued volume expansion due to NiO formation occurs towards only to the electrolyte resulting in warping and finally cracking the electrolyte.

Waldbillig et al. (2005) studied the redox behavior of NiO/YSZ anode supported SOFC by electrochemical and microstructural characterization. The effect of redox cycle duration was also investigated. Electrochemical tests showed that the cell performance decreases after each redox cycle and the performance loss is higher especially for redox times greater than 1 h. The similar behavior was seen in the OCV measurement. The OCV was slightly decreased after longer redox cycles indicating the electrolyte fracture. SEM and TEM images confirmed that the microstructure is significantly changed after redox cycling leading to the crack in the electrolyte.

Zhang et al. (2005) investigated the effect of redox cycling on a NiO/YSZ (50:50 wt. %) anode prepared by tape casting with dimension of 80 mm x 8 mm x 0.8 mm. It was shown that the re-oxidation temperature has a great impact on the anode microstructure. Redox cycling at 800 °C resulted in a continuous decrease in the primary crystallite size of NiO and high dispersion of the Ni particles. NiO aggregates were also found to grow continuously. However, redox cycling below 600 °C did not lead to particle size alteration and the conversion of Ni to NiO was found to decrease.

Fouquet et al. (2003) showed that the kinetics of redox for Ni/YSZ anode cermets. The effects of particle size, particle size ratio and sintering temperatures on redox were investigated. The increase in the polarization resistance due to cyclic reduction and oxidation was reported and ascribed to the formation of micro-cracks in the anode. The results showed that the reduction causes no length change due to stabilizing role of YSZ whereas re-oxidation resulted in an increase in the length of the samples depending on the microstructure. The samples sintered below 1300 °C showed less expansion and were found to withstand redox cycles much better than those sintered at high temperatures. It was found that it is possible to decrease the expansion due to re-oxidation by reducing the NiO particle size and using a NiO/YSZ particle size ratio of 3:2.

Pihlatie et al. (2009) tested the dimensional behavior of NiO/YSZ anode during redox cycling in a dilatometry. The effects of humidity and redox temperature were investigated. It was shown that the degree of reversibility of the redox strain decreases with increasing temperature. In addition, the temperature of re-oxidation played a significant role. The re-oxidation strain was measured as about 1 % when re-oxidation was carried out at 850 or 1000 °C whereas it was between 0.31 and 0.36 % when the re-oxidation was performed at 600 or 750 °C. Moreover, it was found that at 850°C, 6 % steam and very high partial pressure ratio of steam and hydrogen is detrimental for redox stability.

Pihlatie et al. (2009) also measured the mechanical properties of Ni/YSZ and NiO/YSZ anode depending on the redox cycling. Mechanical degradation due to redox cycling was observed and a decrease in both Young's modulus and stiffness was reported. It

was found that the mechanical degradation started at about 0.5 % dL/L_o strain and the samples lost integrity when the redox strain exceeded 2.5 %.

Faes et al. (2010) investigated the effect of redox cycles on curvature and strength of half cells comprised NiO/YSZ anode support, NiO/YSZ anode functional layer and YSZ electrolyte. Tests showed that the cell temperature increases with redox cycles due to creep in the anode structure as a result of the nickel oxidation. It was found that higher cycle temperature favors the creep resulting in higher curvature. The effect of redox treatment on the curvature was lowered when the initial porosity of the anode was higher. This was attributed to more freely nickel re-oxidation in porous microstructure. It was shown that the strength of the cell increased with the increasing reduction temperature, however, the strength of the cell reduced after five redox cycles.

Dikwal et al. (2008) and Pusz et al. (2007) focused on the micro-tubular SOFCs. Dikwal et al. (2008) investigated the redox tolerance of Ni-YSZ anode supported micro-tubular SOFC at 800 °C in partial reduction and oxidation conditions. It was found that the redox cycling causes significant degradation in the microstructure of micro-tubular SOFC. Two degradation modes due to redox cycling were determined: i) micro-crack formation in anode and ii) delamination at anode/electrolyte interface. Moreover, 3 % performance degradation per cycle was detected and it was attributed to stress accumulation during redox cycling. Pusz et al. (2007), on the other hand, investigated the effect of the particle size on the redox behavior of micro-tubular SOFC anodes. NiO/YSZ tubular anodes were fabricated using fine and coarse particle size powders. The fracture strength of micro-tubular SOFC anodes was also measured after several redox cycles. The mechanical tests showed that the mechanical strength of the fine-structured anode was increased by 77 % after three redox cycles whereas redox cycling resulted in decrease in the mechanical stability of the coarse-structured anode. The electrochemical testing of the coarse-structured anode was impossible since it did not recover after the first redox cycle at 800°C. The cell fabricated using fine anode powder, on the other hand; showed 40 % performance improvement. The increase in the cell performance was attributed to better adhesion between the anode and Ni current collector.

Laurencin et al. (2010) studied the impact of redox cycles on the performance of electrolyte supported SOFC by impedance spectroscopy and SEM. The cell comprised 3 mol % yttria stabilized zirconia electrolyte (3YSZ) support, 15 % porous YSZ interlayer between NiO/YSZ anode and the electrolyte and LSM cathode. A global degradation of the cell performance was noticed after several redox cycles at 800 °C. The performance degradation was due to the increase in the polarization resistance indicating bulk-deterioration of the NiO/YSZ anode. SEM investigations confirmed the electrochemical results. It was found that the anode microstructure was strongly impacted (densification and coarsening) by the redox cycles although no delamination was observed. The ohmic resistance, on the other hand, was not impacted by redox cycling confirming that no electrode delamination occurred.

Blennow et al. (2011) developed Fe-Cr (22 % Cr based) metal supported SOFC and investigated the redox behavior of the cell. The cell included Fe-Cr based metal support, metal-YSZ anode backbone, Sc₂O₃ and Y₂O₃ co-doped ZrO₂ electrolyte, LSCF/GDC cathode and LSC cathode contact layer. The metal support, the anode backbone and the electrolyte were fabricated by tape casting and laminated. Then the infiltration solution of 10 wt. % nickel and GDC were impregnated into the anode backbone. Finally, cathode and cathode contact layers were screen printed. The cell was subjected to 100 redox cycles at 800 °C with 1 minute (cycle 1-50) and 10 minutes (cycle 51-100) of re-oxidation periods. The metal supported cell showed a promising redox tolerance without significant degradation or failure. The redox stability of the cell was attributed to the small amount of Ni in the structure acting only as a catalyst. Thus, the re-oxidation did not result in mechanical failure or nickel agglomeration. However, the redox periods applied in this paper seems to be very short when compared the other studies. The short re-oxidation period may keep anode from fully oxidation thus the volumetric changes during re-oxidation may be tolerated.

Iwanschitz et al. (2010) compared the degradation behavior of cells with Ni/YSZ and Ni/GDC40 (40 % mol gadolinium doped ceria) anodes upon redox cycles by impedance spectroscopy for electrolyte supported SOFC. After eight redox cycles (30 min. in H₂ and 30 min. in air) at 950°C, the cell with Ni/YSZ anode showed an increase in the polarization resistance whereas increase in both ohmic and polarization resistance were

detected for the cell with Ni/GDC40 anode. Microstructural investigations showed that Ni agglomeration and damaged anode network occur due to redox cycling in both cells leading to increase in the cell resistance.

Fujita et al. (2009), on the other hand, studied the stack scale redox stability for segmented-in-series solid oxide fuel cells (SIS-SOFCs). The stack of the SIS-SOFC included 16 flattened tubes of Ni-doped MgO based porous substrate supported cells. The stack performance was found to degrade approximately 0.15 % per cycle. The high redox tolerance was attributed to that the porous substrate acted as an oxidation barrier preventing the NiO/YSZ anode from full oxidation. Although the anode was partially oxidized, the amount of the microstructural change was found to be smaller compared to that detected in a typical anode supported cells.

The electrochemical re-oxidation of the nickel is also possible during SOFC operation especially when the overpotential is very high under high fuel utilization just like the case of fuel starvation. Furthermore, electrochemical oxidation has a significant advantage that it can control the degree of oxidation (Mosh et al., 2007). While nickel is re-oxidized chemically by oxygen gas in the case of the chemical oxidation, oxygen ions re-oxidize the nickel during electrochemical oxidation via the following reaction:



However, there are a few reports in the literature on the effects of electrochemical oxidation. Among them, Sarantaridis et al. (2005) compared the effects of these oxidation modes on NiO/YSZ anode supported cells. The critical degree of oxidation without irreversible mechanical damage was also investigated for both modes. It was found that the cell oxidized chemically in air showed electrolyte cracking after oxidation of 50 % Ni. On the other hand, cells oxidized electrochemically suffered by substrate cracking after only ca. 5% of the Ni oxidation. It was attributed to non-uniform oxidation caused by the electrochemical oxidation.

Hatae et al. (2009) investigated the initial damage before cell failure by redox cycles. In order to prevent the cell from complete failure, partial and electrochemical oxidation

was used. The anode supported planar cell comprised NiO/YSZ anode support, NiO/3ScSZ anode functional layer, YSZ electrolyte, SDC interlayer and LSCF cathode. However, there was an active cell area where the cathode was printed on the electrolyte and an inactive cell area without the cathode. The cell performance was found to decrease after electrochemical and partial oxidation without a decrease in the open circuit potential. Microstructural investigations showed that there exist micro-cracks between ScSZ and Ni particles in the active cell area whereas there was no micro-crack observed in the inactive cell area. Only Ni particles near the electrolyte and in the active cell area were found to be oxidized in the electrochemical oxidation. It was concluded that, the micro-cracks in the anode functional layer were the initial damage causing the degradation of the cell performance.

Hatae et al. (2009) also studied the microstructural changes in the NiO/YSZ anode during the electrochemical oxidation under 25 mAcm^{-2} and 250 mAcm^{-2} current densities at 800°C . An anode supported single cell comprising NiO/YSZ anode support, NiO/ScSZ anode functional layer, YSZ electrolyte, SDC interlayer and LSCF cathode was fabricated. The redox treatment was performed after reduction by purging pure N_2 and air to the anode and cathode side, respectively. The microstructural investigations of the cell after three redox cycles at 25 mAcm^{-2} showed that there exist micro-cracks in the anode located between Ni and ScSZ particles but the change in the morphology of both Ni and anode was found very small. On the other hand, both micro-cracks and delamination at the interface between anode and the electrolyte layer were determined from the cell oxidized at 250 mAcm^{-2} . In addition, the Ni particles divided into smaller ones. The change in the microstructure was attributed to the rapid electrochemical oxidation because of the high operation current density of 250 mAcm^{-2} . Both cells showed performance loss due to damaged anode network and interface between the anode and the electrolyte.

The differences in the destruction modes caused by two different degrees of electrochemical oxidation were investigated by the same research group (Hatae et al., 2010). The same cells were fabricated and then subjected to the same electrochemical oxidation as presented in the previous study. The degree of oxidation in the anode layers was controlled by the amount of the total charge during the electrochemical oxidation

process. In the cell which was oxidized about 0.6 % and re-reduced for 17 times, the delamination between the anode and the electrolyte layer was detected. It is attributed to the damaged anode network accumulated as the redox cycles increased which finally resulted cracks in the electrolyte. On the other hand, a crack was suddenly occurred in the cell oxidized about 31 % and re-reduced only for 2 times. The results showed that the degree of oxidation has a significant impact on the mechanical properties of the cell.

2.3 Solutions to Redox Problem

It is possible to categorize the solutions suggested in the literature to redox problems of nickel containing SOFC anodes into material/component and system solutions as reported by Wood et al. (2006). The material or component solutions are generally related to the microstructure and the type of the anode materials whereas system solutions may include cell reversal, purge gas or steam purging. However, system solutions may lead to high system cost since the extra electricity or the installation/integration of new system component is required.

Wood et al. (2006) suggested that steam can be used to produce reducing hydrogen gas ($\text{H}_2\text{O} + \text{Ni}_\text{s} \rightarrow \text{NiO}_\text{s} + \text{H}_2$) by means of a reformer or nickel-containing bed until the stack is at a lower temperature. Preliminary test results showed that in case of the steam purge the cumulative voltage degradation at 0.74 Acm^{-2} current density was around 2 % for $10 \times 10 \text{ cm}$ cells whereas it was 11 % when air is used instead of the steam. Mechanical test showed that under a load of 25 kg fine structured NiO/YSZ anode functional layer showed around 2.5 % displacement during re-oxidation whereas that of coarse structured NiO/YSZ anode was only 0.2 % and almost constant for 60 h of re-oxidation period. The degradation in the performance was attributed to this dimensional change of the anode functional layer.

Waldbillig et al. (2005) found that the amount of volume expansion in the course of re-oxidation can be lowered by decreasing the oxidation temperature or reducing the Ni content in the anode. Waldbillig et al. (2007) also showed that it is possible to enhance

the redox tolerance of NiO/YSZ based anode supported SOFCs by microstructural modification. In this aspect, two modifications were made: anode functional layer was functionally graded and an oxidation barrier was added to the bottom of the anode support. TMA analysis revealed that when the NiO content in the anode functional layer is between 30-57 wt. % it expands less than the standard 57 wt. % NiO samples. Since the anode functional layer should have a sufficient amount of Ni to satisfy the required electronic conductivity, the number of the triple phase boundaries and porosity, it was decided to grade Ni content in the anode functional layer functionally such that Ni content is high near the anode support and lower near the electrolyte. It was found that grading the AFL with 45 wt % NiO enhanced the redox tolerance of the cell by about 28 %. The application of the oxidation barrier to the bottom of the cell was also found to improve the redox tolerance of the cell. The redox tolerance of the cell having no oxidation barrier was increased by 37 % when an oxidation barrier of 57 wt. % NiO and 43 wt. % YSZ was applied. The improvement of the redox tolerance with an oxidation barrier was attributed to that it restricts the rate that oxygen penetrates into the cell since it oxidizes rapidly and densifies in oxidizing conditions.

Busawon et al. (2008), on the other hand, proposed Ni infiltration as a possible solution to the redox problem of SOFC anodes. 0.3 M solution of $\text{Ni}(\text{Ni}_3)_2 \cdot 6\text{H}_2\text{O}$ in ethanol is infiltrated to the porous YSZ fabricated by dry pressing. After one redox cycle, no dimensional change was observed for the samples having 12-16 wt. % Ni. The dimensional stability was attributed to the microstructure produced by infiltration which allows Ni more free zones to expand during oxidation and to contract during reduction. However, the electrical measurements showed that the conductivity of the cermet dropped by 20 % after one redox cycle. Microstructural investigation revealed that Ni does not form a continuous network restricting the interconnectivity and agglomeration of Ni occurred resulting in lower conductivity.

Vedasri et al. (2010) investigated the cooling rate during air exposure as a possible solution to mechanical failure of Ni based anode supported cells due to redox cycling. When the cooling rate < 3 °C/min during air exposure, cracks in the electrolyte due to the volumetric change caused by oxidation were reported. This was attributed to that the anode has available and sufficient time for substantial NiO formation due to low cooling

rates. On the other hand, the cooling rates >3 °C/min significantly slowed down the oxidation of Ni due to partial oxidation. It was seen that more extensive Ni oxidation occurs in the outer regions of the anode than that of closer to the electrolyte layer preventing electrolyte from cracking due to reduced volumetric change of the anode functional layer. It was concluded that the electrolyte can resist cracking when the nearby Ni particles are prevented from oxidizing to an extent of more than 65%.

Another approach in the literature to improve the redox stability of SOFC anodes is to develop new anode materials as an alternative to conventional Ni-based anode. However, relatively low cell performances were reported with new anodes. In this aspect, doped SrTiO₃ is the most common anode material studied. Ma et al. (2010), for example, developed Y doped SrTiO₃ anode material and investigated the redox stability. The cells based on 1.2 mm Sr_{0.895}Y_{0.07}TiO₃ (SYT) anode support, 3 μm (Sr_{0.89}Y_{0.07})_{0.91}TiO_{2.91} / YSZ (2:1 in volume, SYT2–YSZ) anode functional layer, 14 μm YSZ electrolyte, 1 μm Ce_{0.8}Gd_{0.2}O_{1.9} interlayer and 50 μm La_{0.6}Sr_{0.4}CoO_{3-δ} (LSC) were fabricated. 3 wt. % Ni in the form of Ni nitrate was also infiltrated into both anode layers via wet impregnation. The cell having 5x5 cm² active area was then subjected to redox cycles (10 min. in H₂ and 10 min. in air at 750°C) and the cell performance was measured at 750°C as a function of the number of redox cycles. After 200 redox cycles, OCV decreased by only 1.3 % although Ti was found to diffuse from anode to electrolyte. On the other hand, in spite of the slow redox kinetics of SYT, the cell performance decreased by 35 % (from ~500 mWcm⁻² to ~325 mWcm⁻²). It was suggested that the continuous decrease in the performance can be prevented by prolonging the reducing time during the redox cycles.

Smith et al. (2011) investigated Ta doped SrTiO₃ (STT)/YSZ as a potential SOFC anode material. SrTa_xTi_{1-x}O₃ for x=0.01, 0.05 and 0.1 was studied. Porous STT/YSZ composites were prepared by casting slurries. The dried slurries were then cut into rectangular bars and sintered. The reduction was performed at 1400 °C for 10 h in H₂ whereas the oxidation of the sample was carried out in air at various temperatures for 5 h. The conductivity measurement showed that lower dopant concentrations results in higher redox stable conductivities. Especially, the samples doped with 1 % Ta exhibited almost constant conductivity of 0.9 S/cm at all oxidation temperatures studied.

Blennow et al. (2008), on the other hand, developed Nb doped SrTiO₃/YSZ anode material. The defect and electrical transport properties were investigated. The electrochemical properties by means of an electrochemical impedance spectroscopy and redox behavior of Sr_{0.94}Ti_{0.9}Nb_{0.1}O₃ were also investigated (Blennow et al., 2009). Although the redox cycling at 850°C showed that Nb doped SrTiO₃/YSZ anode promising redox stability, the catalytic activity of the anode was found insufficient for hydrogen oxidation. Thus, it was suggested that titanates can be used as an anode material as long as another material providing the essential catalytic activity is employed.

Gross et al. (2009) developed SrNb_xTi_{1-x}O₃ (SNT)-YSZ anode material for x = 0.01, 0.05 and 0.2. The conductivity of dense SNT for x = 0.2 was measured as 90 S/cm and found to independent of temperature whereas those for x = 0.01 and x = 0.05 was measured as 10 and 20 S/cm, respectively indicating that increasing the doped content tends to increase the conductivity. However, when the redox cycling was considered, using higher dopant levels showed no benefit. SNT/YSZ composite showed 1 S/cm conductivity for x = 0.01 and x = 0.05 while it was 0.5 S/cm for x = 0.2. The cell composed of 1 wt % Pd and 3 wt. % CeO₂ infiltrated SNT/YSZ anode provided 415 mW/cm² peak power density at 800 °C.

Bastidas et al. (2006) developed a redox stable symmetrical solid oxide fuel cell using (La_{0.75}Sr_{0.25})Cr_{0.5}Mn_{0.5}O₃ (LSCM) for both electrodes. Half cells composed of 200 μm thick yttria-stabilized zirconia (YSZ) electrolyte support coated with 50 μm LSCM electrode having 1cm² active area were fabricated. Half cells were then subjected to five redox cycles at 900 °C in humidified hydrogen, in reformat and in humidified oxygen sequentially. The polarization measurements at 900 °C in both hydrogen and oxygen atmospheres indicated that there is little evidence for degradation on cycling since only slight changes in electrode resistance are detected. Then a symmetrical fuel cell was manufactured by applying 50 μm thick LSCM to both sides of a 200 μm thick YSZ electrolyte with 1cm² active area. The cell produced 300 mWcm⁻² peak power density at 900 °C under H₂ fuel.

Ouweltjes et al. (2009) developed a reduced Ni content $\text{La}_{0.9}\text{Mn}_{1-x}\text{M}_x\text{O}_{3-\delta}$ ($\text{M}=\text{Ni}, \text{Fe}, 0 < x < 0.2$) anode material for high redox stability and performance. Conductivity measurements showed that among these oxides, $\text{La}_{0.9}\text{Mn}_{0.8}\text{Ni}_{0.2}\text{O}_{3-\delta}$ perovskite has the highest electrical conductivity. During the redox cycling at 850 °C, the cell with bilayered anode composed of 80 wt. % GDC infiltrated with 20 % Ni anode functional layer and an anode contact layer comprising 70 wt. % Ni and 30 wt. % $\text{La}_{0.9}\text{Mn}_{0.8}\text{Ni}_{0.2}\text{O}_{3-\delta}$ showed the highest redox tolerance. The current density of the cell at 0.7 V degraded 10 % after 50 redox cycles and 23 % after 100 redox cycles. Microstructural observations confirmed that although the anode includes reduced Ni content, the main reason behind the cell degradation is the nickel agglomeration.

2.4 SOFC Mechanical Modeling: Thermal Stress and Redox

During the operation of solid oxide fuel cells (SOFCs), nonhomogeneous electrochemical reactions in both anode and cathode electrodes, boundary conditions and thermal cycling may lead to a temperature gradient in the cell which may result in the development of thermal stresses due to various thermal expansion behaviors of the cell components finally causing the failure of the cell. Since the working temperature of SOFC is very high (600°C-1000°C), it is difficult to measure the temperature and stress distributions during the operation. Therefore, most of the studies investigating the thermal stress and temperature distribution are the estimations based on the numerical analyses of the mathematical models developed. The mathematical models are usually validated by comparing with the experimental performance curves and then parametric numerical studies are performed. The numerical studies, in general, showed that the flow configuration and the operating current density are the main factors affecting the temperature distribution thus the stress distribution in a SOFC short stack and multiple cells stack.

Although there exist some studies (Selçuk et al., 2001; Montross et al., 2002; Yakabe et al., 2004a, Yakabe et al., 2004b and Fischer et al., 2005) focused on the residual stresses for a certain temperature change without considering the temperature gradients in the cell during the operation, using the temperature field within the SOFC predicted from the thermo-fluid model by finite volume analysis as an input to a finite element analysis

seems to be the most common way in the literature to calculate the thermal stresses numerically. Among them Yakabe et al. (2001) firstly built a three-dimensional thermo-fluid mathematical model for a single planar SOFC to predict the temperature distribution. The thickness of the electrolyte, anode and cathode were 0.1 mm, 0.1 mm and 0.15mm, respectively. The interconnectors were also included in the model geometry. However, numerical calculations were performed for a single channel in the middle of the single cell which is located at the center of the stack in order to reduce the calculation time. Thus, all boundaries were assumed to be adiabatic. Secondly, using the calculated temperature distribution by applying finite volume method to the thermo-fluid model, the stress distribution was estimated using finite element method for both co- and counter-flow configurations. The calculated temperature difference for the counter-flow case was about 320 °C and the maximum temperature was almost at the middle of the cell. On the other hand, co-flow configuration showed about 290 °C temperature difference and the regions close to outlets were found to have the highest temperature. Thus, the co-flow configuration was reported to be advantageous to mitigate the steep temperature gradient, and hence to reduce the internal stress. The same approach of using the temperature field within the SOFC predicted from the thermo-fluid model as an input to a finite element analysis was also used by Selimovic et al. (2005). However, they improved the Yakabe's study (2001) by adding transient stress analysis in addition to steady state model. The effects of interconnector material (ceramic and metallic), flow configurations (co-, counter- and cross-flow) and operating voltage on the steady state thermal gradient and thermal stress were also numerically investigated. However, thermal stress analysis was numerically calculated for only three layered cell structure. The predicted maximum principle stress in case of metallic interconnector was found to be reduced significantly which was explained by the high thermal conductivity of the metallic interconnector. Although the counter-flow case showed the highest cell performance, the co-flow configuration provided the lowest thermal stress as concluded by Yakabe et al. (2001). The maximum principal stress was found to vary exponentially with the operation voltage. The operation at lower voltages resulted in higher stresses due to the higher temperature gradient as a result of the higher local current. In the transient analysis, on the other hand, three different operation modes were considered i.e. heat-up, start-up and shut-down. However, the transient term was added to the energy equation only. The heating during heat-up and

the cooling during shut-down were modeled by feeding hot and cold air streams, respectively. The temperature of the air inlet was set to a temperature 100 K higher than the minimum solid temperature in the cell during heat-up, while it was set to a temperature 100 K lower than the maximum solid temperature in the cell for shut-down process. It was shown that the thermal stress occurring during both heat-up and shut-down with the corresponding heating and cooling regimes selected does not exceed the material limits of the cell components.

Chiang et al. (2008) also applied the same methodology to a single anode supported SOFC. The numerical results revealed that lower operating voltage results in a higher current and power densities and yields a higher temperature field and higher temperature gradients. Thus, thermal stresses are much higher at a lower operating voltage which is in good agreement with the result of Yakabe's (2001) and Selimovic's study (2005). In addition to this, the effect of the inlet temperature on the stress distribution was also numerically investigated. The preheating of the inlet gases was found to be beneficial to minimize the temperature gradient hence to reduce the thermal stress. In the following study by the same group (Chiang et al., 2010), the effects of a uniform load to the upper interconnect (0.5-5 kg) and the anode layer porosity (0.2-0.5) on the thermal stresses were numerically investigated. It was found that the maximum principal stress increases slightly with an increasing load indicating that the stress is mainly dominated by the thermal gradient. The cell performance was found to increase with the anode porosity. Thus, the maximum principal stress is higher at low anode porosities at all operating voltage simulated.

Lin et al. (2007), on the other hand, performed thermal stress analysis of a three-cell stack using the same methodology. Like the study by Selimovic et al. (2005), the thermal stress analyses were performed at shut-down, start-up and steady state stages, after importing the transient and steady state temperature profiles obtained from thermo-fluid model previously developed (Chyou et al., 2005) into the finite element model. It was concluded the most critical element in the stack is the glass ceramic sealant at operation temperature. In addition, at shut-down and steady state stages, localized plastic deformations in the interconnectors were reported. They later included the effects of the applied assembly load to ensure the electrical contact and the sealing

design on the thermal stress distribution for three-cell SOFC stack (Lin et al., 2009). It was shown that the applied assembly load between 0.06 MPa and 0.6 MPa can eliminate the bending deformation of the cell. However, the further increase in the assembly load was found to be dangerous for both mica and glass ceramic sealants. The replacement of the glass ceramic sealant by a mica seal gasket was considered to be favorable at room temperature but found to significantly increase the critical stress in the cell at the operating temperature.

Nakajo et al. (Nakajo et al., 2009a; Nakajo et al., 2009b; Nakajo et al., 2012a and Nakajo et al., 2012b) improved the usual method by adding the probability of failure by Weibull analysis for the cell and stack components. Nakajo et al. (2009a) firstly focused on the probability of failure of the cell at room and operating temperature. The flow configuration (co- and counter-flow) and the reformer type (partial oxidation and internal steam reforming) were also considered in the study. They showed that when the thermal stress is the issue, thermal partial oxidation with co-flow configuration is favorable. On the other, the opposite was found to be more favorable for the cell performance issues. In the following part (Nakajo et al., 2009b), they investigated the occurrences of loss of gas-tightness in the compressive gaskets and/or electrical contact in the gas diffusion layer. Besides, the thermal buckling possibilities were also analyzed with a simple separate model. The analyses revealed in spite of the plastic strain, the contact was prevented between the cell and gas diffusion layer. However, a large decrease of contact pressure was reported in the gasket indicating gas leakage. Especially, when no load was applied to the upper interconnector, almost complete release occurred at some particular locations. In addition, the buckling of the metallic interconnectors was considered to be likely and possibly harmful phenomenon. In the recent studies of the same group (Nakajo et al., 2012a and Nakajo et al., 2012b), the modeling of the effect of operating conditions and design alternatives on the reliability and the modeling of mechanical failure during aging and cycling were presented, respectively.

The other but the most significant mechanism that creates large amount of stresses in the SOFC is the continuous reduction and oxidation of nickel in the anode layer which is known as redox cycling. However, there can be found very little efforts in the

literature on the redox modeling of nickel based SOFC anode. Clague et al. (2012), for example, considered only the reduction part in their stress model by considering the material properties change due to the chemical reduction reaction. They developed a finite element model to predict the stress in ceramic components of an anode supported SOFC for an idealized operating cycle presenting cool-down from sintering, heat-up, reduction, operating and cool-down from the operation temperature of 800 °C. The change in the anode material properties due to the reduction was introduced by defining porosity dependent material properties. The porosity of the unreduced anode and reduced anode was assumed as 20 % and 40 %, respectively and the corresponding values for elastic modulus and Poisson's ratios obtained from the literature for a temperature of interest were used. The numerical results showed a reduction in peak stress of all ceramic cell components after reduction of nickel oxide. Especially, 15 % reduction in the peak stress of the cathode layer was reported when the anode undergoes chemical reduction.

Similar findings were also reported by Laurencin et al. (2008) who presented a modeling study to determine the strain range where mechanical damage occurs for both anode and electrolyte supported cells composed of standard materials (NiO-YSZ/YSZ, LSM). They simulated the reduction such that it causes only the decrease in the anode elastic constants as later considered by Clague et al. (2012). The first re-oxidation step was also analyzed in the study by imposing an oxidation strain to the anode layer with introducing a thermal expansion for the anode layer only induced by a fictive cell heating. However, the effect of the temperature gradient due to inhomogeneous current density distribution during the cell operation on the cell stress state was not investigated in this study. Like concluded by Clague et al. (2012), the reduction of nickel oxide in the anode layer was found to allow relaxing stress level in the cell. It was concluded that to avoid cathode damage the anodic strain should be less than 0.05-0.09 % whereas the electrolyte fracture is likely to occur for 0.12-0.15 % anodic strain. For the electrolyte supported cell, on the other hand, the re-oxidation was found to cause delamination of the electrolyte/anode interface unless the anodic strain is less than 0.30-0.35 percent.

Laurencin et al. (2012) improved their previous model (Laurencin et al., 2008) by acquiring the data for the simulations from the experimental oxidation kinetics

measurements performed at three different temperatures but still only one redox cycle was investigated. In addition to the changes in the anode dimensions and Young's modulus of anode, the oxidation rate as a function of degree of oxidation obtained from the experimental work was directly implemented in the model. At 800 °C, for example, the oxidation strain was measured as 0.97 % after the full oxidation. It was found that the electrolyte cracking is expected to start when degree of re-oxidation is 59 % at 600 °C while it is 66 % at 800 °C. However, the critical time of re-oxidation tends to decrease with the increasing temperature. This behavior was attributed to the improved oxidation reaction kinetics at high temperatures. Pihlatie et al. (2010) simulated seven experimental cases of high temperature redox dilatometry for NiO/YSZ anode but again only one cycle was modeled. The cases included isothermal reduction and re-oxidation at the same temperatures (600 °C, 750 °C, 850 °C and 1000 °C) and high temperature (1000 °C) reduction followed by low temperature (600 °C, 750 °C and 800 °C) re-oxidation. The model considered the chemical strain of the nickel in the anode, anelastic expansion of YSZ and creep with some semi-empirical correlations for Ni coarsening, NiO particle growth during the oxidation and grain growth of Ni and NiO. However, the effect of the temperature gradient due to cell operation on the stress distribution was not considered in the study. Different from Laurencin et al. (2008), the mechanical materials properties were defined as a function of temperature and the reduction/oxidation strain was considered as 0.16 times the degree of oxidation. It was found that the high reduction temperature negatively affects the redox stability and similarly the re-oxidation strain increases with the re-oxidation temperature.

2.5 SOFC Thermo-Fluid Modeling

There can be found numerous studies in the literature on the mathematical modeling and numerical simulation of solid oxide fuel cell. The aim of these studies is generally to predict the current, temperature and species distributions in order to optimize repeating cell by investigating the effects of important operation and fabrication parameters such as the thicknesses and porosities of the cell components, the operation temperature/pressure, the composition of electrodes, the fuel type etc. A commercial computational fluid dynamics package or developed computer codes as well as combination of two methods have been conducted generally with a finite volume

approach to solve thermo-fluid model developed including species, momentum, energy equations and electrochemistry. It is possible to categorize SOFC thermo-fluid models into two: micro- and macro-scale models.

2.5.1 Micro-modeling of SOFC

Micro-SOFC models in the literature usually consider the micro characteristics of a single electrode such as the porosity, the powder size and the thickness. Costamagna et al. (1998), for example, developed an anode micro-model and solved for EDB (erbium doped bismuth oxide)/Pt and YSZ/LSM cathodes and YSZ/Ni anodes. It was concluded that the morphology of the electrodes strongly influences the electrode resistance and the thickness of the electrodes should be optimized with considering the active area and the ohmic losses. Another anode micro model was presented by Chan and Xia (2001) with considering the transports of electrons, ions and gas molecules as well as electrochemical reactions. The effects of anode particle size, anode thickness and water vapor content in the fuel on the anode polarization were investigated. The overall anode polarization was found to be decreased with the decreasing the particle size in the anode microstructure at a certain point. However, very small particle size resulted in high concentration polarization which was attributed to limited gas flows. The dilution of hydrogen fuel with steam was found to be effective to lower the anode polarization. It was suggested that a careful balance between the particle size and the thickness of the anode layer is needed in order to reduce the overall polarization of the anode. When the bigger the particle size is used in the anode structure, the anode should be relatively thick to provide sufficient electrochemical reaction sites. Xia et al. (2004) improved their previous work (Chan and Xia, 2001) by particularly considering the true internal exchange current density in the charge transfer current equation accounting for the activities of reactants and products at any anode locations. The model was validated against experimental data for different cermet particle sizes, anode thicknesses, and water content in the hydrogen and showed a good agreement.

On the other hand, Chan et al. (2004) and Chen et al. (2004) focused on the micro-modeling of SOFC cathodes. The model proposed by Chan et al. (2004) considered the combined effect of transport phenomena, electrochemical reactions and microstructure

together with the all possible polarizations on the cathode overpotential under different operation conditions. They performed parametric studies for LSM/YSZ cathode in order to investigate the effects of particle size ratio, YSZ volume fraction, cathode thickness, operational current density and oxygen partial pressure. The lowest overpotential was reported when the particle sizes of YSZ and LSM are equal to 0.1 μm with 0.6 YSZ volume fraction. It was found that the lower the current density or the higher the oxygen partial pressure, the smaller the particle size should be. Similar results were concluded by Chen et al. (2004) who numerically investigated the performance of YSZ/LSM composite cathode with a similar polarization based mathematical model. They also fabricated a single cell for validation of the model. It was found that the lower the oxygen partial pressure, the larger the particle size should be used in order to reduce overpotential. In addition, parametric studies showed that the higher the particle size ratio of YSZ to LSM, the more the YSZ is needed. Too thin cathodes were found to show poor performance due to insufficient electrochemical active areas.

There can be found some other micro-modeling studies in the literature interested in specific topics such as modeling of triple phase boundaries (Deng and Petric, 2005; Haschka et al., 2006; Janardhanan et al., 2008 and Ali et al., 2008), interface structure (Huang et al., 2005 and Schmidt et al., 2008) and micro-machined SOFCs (Srikanth et al., 2004).

2.5.2 Macro-modeling of SOFC

Macro-models, on the other hand, are interested in overall operational behavior of SOFC at macroscopic scale. Generally, differential forms of mass, momentum, charge, species and energy conservation equations are solved to obtain temperature, charge and species profiles in a system. Among them Iwata et al. (2000) established a simulation code for a planar SOFC unit considering mass, charge and energy balance to estimate the current density and temperature profile using the Nernst potential and overvoltages by activation, concentration and resistance along the flow direction. The flow configurations (co-, counter- and cross-flow) were also considered in the study. When the upper and lower surfaces of the unit cell are assumed to be adiabatic, the temperature increase for counter-flow case was found to be larger than that of co-flow

configuration. However, when the radiation is considered for the upper and lower surfaces of the unit cell, the temperature profiles for all flow configurations were found to be flat. In addition, increasing the operation pressure also provided relatively low temperature increase which was attributed to increased cell power. Yakabe et al. (2001) also constructed a three-dimensional mathematical model for a planar SOFC. The model was numerically solved for species, temperature, current density and potential distribution of a single unit with double channels of co- and counter flow patterns using finite volume method based on the fundamental laws of mass, energy and electrical charge. They assumed that the gas flow in the anode is governed by Darcy's Law and the species are transferred to the electrolyte/anode interface mainly by diffusion in a multi component mixture system. They showed that the co-flow configuration is advantageous since it provides relatively low temperature gradient in the cell. Xia et al. (2009), on the other hand, found the opposite. The three dimensional model coupling the electrochemical kinetics with fluid dynamics was constructed to predict the heat and mass transfer in the one-cell stack of planar solid oxide fuel cells. The simulation results showed that counter-flow case offers much more uniform current and temperature distribution due to the relatively uniform air and fuel flows, as well as higher power output, fuel utilization factor and fuel efficiency. It was found that the temperature gradient for counter low case can be decreased by increasing the air inlet flow-rate or decreasing the flow-rate and temperature of the fuel inlet and anode pore size.

Another three-dimensional model for a planar SOFC was reported by Ji et al. (2006) who numerically investigated the dependence of the temperature, the mass transport, the local current and power densities on the gas channel size for a planar SOFC and considered the cathode and the electrolyte. They concluded that when the channel height is decreased, the higher cell efficiency is obtained due to a shorter current length together with the higher heat and mass transfer coefficients. The smaller ratios of the flow channel width to rib width were found to improve the cell due to a reduced ohmic loss at the interface. It was also shown that the higher gas inlet temperature enhances the cell performance. Yuan et al. (2003) previously presented an improved study by adding interconnector effect also to a planar SOFC composed of a gas channel, an anode and an interconnector. Thermal boundary conditions on solid walls, mass transfer and gas permeation across the interface were applied in the analysis. Characteristic

ratios: hydraulic diameter ratio and the permeation ratio, permeation rate ratios are proposed as the important parameters affecting the SOFC performance. The gas flow and the heat transfer were investigated based on these ratios considering the friction factors and Nusselt numbers. The anode characteristics and the channel size are shown to have great importance for mass transport and the heat transfer. Similarly, Akhtar et al. (2009) developed a three-dimensional numerical model of a single-chamber solid oxide fuel cell accounting for all transport phenomena and cell potential. It was found that increasing the porosity of the catalyst layers reduces the available active area for electrochemical reaction as expected. On the other hand, it was implied that although fine pores can increase the cell performance by increasing the electrochemically active sites, it can cause a large pressure drop leading to a hydrodynamic problem.

Zhu and Kee (2003) developed a general mathematical model to analyze the effects of various polarization resistances of both electrodes on the cell performance. This model was later improved by Hussain et al. (2006) who developed a mathematical model to predict the performance of planar SOFC. The important characteristics of the model are being fuel flexible and the consideration of the reaction zone layers as finite volumes. In addition, the effect of Knudsen diffusion was also accounted in the porous electrodes. The predicted performance was validated with the experimental data found in the literature and an excellent agreement was reported. The effects of different operational and design parameters on the cell performance of SOFC were numerically studied. Ohmic overpotential was found to be the largest contributor to the cell potential loss especially for the anode supported design. Patcharavorachot et al. (2008), on the other hand, established a electrochemical model taking into account structural and operational parameters and gas diffusion at the electrodes and numerically investigated the effect of support structure (i.e. electrolyte, cathode and anode supported design). In addition to the effect of support layer thickness, the effects of operating pressure, operating temperature and fuel composition on the cell performance were also included in the study. Like indicated by Hussain et al. (2006), the ohmic loss was found be the major loss for both anode and electrolyte supported cells. However, the cathode supported structure showed relatively high concentration polarization especially at higher current density operation. The increase in the operation pressure resulted in enhanced cell performance as previously concluded by Iwata et al. (2000). It was also revealed that a

decrease in operating temperature leads to the cell to operate at a lower range of current density. This was believed as a result of an increase in both the ohmic and the activation overpotentials.

Some numerical studies were interested in specific SOFC designs rather than planar or tubular ones. Costamagna et al. (2004), for example, presented an electrochemical based simulation model for the integrated planar solid oxide fuel cell pioneered by Rolls Royce. The electrochemical model consisted of local electrochemical kinetics including the ohmic, the activation and the concentration losses as well as mass transport. The model results were compared to experimental data and a good agreement was reported for both small scale module and full size prototype. Similarly, Murthy and Federov (2003) established a mathematical model based on heat and mass transport for a monolithic type SOFC to investigate the radiation effect. They showed that radiation heat transfer effects are significant for accurate prediction of the temperature field and the fuel cell performance although it is commonly neglected. Lu et al. (2005), on the other hand, focused on the modeling of flat-tube SOFC design developed by Siemens Westinghouse. The steady state heat/mass transfer and fluid flow were included in the model. The effect of current output on the variation of temperature, species and flow fields were numerically investigated. The model was found to be a helpful tool to optimize the design and operation of flat tube SOFC design in practical stack application. Similarly, Suzuki et al. (2008) numerically studied heat and mass transfer as well as electrochemical reactions for flat-tube SOFC. The numerical results showed that the distribution of the reaction fields in flat-tube is similar to those of the conventional planar cell with co-flow configuration. The pore diameter of the anode was found to have a significant effect on the cell performances. It was shown that the anode with larger pore diameter provides a higher output voltage for a fixed activation overpotential model. Park et al. (2011), on the other hand, numerically investigated the effect of various channel design on the current density and the temperature distribution of flat-tube SOFC. They showed that with a gradually increasing width from inlet to outlet can increase the performance, maintain the mechanical strength and reduces the pressure drop.

CHAPTER III

EXPERIMENTAL STUDIES

The main purpose of the experimental study is to validate both mathematical models (i.e. thermo-fluid and mechanical modeling) by optimizing the required modeling parameters such as j_o , $\alpha_{a,c}$ and B . Therefore, anode supported cells having properties the same as those defined in the model are fabricated by using tape casting, co-sintering and screen printing routes. The cell used for validation of the mathematical model is called as the base cell which has 10 μm thick electrolyte and 40 % anode porosity. The electrochemical and mechanical performances of the base cell are measured via fuel cell test station and three-point bending test apparatus, respectively. In addition, the cells with various anode porosities and electrolyte thickness are also fabricated in order to investigate their effects on the electrochemical and mechanical performance of the cell. The details of the experimental study are reported in the following sections.

3.1 Base Cell Fabrication

A block diagram of the fabricated anode supported base cell identical to that of considered in the model is shown Figure 3.1. The cell comprises mainly three components: Nickel oxide (NiO) / yttria stabilized zirconia (YSZ) anode support, YSZ electrolyte and Lanthanum Strontium Manganite (LSM) / YSZ cathode. The anode support and the electrolyte are fabricated via tape casting and co-sintering routes whereas the cathode layer is coated by applying screen printing technique. The details of the cell fabrication process are summarized in Figure 3.2. Fifteen anode supported cells with various properties are manufactured with 1 cm^2 active area and ten identical ones having 16 cm^2 active area for mechanical test in order to minimize the experimental errors.

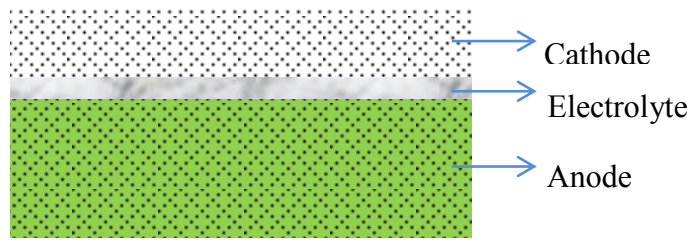


Figure 3.1. The structure of the anode supported cell (not to scale)

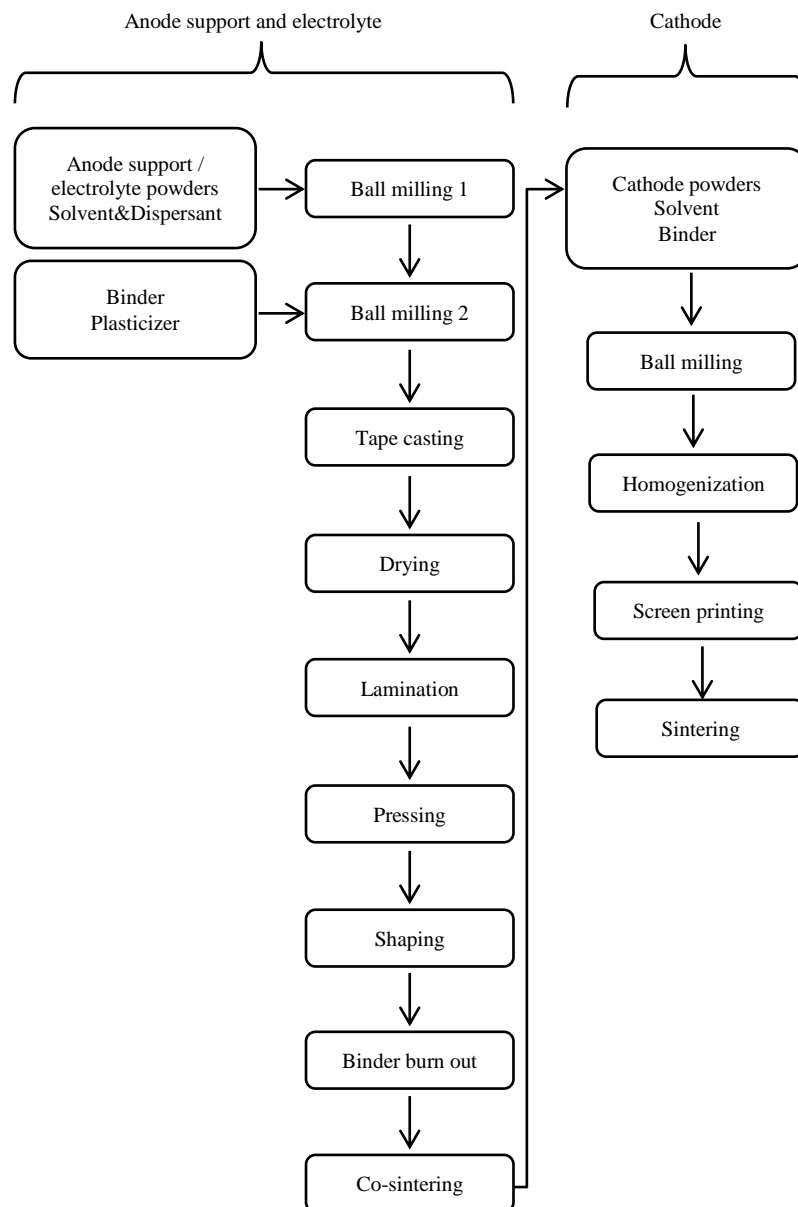


Figure 3.2. The flowchart of the cell fabrication

3.1.1 Fabrication of the electrolyte and the anode support for the base cell

High purity yttria stabilized zirconia (YSZ) powders ($(Y_2O_3)_{0.08}(ZrO_2)_{0.92}$) are purchased from Nextech Materials (Ohio, USA). An alcohol-based tape casting slurry of YSZ is prepared by ball milling at two stages. In the first stage, some certain amount of organic dispersant and solvent are added to the YSZ powders and the mixture is ball milled for around 24 h. In the second stage, organic binder and plasticizer are added with suitable ratios and the ball milling is continued for another 24 h. Then the YSZ slurry is tape cast on a mylar strip via a laboratory scale tape casting equipment with a blade gap of 45 μm . After drying in atmospheric air for 30 min, the thickness of the green tape is measured as about 14 μm .

Similarly, nickel oxide (NiO) powders (Novamet, New Jersey, USA) are mixed with YSZ powders corresponding to a weight ratio of 1:1, respectively. Some amount of organic solvent and dispersant are also added. After the ball milling for around 24 h, organic binder, pore former and plasticizer are added with suitable ratios the ball milling is continued for another 24 h. Then the anode support slurry is tape casted again on a mylar tape with a blade gap of 210 μm . After drying in atmospheric air for 30 min, the thickness of the anode support green tape is measured as about 55 μm .

Ten tapes of anode support and one tape of electrolyte are stacked together and pre-laminated via a laboratory scale uniaxial press under 20 MPa pressure for 2 minutes in order to create an adequate adhesion between tapes before the isostatic pressing step. The laminate is then pressed isostatically under 40 MPa pressure at 70 $^{\circ}\text{C}$ for 10 minutes. After shaping by a laser cutter in the form of a square with 80 mm x 80 mm outer dimensions, the anode supported electrolyte structure is subjected to two different sintering regimes. Firstly, the electrolyte is heated to 1000 $^{\circ}\text{C}$ with 2 $^{\circ}\text{C min}^{-1}$ temperature increment and held for 2 hours at this temperature to remove the organic additions. Pre-sintered structure is then moved to the high temperature furnace for the second sintering stage and sintered there at 1350 $^{\circ}\text{C}$ for 5 hours with a rate of 3 $^{\circ}\text{C min}^{-1}$ to obtain fully dense electrolyte. The final dimensions of the anode supported electrolyte are measured as 15 mm x 15 mm.

3.1.2 Fabrication of the cathode electrode for the base cell

Lanthanum strontium manganite, LSM, $((\text{La}_{0.80}\text{Sr}_{0.20})_{0.95}\text{MnO}_{3-x})$, Nextech Materials) powders are mixed with YSZ powders corresponding to a weight ratio of 1:1, respectively. An appropriate amount of ethyl cellulose binder and terpineol solvent (both from Sigma-Aldrich, Munich, Germany) is also added to prepare a printable cathode ink. Some amount of pore former is also added to the cathode screen printing solution. After ball milling for around 12 h and homogenization via a three rolls mill, the ink is screen printed on the electrolyte with the active area of 1 cm^2 ($10 \text{ mm} \times 10 \text{ mm}$) which is the same as that of the model geometry. After sintering of the cathode layer at $1000 \text{ }^\circ\text{C}$ for 2.5 h, all cells are then ready for testing. The photo of the final cell is shown in Photo 3.1.

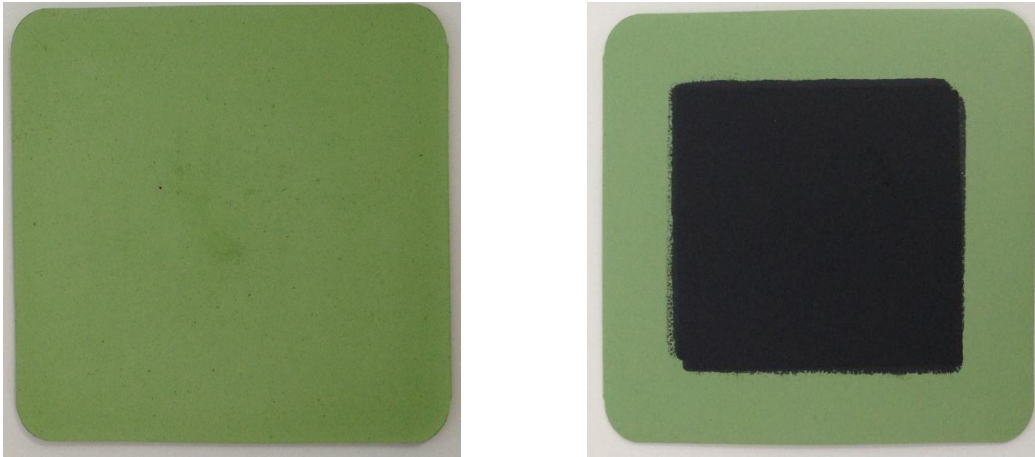


Photo 3.1. The photo of the final anode supported cell with 1 cm^2 active area

3.1.3 Cases considered for the cell fabrication

Since the most important fabrication parameters that influence the cell electrochemical and mechanical performance are the anode porosity and the electrolyte thickness, the cell having various anode porosities and electrolyte thicknesses are also fabricated. The porosity of the anode layer is controlled by the pore former added into the tape casting solution whereas the electrolyte thickness is controlled by changing the doctor blade gap. In this aspect, beside the base case, the porosity of the anode is adjusted as 0.3 and 0.5 while the electrolyte thickness is kept the same as $10 \text{ }\mu\text{m}$. In order to measure the

porosity, only anode supports prepared with different amount of pore former are fabricated. The porosity of the anode supports is measured via Archimedes technique which is based on the density measurements. In addition, the cells with the 4 and 6 μm thick electrolyte are also manufactured while the porosity is 0.4 for these cells. The thickness of the electrolyte is measured via scanning electron microscope. In order to eliminate the experimental errors, three cells for each case are fabricated.

3.2 Cell characterization

In order to investigate the effect of redox cycling on the electrochemical and mechanical performance of the anode supported cell, two redox experiments are performed for two different SOFC short stacks. In the first one, the short stack is built by using two interconnectors, current collecting meshes and pastes, glass ceramic sealing and MEG. The electrochemical performance of the cell before and after 1 redox cycles is characterized via performance measurements. These tests are repeated for three identical MEGs for each case to eliminate the experimental error. Due to the sintering of the current collecting paste and the chemical bonding of the glass ceramic sealing to both MEG and interconnectors during the operation, it is almost impossible to remove MEG safely out of the short stack for the mechanical tests. In other words, it is not possible to perform both mechanical and electrochemical tests for the same cell. Therefore, the short stack conducted in the second redox experiment is built by using an identical MEG, two interconnectors, current collecting meshes and mica sealing without using glass ceramic sealing and current collecting pastes to achieve safe removal of the anode supported cell which is to be used in the mechanical tests. The same redox procedure is then applied and the mechanical performances of the cells are measured via three point bending tests before and after 1 redox cycles. To improve the reliability of the mechanical test, five identical MEGs are tested for each case. The details of the each cell characterization tests are explained in the following sections.

3.2.1 Electrochemical measurements

For the performance characterization of the cell, fabricated MEG is inserted between two Crofer® interconnectors with flow channels machined. Crofer® mesh is used as the

current collector for both the anode and the cathode. The sealing is achieved by glass ceramic material fabricated via similar tape casting route. Silver ink (Nextech Materials) is applied as a current collecting paste for both electrodes. Then the short stack is placed in a temperature controlled furnace connected to the fuel cell test station (Arbin Instruments, FCTS, Texas, USA). The furnace has also a push rod pressing capability for better current collection. The current and voltage sensing probes of the test station are mounted directly to the gas pipes welded to the interconnectors as shown in Photo 4.2 while the short stack configuration is given in Figure 3.3. The performance curves are obtained via the available software in the fuel cell test station while microstructural investigations are through a SEM (scanning electron microscope: Carl Zeiss, Evo 40, London, England).



Photo 3.2. The experimental setup

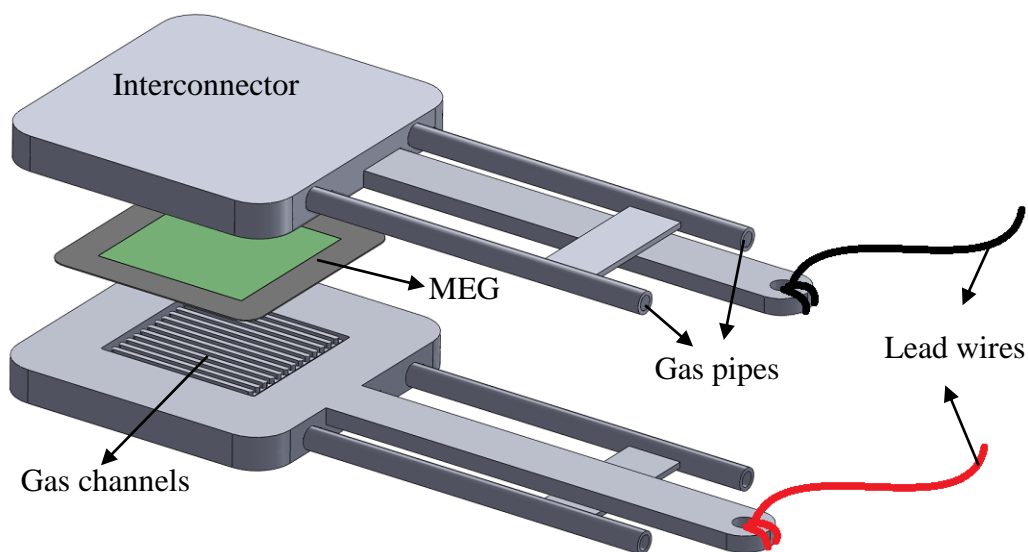


Figure 3.3. Short stack configuration

In order to investigate the effect of various redox cycles on the short stack performance, a high temperature redox test schedule is developed including the following steps:

1. The short stack is heated to 800 °C operation temperature.
2. The anode is reduced by hydrogen for 2 hours.
3. The performance measurements are performed.
4. The anode is re-oxidized by air for 2 hours.
5. The anode is re-reduced by hydrogen for 2 hours.
6. The performance measurements are performed.

The steps 4-6 are repeated 1-3 times in order to investigate the effect of various redox cycles on the cell performance. In addition, these tests are repeated for five identical anode supported cells to eliminate any experimental error.

3.2.2 Samples for mechanical tests

In order to investigate the effect of redox cycles on the mechanical performance of the anode supported cell, a similar short stack is installed but with a cell having 16cm² active area fabricated by using the similar techniques since the large cell size is required

for the three point bending test apparatus. However, mica seal is used instead of glass ceramic one and no current collecting paste is applied. Thus, this short stack design enables to remove MEG safely after redox tests. Then the three points bending tests are performed for the cells before and after 1 redox cycle with the same redox procedure explained in the previous section. Five identical MEGs are tested for each case in order to minimize the experimental error.

3.2.3 Mechanical tests

The mechanical performance of anode supported cells subjected to a redox cycle is analyzed by applying three point bending test. The apparatus used for the test is represented in Figure 3.4 schematically. Three point bending tests are performed on a testing machine (Shimadzu Autograph AG-IS, Kyoto, Japan) with a data acquisition maintained by a digital interface board utilizing a specialized computer program. The radius of both support cylinders is $R=15$ mm and loading cylinder has $r=5$ mm radius. The distance between supports is chosen as $L=50$ mm and bending speed is 1 mm/min in order to see the fast crack. The load applied to the test specimen and the corresponding deflection is measured until the specimen fractured. The bending tests are performed five times for each specimen in order to increase the reliability of the results.

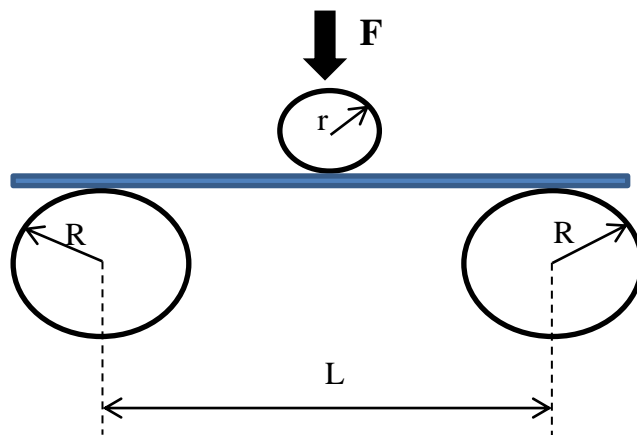


Figure 3.4. The schematic of three point bending test bench

CHAPTER IV

MATHEMATICAL MODELING

4.1 Model Description

The 3D model geometry which mimics the short stacks installed for the experimental studies is illustrated in Figure 4.1(a) while the details are given in Figure 4.1(b). The short stack consists of an anode supported SOFC MEA with 1 cm² active area, two interconnectors with flow channels machined and sealants. The depth and the width of the both anode and cathode serpentine type flow channels are 2 mm. In order to obtain a meshed structured composed of structural meshes, each domain are divided into smaller volumes as shown in Figure 4.1(b). In this aspect, the electrolyte and both electrodes comprise 15 and the sealant has 20 smaller domains whereas both interconnectors are divided into 22 small volumes. All these issues are modeled via commercially available COMSOL Multiphysics® finite element software.

4.2 Governing Equations

4.2.1 Continuity equation

The continuity equation describing the transport of a conserved quantity for all domains is given below:

$$\frac{d(\varepsilon\rho)}{dt} + \nabla \cdot (\rho u) = \sum S_j \quad (4.1)$$

In the above equation, ε is porosity and ρ stands for the density of the gas mixture which can be calculated via the following equation:

$$\rho = \sum_{j=1}^N \rho_j c_j \quad (4.2)$$

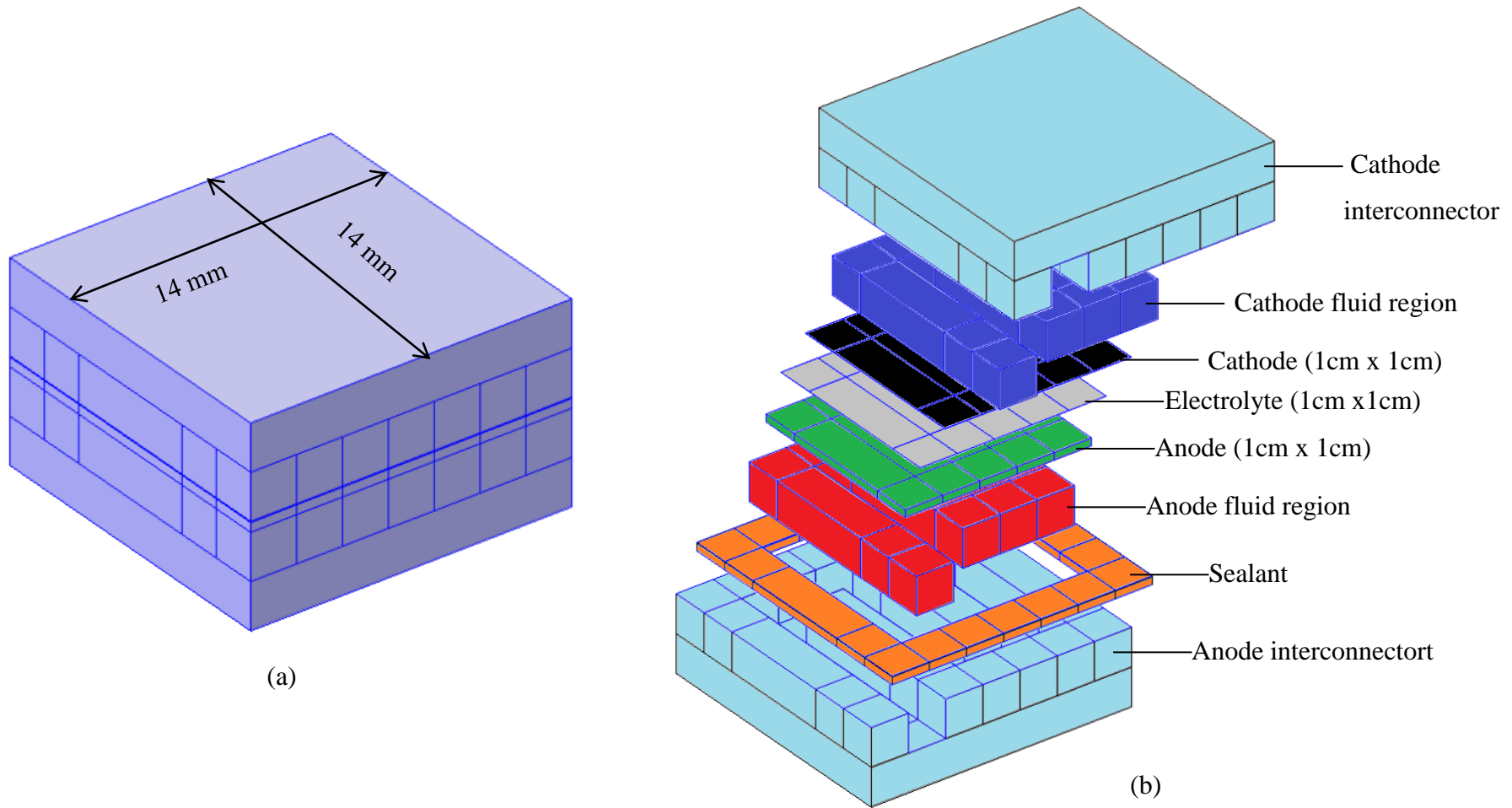


Figure 4.1. The SOFC short stack geometry of interest

In Equation (4.2) ρ_j and c_j are the density and concentration of the specie j and N is the number of the species. The density of the species, on the other hand, can be estimated from ideal gas law:

$$\rho_j = \frac{P_j}{R_{s,j}T} \quad (4.3)$$

where P_j and $R_{s,j}$ is the partial pressure and specific gas constant of the specie j , respectively whereas T is the temperature calculated from the energy equation which is explained in the following sections.

The term in the right hand side of the Equation (4.1) is the species source term. In SOFC anode hydrogen is consumed while water is formed. The depletion of hydrogen and production of water can be adapted into the continuity equations via following two equations, respectively.

$$S_{H_2}^a = \frac{-i_{exc}^a}{n_{H_2}F} MW_{H_2} \quad (4.4)$$

$$S_{H_2O}^a = \frac{i_{exc}^a}{n_{H_2O}F} MW_{H_2O} \quad (4.5)$$

On the other hand, in SOFC cathode only oxygen is depleted. The consumption of oxygen can be calculated as follows:

$$S_{O_2}^c = \frac{-i_{exc}^c}{n_{O_2}F} MW_{O_2} \quad (4.6)$$

In equations (4.4)-(4.6), F is the Faraday's constant while MW is the molecular weight of the corresponding gases and n is the number of electrons involved in the reaction to consume or produce one mole of the corresponding gases. $i_{exc}^{a,c}$, on the other hand, is the exchange current density of electrodes which is explained in the following sections.

4.2.2 Species balance

Maxwell-Stefan equation for multi component species transport is given below:

$$\frac{d(\varepsilon\rho w_j)}{dt} + \nabla \cdot (j_j + \rho w_j u) = \sum R_j \quad (4.7)$$

R_j is the generation or consumption rate of each species calculated from Equations (4.2)-(4.4) and j_j is the diffusive term presenting the interaction of each species with others together with the effect of temperature and can be calculated as follows:

$$j_j = - \left\{ \rho w_j \sum_k D_{jk} d_k + D_j^T \frac{\nabla T}{T} \right\} \quad (4.8)$$

The second term in Equation (4.8) which is known as Soret effect, accounts for the influence of temperature gradient on diffusion. Since it is very small compared to the second term, it is neglected. d_k is the diffusion driving force:

$$d_k = \nabla x_k + \frac{\nabla p_A}{p_A} [(x_k - w_k)] \quad (4.9)$$

The subscript j represents hydrogen and water vapor for the anode and the anode channel while it is oxygen for the cathode and cathode channel. The steam and nitrogen is considered to be background species in the anode and cathode fluid regions, respectively. w_j , on the other hand, is the mass fraction of other species can be calculated by using Equation (4.10).

$$\sum_{j=1}^n w_j = 1 \quad (4.10)$$

D_{jk} terms in the Equation (4.8) are the Maxwell-Stefan diffusivities and can be calculated from binary diffusion coefficients from the equation given below:

$$D_{jk} = \frac{k_d T^{1.75}}{p M_{jk}^{1/2} (V_j^{1/3} + V_k^{1/3})^2} \quad (4.11)$$

In the above equation, p is the pressure in bars, V_j is the kinetic volume (Table 4.1) and k_d is the reference diffusivity which is assumed to be $3.16 \times 10^{-8} \text{ m}^2/\text{s}$ in this study. M_{jk} stands for the combined molecular weight and can be calculated as follows:

$$M_{jk} = 2 \left(\frac{1}{M_j} + \frac{1}{M_k} \right)^{-1} \quad (4.12)$$

However, the diffusion coefficients especially in the porous anode and cathode layers should be correlated with the porosity of the medium. The effective diffusion coefficients for the anode and cathode layers can be calculated as follows:

$$D_{jk}^{eff} = D_{jk} \epsilon^{1.5} \quad (4.13)$$

Table 4.1. Kinetics volumes of the considered species

Species	Kinetic volume
O ₂	16.6×10^{-6}
N ₂	17.9×10^{-6}
H ₂	6×10^{-6}
H ₂ O	12.7×10^{-6}

4.2.3 Momentum equation

The momentum equation is given below:

$$\frac{\partial(\rho u)}{\partial t} + \rho u \cdot \nabla u = \nabla \cdot \left(-pI + \mu(\nabla u + (\nabla u)^T) - \frac{2}{3}(\nabla \cdot u)I \right) + \rho g \quad (4.14)$$

This equation is solved for both the anode and cathode flow channels whereas converted to Brinkman equation representing the transport in porous medium for the electrodes as follows:

$$\frac{\partial}{\partial t} \left(\frac{\rho u}{\epsilon} \right) + \rho u \cdot \nabla u = \nabla \cdot \left(-pI + \frac{\mu}{\epsilon} (\nabla u + (\nabla u)^T) - \frac{2}{3\epsilon} (\nabla \cdot u)I \right) + \rho g - \frac{\mu}{K} u \quad (4.15)$$

where K is the permeability.

4.2.3 Energy conservation

The conservation of the energy can be written as a function of thermal conductivity (k) and temperature (T) as follows:

$$\frac{\partial(\rho c_p T)}{\partial t} + \rho c_p u \cdot \nabla T = \nabla \cdot (k \nabla T) + Q \quad (4.16)$$

The specific heat for the flow channels and electrodes can be calculated as:

$$c_p = \sum_j^N w_j c_{p,j} \quad (4.17)$$

The thermal conductivity (k) in the energy equation and the dynamic viscosity (μ) in the momentum equation are both calculated similar to Equation (4.17). In addition, the specific heat, thermal conductivity and dynamic viscosity of each species are defined as a function temperature (Table 4.2).

Table 4.2. Temperature dependent parameters of each species

Species	Specific heat (J/(kgK))	Dynamic viscosity ($\times 10^7$ Pa.s)	Thermal conductivity (W/(m.K))
H ₂	12986+5.421*T-0.0045*T ²	46.96+0.156*T	0.0784+3.73*10 ⁻⁴ *T
H ₂ O	1672+0.477*T+0.00019*T ²	-9.88+0.361*T	0.0784+8.37*10 ⁻⁵ *T
O ₂	896+0.0115*T+0.00026*T ²	101.93+0.306*T	0.00850+6.3*10 ⁻⁵ *T
N ₂	1070-0.198*T+ 0.00034*T ²	114.5+0.371*T	0.0116+5.39*10 ⁻⁴ *T

The last term from the right hand side of the Equation (4.16) is the source term due to electrochemical reactions. This term is given at the anode side only via the formula given below:

$$Q = (E_{max} - V_{cell})i_{local} \quad (4.18)$$

where E_{max} is the maximum theoretical voltage and can be calculated by using the formation enthalpy of water (h_{f,H_2O}) as follows:

$$E_{max} = \frac{h_{f,H_2O}}{2F} \quad (4.19)$$

4.2.4 Charge balance

The general form of the charge equation is given below:

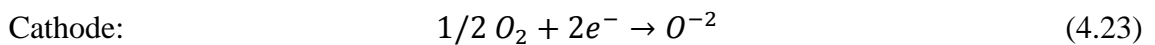
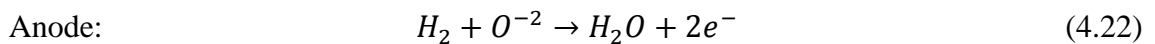
$$\frac{\partial \rho_e}{\partial t} + \nabla \cdot \vec{j} = S_c \quad (4.20)$$

In Equation (4.20), ρ_e represents the ionic or electronic charge density while \vec{j} is the ionic or electronic current density and can be calculated as a function of ionic/electronic electrical potential (ϕ) and ionic/electronic conductivity (σ) as:

$$\vec{j} = -\sigma \nabla \phi \quad (4.21)$$

4.1.4 Electrochemical reactions

The anode and the cathode electrochemical reactions occurring in a hydrogen fuelled SOFC are given below:



4.2.5 Electrochemical model

The current that is produced during SOFC in operation is defined as concentration dependent form of the Butler Volmer equation as:

$$i = A_v j_o \left[C_R \exp\left(\alpha_a \frac{nF\eta_{act}}{RT}\right) - C_O \exp\left(-\alpha_c \frac{nF\eta_{act}}{RT}\right) \right] \quad (4.24)$$

In the above equation, η_{act} and j_o is the activation polarization and exchange current density, respectively while $\alpha_{a,c}$ and n is the anodic/cathodic charge transfer constant and number of electrons involved in the electrochemical reaction, respectively. A_v , on the other hand, stands for the specific area representing the triple phase boundaries where electrochemical reactions take place and can be calculated as follows:

$$A_v = \frac{S}{V} \quad (4.25)$$

where S is the total catalyst surface area and V is the total catalyst volume. C_R and C_O is the concentration ratio of the reduced and oxidized species, respectively and can be calculated by dividing the concentration of a specie at any location to a reference concentration of the same species.

The exchange current density and anodic/cathodic charge transfer coefficient of both electrodes are used to fit the numerical performance curve to that of experimentally measured one. More detailed information about the validation of the mathematical model is given in Chapter 6.

4.2.5 Solid mechanics

The effect of temperature change with respect to a base/reference temperature can be added to the three normal strains as follows:

$$\varepsilon_{xx} = \frac{1}{E}(\sigma_{xx} - \nu\sigma_{yy} - \nu\sigma_{zz}) + \alpha\Delta T \quad (4.26)$$

$$\varepsilon_{yy} = \frac{1}{E}(-\nu\sigma_{xx} + \sigma_{yy} - \nu\sigma_{zz}) + \alpha\Delta T \quad (4.27)$$

$$\varepsilon_{zz} = \frac{1}{E}(-\nu\sigma_{xx} - \nu\sigma_{yy} + \sigma_{zz}) + \alpha\Delta T \quad (4.28)$$

In the above equation, E is the elastic modulus, ν is Poisson's ratio and α represents the coefficient of thermal expansion. Since all stack components are assumed to be linearly elastic and isotropic, a temperature change only produces normal stresses (σ_{xx} , σ_{yy} and σ_{zz}). Thus, no change in the shear strain (γ)-shear stress (τ) relation is needed.

In the matrix form, three-dimensional stress-strain relations are given below:

$$\begin{bmatrix} \sigma_{xx} \\ \sigma_{yy} \\ \sigma_{zz} \\ \tau_{xy} \\ \tau_{yz} \\ \tau_{zx} \end{bmatrix} = \begin{bmatrix} \hat{E}(1-\nu) & \hat{E}\nu & \hat{E}\nu & 0 & 0 & 0 \\ \hat{E}\nu & \hat{E}(1-\nu) & \hat{E}\nu & 0 & 0 & 0 \\ \hat{E}\nu & \hat{E}\nu & \hat{E}(1-\nu) & 0 & 0 & 0 \\ 0 & 0 & 0 & G & 0 & 0 \\ 0 & 0 & 0 & 0 & G & 0 \\ 0 & 0 & 0 & 0 & 0 & G \end{bmatrix} \begin{bmatrix} \varepsilon_{xx} \\ \varepsilon_{yy} \\ \varepsilon_{zz} \\ \gamma_{xy} \\ \gamma_{yz} \\ \gamma_{zx} \end{bmatrix} - \frac{E\alpha\Delta T}{1-2\nu} \begin{bmatrix} 1 \\ 1 \\ 1 \\ 0 \\ 0 \\ 0 \end{bmatrix} \quad (4.29)$$

Where G is the shear modulus and \hat{E} is the effective modulus calculated by:

$$\hat{E} = \frac{G}{(1+\nu)(1-2\nu)} \quad (4.30)$$

In addition, the relations between G , E and ν can be expressed as:

$$G = \frac{E}{2(1+\nu)} \quad (4.31)$$

4.2.6 Redox model

The mechanical damage leading to performance loss due to re-oxidation of nickel is described with a damage function D which is as follows:

$$D = B(\nabla\varepsilon) \quad (4.32)$$

In the above equation, D is the damage function and ε is the strain while B denotes the damage coefficient which is to be found from the change of cell performance after redox. The total strain during the SOFC operation can be defined as:

$$\varepsilon_{total} = \varepsilon_{thermal} + \varepsilon_{redox} \quad (4.33)$$

where $\varepsilon_{thermal}$ is the thermal strain due to the temperature gradient that occurs during the SOFC operation as a result of the nonhomogeneous electrochemical reactions and boundary conditions. ε_{redox} , on the other hand, is the strain due to re-oxidation of nickel in the anode which is given below (Laurencin et al. 2012):

$$\varepsilon_{redox} = 0.0097DoO \quad (4.34)$$

In Equation (4.34), DoO shows the degree of oxidation which is the ratio of the re-oxidized nickel with respect to the total nickel in the anode.

Since the mechanical damage in the anode region due to the re-oxidation of the nickel affects the electrochemical reaction zones, the electrochemical performance of the cell is also expected to drop. This decrease in the local current density is introduced as follows:

$$i = (1 - D)A_v j_o \left[C_R \exp\left(\alpha_a \frac{nF\eta_{act}}{RT}\right) - C_O \exp\left(-\alpha_c \frac{nF\eta_{act}}{RT}\right) \right] \quad (4.35)$$

The experimental electrochemical performance of the cell after redox is compared with the numerical one in order to obtain the damage coefficient B by normalization of D .

4.2.7 Boundary conditions and assumptions

In the Maxwell-Stefan equations, the ratio of the hydrogen and oxygen at the inlet of the anode and cathode, respectively are kept constant. The flow in the anode and cathode channel is created by the pressure difference between the inlet and outlet of the channels

as 10 Pa and 30 Pa, respectively. The temperatures of the inlet gases are assumed to be 800 °C while the remaining boundaries are assumed to be adiabatic. In addition, no-slip boundary condition is used for all walls. In the solid mechanic model, 5 kg load is applied to the top of the cathode interconnector in the z direction which mimics the pushing rod in the experimental studies for better current collection. The top surface of the cathode interconnector is fixed in x and y directions while the bottom surface of the anode interconnector is fixed in all directions.

4.3 Meshing

The meshed structure of the geometry of interest is depicted in Figure 4.2. The structural type mesh is used for the whole domain in order to reduce the solution time as well as for the consistent results. The mesh size is selected after mesh independency test. The distribution of the meshes is selected such that the meshes near the boundaries are smaller and dense for the convergence.

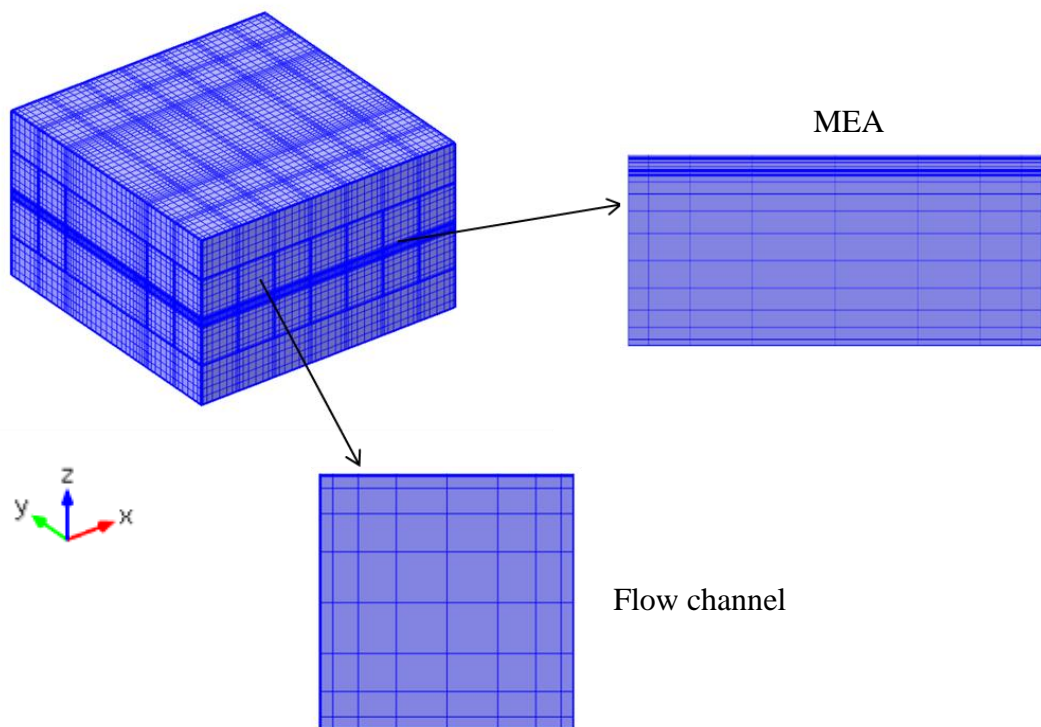


Figure 4.2. Meshed structure of the geometry of interest

The anode and cathode flow channels and the parts of the interconnectors are divided into 9 nodes which are symmetrically distributed with an element ratio of 4 in all directions. The number of nodes of the anode support, the electrolyte and the cathode is kept the same as the previous one. In the z direction, the anode support and the electrolyte are divided into 11 and 4 nodes, respectively whereas the cathode has 5 nodes. The sealant also has the same mesh distribution. Since the electrical conductivity is the only issue, 6 nodes are used for the top part of the cathode interconnector and the bottom part of the anode interconnector. The final short stack geometry has 137984 meshes in total.

4.4 Numerical Solution Method

The mathematical model developed is solved numerically via COMSOL® V4. The software is selected due to being user friendly in terms of implementing simple formulas without any subroutine and having essential modules for SOFC operation. The secondary current distribution, transport of concentrated species, free and porous media flow, heat transfer and solid mechanics modules, which are already available in the software package, are used. The secondary current distribution module is defined for only MEA in order to estimate the current density distribution in the cell and the cell performance. The transport of concentrated species and free and porous media flow modules are used for the porous anode and the cathode as well as both flow channels to calculate the species distribution and flow properties, respectively. The temperature distribution during SOFC operation is found by using heat transfer module. The stress-strain distributions due to both the temperature gradient and after re-oxidation are estimated via solid mechanics module. All modules except the solid mechanics are solved simultaneously for steady state conditions during SOFC operation since the redox takes place when the cell is not in operation. After determination of the temperature distribution, the model is subjected to redox by introducing re-oxidation strain in the anode layer as a function of degree of oxidation and only the solid mechanics model is solved gathering the required information from the previous solution. The solution takes almost three days with a work station Dell T7500 having 192 GB RAM.

The parameters used in the numerical solution of thermo-fluid model are summarized in Table 4.3. The operation temperature as well as the inlet temperatures is taken as 800 °C which is the temperature set point during the experiments. The properties of MEA such as the porosities of the electrodes and thicknesses are the same as those of fabricated MEA. The performance curve numerically estimated from the thermo-fluid model is validated via experimental performance curve for an anode supported cell with 10 μm electrolyte and 40 % anode porosity. The validation is achieved by optimizing the parameters defined in the electrochemical model such as exchange current densities (j_0) and charge transfer constants (α).

Table 4.3. Thermo-fluid parameters used in the numerical analyses

Parameter	Value
Operation temperature (°C)	800
Anode permeability (m ²)	10 ⁻¹⁰
Anode porosity	0.3-0.5
Anode inlet pressure (Pa)	P _{atm} +10
Anode exit pressure (Pa)	P _{atm}
Anode gas inlet composition (wt. %)	40 H ₂ /60 H ₂ O
Anode electronic conductivity (S/m)	1000
Anode ionic conductivity (S/m)	1
Cathode permeability (m ²)	10 ⁻¹⁰
Cathode porosity	0.4
Cathode inlet pressure (Pa)	P _{atm} +30
Cathode exit pressure (Pa)	P _{atm}
Cathode gas inlet composition (wt. %)	21 O ₂ / 79 N ₂
Cathode electronic conductivity (S/m)	1000
Cathode ionic conductivity (S/m)	1
Electrolyte ionic conductivity (S/m)	5
Interconnector conductivity (S/m)	5000
Electrolyte thickness (μm)	4-10
Anode support thickness (μm)	400
Cathode thickness (μm)	30
DoO (%)	10-100
Operation voltage (V)	0.05-0.9

After validation of the thermo-fluid model for the base cell, the anode porosity and the electrolyte thickness are varied in order to investigate their effects on the electrochemical performance of the cell. The numerical and the experimental results are also compared. Then, the changes in the elasticity modulus of the anode with porosity are obtained from Biswas et al. (2009) since the mechanical properties are influenced by the porosity. The parameters used in the solid mechanic model are listed in Table 4.4. The effects of the anode porosity and the electrolyte thickness on the damage function are investigated at an operation voltage of 0.6 V which is a typical value for SOFCs.

Table 4.4. Solid mechanics parameters used in the numerical analyses

Parameter	Value
DoO (%)	10-100
Operation voltage (V)	0.6
Elasticity modulus of the electrolyte (GPa)	190
Poisson's ratio of the electrolyte	0.308
Elasticity modulus of the cathode (GPa)	35
Poisson's ratio of the cathode	0.36
Elasticity modulus of the anode with 0.3 porosity (GPa)	86
Elasticity modulus of the anode with 0.4 porosity (GPa)	70
Elasticity modulus of the anode with 0.5 porosity (GPa)	47
Poisson's ratio of the anode	0.3
Elasticity modulus of the sealant (GPa)	67
Poisson's ratio of the anode of the sealant	0.3
Elasticity modulus of the interconnector (GPa)	160
Poisson's ratio of the anode of the interconnector	0.3
Coefficient of thermal expansion for the electrolyte (1/K)	10.8e-6
Coefficient of thermal expansion for the cathode (1/K)	11.7e-6
Coefficient of thermal expansion for the anode (1/K)	12.5e-6
Coefficient of thermal expansion for the sealant (1/K)	12.6e-6
Coefficient of thermal expansion for the interconnector (1/K)	12.6e-6

CHAPTER V

EXPERIMENTAL RESULTS AND DISCUSSION

5.1 Base Cell

The performances of the base cell obtained at 700 °C, 750 °C and 800 °C are illustrated in Figure 5.1. It is seen that the peak power of the cell tends to increase with the operation temperature due to the enhanced electrochemical reactions at elevated temperature. The cell provides 1.00 W/cm² peak power density at 800°C while it shows 0.46 W/cm² at an operation temperature of 700 °C. The open circuit voltage (OCV) values are measured as 1.14 V at 700 °C, 1.12 V at 750 °C and 1.10 V at 800 °C. Although OCV values are decreasing with the increasing temperature as expected, they are very close to the theoretical values indicating that thin electrolyte is fully and crack/pinhole free. The performance data obtained at 800 °C is used to validate the mathematical model by fitting the performance curve estimated from the model.

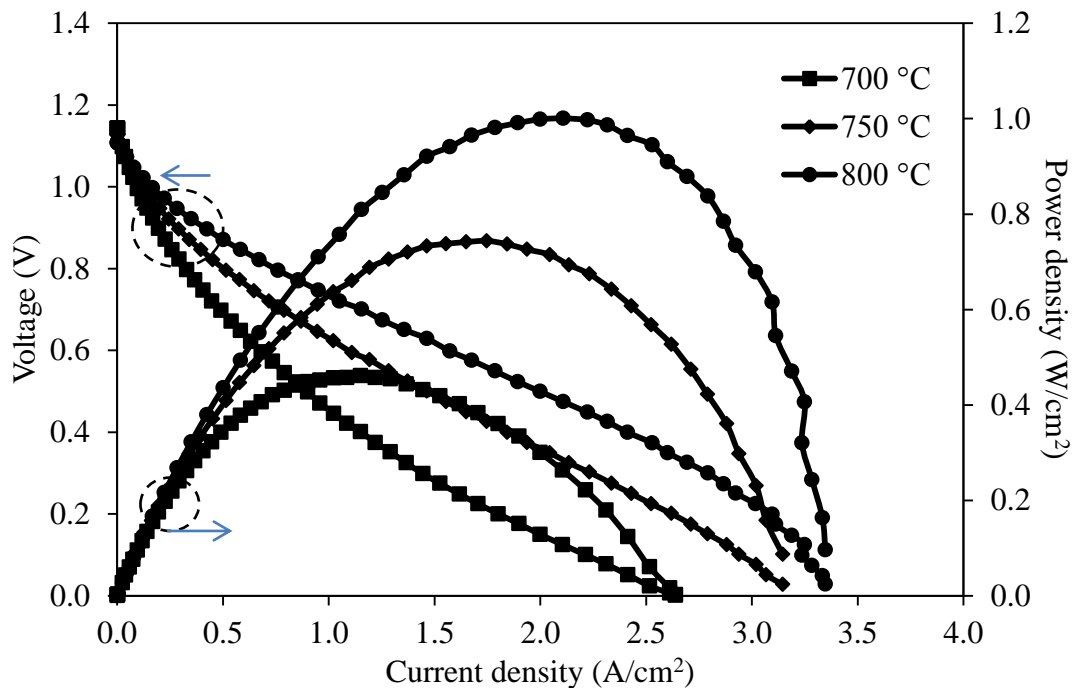


Figure 5.1. The performance curves obtained from the base cell at 700, 750 and 800°C

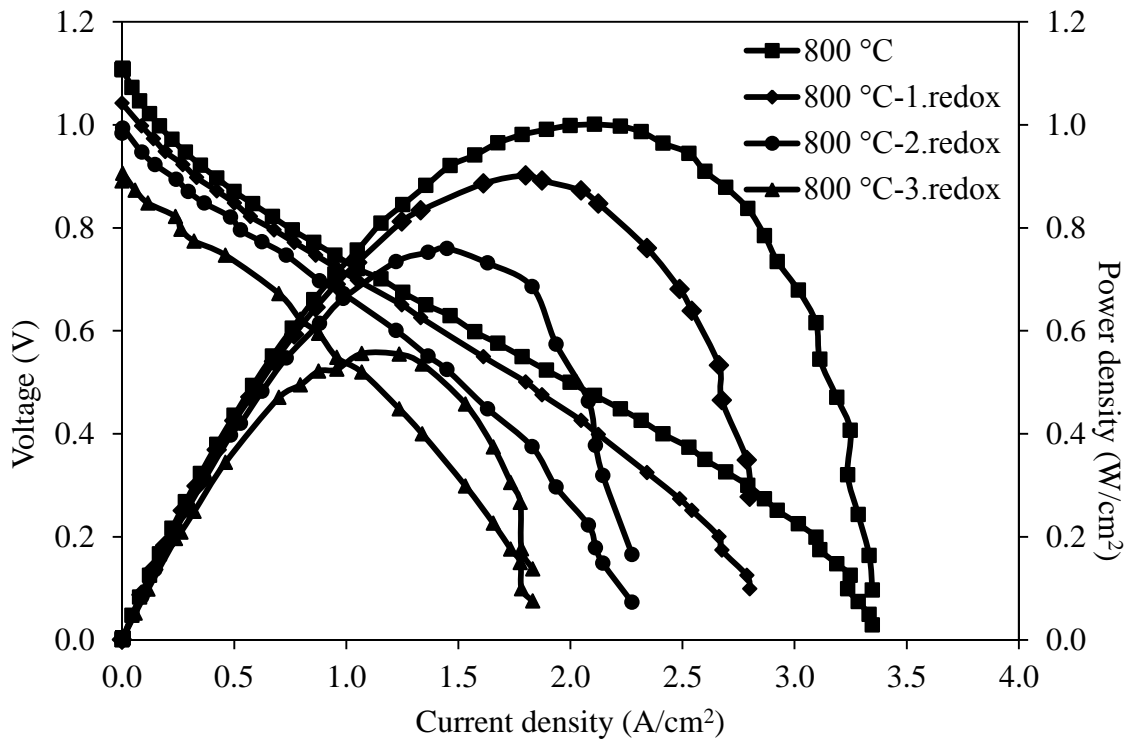


Figure 5.2. Effect of redox cycles on the cell performance at 800 °C

After completion of the performance measurements, redox tests are performed. The anode side of the cell is fed with air for 2 h in order to re-oxidize the nickel in the anode and then re-reduced with hydrogen for another 2 h as decided in the redox procedure. These steps are repeated three times and the performance measurements are performed after each redox cycle. The results are depicted in Figure 5.2. It is seen that the performance tends to decrease with the increasing number of redox cycles. The cell exhibits 0.90 W/cm^2 peak power density after the first redox cycle while that of after the third redox cycle is measured as 0.55 W/cm^2 . This behavior can be attributed to the mechanical damages in anode support due to the volumetric changes because of the formation of Ni-NiO-Ni which may cause damaged or broken NiO/YSZ network (micro-cracks). It is also seen that the damage accumulates as the redox cycle increases. The drop in the cell performance is calculated as 9.89 % after the first redox cycle while it is 15.7 % and 26.87 % after second and third redox cycle, respectively. Furthermore, even after the first redox cycle, the OCV value is found to decrease to 1.04 V indicating the gas leakage as a result of the micro-crack in the electrolyte layer. The OCV further drops to 0.89 V after the third redox cycle confirming that the damage is accumulating as the redox cycle increases resulting in failure of the cell.

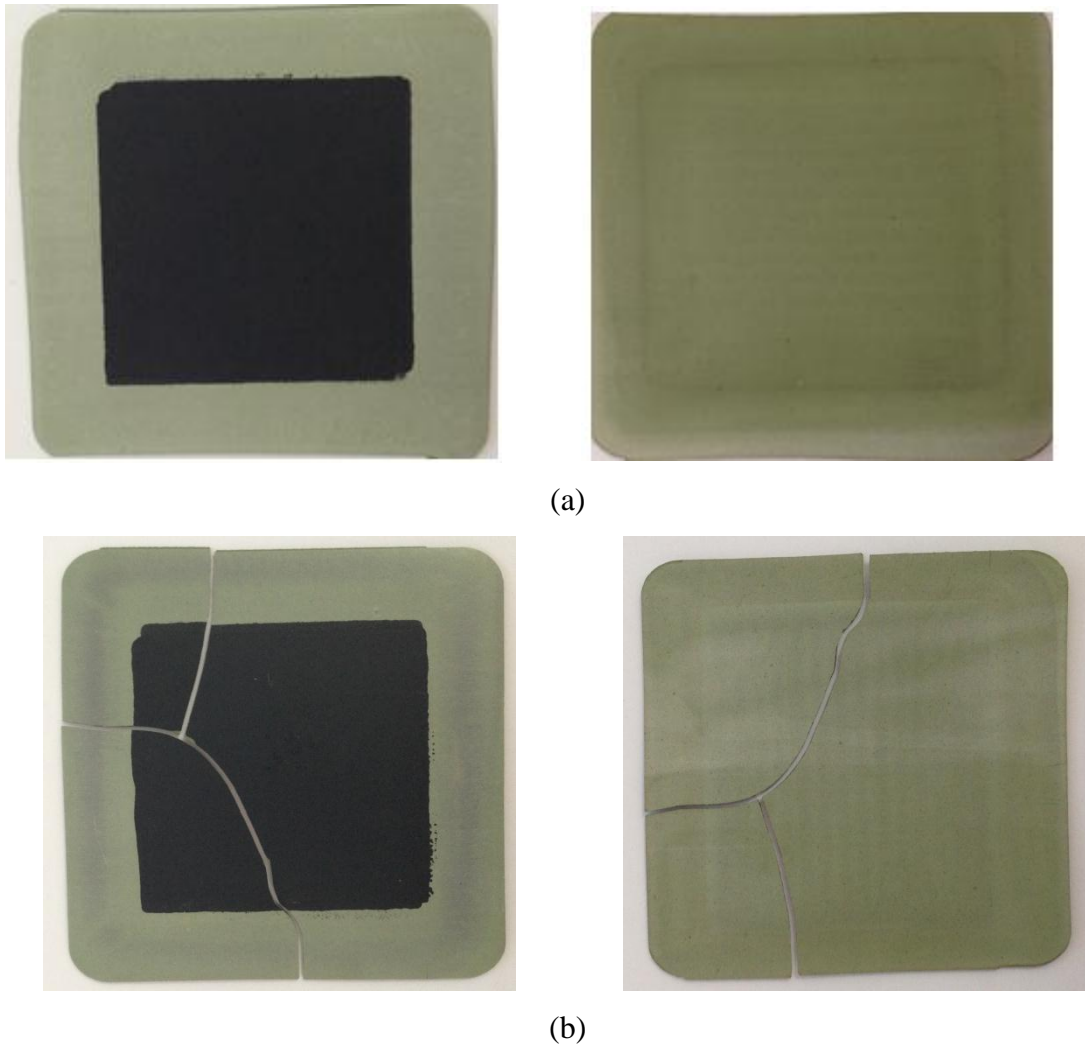


Photo 5.1. Photos of the cell after the first (a) and after third redox cycle (b)

The photos of the anode support and cathode surface of the cell after the first and third redox cycle confirm the performance measurements (Photo 5.1). In addition, the contact points between the interconnector and the anode support is visible in the photos captured from the anode support side. The contact seems to be good enough for an effective current collection without experimental error indicating that the loss in the performance is due to only redox cycling. No crack is observed in the cell after first redox cycle indicating that the drop in the OCV is as a result of the micro-cracks in the electrolyte layer and similarly the loss in the performance is due to the micro-cracks in the anode layer. With the increasing the number of the redox cycle, the damage also increases as can be seen in Photo 5.1(b). Thus, the cell is broken after third redox cycle since the volumetric change after three redox cycles cannot be accommodated within the structure.

5.2 Effect of Anode Support Porosity on the Cell Performance and Redox Behavior

In order to investigate the effect of anode support porosity on both the electrochemical and redox behavior, anode supports having 0.3 and 0.5 reduced porosity are fabricated by changing the pore former content in the anode support tape casting slurries beside the base cell which has 0.4 reduced anode support porosity. The porosities of the samples after reduction are measured via Archimedes' technique by using the following equations:

$$\text{Apperent porosity} = \frac{\text{Soaked weight} - \text{Dry weight}}{\text{Soaked weight} - \text{Suspended weight}} \quad (5.1)$$

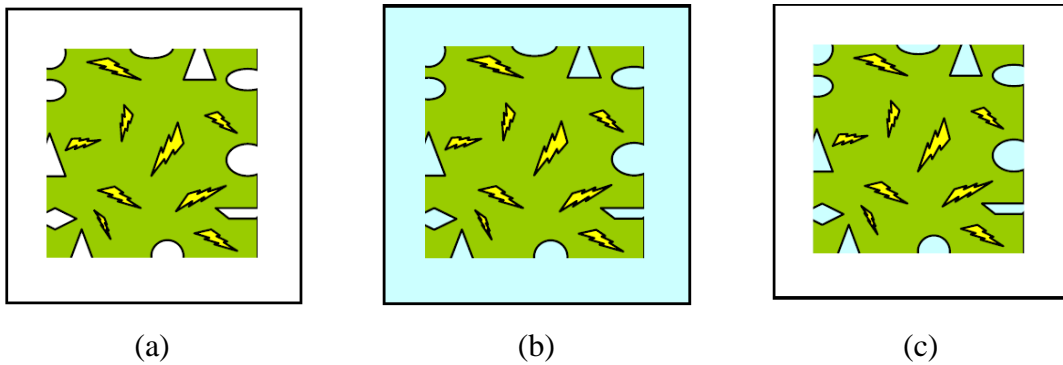


Figure 5.3. Dry (a), soaked (b) and suspended bodies (c)

The dry, soaked and suspended bodies are illustrated in Figure 5.3 while the results are summarized in Table 5.1.

Table 5.1. Calculated porosities via Archimedes' technique

Sample	Dry weight (g)	Soaked weight (g)	Suspended weight (g)	Porosity
Base	1.09	0.96	1.29	0.4
Sample 1	1.15	1.08	1.32	0.3
Sample 2	0.95	0.68	1.22	0.5

After determination of the pore former content that provides the demanded porosities, Cell 1 with 0.3 and Cell 2 with 0.5 anode support porosities are fabricated. The test results obtained at an operation temperature of 800 °C are compared in Figure 5.4.

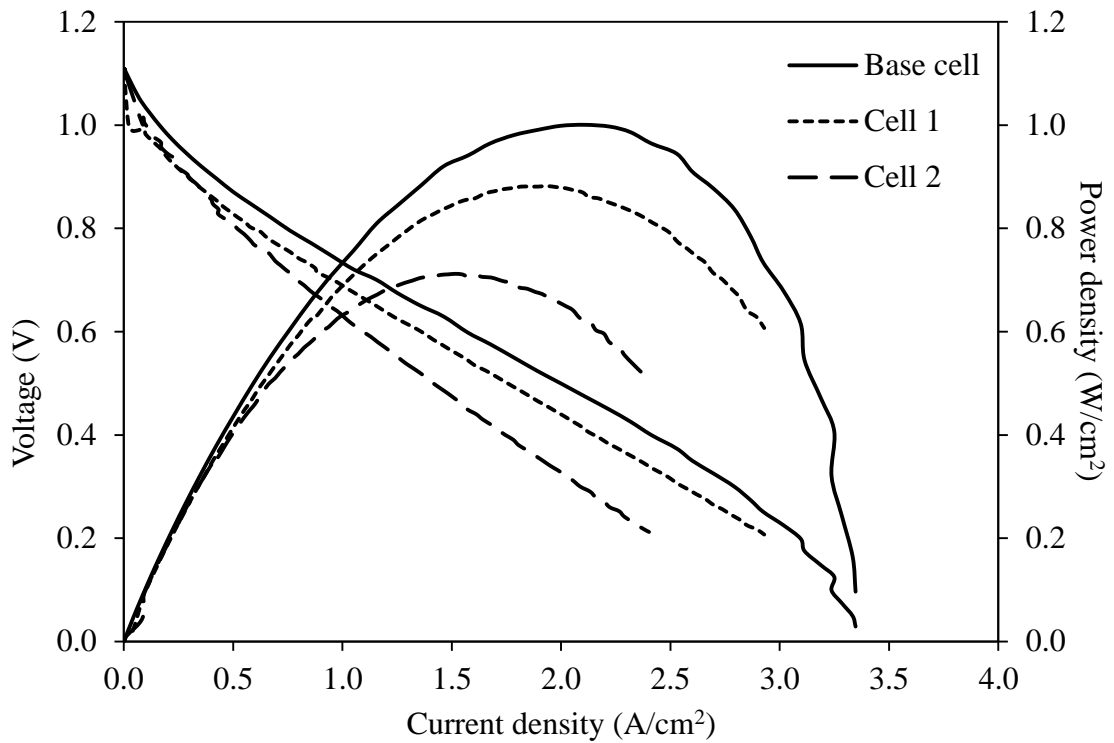


Figure 5.4. Effect of anode support porosity on the cell performance at 800 °C

It is seen that Cell 1 has the highest performance while Cell 2 shows the lowest performance. The porosity of the anode can affect the cell performance in two ways. Firstly, the number of the electrochemical reaction zones in the anode is directly related to the porosity of the anode. In order to obtain high power from a cell, the number of the electrochemical reaction zones should be high which can be achieved at relatively low porosities. Secondly, in addition to the high number of the electrochemical reaction zones, the transport of the reactant to the reaction zones is the other issue which can be easy at relatively high porosities. Therefore, Cell 1, which has the lowest anode porosity, exhibits a lower performance than that of the base cell due to the diffusion polarization as a result of the low porosity, in spite of the increase in the number of the electrochemical reaction zones. Similarly, the low performance of Cell 2, which has the highest anode porosity, can be attributed to the decrease in the number of the electrochemical reaction areas as a result of the high porosity although the transport of the reactant to the reaction zones is relatively easy again due to the high porosity. For the base cell, on the hand, the porosity seems to be optimum for balancing the gas transport and the number of the number of electrochemical reaction zones.

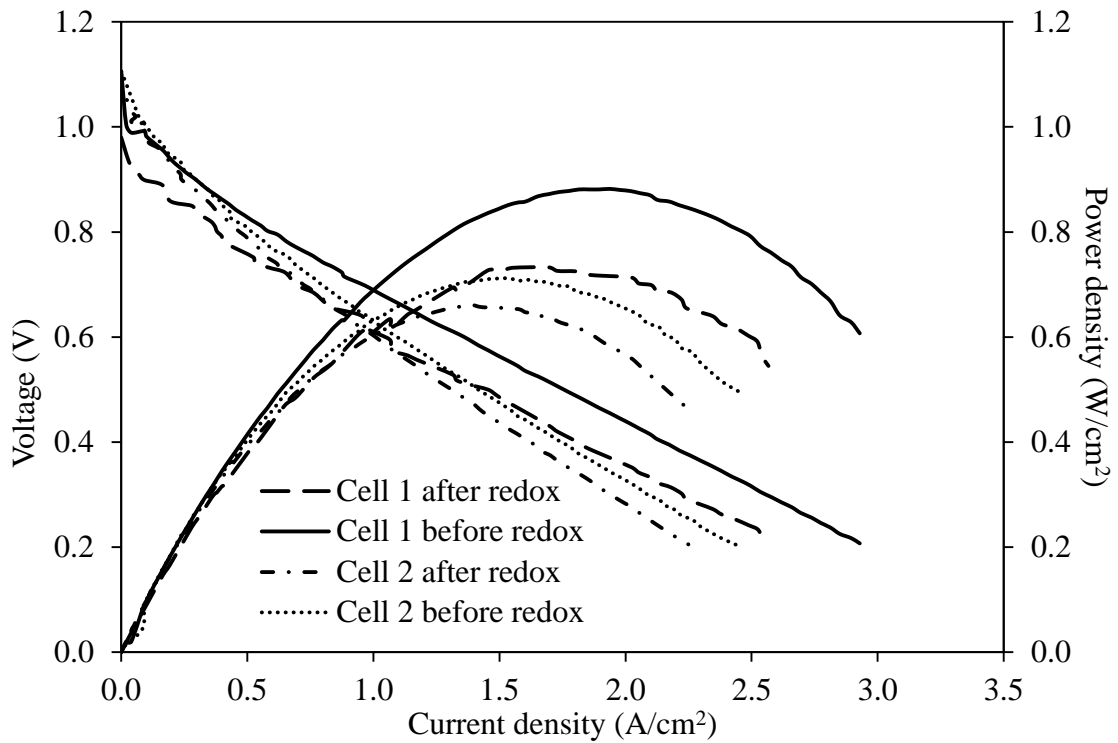


Figure 5.5. Performance curves of Cell 1 and Cell 2 before and after redox at 800 °C

The effect of the anode porosity on the redox stability is shown in the Figure 5.5. Results reveal that the redox stability of an anode supported cell is directly related to the anode porosity. It is seen that both performances of Cell 1 and Cell 2 tends to decrease after one full redox cycle as expected.

However, the rate of decrease in the performance of Cell 1 is about 16.92 % whereas it is only 7.17 % for Cell 2 which is also lower than the base cell with 0.4 anode porosity. This can be explained by the porosities that the cells have. If the volumetric change during redox cycles cannot be accommodated within the structure, cracks will develop. Therefore, the microstructure of the anode support should have enough space for re-oxidation of Ni particle which can be achieved by increasing the porosity. It is seen that the rate of decrease in the cell performance decreasing with the porosity. However, at high porosities the cell performance decreases due to decrease in the number of the reaction zones.

Moreover, the drop in the OCV value of Cell 1 after re-oxidation is measured as 0.126 V while that of Cell 2 is about 0.005 V. This may be attributed to that the stress created

in Cell 1 due to volumetric change during the conversion of Ni-NiO damages not only the anode microstructure but it results in cracks in the electrolyte layer also explaining the higher power loss. However, OCV value measured after redox cycling for Cell 3 does not vary significantly indicating that the decrease in the cell performance is mainly due to the microstructural damage within the anode layer especially due to broken Ni-YSZ network which negatively influences the number of the electrochemical reaction zones.

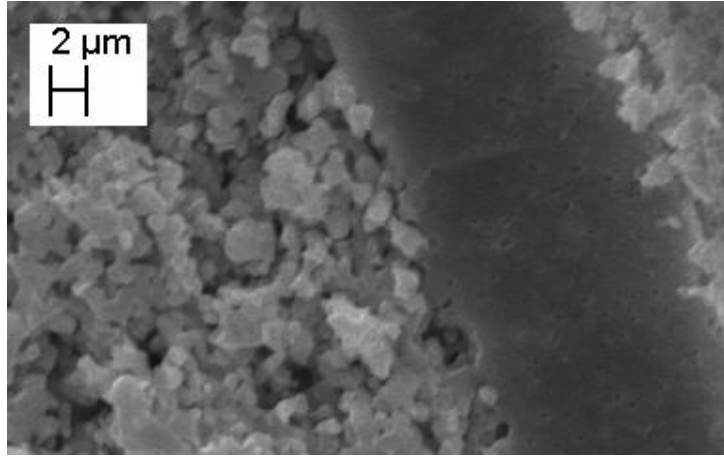
Therefore, the porosity of the anode layer should be decided carefully for not only gas transport or high number of reaction zones, but for high redox stability also.

5.3 Effect of Electrolyte Thickness on the Cell Performance and Redox Behavior

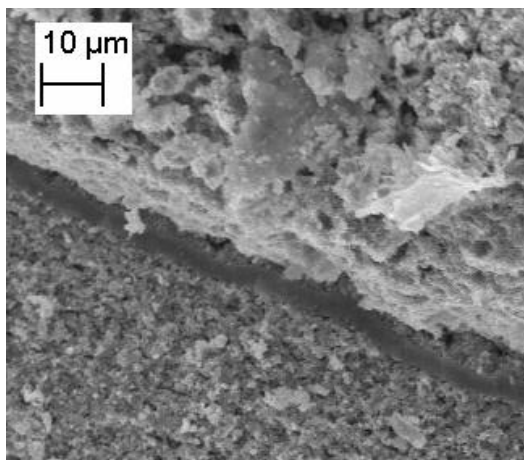
In order to investigate the effect of the electrolyte thickness on the cell performance and the redox stability of the cell, two other cells with 4 μm and 6 μm thick electrolytes are fabricated namely Cell 3 and Cell 4, respectively beside the base cell whose electrolyte is 10 μm thick. However, all cells have the anode porosity of 0.4 according to the pervious results. The thickness of the electrolytes is controlled by changing the blade gap during tape casting. SEM images captured from the cells are illustrated in Figure 5.6. All electrolytes seem to be fully dense and neither crack nor pinhole is visible.

The comparison of the cell performances at an operation temperature of 800 $^{\circ}\text{C}$, on the other hand, is depicted in Figure 5.7. It is seen that the cell performances increases with the decreasing electrolyte thickness. Cell 3 and Cell 4 exhibit 1.16 W/cm^2 and 1.21 W/cm^2 peak power, respectively. The improvement in the cell performance is due to the decrease in the ohmic loss due to decreasing the electrolyte thickness.

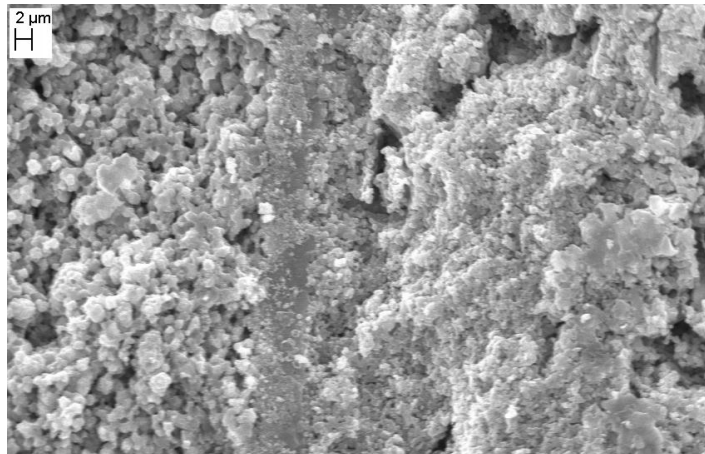
Furthermore, OCV values are very close to each other indicating that the thin electrolytes are also fully dense and crack free which confirm the microstructural investigations.



(a)



(b)



(c)

Figure 5.6. The microstructural images captured from the base cell (a), Cell 3 (b) and Cell 4 (c)

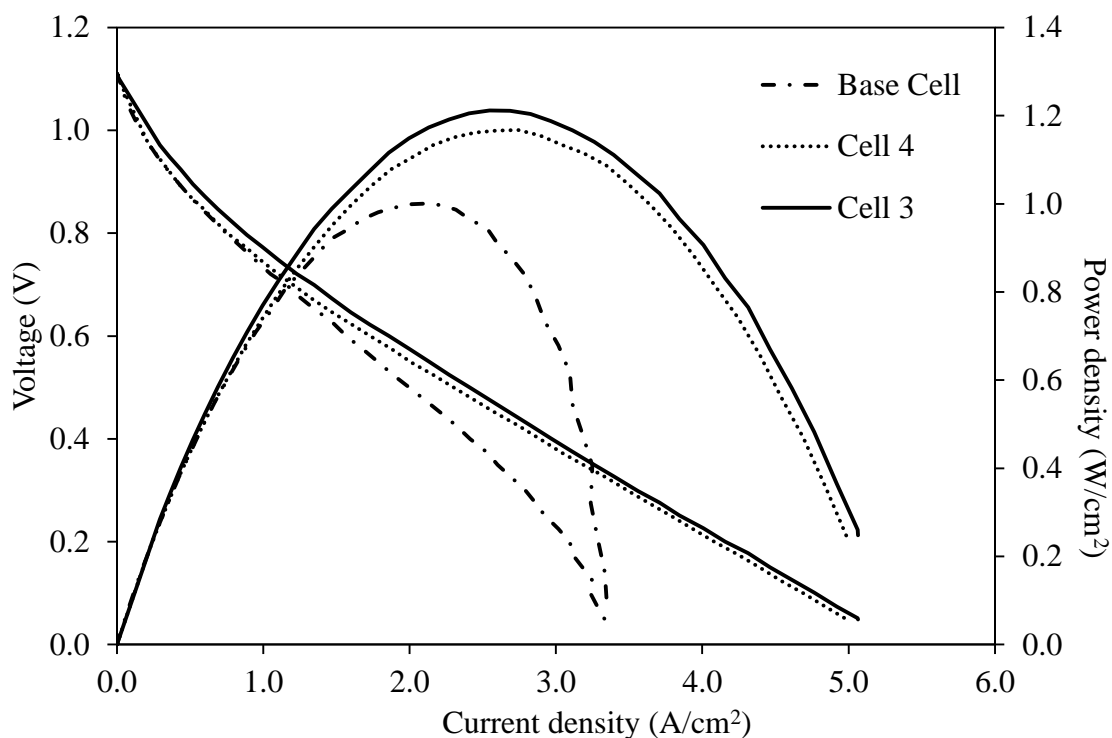


Figure 5.7. Effect of electrolyte thickness on the cell performance at 800 °C

The cell performances after full re-oxidation are shown in Figure 5.8. It is seen that both performances significantly drop after the redox. The rate of performance decrease for Cell 3 is calculated as 22 % while that of Cell 4 is more than 50 %. The results reveal that the loss in the performance as a result of the re-oxidation is more dramatic for the cells having thinner electrolytes. This can be attributed that thin electrolytes cannot tolerate the stress generated as a result of the volumetric changes due to re-oxidation nickel particles. Sudden drops in the OCV values clearly show cracks in the electrolyte layers of both Cell 3 and Cell 4. Since Cell 4 has the thinnest electrolyte, the damage is much more dramatic. According to these results, it can be concluded that the performance of the anode supported cells is improved with decreasing the electrolyte thickness however; the cells with thinner electrolyte cannot keep their structural durability due to the stress generated during re-oxidation of nickel particles.

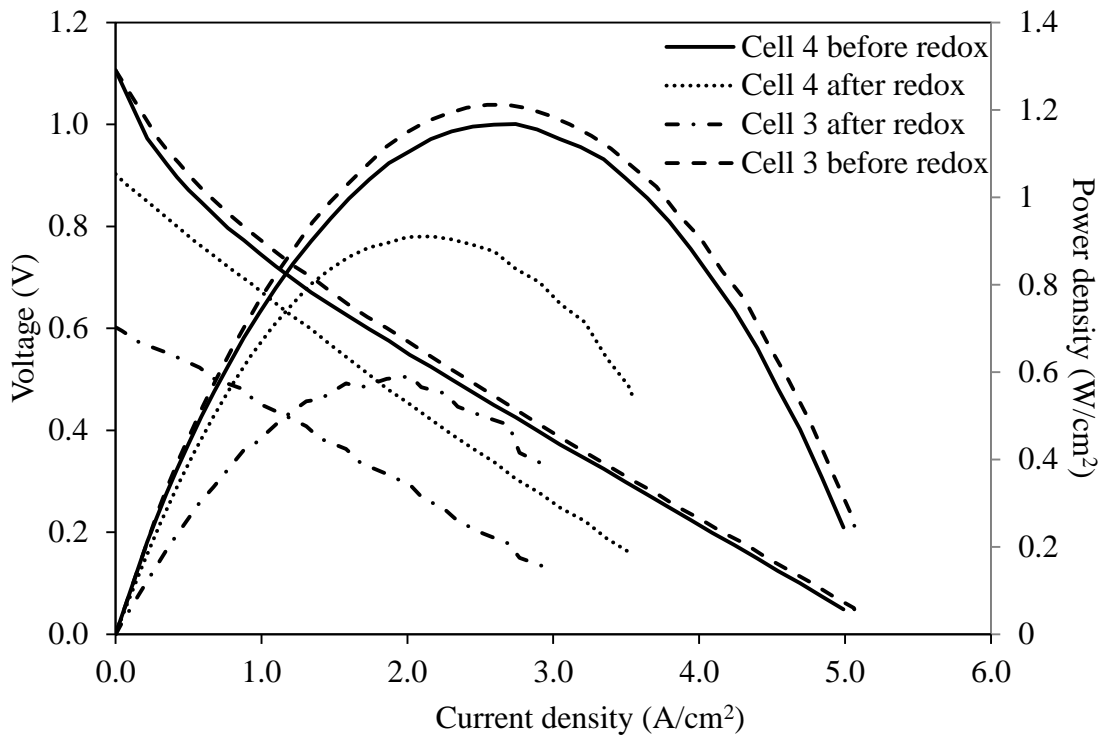


Figure 5.8. The performances of Cell 3 and Cell 4 before and after anode re-oxidation

5.4 Three Point Bending

In order to investigate the effect of redox cycle on the mechanical properties of the cells, the force-displacement curves for the base cell before and after redox are obtained from three point bending test. The results are illustrated in Figure 5.9. It is seen that the maximum force and displacement values obtained from the cell before redox is 4.86 N and 1.026 mm, respectively while these are measured as 2.58 N and 0.68 mm for the cell after redox, respectively. The poor mechanical properties measured the cell subjected to redox can be attributed to the micro-cracks in the electrolyte as well as in the Ni-YSZ ceramic backbone within the anode support. Moreover, the loss in the mechanical properties after one redox cycle can be calculated as around 47% by using the maximum force data. However, the loss in the cell performance was only about 10%. These findings reveal that the mechanical and electrochemical performance of the cell is influenced in different ways after the redox. In spite of the large number of micro-cracks in the anode layer, the electrochemical reaction zones are not influenced at the same rate. Thus, the damage function gets related to the electrochemical results only.

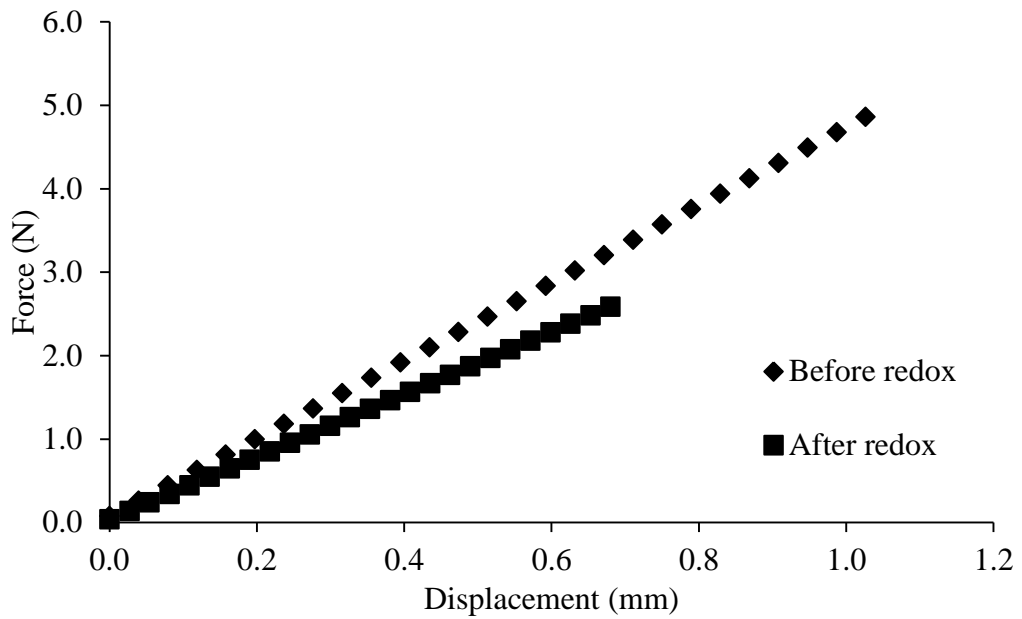


Figure 5.9. Force-displacement curves of cells before and after redox

The fracture surfaces of the specimens are shown in Photo 5.10. It is seen that the crack in the cell before redox follows a straight line whereas after the redox the crack line is not straight. This behavior may be attributed to the non-homogenous oxidation of nickel particles.

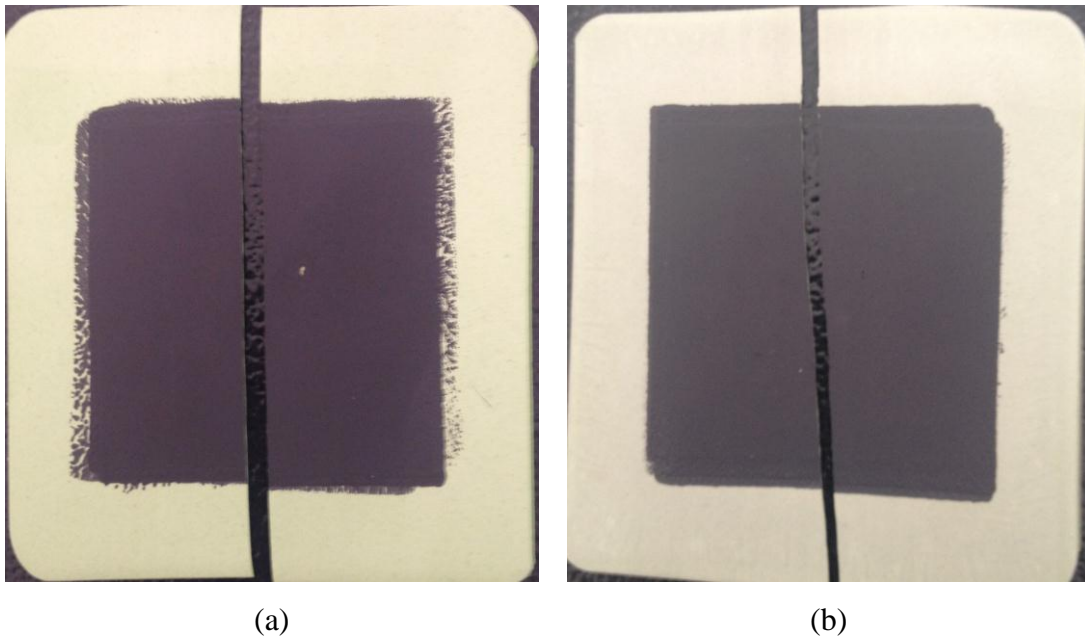


Photo 5.2. Fracture surfaces of the cell before (a) and after (b) redox cycle

CHAPTER VI

NUMERICAL RESULTS AND DISCUSSION

6.1 Validation of the Mathematical Model

The comparison of the performance curves obtained from the experiments with that of estimated from the thermo-fluid model for the base cell is given in Figure 6.1. Values of the fitting parameters used in the model, on the other hand, are listed in Table 6.1. It is seen that the numerical and experimental results agree well. The maximum error is calculated as 6.1 % which can be considered to be acceptable for a finite element simulation. Therefore; the fitting parameters listed in Table 6.2 are used for all simulations.

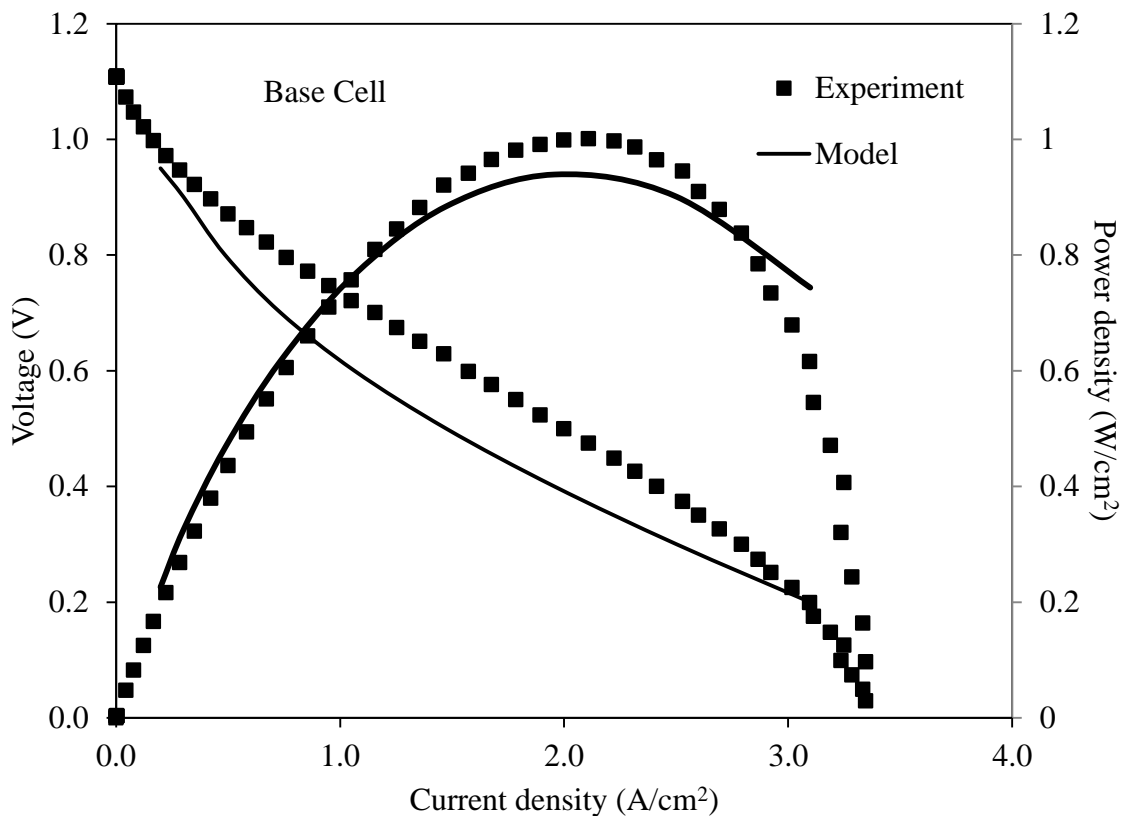


Figure 6.1. Comparison of experimental and numerical performance of the base cell

Table 6.1 Fitting parameters

Parameter	Value
$j_{o,anode}$ (A/m ²)	0.1
$\alpha_{a,anode}$	0.5
$\alpha_{c,anode}$	1.5
$j_{o,cathode}$ (A/m ²)	0.01
$\alpha_{a,cathode}$	3.5
$\alpha_{c,cathode}$	0.5

The similar comparisons for Cell 1-4 are illustrated in Figure 6.2. The mathematical model is found to agree reasonable with experimental data for all cases considered. The maximum error for Cell 1-4 is calculated as around 7%.

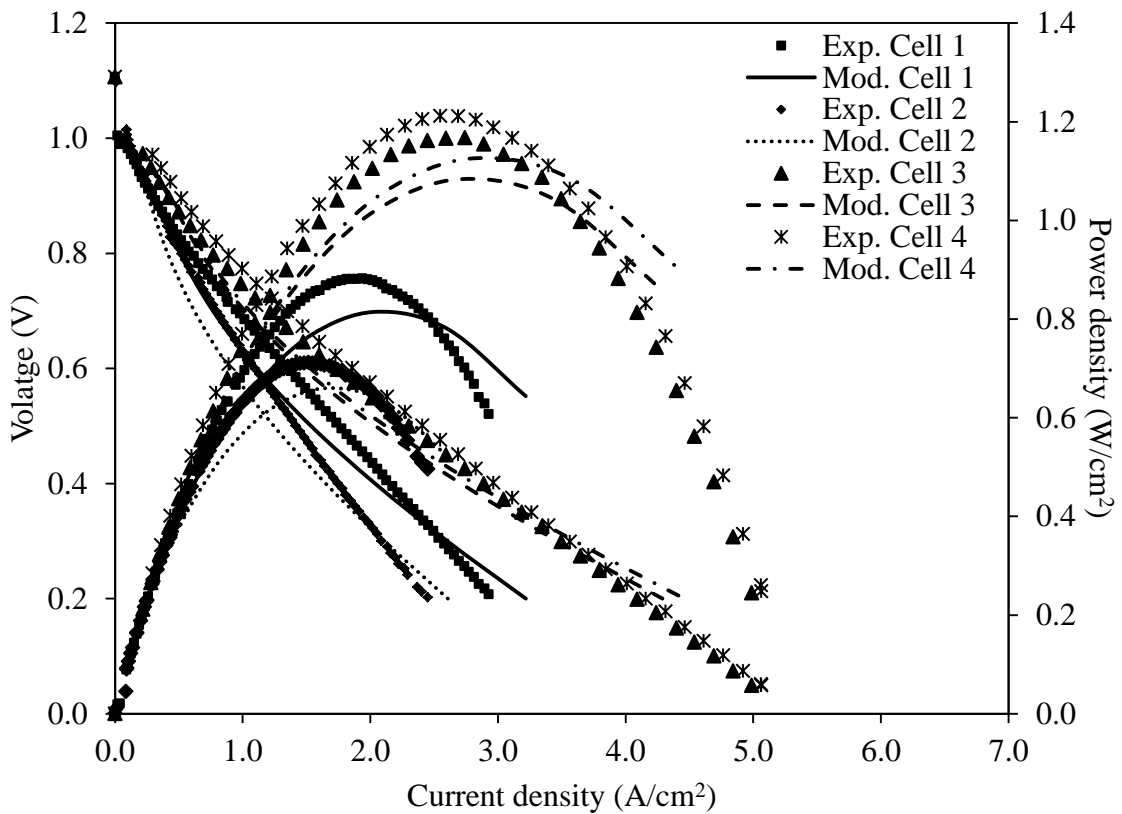


Figure 6.2. Comparison of experimental and numerical performance of Cell 1-4

6.2 Thermo-Fluid Model

The velocity profiles estimated in the anode and cathode flow channels are shown in Figure 6.3(a) and Figure 6.3(b), respectively. It is seen that with the given pressure difference of 10 Pa between the anode exit and inlet, the velocity in the anode flow channel reaches around 3 m/s. Since the pressure difference between the cathode outlet and inlet is defined as 30 Pa, the velocity in the cathode flow channel is found to be higher than that the anode gas flow. The maximum velocity is in the center of the channel for both flow channels as expected.

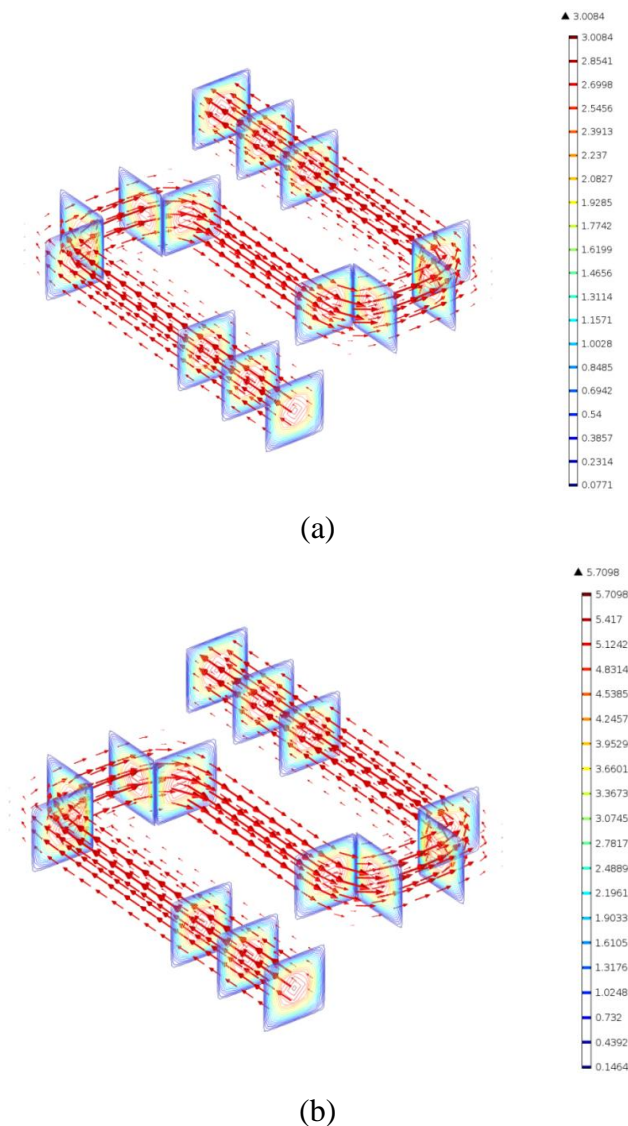


Figure 6.3. Velocity contours (in m/s) at the anode (a) and at the cathode channel (b) of the base cell

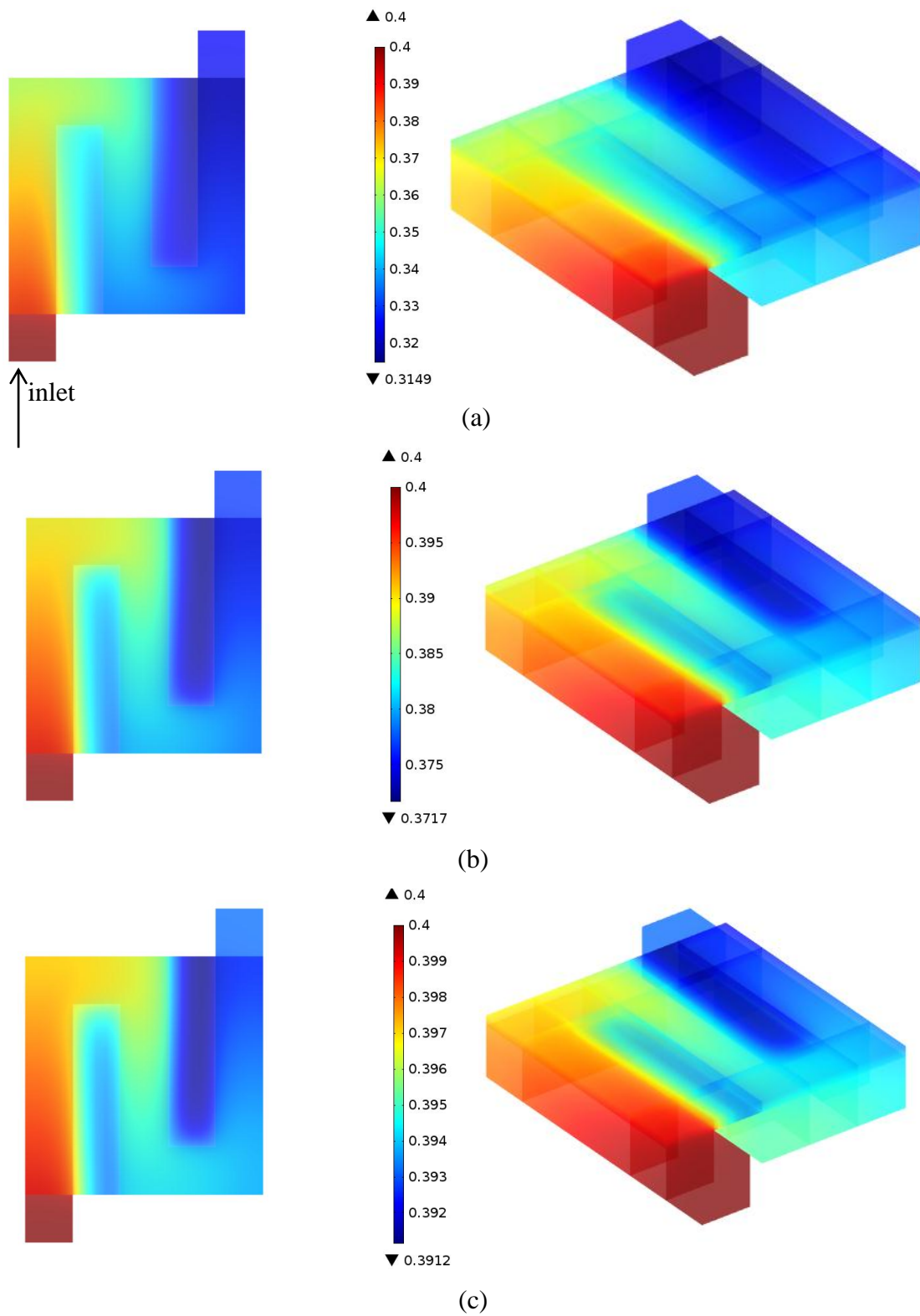


Figure 6.4. Hydrogen distribution (weight fraction) in the anode and in the anode flow channel of the base cell at 0.1 V (a), 0.6 V (b) and 0.9 V (c)

The effect of operation voltage on the hydrogen consumption is illustrated in Figure 6.4. It is seen that the hydrogen weight fraction tends to decrease from the inlet to the outlet at all operation voltages considered due to the continuous hydrogen consumption in the electrochemical reactions. However, the rate of hydrogen consumption is found to increase with the decreasing cell voltage. The difference is more obvious in Figure 6.5. This trend is reasonable since the current density is higher at low voltages. In order to obtain high current density demanded, the number of electrochemical reactions should increase which requires higher amount of reactant. Moreover, the hydrogen concentration seems to be lower in the regions under the interconnector ribs. This can be explained by the limited diffusion of hydrogen gas as well as the limited removal of the water generated because of the interconnector ribs.

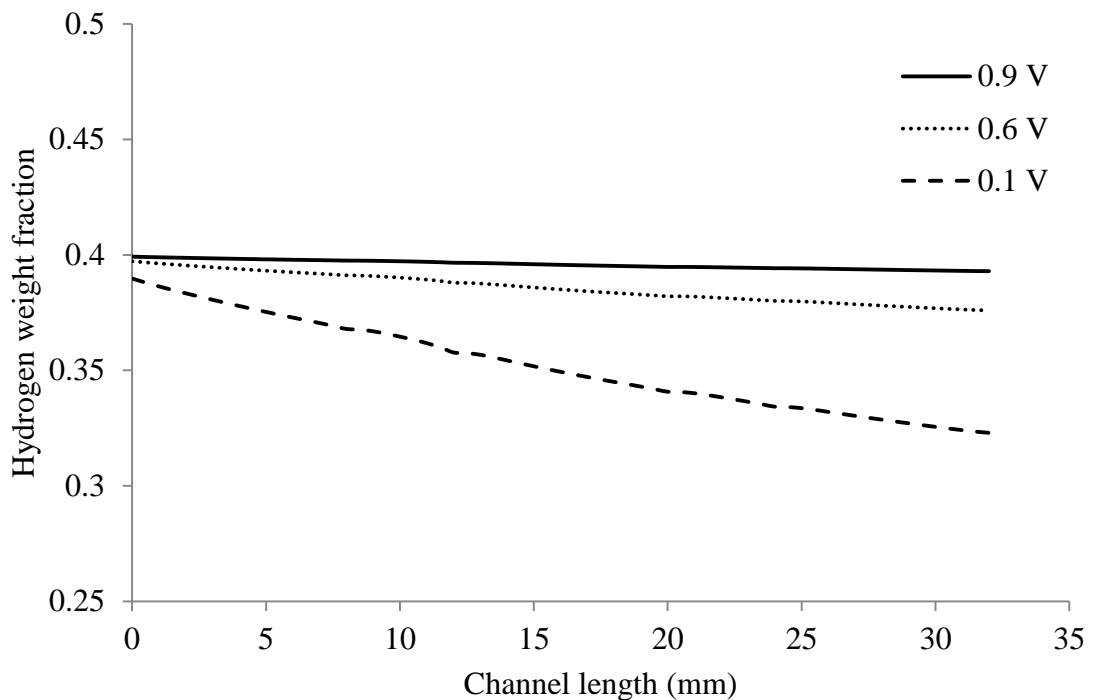


Figure 6.5. Hydrogen consumption in the base cell along with the anode flow channel at various operational voltages

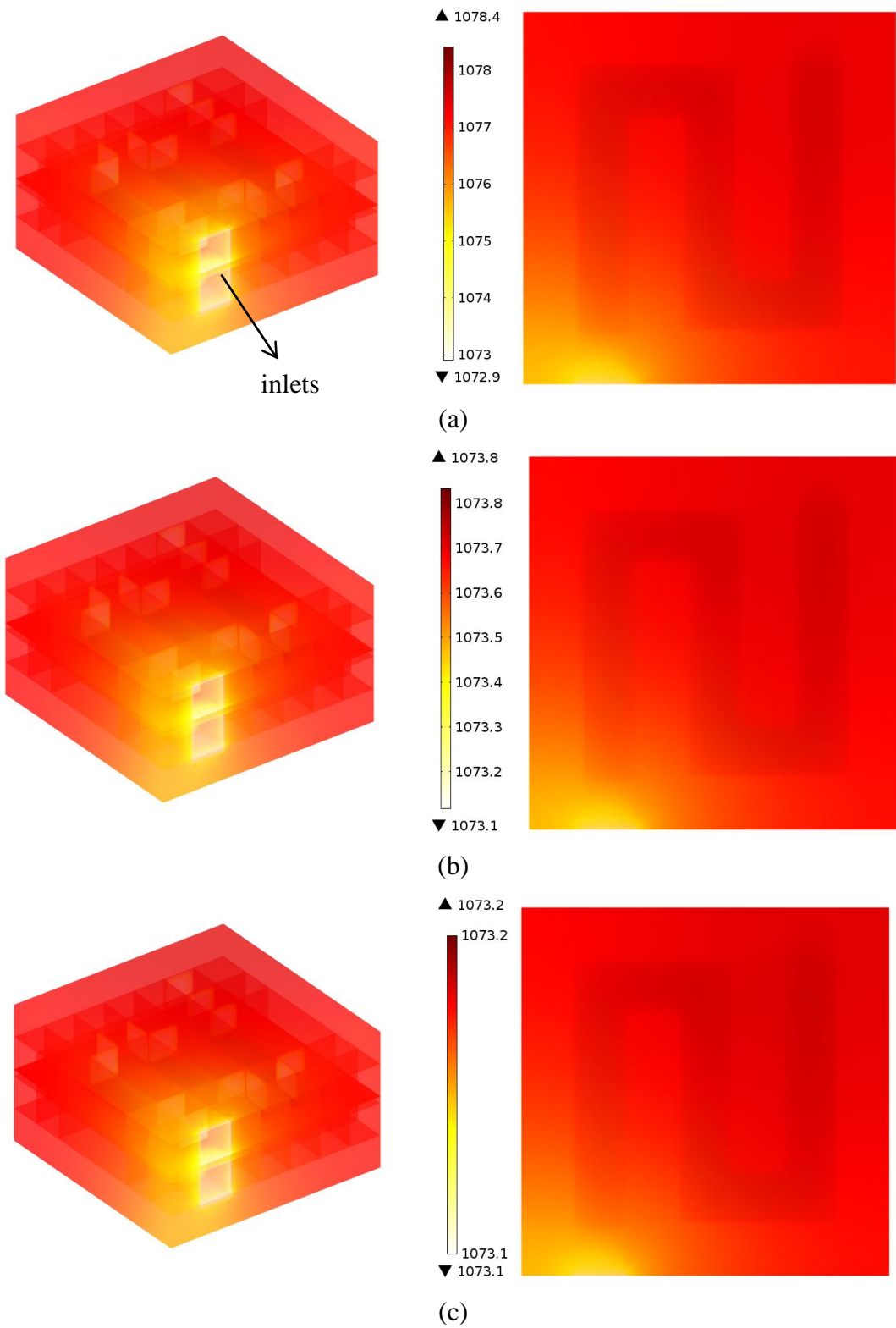


Figure 6.6. The estimated temperature profile (in K) in the base cell at 0.1 V (a), 0.6 V (b) and 0.9 V (c)

The steady-state temperature distribution in the cell during the operation at various voltages is shown in Figure 6.6. It is seen that the temperature is relatively lower at the inlet sections of the cell in all cases. This can be explained by the continuous heat generation as a result of the electrochemical reaction. In addition, the higher temperature of the flow channels indicates that some amount of the heat generation is removed by convection. Furthermore, the temperature of the cell is found to increase at all operation voltages investigated. On the other hand, the rate of increase in the temperature of the cell is calculated to be higher for low voltages. It is due to the higher current densities at low voltages. The amount of heat generation in the cell is directly proportional to the operational current density. The higher the current density, the higher the amount of heat generation is as given in Equation (4.16). Therefore, the temperature increase in the cell at low voltages is found to be higher than that of at high operation voltages.

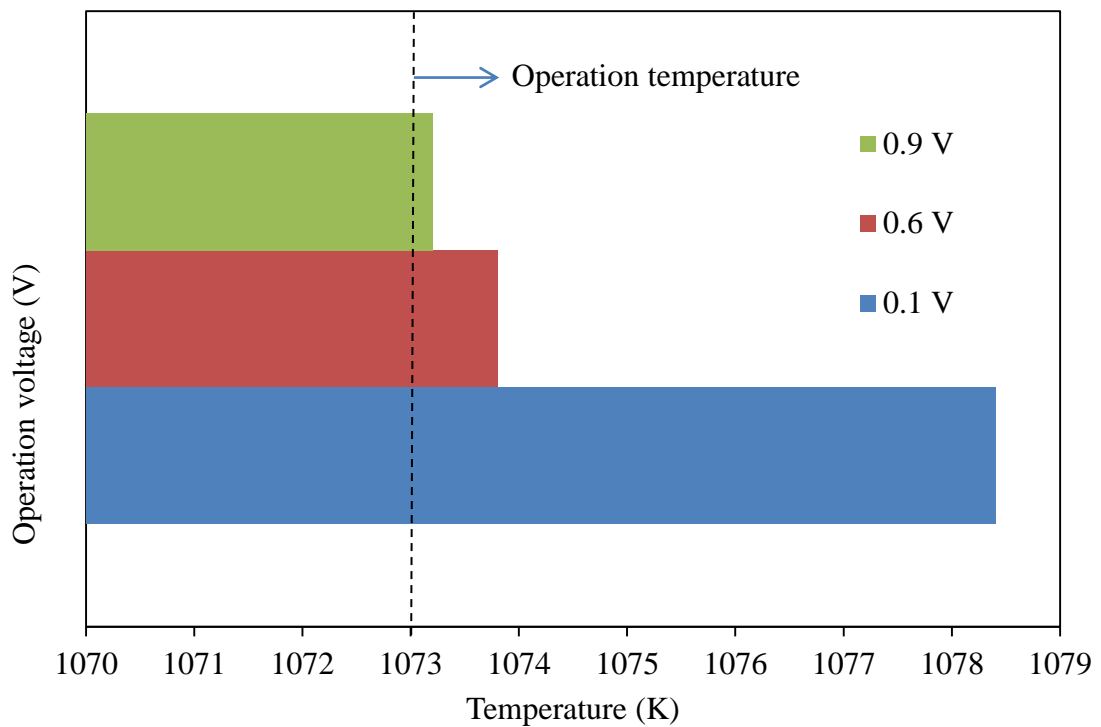


Figure 6.7. Comparison of the maximum temperatures in the base cell at various operation voltage

The maximum base cell temperatures at various operational voltages are compared in Figure 6.7. The maximum temperature of the cell is estimated to be 1073.2 K and 1073.8 K at an operation voltage of 0.9 V and 0.6 V, respectively. This small increase in the cell is reasonable since the cell has only 1cm^2 active area and the electrochemical heat generation is lower at high operation voltages. Although the cell has only 1cm^2 active area, the rate of increase in the cell temperature during the operation at 0.1 V is about 5 K. Since the temperature gradient in the cell creates thermal stress because of the thermal expansion mismatch of the cell components, the operation voltage should be carefully decided especially for the large cells in order to avoid cell cracking.

The comparison of the hydrogen consumption of Cell 1-4 and the base cell is given in Figure 6.8 for 0.6 V operation voltage which is a typical operation voltage for SOFCs. It is seen that the numerical results agree reasonable with the experimental performance curves given in Figure 5.4 and Figure 5.7 and the numerical performance curves given in Figure 6.2. The electrochemical performances of Cell 1 having 0.3 anode support porosity and Cell 2 having 0.5 anode support porosity are found to be lower than that of the base cell. The hydrogen consumption of these cells (Figure 6.8(a) and Figure 6.8(b)) is estimated to be relatively lower confirming the experimental measurements. The lower performance of Cell 1 may be due to the difficult hydrogen gas diffusion to the reaction zones with decreasing the porosity while Cell 2 provides lower performance because of the decrease in the number of the electrochemical reaction zones with increasing the anode porosity. Similarly, the electrochemical performances of Cell 3 having $4\mu\text{m}$ electrolyte thickness and Cell 4 having $6\mu\text{m}$ electrolyte thickness are found to be higher than that of the base cell. The hydrogen consumption of these cells (Figure 6.8(c) and Figure 6.8(d)) is obtained to be relatively higher confirming the experimental measurements. The improved performance thus the higher hydrogen consumption of Cell 3 and Cell 4 can be attributed to the decrease in the ohmic loss with decreasing the electrolyte thickness.

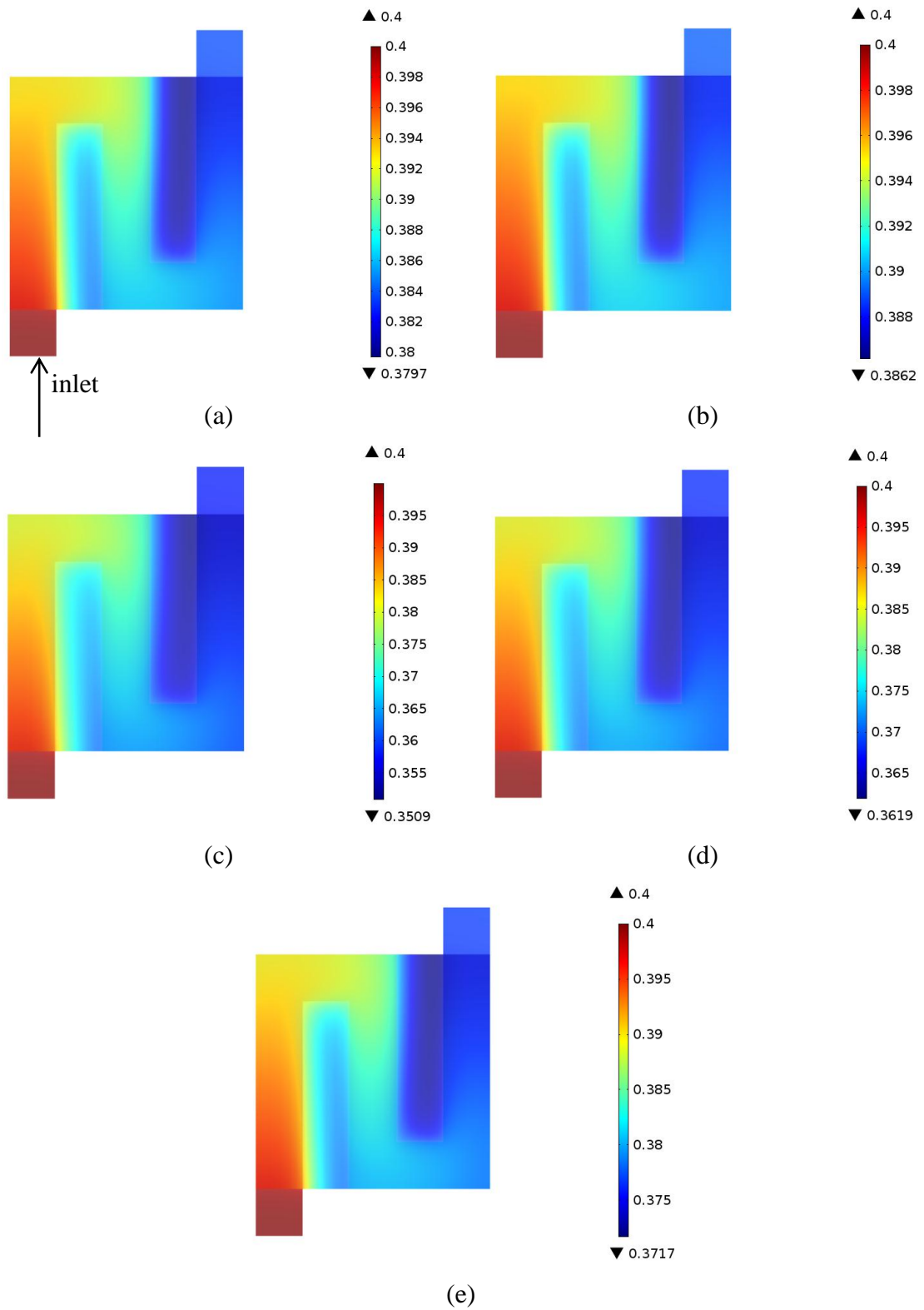


Figure 6.8. Hydrogen consumption (weight fraction) in Cell 1-4 (a-d) and the base cell (e) at 0.6 V

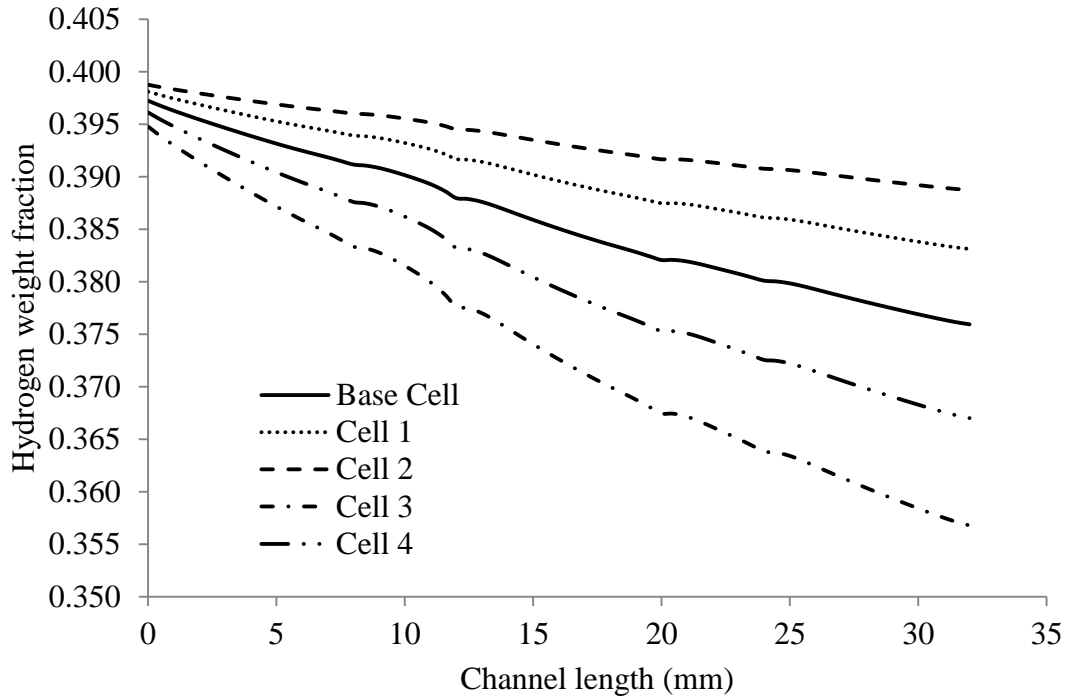


Figure 6.9. Hydrogen consumption along with the anode flow channel

The variation of the hydrogen concentration on the electrolyte/anode interface along with the anode flow channel for Cell 1-4 and the base cell is compared in Figure 6.9 at an operation voltage of 0.6V. It is seen that the hydrogen concentration decreases continuously along with the anode flow channel due to the continuous electrochemical reactions in all cases considered as expected. However, the rates of the hydrogen concentration drop of cells are different since the performances of cells are different. Thus, the hydrogen consumption of Cell 3, which has the highest performance, is the highest and that of Cell 2, which has the lowest performance, is the lowest. The temperature distributions of Cell 1-4 and the base cell are compared in Figure 6.10 and the maximum temperatures are given in Figure 6.11 again for the operation voltage of 0.6 V. The maximum cell temperature is found to be 1073.6 K for Cell 1, 1073.3 K for Cell 2, 1075.9 K for Cell 3, 1075 K for Cell 4 and 1073.8 K for the base cell. It is seen that Cell 2 having the lowest performance shows the smallest temperature increase and Cell 3 having the highest performance provides the largest temperature increase. At a given operation voltage, the electrochemical heat generation is expected to be higher for the cells having relatively higher performance. Therefore, this trend in the temperature profiles is reasonable and mainly due to the change in the electrochemical heat generation due to the change in the cell current density or the performance.

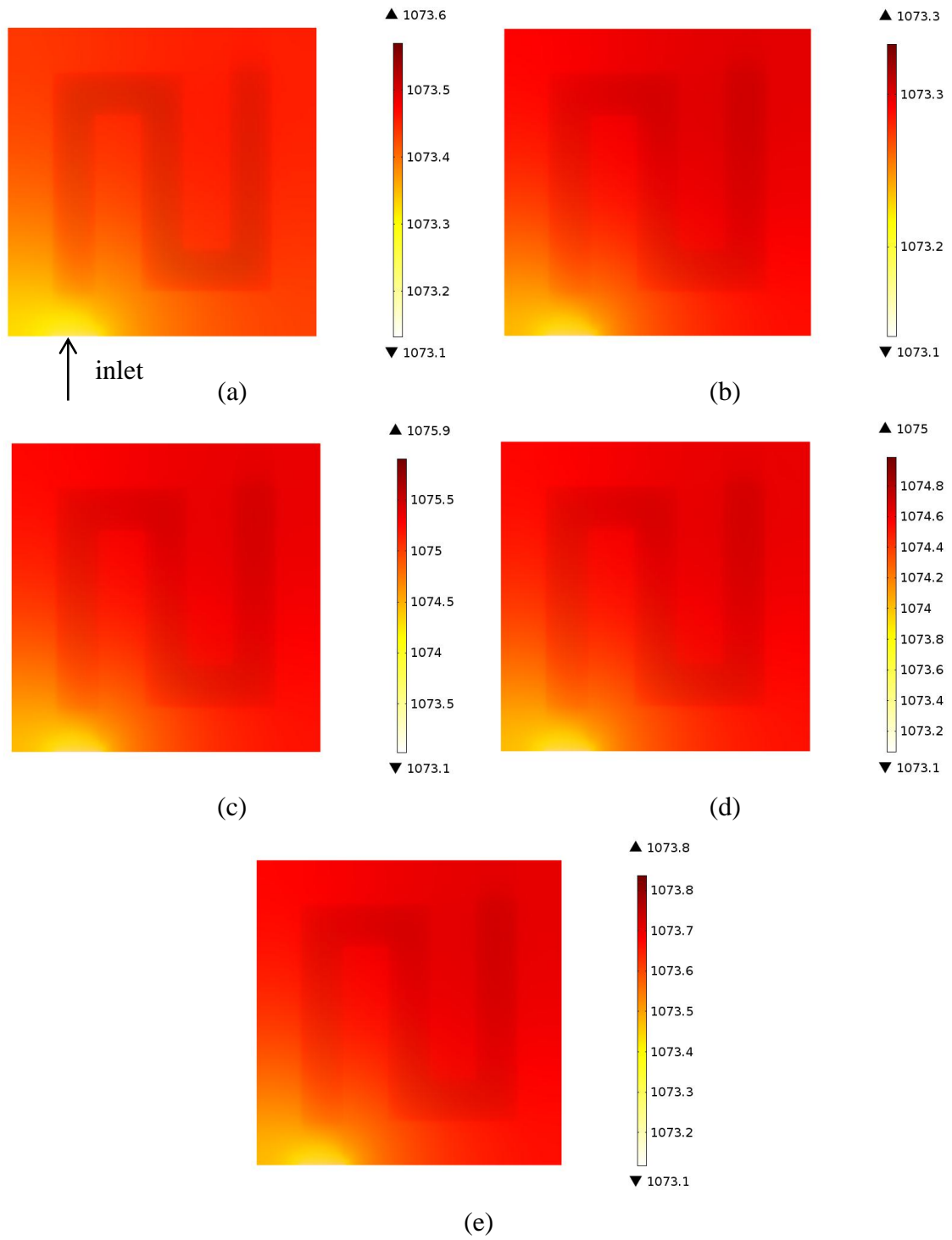


Figure 6.10. The temperature profiles (in K) in Cell 1-4 (a-d) and the base cell (e)

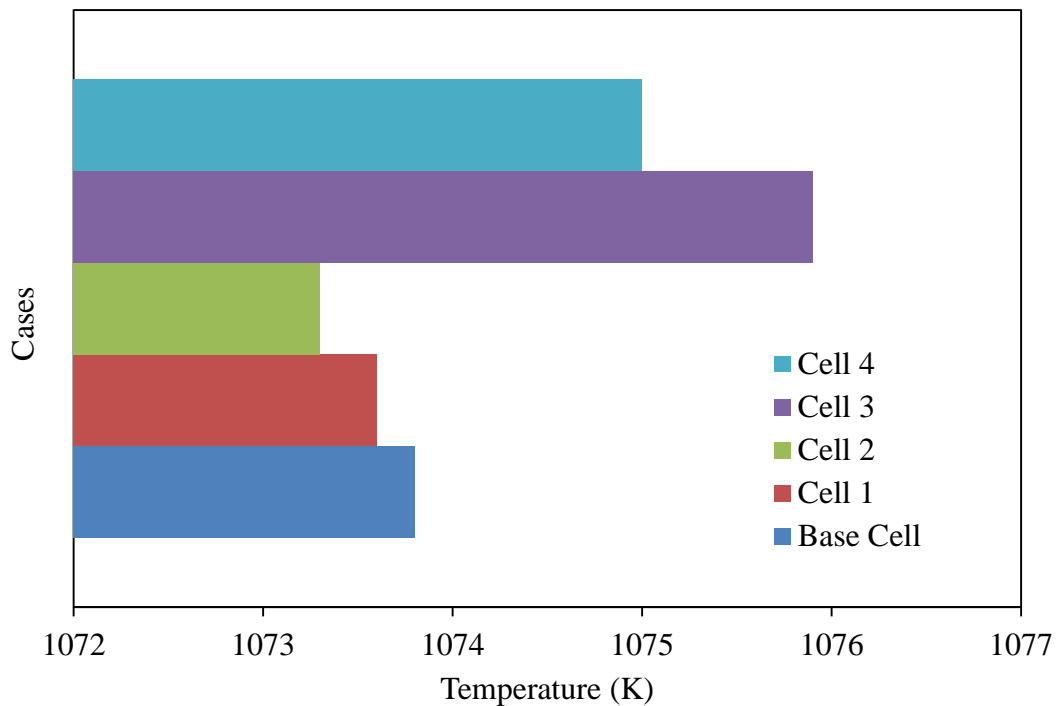


Figure 6.11. The maximum temperatures in Cell 1-4 and the base cell

6.3 Solid Mechanics Model

6.3.1 Base cell

The mechanical stress estimated is due to only the temperature gradient and the boundary load is shown in Figure 6.12. It is seen that the stress values are very small. The results show that the thermal stress increases with the decreasing operation voltage confirming the temperature profile given in Figure 6.8. At high current densities, the temperature differences in the cell increase due to the increase in the electrochemical reactions leading to higher amount of heat generation. Therefore, the maximum thermal stress as a result of the thermal expansion mismatch occurs at low operation voltages. The maximum stress is calculated as 2.63 MPa and 3.36 MPa at 0.9 V and 0.6 V, respectively while that of at 0.1 V is 9.11 MPa.

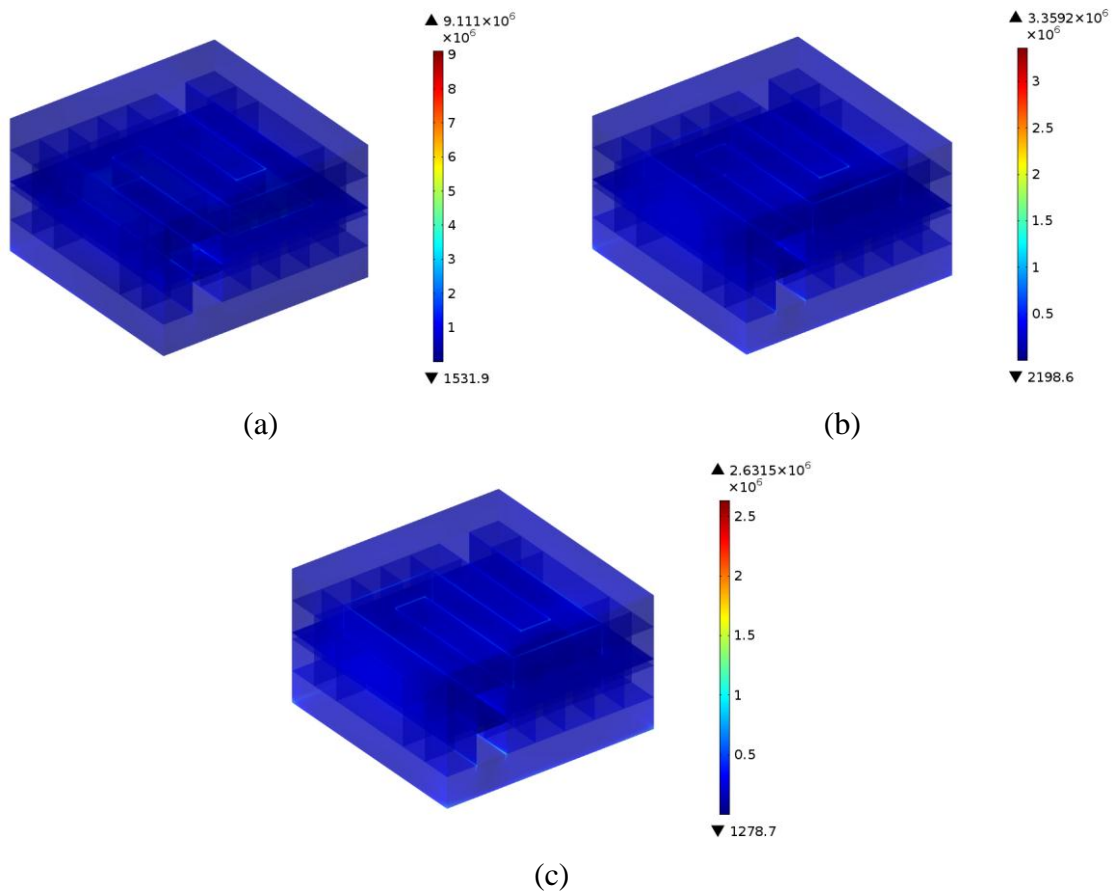


Figure 6.12. Estimated stresses (in Pa) at 0.1 V (a), 0.6 V (b) and 0.9 V (c) in the base cell

The contribution of the re-oxidation strain to the stress distribution and deformations with a scale factor of 20, on the other hand, is shown in Figure 6.13. The maximum stress is found to increase to 263 MPa due to full re-oxidation of nickel particles in the anode support. The most critical component seems to be MEG especially the regions in contact with the interconnector ribs as shown in the bottom of the figure.

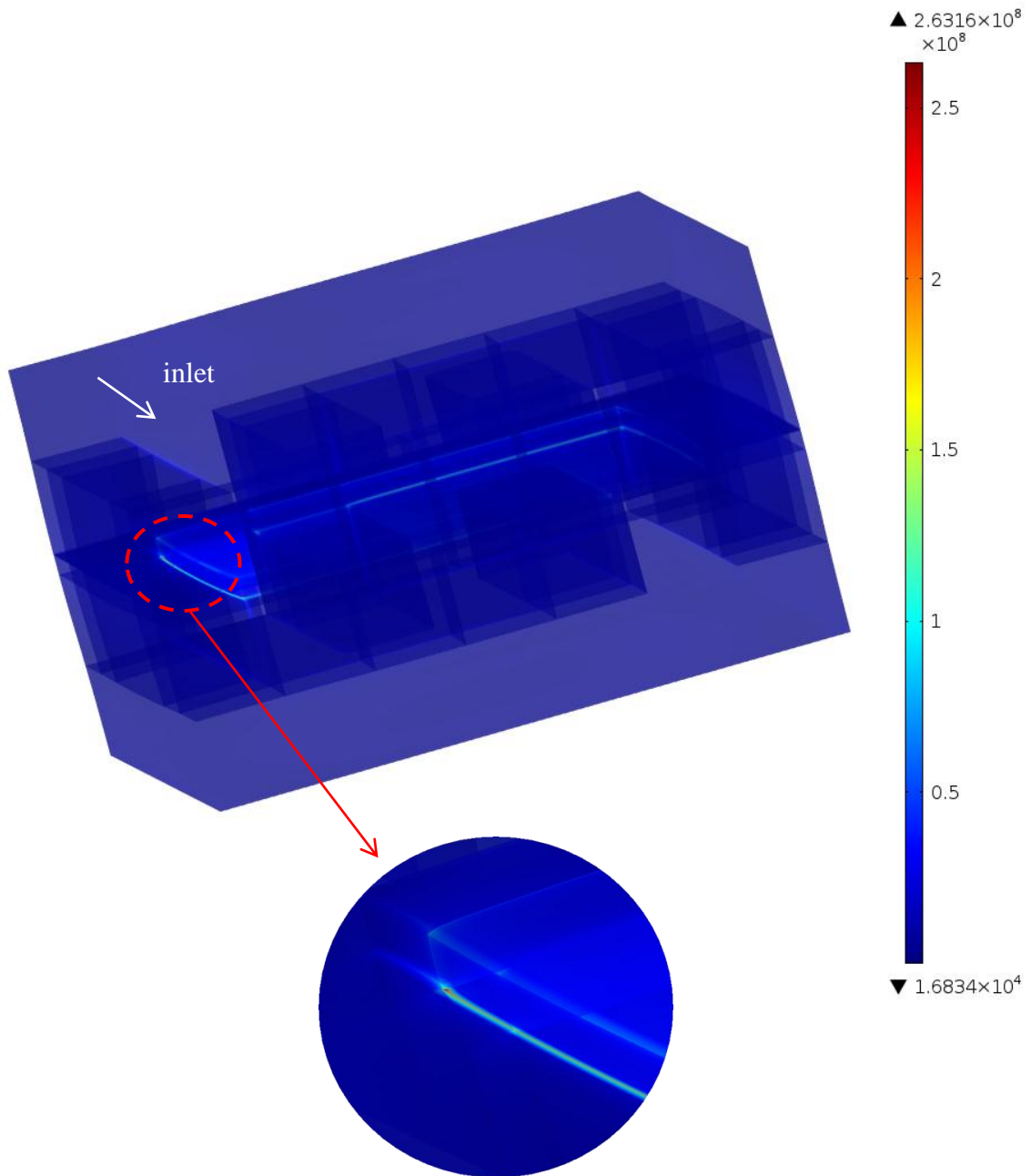


Figure 6.13. The calculated stress distribution (in Pa) in the base cell after one redox cycle

The damage value for the base cell numerally calculated after full oxidation as in the case of the experiment is shown in Figure 6.14. It is seen that the damage is varying from 2.9735 to 3.033. This almost homogenous behavior is reasonable since the temperature distribution in the anode is almost uniform and the re-oxidation strain is assumed to be isotropic. In addition, the strain thus the damage is found to be slightly

higher in the flow channel regions of the anode than that of the anode regions which are in contact with the interconnector. This behavior can be attributed to the boundary load applied on the top of the cathode interconnector. Since, there is no obstacle in the anode regions which is in contact with the anode flow channel; the strain thus the damage is estimated to be higher for these regions.

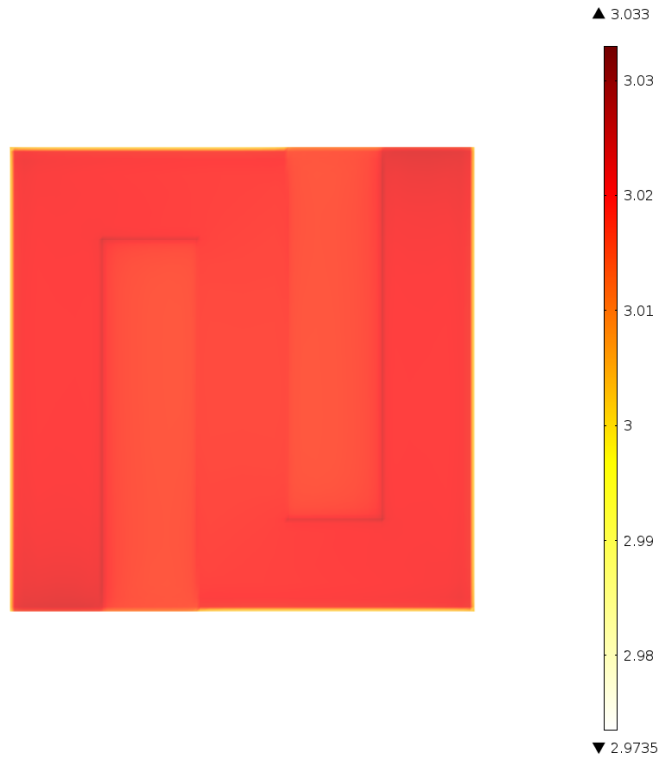


Figure 6.14. The distribution of the damage function in the anode support layer of the base cell after full oxidation

After the estimation of the damage function, the corrected damage parameter, B_{cor} , is determined by dividing the rate of the decrease of the cell performance after redox which was 0.0989 to the volume averaged numerical damage value which is calculated to be 3.019. This can be formulized as follows:

$$B_{cor} = \left(\frac{PP_{before\ redox} - PP_{after\ redox}}{PP_{before\ redox}} \right) / D \quad (6.1)$$

where PP is the peak power and D is the numerical damage obtained from Equation (4.30) while B is equal to 1. The corrected damage calculated by using Equation (4.30) with the corrected damage coefficient is shown in Figure 6.15.

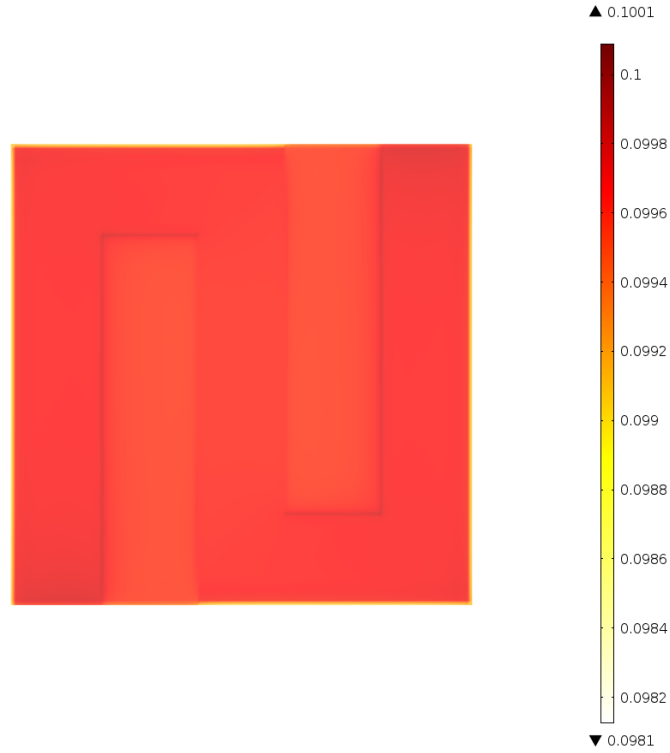


Figure 6.15. The corrected damage distribution in the anode layer of the base cell after full oxidation

The effect of degree of oxidation on the damage distribution is given in Figure 6.16. The degree of oxidation (DoO) presents the ratio of the amount of nickel particle oxidized to the total amount. Therefore, the strain due to re-oxidation is directly proportional to the DoO as formulated in Equation (4.32). The damage is found to increase with the increasing of DoO as expected since the number of volumetric growth during re-oxidation, which creates damage, increases with the increasing DoO as listed in Table 6.2.

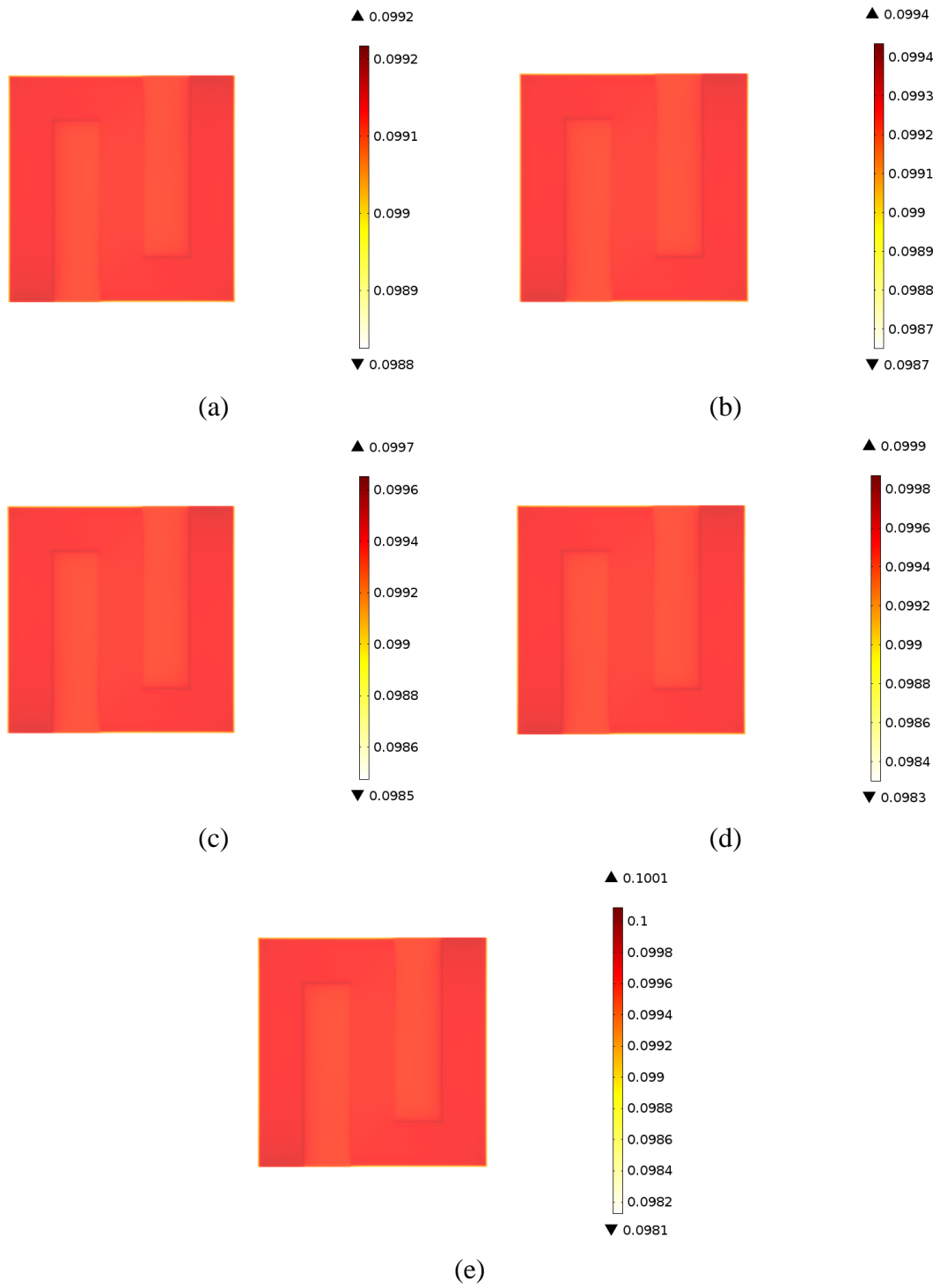


Figure 6.16. The effect of degree of oxidation after operation at 0.6 V: (a) DoO=0.2, (b) DoO=0.4, (c) DoO=0.6, (d) DoO=0.8 and (e) DoO=1.0

Table 6.2. Maximum damages in the base cell for various DoO

DoO	Maximum damage (%)
0.2	9.92
0.4	9.94
0.6	9.97
0.8	9.99
1.0	10.01

6.3.2 Effect of anode porosity on the damage function

The effect of anode porosity on the damage function is shown in Figure 6.17. The estimated stress distribution is also given at right hand side in the figure. All results are obtained for 0.6 V operation. The corrected damage coefficient for Cell 1 and Cell 2 is calculated as 0.055 and 0.020, respectively by using Equation (6.1). It is seen that the resulting damages numerically calculated are in agreement with the experimental performances measured after the redox cycle. The damage is found to be higher for Cell 1 which shows the highest performance loss after redox and Cell 2 having the lowest performance loss after redox gives the lowest damage as expected. The stress distributions are also comparable with the experimental observations. It is seen that the stress in Cell 1 is higher than that of in Cell 2 explaining the OCV drop of Cell 1 due to micro-cracks in the electrolyte layer. In addition, the modulus of elasticity values used in the model decreases with the increasing porosity. This may be another reason for obtaining low stress values at high porosities.

6.3.3 Effect of the electrolyte thickness on the damage function

The variation of the damage with the electrolyte thickness is illustrated in Figure 6.18. The corresponding stresses are also included in the right hand side of the figure. The corrected damage coefficient for Cell 3 and Cell 4 is calculated as 0.170 and 0.073, respectively by using Equation (6.1). The maximum damage is found to occur in MEG especially at the interface between the interconnector and MEG. Since the re-oxidation strain is the same for all cases, the stress values seem to decrease with the decreasing electrolyte thickness as expected.

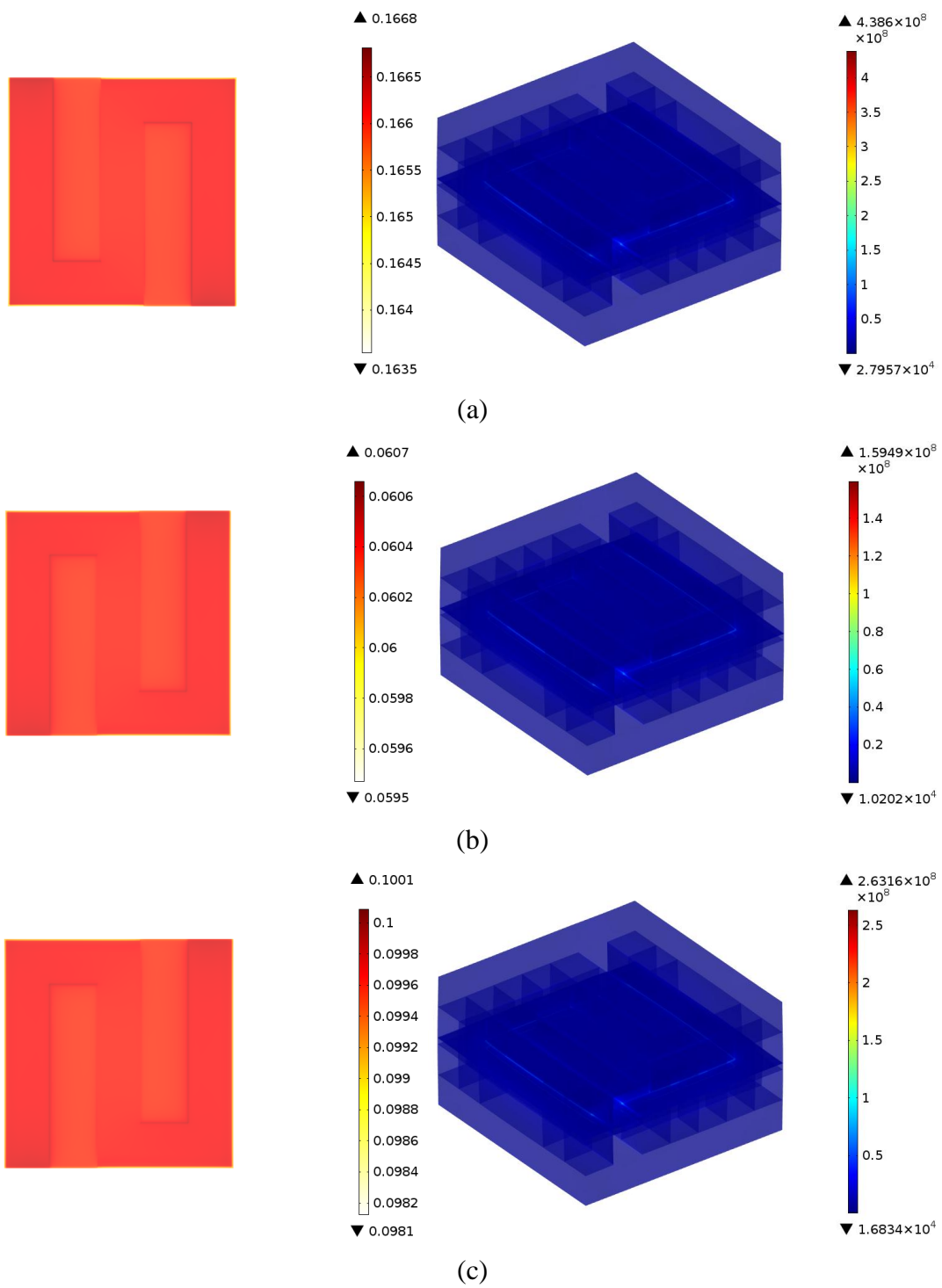


Figure 6.17. Damage (left) and stress (right) distribution in Cell 1 (a), Cell 2 (b) and the base cell (c)

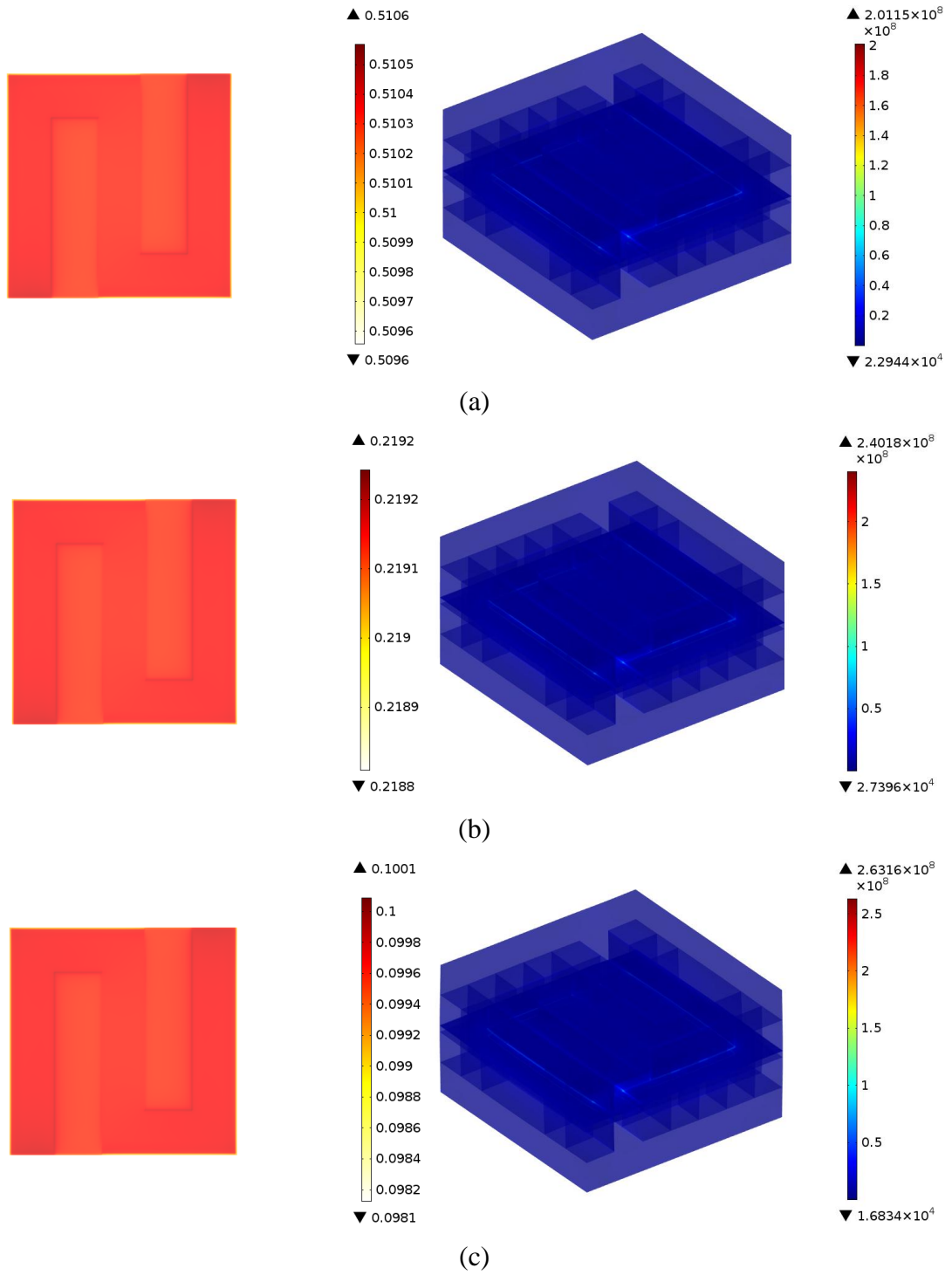


Figure 6.18. Damage (left) and stress (right) distribution in Cell 3 (a), Cell 4 (b) and the base cell (c)

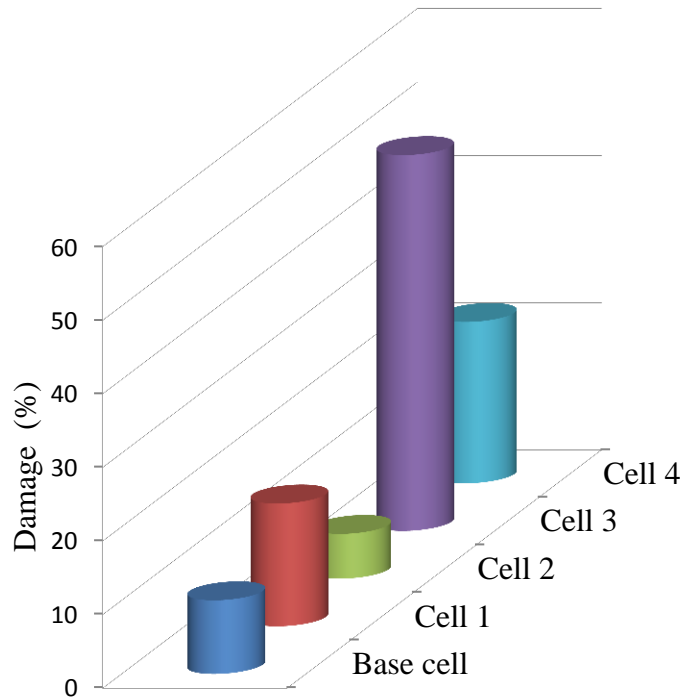


Figure 6.19. Comparison of the maximum damage for Cell 1-4 and the based cell

The maximum damages numerically calculated for Cell 1-4 and the base cell are compared in Figure 6.19. It is seen that Cell 3 shows the highest maximum damage among the cases considered. Similarly, the rate of performance degradation of Cell 3 after the redox was experimentally found to be the highest. Thus, the damage representing the mechanical damage in the triple phase boundaries is found to be highest for Cell 3.

6.4 Modeling of the Damage Coefficient

According to the experimental and numerical analyses, the variation of the damage coefficient (B) with the anode porosity and the electrolyte thickness is modeled by using 3D surface fitting method. The obtained surface is depicted in Figure 6.20. It is seen that the generated surface shows good agreement with the experimental and numerical analyses. The function of the created surface is given in Equation (6.2) while the constants are listed in Table 6.3.

$$B = a + b/p + ct + dt^2 \quad (6.2)$$

In the above equation, p stands for the anode support porosity and t is the electrolyte thickness.

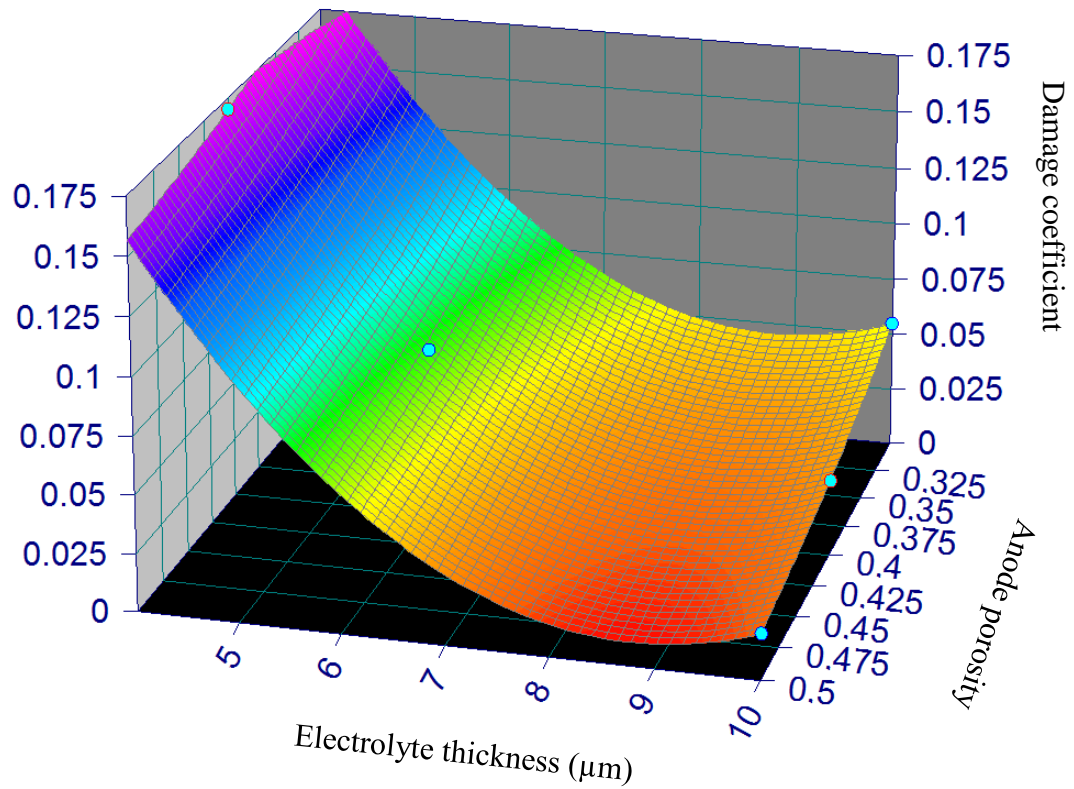


Figure 6.20. 3D surface modeling result of the damage coefficient

Table 6.3. Surface fitting parameters

Parameter	Value
a	0.4524
b	0.02626
c	-0.11270
d	0.0064

The comparison of the damage coefficient obtained from Equation (6.3) and that of experimentally and numerically obtained is given Figure 6.21. The Chisquare parameter (R^2) is calculated as 0.9999 for the used model.

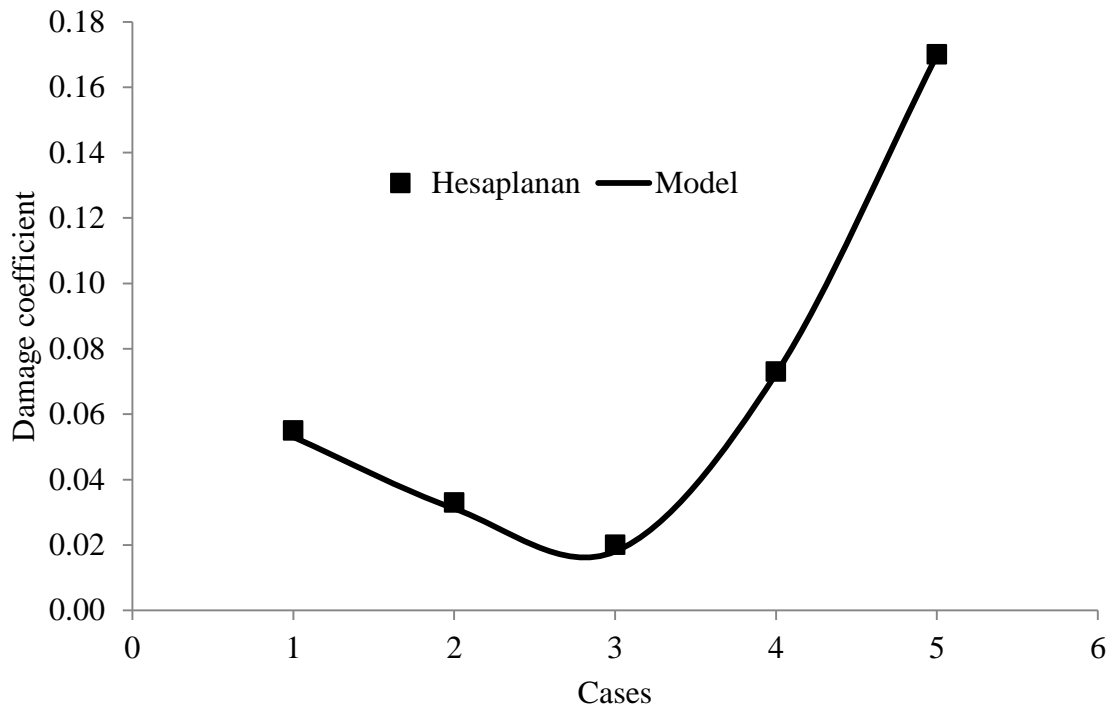


Figure 6.21. Model validation for the damage coefficient

CHAPTER VII

CONCLUSION

In this study, the effects of anode fabrication parameters on the anode supported cell performance and redox stability of the anode supported cells are investigated experimentally and numerically. In the experimental study, anode supported cells having various anode porosities and electrolyte thicknesses are developed and tested. In the theoretical program, a mathematical model is developed presenting the SOFC operation and a redox model is also implemented into the model in order to investigate the mechanical damage in the electrochemical reaction zones that affect the cell performance. According to the experimental and numerical results, following conclusions are obtained:

- The anode porosity is found to have a significant effect on the cell performance. At lower porosities, the cell performance is found to degrade as a result of the gas diffusion problem while at higher porosities the loss in the cell performance is due to the decrease in the number of the electrochemical reaction zones. Thus, the porosity of the anode layer is optimized to be 0.4.
- The cell performance is found to improve with the decreasing of the electrolyte thickness. The cell with 4 μm thick electrolyte exhibits the highest performance.
- The redox stability of the cell is found to be improved with the increasing anode support porosity and the electrolyte thickness.
- The mathematical model is found to agree reasonable with experimental data.
- The numerical results show that the mechanical damage in the cell increases with the decreasing anode porosity and the electrolyte thickness.
- The most critical regions are found to be the interfaces between the MEG and interconnector ribs.

REFERENCES

- Akhtar, N., Decent, S.P., Loghin, D. and Kendall, K., “A three-dimensional numerical model of a single-chamber solid oxide fuel cell”, *International Journal of Hydrogen Energy*, 34, 8645–8663, 2009.
- Ali, A., Wen, X., Nandakumar, K., Luo, J. and Chuang, K.T., “Geometrical modeling of microstructure of solid oxide fuel cell composite electrodes”, *Journal of Power Sources*, 185, 961–966, 2008.
- Ana, C.M., Song, J.H., Kang, I. and Sammes, N., “The effect of porosity gradient in a nickel/yttria stabilized zirconia anode for an anode-supported planar solid oxide fuel cell”, *Journal of Power Sources*, 195, 821–824, 2010.
- Avrami, M., “Kinetics of phase change. I General theory”, *Journal of Chemical Physics*, 7, 1103–1112, 1939.
- Avrami, M., “Kinetics of phase change. II Transformation-time relations for random distribution of nuclei”, *Journal of Chemical Physics*, 8, 212–224, 1940.
- Avrami, M., ”Granulation, phase change and microstructure kinetics of phase change. III”, *Journal of Chemical Physics*, 9, 177–184, 1941.
- Bandrowski, J., Bickling, C.R., Yang, K.H. and Hougen, O.A., “Kinetics of the reduction of nickel oxide by hydrogen”, *Chemical Engineering Science*, 17, 379–390, 1962.
- Bastidas, D.M., Tao, S. and Irvine J.T.S., “A symmetrical solid oxide fuel cell demonstrating redox stable perovskite electrodes”, *Journal of Materials Chemistry*, 16, 1603–1605, 2006.

Baxter, G.P. and Parsons, L.W., “A comparison of the atomic weights of terrestrial and meteoric nickel I. The reduction of nickelous oxide”, *Journal of the American Chemical Society*, 43, 507–518, 1921.

Benton, A.F. and Emmett, P.H., “The reduction of nickelous and ferric oxides by hydrogen”, *Journal of the American Chemical Society*, 46, 2728–2737, 1924.

Biswas, S., Nithyanantham T., Saraswathi, N. T. and Bandopadhyay, S., “Evaluation of elastic properties of reduced NiO-8YSZ anode supported bi-layer SOFC structures at elevated temperatures in ambient air and reducing environments”, *Journal of Materials Science*, 44, 778–785, 2009.

Blennow, P., Hagen, A., Hansen, K.K., Wallenberg, L.R. and Mogensen, M., “Defect and electrical transport properties of Nb-doped SrTiO₃”, *Solid State Ionics*, 179, 2047–2058, 2008.

Blennow, P., Hansen, K.K., Wallenberg, L.R. and Mogensen, M., “Electrochemical characterization and redox behavior of Nb-doped SrTiO₃”, *Solid State Ionics*, 180, 63–70, 2009.

Blennow, P., Hjelm, J., Klemensø, T., Ramousse, S., Kromp, A., Leonide, A. and Weber, A., “Manufacturing and characterization of metal-supported solid oxide fuel cells”, *Journal of Power Sources*, 196, 7117–7125, 2011.

Busawon, A.N., Sarantaridis, D. and Atkinson, A., “Ni infiltration as a possible solution to the redox problem of SOFC anodes”, *Electrochemical and Solid-State Letters*, 11, B186–B189, 2008.

Chan, S.H. and Xia Z.T., “Anode micro model of solid oxide fuel cell”, *Journal of The Electrochemical Society*, 148, A388–A394, 2001.

Chan, S.H., Chen, X.J. and Khor, K.A., “Cathode micromodel of solid oxide fuel cell”, *Journal of The Electrochemical Society*, 151, A164–A172, 2004.

Chen, X.J., Chan, S.H. and Khor, K.A., “Simulation of a composite cathode in solid oxide fuel cells”, *Electrochimica Acta*, 49, 1851–1861, 2004.

Cheng, Z., Zha, S., Aguilar, L. and Liu, M., “Chemical, electrical, and thermal properties of strontium doped lanthanum vanadate”, *Solid State Ionics*, 176, 1921 – 1928, 2005.

Chiang, L.-K., Liu, H.-C., Shiu, Y.-H., Lee, C.-H. and Lee, R.-Y., “Thermo-electrochemical and thermal stress analysis for an anode-supported SOFC cell”, *Renewable Energy*, 33, 2580– 2588, 2008.

Chiang, L.-K., Liu, H.-C., Shiu, Y.-H., Lee, C.-H. and Lee, R.-Y., “Thermal stress and thermo-electrochemical analysis of a planar anode-supported solid oxide fuel cell: Effects of anode porosity”, *Journal of Power Sources*, 195, 1895–1904, 2010.

Chyou, Y.-P., Chung, T.-D., Chen, J.-S. and Shie, R.-F., “Integrated thermal engineering analyses with heat transfer at periphery of planar solid oxide fuel cell”, *Journal of Power Sources*, 139, 126–140, 2005.

Clague, R., Marquis, A.J. and Brandon, N.P., “Finite element and analytical stress analysis of a solid oxide fuel cell”, *Journal of Power Sources*, 210, 224– 232, 2012.

Costamagna, P., Costa, P. and Antonucci, V., “Micro-modeling of solid oxide fuel cell electrodes”, *Electrochimica Acta*, 43, 375–394, 1998.

Costamagna, P., Selimovic, A., Borghi, M.D. and Agnew, G., “Electrochemical model of the integrated planar solid oxide fuel cell (IP-SOFC)”, *Chemical Engineering Journal*, 102, 61–69, 2004.

Deng, X. and Petric, A., “Geometrical modeling of the triple-phase-boundary in solid oxide fuel cells”, *Journal of Power Sources*, 140, 297–303, 2005.

Dikwal, C.M., Bujalski, W. and Kendall, K., “Characterization of the electrochemical performance of micro-tubular SOFC in partial reduction and oxidation conditions”, *Journal of Power Sources*, 181, 267–273, 2008.

Ettler, M., Blaß, G., and Menzler, N.H., “Characterisation of Ni–YSZ-cermets with respect to redox stability”, *Fuel Cells*, 7, 349-355, 2007.

Ettler, M., Timmermann, H., Malzbender, J., Weber, A. and Menzler, N.H., “Durability of Ni anodes during reoxidation cycles”, *Journal of Power Sources*, 195, 5452–5467, 2010.

Faes, A., Nakajo, A., Wyser, A.H., Dubois, D., Brisse, A., Modena, S. and Van Herle, J., “RedOx study of anode-supported solid oxide fuel cell”, *Journal of Power Sources*, 193, 55–64, 2009.

Faes, A., Frandsen, H.L., Pihlatie, M., Kaiser, A. and Goldstein D.R., “Curvature and strength of Ni-YSZ solid oxide half-cells after redox treatments”, *Journal of Fuel Cell Science and Technology*, 7, 1-8, 2010.

Faes, A., Fuerbringer, J.M., Mohamedic, D., Wysera, A.H., Cabochech, G. and Van Herle, J., “Design of experiment approach applied to reducing and oxidizing tolerance of anode supported solid oxide fuel cell. Part I: Microstructure optimization”, *Journal of Power Sources*, 196, 7058–7069, 2011.

Faes, A., Wullemin, Z., Tanasini, P., Accardo, N. and Van Herle, J., “Redox stable Ni–YSZ anode support in solid oxide fuel cell stack configuration”, *Journal of Power Sources*, 196, 3553–3558, 2011.

Finnerty, C.M., Coe, N.J., Cunningham, R.H. and Ormerod, R.M., “Carbon formation on and deactivation of nickel-based/zirconia anodes in solid oxide fuel cells running on methane”, *Catalysis Today*, 46, 137–145, 1998.

- Fischer, W., Malzbender, J., Blass, G. and Steinbrech, R.W., “Residual stresses in planar solid oxide fuel cells”, *Journal of Power Sources*, 150, 73–77, 2005.
- Fouquet, D., Müller, A.C., Weber, A and Ivers-Tiffée, E., “Kinetics of oxidation and reduction of Ni/YSZ cermets”, *Ionics*, 103–108, 2003.
- Fu, Q.X., Tietz, F., Lersch, P. and Stöver, D., “Evaluation of Sr- and Mn-substituted LaAlO₃ as potential SOFC anode materials”, *Solid State Ionics*, 177, 1059–1069, 2006.
- Fujita, K., Somekawa, T., Horiuchi, K. and Matsuzaki, Y., “Evaluation of the redox stability of segmented-in-series solid oxide fuel cell stacks”, *Journal of Power Sources*, 193, 130–135, 2009.
- Gross, M.D., Carver, K.M., Deighan, M.A., Schenkel, A., Smith, B.M. and Yee, A.Z., “Redox stability of SrNb_xTi_{1-x}O₃-YSZ for use in SOFC anodes”, *Journal of The Electrochemical Society*, 156, B540–B545, 2009.
- Gunji, A., Wen, C., Otomo, J., Kobayashi, T., Ukai, K., Mizutani, Y. and Takahashi, H., “Carbon deposition behaviour on Ni-ScSZ anodes for internal reforming solid oxide fuel cells”, *Journal of Power Sources*, 131, 285–288, 2004.
- Hagen, A., Poulsen, H.F., Klemensø, T., V.Martins, R., Honkimäki, V., Buslaps T. and Feidenshans’l, R., “A depth-resolved in-situ study of the reduction and oxidation of Ni-based anodes in solid oxide fuel cells”, *Fuel Cells*, 6, 361–366, 2006.
- Haldane, M.A. and Etsell, T.H., “Fabrication of composite SOFC anodes”, *Materials Science and Engineering B*, 121, 120–125, 2005.
- Haschka, M., Weickert, T., Krebs, V., Schafer, S. and Tiffée, E.I., “Identification of a nonlinear model for the electrical behavior of a solid oxide fuel cell”, *Journal of Power Sources*, 156, 71–77, 2006.

Hatae, T., Matsuzaki, Y., Yamashita, S. and Yamazaki, Y., “Initial damage to anode microstructure caused by partial redox cycles during electrochemical oxidation”, *Journal of The Electrochemical Society*, 156, B609–B613, 2009.

Hatae, T., Matsuzaki, Y., Yamashita, S., and Yamazaki, Y., “Current density dependence of changes in the microstructure of SOFC anodes during electrochemical oxidation”, *Solid State Ionics*, 180, 1305–1310, 2009.

Hatae, T., Matsuzaki, Y., Yamashita, S., and Yamazaki, Y., “Destruction modes of anode-supported SOFC caused by degrees of electrochemical oxidation in redox cycle”, *Journal of The Electrochemical Society*, 157, B650–B654, 2010.

He, H., Huang, Y., Vohs, J.M. and Gorte, R.J., “Characterization of YSZ–YST composites for SOFC anodes”, *Solid State Ionics*, 175, 171–176, 2004.

Horita, T., Kishimoto, H., Yamaji, K., Xiong, Y., Sakai, N., Brito, M.E. and Yokokawa, H., “Materials and reaction mechanisms at anode/electrolyte interfaces for SOFCs”, *Solid State Ionics*, 177, 1941–1948, 2006.

Hosomi, T., Matsuda, M. and Miyake, M., “Electrophoretic deposition for fabrication of YSZ electrolyte film on non-conducting porous NiO–YSZ composite substrate for intermediate temperature SOFC”, *Journal of the European Ceramic Society*, 27, 173–178, 2007.

Huang, D.X., Chen, C.L. and Jacobson, A.J., “Interface structures and periodic film distortions induced by substrate-surface steps in Gd-doped ceria thin-film growth”, *Journal of Applied Physics*, 97, 1–5, 2005.

Huang, X., Lu, Z., Pei, L., Liu, Z., Liu, Y., Zhu, R., Miao, J., Zhang, Z. and Su, W., “An anode for solid oxide fuel cells: NiO+(Ce_{0.9}Ca_{0.1}O_{1.9})_{0.25}(YSZ)_{0.75} solid solution”, *Journal of Alloys and Compounds*, 360, 294–297, 2003.

Hussain, M.M., Li, X. and Dincer, I., “Mathematical modeling of planar solid oxide fuel cells”, *Journal of Power Sources*, 161, 1012–1022, 2006.

Iwanschitz, B., Sfeir, J., Mai, A. and Schütze, M., “Degradation of SOFC anodes upon redox cycling: A comparison between Ni/YSZ and Ni/CGO”, *Journal of The Electrochemical Society*, 157, B269–B278, 2010.

Iwata, M., Hikosaka, T., Morita, M., Iwanari, T., Ito, K., Onda, K., Esaki, Y., Sakaki, Y. and Nagata, S., “Performance analysis of planar-type unit SOFC considering current and temperature distributions”, *Solid State Ionics*, 132, 297–308, 2000.

Janardhanan, V.M., Heuveline, V. and Deutschmann, O., “Three-phase boundary length in solid-oxide fuel cells: A mathematical model”, *Journal of Power Sources*, 178, 368–372, 2008.

Jeangros, Q., Faes, A., Wagner, J.B., Hansen, T.W., Aschauer, U., Van Herle, J., Hessler-Wyser, A. and Dunin-Borkowski, R.E., “In situ redox cycle of a nickel–YSZ fuel cell anode in an environmental transmission electron microscope”, *Acta Materialia*, 58, 4578–4589, 2010.

Ji, Y., Yuan, K., Chung, J.N. and Chen, Y.-C., “Effects of transport scale on heat/mass transfer and performance optimization for solid oxide fuel cells”, *Journal of Power Sources*, 161, 380–391, 2006.

Jiang, S.P., Chen, X.J., Chan, S.H., Kwok, J.T. and Khor, K.A., “ $(\text{La}_{0.75}\text{Sr}_{0.25})(\text{Cr}_{0.5}\text{Mn}_{0.5})\text{O}_3/\text{YSZ}$ composite anodes for methane oxidation reaction in solid oxide fuel cells”, *Solid State Ionics*, 177, 149–157, 2006.

Jung, H.Y., Hong, K.S., Kim, H., Park, J.K., Son, J.W., Kim, J., Lee, H.W. and J.H. Lee, “Characterization of thin-film YSZ deposited via EB-PVD technique in anode-supported SOFCs”, *Journal of The Electrochemical Society*, 153, A961–A966, 2006.

Karmhag, R., Niklasson, G.A and Nygren, M., “Oxidation kinetics of large nickel particles”, *Journal of Materials Research*, 14, 3051–3058, 1999.

Kendall, K., Finnerty, C.M., Saunders, G. and Chung, J.T., “Effects of dilution on methane entering an SOFC anode”, *Journal of Power Sources*, 106, 323–327, 2002.

Klemensø, T., Appel, C.C. and Mogensen, M., “In situ observations of microstructural changes in SOFC anodes during redox cycling”, *Electrochemical and Solid-State Letters*, 9, A403–A407, 2006.

Klemensø, T. and Mogensen, M., “Ni–YSZ solid oxide fuel cell anode behavior upon redox cycling based on electrical characterization”, *Journal of the American Ceramic Society*, 90, 3582–3588, 2007.

Koh, J.-H., Yoo, Y.-S., Park, J.-W. and Lim, H.C., “Carbon deposition and cell performance of Ni-YSZ anode support SOFC with methane fuel”, *Solid State Ionics*, 149, 157–166, 2002.

Kuo, Y.L., Lee, C., Chen, Y.S. and Liang, H., “Gadolinia-doped ceria films deposited by RF reactive magnetron sputtering”, *Solid State Ionics*, 180, 1421–1428, 2009.

Laurencin, J., Delette, G., Lefebvre-Joud, F. and Dupeux, M., “A numerical tool to estimate SOFC mechanical degradation: Case of the planar cell configuration”, *Journal of the European Ceramic Society*, 28, 1857–1869, 2008.

Laurencin, J., Delette, G., Sicardy, O., Rosini, S. and Joud, F.L., “Impact of ‘redox’ cycles on performances of solid oxide fuel cells: Case of the electrolyte supported cells”, *Journal of Power Sources*, 195, 2747–2753, 2010.

Laurencin, J., Roche, V., Jaboutian, C., Kieffer, I., Mougin, J. and Steil, M.C., “Ni-8YSZ cermet re-oxidation of anode supported solid oxide fuel cell: From kinetics measurements to mechanical damage prediction”, *International Journal of Hydrogen Energy*, 37, 12557–12573, 2012.

Le, S., Sun, K.N., Zhang, N., Zhu, X., Sun, H., Yuan, Y.X. and Zhou, X., “Fabrication and evaluation of anode and thin Y₂O₃-stabilized ZrO₂ film by co-tape casting and cofiring technique”, *Journal of Power Sources*, 195, 2644–2648, 2010.

Lee, K.-R., Pyo, Y.S., So, B.S., Kim, S.M., Lee, B.K., Hwang, J.H., Kim, J., Lee, J.-H. and Lee, H.-W., “Interpretation of the interconnected microstructure of an NiO-YSZ anode composite for solid oxide fuel cells via impedance spectroscopy”, *Journal of Power Sources*, 158, 45–51, 2006.

Lin, C.-K., Chen, T.-T., Chyou, Y.-P. and Chiang, L.-K., “Thermal stress analysis of a planar SOFC stack”, *Journal of Power Sources*, 164, 238–251, 2007.

Lin, C.-K., Huang, L.-H., Chiang, L.-K. and Chyou, Y.-P., “Thermal stress analysis of planar solid oxide fuel cell stacks: Effects of sealing design”, *Journal of Power Sources*, 192, 515–524, 2009.

Lu, C., An, S., Worrell, W.L., Vohs, J.M. and Gorte, R.J., “Development of intermediate-temperature solid oxide fuel cells for direct utilization of hydrocarbon fuels”, *Solid State Ionics*, 175, 47–50, 2004.

Lu, Y., Schaefer, L. and Li, P., “Numerical study of a flat-tube high power density solid oxide fuel cell Part I. Heat/mass transfer and fluid flow”, *Journal of Power Sources*, 140, 331–339, 2005.

Ma, Q., Tietz, F., Leonide, A. and Tiffée, E.I., “Anode-supported planar SOFC with high performance and redox stability”, *Electrochemistry Communications*, 12, 1326–1328, 2010.

Majhi, S.M., Behura, S.K., Bhattacharjee, S., Singh, B.P., Chongdar, T.K., Gokhale, N.M. and Besra, L., “Anode supported solid oxide fuel cells (SOFC) by electrophoretic deposition”, *International Journal of Hydrogen Energy*, 36, 14930–14935, 2011.

Matsuda, M., Hosomia, T., Murata, K., Fukui, T. and Miyake, M., “Fabrication of bilayered YSZ/SDC electrolyte film by electrophoretic deposition for reduced temperature operating anode-supported SOFC”, *Journal of Power Sources*, 165, 102–107, 2007.

McIntosh, S., Vohs, J.M. and Gorte, R.J., “An examination of lanthanide additives on the performance of Cu-YSZ cermet anodes”, *Electrochimica Acta*, 47, 3815–3821, 2002.

Meng, B., He, X., Sun, Y. and Li, M., “Preparation of YSZ electrolyte coatings for SOFC by electron beam physical vapor deposition combined with a sol infiltration treatment”, *Materials Science and Engineering: B*, 150, 83–88, 2008.

Meng, G., Song, H., Dong, Q. and Peng, D., “Application of novel aerosol-assisted chemical vapor deposition techniques for SOFC thin films”, *Solid State Ionics*, 175, 29–34, 2004.

Montross, C. S. Yokokawa, H. and Dokiya, M., “Thermal stresses in planar solid oxide fuel cells due to thermal expansion differences”, *British Ceramic Transactions*, 101, 85–93, 2002.

Mori, M., Hiei, Y., Itoh, H., Tompsett, G.A. and Sammes, N.M., “Evaluation of Ni and Ti-doped Y₂O₃ stabilized ZrO₂ cermet as an anode in high-temperature solid oxide fuel cells”, *Solid State Ionics*, 160, 1–14, 2003.

Mosch, S., Trofimenko, N., Kusnezoff, M., Betz, T. and Kellner, M., “Long-term and redox stability of electrolyte supported solid oxide fuel cells under various operating conditions”, *ECS Transactions*, 7, 381–388, 2007.

Murthy, S. and Fedorov, A.G., “Radiation heat transfer analysis of the monolith type solid oxide fuel cell”, *Journal of Power Sources*, 124, 453–458, 2003.

Nakajo, A., Wullemin, Z., Van herle, J. and Favrat, D., “Simulation of thermal stresses in anode-supported solid oxide fuel cell stacks. Part I: Probability of failure of the cells”, *Journal of Power Sources*, 193, 203–215, 2009.

Nakajo, A., Wullemin, Z., Van herle, J. and Favrat, D., “Simulation of thermal stresses in anode-supported solid oxide fuel cell stacks. Part II: Loss of gas-tightness, electrical contact and thermal buckling”, *Journal of Power Sources*, 193, 216–226, 2009.

Nakajo, A., Mueller, F., Brouwer, J., Van herle, J. and Favrat, D., “Mechanical reliability and durability of SOFC stacks. Part II: Modelling of mechanical failures during ageing and cycling”, *International Journal of Hydrogen Energy*, 37, 9269–9286, 2012.

Nakajo, A., Mueller, F., Brouwer, J., Van herle, J. and Favrat, D., “Mechanical reliability and durability of SOFC stacks. Part I : Modelling of the effect of operating conditions and design alternatives on the reliability”, *International Journal of Hydrogen Energy*, 37, 9249–9268, 2012.

Ouweltjes, J.P., Van Tuel, M., Sillessen, M. and Rietveld, G., “Redox tolerant SOFC anodes with high electrochemical performance”, *Fuel Cells*, 9, 873–882, 2009.

Park, H.G., Moon, H., Park, S.C., Lee, J.J., Yoon, D., Hyun, S.H. and D.H. Kim, “Performance improvement of anode-supported electrolytes for planar solid oxide fuel cells via a tape-casting/lamination/co-firing technique”, *Journal of Power Sources*, 195, 2463–2469, 2010.

Park, J., Bae, J. and Kim, J.-Y., “The current density and temperature distributions of anode-supported flat-tube solid oxide fuel cells affected by various channel designs”, *International Journal of Hydrogen Energy*, 36, 9936–9944, 2011.

Parravano, G., “The reduction of nickel oxide by hydrogen”, *Journal of the American Chemical Society*, 74, 1194–1198, 1952.

Patcharavorachot, Y., Arpornwichanop, A. and Chuachuensuk, A., “Electrochemical study of a planar solid oxide fuel cell: Role of support structures”, *Journal of Power Sources*, 177, 254–261, 2008.

Peraldi, R., Monceau, D., and Pieraggi, B., “Correlations between growth kinetics and microstructure for scales formed by high-temperature oxidation of pure nickel. II. growth kinetics”, *Oxidation of Metals*, 58, 275–295, 2002.

Pihlatie, M., Kaiser, A. and Mogensen, M., “Mechanical properties of NiO/Ni–YSZ composites depending on temperature, porosity and redox cycling”, *Journal of the European Ceramic Society*, 29, 1657–1664, 2009.

Pihlatie, M., Kaiser, A. and Mogensen, M., “Redox stability of SOFC: Thermal analysis of Ni–YSZ composites”, *Solid State Ionics*, 180, 1100–1112, 2009.

Pihlatie, M., Kaiser, A., Larsen, P.H. and Mogensen, M., “Dimensional behavior of Ni–YSZ composites during redox cycling”, *Journal of The Electrochemical Society*, 156, B322–B329, 2009.

Pihlatie, M.H., Frandsen, H.L., Kaiser, A. and Mogensen, M., “Continuum mechanics simulations of NiO/Ni–YSZ composites during reduction and re-oxidation”, *Journal of Power Sources*, 195, 2677–2690, 2010.

Pryds, N., Toftmann, B., Bilde-Sørensen, J.B., Schou, J. and Linderøth, S., “Thickness determination of large-area films of yttria-stabilized zirconia produced by pulsed laser deposition”, *Applied Surface Science*, 252, 4882–4885, 2006.

Pudmich, G., Boukamp, B.A., Gonzalez-Cuenca, M., Jungen, W., Zipprich, W. and Tietz, F., “Chromite/ titanate based perovskites for application as anodes in solid oxide fuel cells”, *Solid State Ionics*, 135, 433–438, 2000.

Pusz, J., Smirnova, A., Mohammadi, A. and Sammes, N.M., “Fracture strength of micro-tubular solid oxide fuel cell anode in redox cycling experiments”, *Journal of Power Sources*, 163, 900–906, 2007.

Radovic, M. and Lara-Curzio, E., “Mechanical properties of tape cast nickel-based anode materials for solid oxide fuel cells before and after reduction in hydrogen”, *Acta Materialia*, 52, 5747–5756, 2004.

Richardson, J.T., Scates, R. and Twigg, M.V., “X-ray diffraction study of nickel oxide reduction by hydrogen”, *Applied Catalysis A: General* 246, 137–150, 2003.

Rodrigo, K., Knudsen, J., Pryds, N., Schou, J. and Linderoth, S., “Characterization of yttria-stabilized zirconia thin films grown by pulsed laser deposition (PLD) on various substrates”, *Applied Surface Science*, 254, 1338–1342, 2007.

Sarantaridis, D., Chater, R.J. and Atkinson, A., “Changes in physical and mechanical properties of SOFC Ni–YSZ composites caused by redox cycling”, *Journal of The Electrochemical Society*, 155, B467–B472, 2008.

Sarantaridis, D., Rudkin, R.A. and Atkinson, A., “Oxidation failure modes of anode-supported solid oxide fuel cells”, *Journal of Power Sources*, 180, 704–710, 2008.

Sasaki, K., Muranaka, M., Suzuki, A. and Terai, T., “Synthesis and characterization of LSGM thin film electrolyte by RF magnetron sputtering for LT-SOFCS”, *Solid State Ionics*, 179, 1268–1272, 2008.

Sauvet, A.-L. and Fouletier, J., “Catalytic properties of new anode materials for solid oxide fuel cells operated under methane at intermediary temperature”, *Journal of Power Sources*, 101, 259–266, 2001.

Sauvet, A.L. and Irvine, J.T.S., “Catalytic activity for steam methane reforming and physical characterisation of $\text{La}_{1-x}\text{Sr}_x\text{Cr}_{1-y}\text{Ni}_y\text{O}_{3-\delta}$ ”, *Solid State Ionics*, 167, 1–8, 2004.

Schmidt, M.S., Hansen, K.V., Norrman, K. and Mogensen, M., “Characterisation of the Ni/ScYSZ interface in a model solid oxide fuel cell anode”, *Solid State Ionics*, 179, 2290–2298, 2008.

Selçuk, A., Merere, G. and Atkinson, A., “The influence of electrodes on the strength of planar zirconia solid oxide fuel cells”, *Journal of Materials Science*, 36, 1173–1182, 2001.

Selimovic, A., Kemm, M., Torisson, T. and Assadi, M., “Steady state and transient thermal stress analysis in planar solid oxide fuel cells”, *Journal of Power Sources*, 145, 463–469, 2005.

Skarmoutsos, D., Tsoga, A., Naoumidis, A. and Nikolopoulos, P., “5 mol% TiO₂-doped Ni–YSZ anode cermets for solid oxide fuel cells”, *Solid State Ionics*, 135, 439–444, 2000.

Smith, B.H., Holler, W.C. and Gross, M.D., “Electrical properties and redox stability of tantalum-doped strontium titanate for SOFC anodes”, *Solid State Ionics*, 192, 383–386, 2011.

Srikanth, V.T., Turner, K.T., Lee, T.Y.A. and Spearing, S.M., “Structural design considerations for micromachined solid-oxide fuel cells”, *Journal of Power Sources*, 125, 62–69, 2004.

Stathis, G., Simwonis, D., Tietz, F., Moropoulou, A. and Naoumidis, A., “Oxidation and resulting mechanical properties of Ni/8Y₂O₃-stabilized zirconia anode substrate for solid-oxide fuel cells”, *Journal of Materials Research*, 17, 951–958, 2002.

Sumi, H., Kishida, R., Kim, J.Y., Muroyama, H., Matsui, T. and Eguchi, K., “Correlation between microstructural and electrochemical characteristics during redox cycles for Ni–YSZ anode of SOFCs”, *Journal of The Electrochemical Society*, 157, B1747–B1752, 2010.

Suzuki, M., Shikazono, N., Fukagata, K. and Kasagi, N., “Numerical analysis of coupled transport and reaction phenomena in an anode-supported flat-tube solid oxide fuel cell”, *Journal of Power Sources*, 180, 29–40, 2008.

Taylor, G.B. and Starkweather, H.W., “Reduction of metal oxides by hydrogen”, *Journal of the American Chemical Society*, 52, 2314–2325, 1930.

Tikekar, N.M., Armstrong, T.J. and Virkar, A.V., “Reduction and reoxidation kinetics of nickel-based SOFC anodes”, *Journal of the Electrochemical Society*, 153, A654–A663, 2006.

Utigard, T.A., Wu, M., Plascencia, G. and Marin, T., “Reduction kinetics of Goro nickel oxide using hydrogen”, *Chemical Engineering Science*, 60, 2061–2068, 2005.

Vedasri, V., Young, J.L. and Birss, V.I., “A possible solution to the mechanical degradation of Ni–yttria stabilized zirconia anode-supported solid oxide fuel cells due to redox cycling”, *Journal of Power Sources*, 195, 5534–5542, 2010.

Waldbillig, D., Wood, A. and Ivey, D.G., “Thermal analysis of the cyclic reduction and oxidation behaviour of SOFC anodes”, *Solid State Ionics*, 176, 847–859, 2005.

Waldbillig, D., Wood, A. and Ivey, D.G., “Electrochemical and microstructural characterization of the redox tolerance of solid oxide fuel cell anodes”, *Journal of Power Sources*, 145, 206–215, 2005.

Waldbillig, D., Wood, A. and Ivey, D.G., “Enhancing the redox tolerance of anode-supported SOFC by microstructural modification”, *Journal of The Electrochemical Society*, 154, B133–B138, 2007.

Wang, C., Luo, L., Wu, Y., Hou, B. and Sun, L., “A novel multilayer aqueous tape casting method for anode-supported planar solid oxide fuel cell”, *Materials Letters*, 65, 2251–2253, 2011.

Wang, S., Ando, M., Ishihara, T. and Takita, Y., “High performance Ni–Sm_{0.15}Ce_{0.85}O_{2-d} cermet anodes for intermediate temperature solid oxide fuel cells using LaGaO₃ based oxide electrolytes”, *Solid State Ionics*, 174, 49–55, 2004.

Wood, A., Pastula, M., Waldbillig D. and Ivey, D.G., “Initial testing of solutions to redox problems with anode-supported SOFC”, *Journal of The Electrochemical Society*, 153, A1929–A1934, 2006.

Xia, W., Yang, Y. and Qiusheng, W., “Effects of operations and structural parameters on the one-cell stack performance of planar solid oxide fuel cell”, *Journal of Power Sources*, 194, 886–898, 2009.

Xia, Z.T., Chan, S.H. and Khor, K.A., “An improved anode micro model of SOFC”, *Electrochemical and Solid-State Letters*, 7, A63–65, 2004.

Xie, Z., Zhu, W., Zhu, B. and Xia, C., “Fe_xCo_{0.5-x}Ni_{0.5}–SDC anodes for low-temperature solid oxide fuel cells”, *Electrochimica Acta*, 51, 3052–3057, 2006.

Yakabe, H., Ogiwara, T., Hishinuma, M. and Yasuda, I., “3-D model calculation for planar SOFC”, *Journal of Power Sources*, 102, 144–154, 2001.

Yakabe, H., Baba, Y., Sakurai, T. and Yoshitaka, Y., “Evaluation of the residual stress for anode-supported SOFCs”, *Journal of Power Sources*, 135, 9–16, 2004.

Yakabe, H., Baba, Y., Sakurai, T., Satoh, M., Hirosawa, I. and Yoda, Y., “Evaluation of residual stresses in a SOFC stack”, *Journal of Power Sources*, 131, 278–284, 2004.

Yang, D., Zhang, X., Nikum, S., Petit, C.D., Hui, R., Maric, R. and Ghosh, D., “Low temperature solid oxide fuel cells with pulsed laser deposited bi-layer electrolyte”, *Journal of Power Sources*, 164, 182–188, 2007.

Yin, Y., Li, S., Xia, C. and Meng, G., “Electrochemical performance of gel-cast NiO–SDC composite anodes in low-temperature SOFCs”, *Electrochimica Acta*, 51, 2594–2598, 2006.

Young, J.L. and Birss, V.I., “Crack severity in relation to non-homogeneous Ni oxidation in anode-supported solid oxide fuel cells”, *Journal of Power Sources*, 196, 7126–7135, 2011.

Yuan, J., Rokni, M. and Sunden, B., “Three-dimensional computational analysis of gas and heat transport phenomena in ducts relevant for anode-supported solid oxide fuel cells”, *International Journal of Heat and Mass Transfer*, 46, 809–821, 2003.

Zhang, Y., Liu, B., Tu, B., Dong, Y. and Cheng, M., “Redox cycling of Ni–YSZ anode investigated by TPR technique”, *Solid State Ionics*, 176, 2193–2199, 2005.

Zhu, H. and Kee, R.J., “A general mathematical model for analyzing the performance of fuel-cell membrane-electrode assemblies”, *Journal of Power Sources*, 117, 61–74, 2003.

Zhu, W., Xia, C., Fan, J., Peng, R. and Meng, G., “Ceria coated Ni as anodes for direct utilization of methane in low-temperature solid oxide fuel cells”, *Journal of Power Sources*, 160, 897–902, 2006.

Zhu, W.Z. and Deevi, S.C., “A review on the status of anode materials for solid oxide fuel cells”, *Materials Science and Engineering*, A362, 228–239, 2003.

CURRICULUM VITAE

Bora TIMURKUTLUK was born in 25.12.1982 in Sivas, Turkey. He has completed the primary education in Sivas. He graduated from the Mechanical Engineering Department of Middle East Technical University in 2004. He completed MS studies at the same department in 2007. He worked as a technical leader in the Hydrogen Technologies Laboratory in Nigde University between 2006 and 2010. Since 2010, he has worked as a specialist R&D mechanical engineer in Vestel Defence Industries A.Ş.